



**3D Geomodeling for Europe**  
*Project number: GeoE.171.005*

## **Deliverable 6.4**

**Optimized 3D reconstruction  
workflow based on  
gravimetric, structural and  
petrophysical data.**

Authors and affiliation:

**Emilio L. Pueyo (IGME/CSIC)**  
**Conxi Ayala (IGME/CSIC\*)**  
**Esther Izquierdo-Llavall (UPPA)**  
**Félix M. Rubio (IGME/CSIC)**  
**Pablo Santolaria (UB)**  
**Pilar Clariana (IGME/CSIC)**  
**Ruth Soto (IGME/CSIC)**  
**Christian Olaf Müller (LAGB)**  
**Carmen Rey-Moral (IGME/CSIC)**  
**Björn Zehner (BGR)**  
**Adrià Ramos (IGME/CSIC)**  
**Alexander Malz (LAGB)**  
**Gregor Goetzl (GSA)**  
**Rosibeth Toro (UZ)**  
**Teresa Roman Berdiel (UZ)**  
**Antonio M. Casas (UZ)**  
**José L. G<sup>a</sup> Lobón (IGME/CSIC)**

[IGME/CSIC] [UPPA] [UB] [LAGB] [BGR] [GSA] [UZ]

E-mail of lead author:

[unaim@igme.es](mailto:unaim@igme.es)

Version 3: 27-10-2021

This report is part of a project that has received funding by the European Union's Horizon 2020 research and innovation programme under grant agreement number 731166



<b>Deliverable Data</b>		
<b>Deliverable number</b>	D6.4	
<b>Dissemination level</b>	Public	
<b>Deliverable name</b>	<b>Optimized 3D reconstruction workflow based on gravimetric, structural and petrophysical data.</b>	
<b>Work package</b>	WP6, Optimizing reconstructions of the subsurface to reduce structural uncertainty in 3D models	
<b>Lead WP/Deliverable beneficiary</b>	IGME	
<b>Deliverable status</b>		
<b>Submitted (Author(s))</b>	27/10/2021	Emilio L. Pueyo
<b>Verified (WP leader)</b>	27/10/2021	Emilio L. Pueyo (IGME/CSIC)
<b>Approved (Coordinator)</b>	29/10/2021	Stefan Knopf

(\*): present address Geosciences Barcelona-CSIC

**Cite this report as:** Pueyo, E.L.; Ayala, C.; Izquierdo-Llavall, E.; Rubio, F.M.; Santolaria, P.; Clariana, P.; Soto, R.; Müller, C.O.; Rey-Moral, C.; Zehner, B.; Ramos, A.; Malz, A.; Goetzl, G.; Toro, R.; Roman-Berdiel, M.T.; Casas, A.M.; García-Lobón, J.L. (2021). Deliverable 6.4. Optimized 3D reconstruction workflow based on gravimetric, structural and petrophysical data. GEOERA 3DGEO-EU, 3D Geomodeling for Europe, project number GeoE.171.005. Report, 264 p.

## Abstract for stakeholders

For several reasons, 3D geological modeling harmonization was one of the main goals of the 3DGEO-EU project. Beyond deeply explored regions in Europe (e.g. North Sea), **large portions of the continent display scarce subsurface information** (seismic exploration and wells) because they were ruled out for hydrocarbon research; the geological setting precluded the oil maturation (shallow basins or, the other way around, highly-subsiding basins), large portions of the Variscan and Caledonic basements, highly inaccessible mountainous regions (Alps, Pyrenees, Carpathians, etc.). Besides, an additional problem dealing with the data availability inherited from oil industry is the **difficult access to raw information (poor FAIR policies)**, since very often they belong to the private sector, or because (when public) they are considered strategic or are under embargo (even for the Geological Surveys). Finally, even if the access is granted, local **policies limited the third-party sharing of the information** and then, makes very difficult the cross-border harmonization. In conclusion, it is a fact that the European subsurface knowledge is very heterogeneous and it is very poor in some areas. This situation **prevents to fully tackle two key challenges**: the building of a **harmonized Pan-European 3D model** in the near future as well as the **evaluation of some keystones of the European Green Agenda** (and in the Energy System Transition) like: structures for CO<sub>2</sub> and Hydrogen storages, deep geothermal reservoirs, etc..

The WP6 of the 3DGEO-EU project has faced this problem and has focused on **potential field geophysics** (particularly gravimetrics) and classic structural geology techniques as **quick, cost-effective and efficient methods for 3D modeling**, especially useful for the harmonization of cross-borders regions (Northern German/Polish border) or regions with scarce and heterogeneous subsurface information or areas where the access to the subsurface information is restricted (SW Pyrenees).

Since decades, the **gravimetric method** is a well-founded and established technique for subsurface exploration. However, and considering our focus, we emphasize the need of two additional key elements; the use of structural techniques (in particular **balanced and restored cross sections**) and the attaining of **robust petrophysical data** for the modeling. In this document we do not pretend to write a reference book, but a practical manual based on common procedures used by some EGS members (and some universities), a practical review of methods, instrumentation and software, etc. that are later on illustrated with examples from previous works. In conclusion, the “Optimized 3D reconstruction workflow” here introduced, is based on a deep synthesis, discussion and feedback process among many members of the project team and GeoERA Energy community.

## Summarized technical description

The workflow is organized in three levels (sections §) depending upon the degree of the processing and the number of dimensions considered. The first level (top of Fig. 1.4) refers to the raw data needed for the modelling (Subsection 2 in this report). A brief and updated review of theoretical principles, instrumentation and campaign design of gravimetric data (§2.1) together with corrections, software packages, data formats and databases as well as a succinct analysis on uncertainty sources. Then (§2.2), it follows a review of basic concepts and techniques of cross section balancing and restoration, followed by an outline of uncertainty sources and common pitfalls. Later (§2.3), we synthesize field and laboratory procedures involved in petrophysical characterization as well as data formats, databases and, again, a concise analysis on sources of uncertainty. The second level deals with 2D joint modelling of the three variables together (in two ways; gravity maps and cross sections). In §3.1, we succinctly review the processing required to obtain the Bouguer, regional and residual maps, etc., and then (§3.2), the 2D and 2.5D feedback process (forward modelling) usually performed until the calculated gravity anomaly consistently match the observations (2D integrated model) and then validates the 3D reconstruction. Successively, in level 3 (§3.2) an integrated 3D structural model is built merging all data together – petrophysical, geological and gravimetric to obtain a 3D geological model with attributes (and associated uncertainties) can be performed by geophysical inversion in several software platforms during a feedback process that lasts until a reasonable solution is achieved (calculated gravity signal reasonably match the observed one).





---

## TABLE OF CONTENTS

<b>1. Introduction</b>	<b>4</b>
1.1 Motivation and goals	4
1.2 Scope of this workflow and overview of the sections	11
<b>2. Raw data sources before the modelling</b>	<b>14</b>
<b>2.1. Gravity data</b>	<b>14</b>
2.1.1 Theoretical principles	15
2.1.2 Instrumentation	16
2.1.2.1 Gravimeters	16
2.1.2.2 Most common land gravimeters	18
2.1.2.3 GPS receivers	24
2.1.3 Gravimetric survey design and control	27
2.1.3.1 Gravity Bases network	27
2.1.3.2 Local Bases	28
2.1.3.3 Sampling design and station distribution	30
2.1.3.4 Calibration of gravimeters	37
2.1.3.5 Coordinate acquisition using GNSS	40
2.1.4 Gravity corrections	48
2.1.4.1 Observed gravity	49
2.1.4.2 Theoretical gravity	50
2.1.5 Gravimetric data model and databases	55
2.1.6. Common software used in gravity surveys	60
2.1.7 Uncertainty sources in gravimetric data	61
<b>2.2. Balanced and Restored cross-sections</b>	
2.2.1. Introduction	63
2.2.2. Background	63
2.2.3. Cross-section construction	64
2.2.3.1 Cross-section design	65
2.2.3.2 Data projection	66
2.2.3.3 Interpretation of the structure	66
2.2.4. 2D Restoration and balancing	70
2.2.4.1. Concept	70
2.2.4.2. Assumptions and methods	73
2.2.4.3. Forward modelling	75
2.2.5. Uncertainties and pitfalls.	77
2.2.5.1. Data uncertainties (geological and geophysical data)	78
2.2.5.2. Matrix and meso-scale deformation	80
2.2.5.3. Uncertainties related to the determination of line lengths and areas	82
2.2.5.4. Out-of-plane deformation	83



---

2.2.5.5. Extensional faults	83
2.2.5.6. Salt tectonics	84
<b>2.2.6. Examples of 2D restored and balanced cross-sections</b>	<b>87</b>
2.2.6.1. The Puerta-Pareja anticline (Loranca basin, Spain)	87
2.2.6.2. Linking Zone (Iberian Range, Spain)	89
<b>2.2.7. 3D restoration</b>	<b>93</b>
<b>2.2.8. Backstripping</b>	<b>96</b>
<b>2.2.9. Example of backstripping</b>	<b>99</b>

### **2.3. Petrophysics**

<b>2.3.1 Introduction</b>	<b>103</b>
<b>2.3.2 Field and laboratory procedures</b>	<b>107</b>
2.3.2.1 Field sampling and field measurements	107
2.3.2.2 Laboratory procedures	113
2.3.2.3 Paleomagnetic samples	119
2.3.2.4 Data representation and characterization	126
<b>2.3.3 Well Logging data</b>	<b>129</b>
2.3.3.1 Formation density logs	129
2.3.3.2 Borehole Gravimetry	133
2.3.3.3 Dual-energy CT density from borehole cores	120
<b>2.3.4 Petrophysical relationships with other variables</b>	<b>137</b>
2.3.4.1 Magnetic and density relationships (Henkel's plot)	137
2.3.4.2 Density at depth	142
2.3.4.3 Density and other variables	144
<b>2.3.5 Data models and Databases</b>	<b>145</b>
<b>2.3.6 Uncertainty sources in petrophysical data</b>	<b>152</b>

## **3. Interpretation and modelling of gravity data**

<b>3.1. Gravity anomaly maps and enhancement techniques</b>	<b>155</b>
3.1.1 Introduction (beyond Bouguer anomaly maps)	155
3.1.2 Bouguer, Regional and Residual anomalies	157
3.1.3 Filtering	159
3.1.4 Upward-downward continuation	159
3.1.5 Derivatives of the gravity field	161
3.1.6 Continuous and discrete wavelet transforms	163
3.1.7 Euler deconvolution	163
3.1.8. Werner deconvolution	164



---

3.1.9 Some studied cases	166
3.1.9.1 Sinkholes in the Ebro Basin	167
3.1.9.2 Characterization of salt structures	168
3.1.9.3 Assessing structural style lateral variations	176
3.1.9.4 Fault identification in the North German Basin	180
<b>3.2. 2D &amp; 3D Gravity modelling</b>	
3.2.1 Introduction	185
3.2.2 Gravity modelling techniques	186
3.2.2.1 Forward modelling	186
3.2.2.2 Inversion	187
3.2.3 2D & 3D Modelling software	189
3.2.3.1 Gravmag (BGS) and other packages	189
3.2.3.2 2D, 2.5D & 3D Modelling with Oasis Montaj	191
3.2.3.2.1 2D and 2.5D Modelling GM-SYS	192
3.2.3.2.2 3D Modelling GM-SYS 3D	194
3.2.3.3 3D Modelling with 3DGeoModeller	195
3.2.4 Uncertainty in 2D, 2.5D and 3D modelling	200
3.2.5 Case studies	202
3.2.5.1. Linking Zone (Iberian Range, Spain)	202
3.2.5.1.1 Bouguer and residual Bouguer anomaly	203
3.2.5.1.2 2.5D modelling with GMSYS. Feedback geology-geophysics.	204
3.2.5.1.3 3D gravity modelling (forward modelling and stochastic inversion)	210
3.2.5.2. Barbastro anticline (South Pyrenean triangle zone, Spain)	223
3.2.5.3. Gravity modelling in the North German Basin with IGMAS+	225
<b>4. Conclusions, recommendation and lessons to be learnt.</b>	<b>231</b>
<b>5. References</b>	<b>233</b>



## 1 Introduction

### 1.1 Motivation and goals

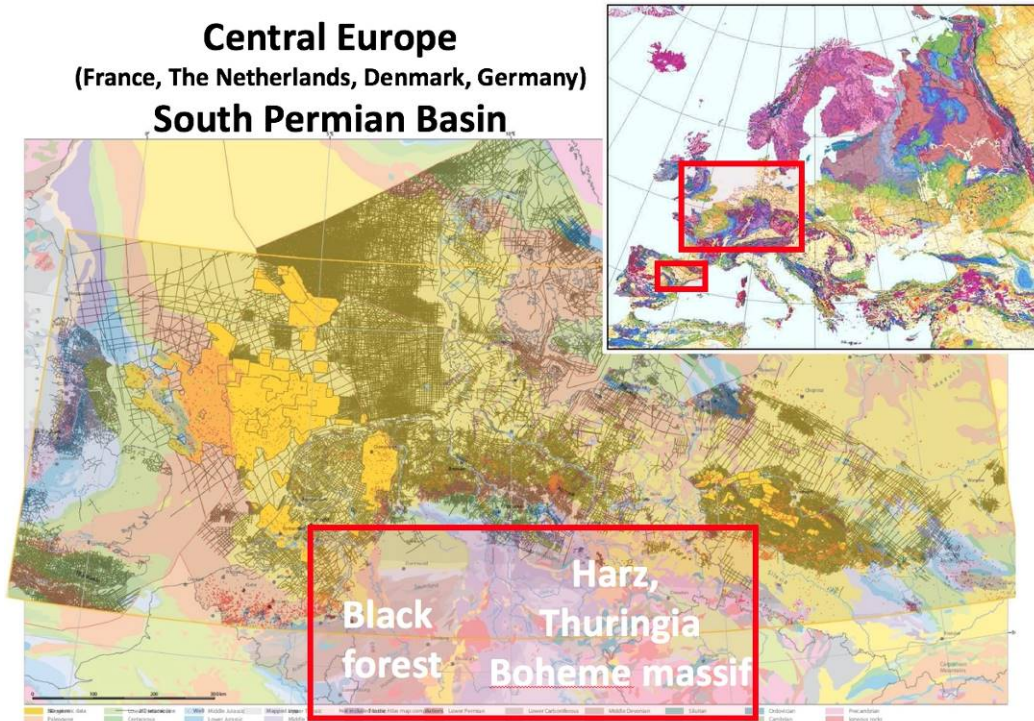
Characterizing and understanding the subsurface geology has always been one of the main targets in Earth Sciences. Nowadays the development of technical tools for 3D modelling allows tackling key socio-economic challenges that depends on various scales. At intermediate depths (from 1 to 5-6 km), and beyond the petroleum geology, some strategic applications stand out; energy and gas reservoirs (pressurized, natural, Hydrogen or CO<sub>2</sub>, etc.), geothermal reservoirs, deep water resources, etc. At much shallower depths, we can highlight risk managements (seismogenic, geotechnical, volcanic, etc.), superficial aquifers (including water energy storages), low-enthalpy geothermal energy, strategic mineral resources, tunnelling, etc.

In the current framework of an energy system still based on an important share of unsustainable sources (fossil fuels), both for its scarcity and for its negative impact on climate, Europe has decided to fully decarbonize its energy system before 2050. This commitment is fully aligned to the United Nations' 2030 Green Agenda (NGA) and expects to reduce European emissions by 50-55% already by 2030. The Green Deal affects some of the 17 Sustainable Development Goals (SDGs) of the NGA, in particular those focused on the energy transition & decarbonisation (Climate, Energy and Mobility: Energy Supply, Communities and Cities, Energy Storage. Low-Carbon and Clean Industries, etc.). The European Commission will strengthen proposals, policies and strategies to reach them. Specifically, the European Green Deal on Clean Energy will boost new and proven technologies for large-scale, subsurface, renewable energy storage (hydrogen, green gas, compressed air, geothermal) deliver the capacity (power and duration) needed for integration of high shares of intermittent renewables.

The scientific community (IPCC, 2018) has identified Carbon Capture and Storage (CCS; Rogeli et al., 2018) technologies and geothermal energy sources as keystones to meet the global climate ambitions of the Paris Agreement (2015) and to transform the energy system in the near future (so called "green transition") since the widespread deployment of geothermal energy could play a meaningful role in mitigating climate change (Goldstein et al., 2011). The Strategic and Research and Innovation Agenda (SRIA; Eurogeosurveys, 2021) of the European Geological Surveys fully supports this vision and has identified these topics in its research priorities. A determined boosting of CCS technologies and geothermal energy (both topics require an integrative and comprehensive subsurface understanding) already had a strong impact on past European research framework programs as well as in subsequent private investments (FP6&FP7&FP8-H2020; see for example the project inventory at <https://www.geothermalresearch.eu/>). It is expected that these topics will be maximized in Horizon Europe (FP9) in the frame of the Green Deal.



### Central Europe (France, The Netherlands, Denmark, Germany) South Permian Basin



### Seismic exploration in NE Spain

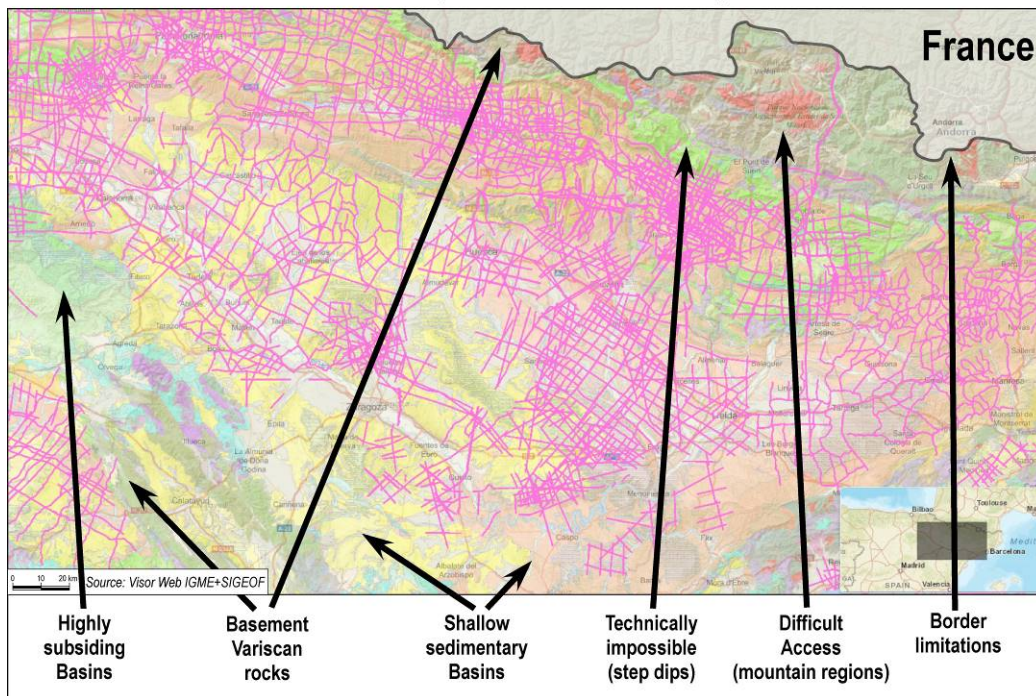


Figure 1.1. Seismic coverage in Central Europe and the North Sea (Doornenbal & Stevenson, 2010) and NE Spain (SIGEOF viewer Plata et al., 2008) highlighting some deficiencies in exploration data of the subsurface caused by a number of different reasons.



This situation is not exempt of paradoxes; the petroleum geology has been the great engine of knowledge and data generation in Earth Sciences for the subsurface geology; multibillion dollar investments in reflection seismic and wells and profuse methodological and conceptual developments during the last 5 decades (or more). Nevertheless, the application of oil industry exploration techniques (mostly reflection seismic and wells) have been very selective; basins with high subsidence and orogenic areas with relatively low deformation (basically, but not only, Cenozoic and Mesozoic basins) or it has been unsuitable due to technical issues (steep dips, geographic remoteness, etc.).

Focusing on Europe, large regions display scarce subsurface information (Fig. 1.1) because they were ruled out for hydrocarbon research (out of the oil window); e.g. shallow basins (thin enough to preclude oil maturation), highly-subsidence basins (beyond the oil window), Variscan and Caledonic basement and highly-deformed areas (although their foreland basins were deeply investigated), highly mountainous regions (Alps, Pyrenees, Carpathians, etc.). An additional problem dealing with the data availability inherited from oil industry is the difficult access to raw data (poor FAIR policies), since very often they belong to the private sector, or because (when public) they are considered strategic. This accessibility problem has seldom solved in many countries. The Netherlands are an exception in this regard, policy makers have ruled specific laws (Article 123 of the Mining Act, 2012, the so-called BRO Law) to fully recover subsurface information from private exploration and exploitation activities in order to serve societal challenges with data repositories guided by FAIR principles under the management of TNO (<https://www.thermogis.nl/en>; Bonté et al., 2012; Vrijlandt et al., 2019).

Interestingly, many regions discarded for oil and gas exploration (Fig. 1.1) could be evaluated in Europe in the near future for:

- its geothermal potentiality (up to 4-5 km in depth and up to 70-90°C or more),
- its suitability as gas reservoirs (Methane, CO<sub>2</sub> or Hydrogen)
- as energy reservoirs (e.g. combined cycles with other renewable sources),
- its potentiality as water storages (especially in southern Europe),
- the occurrence of strategic/technologic minerals,
- or because they are crossed by planned transport networks (tunnelling), etc.

The subsurface geology of the 21<sup>st</sup> century has to face this situation and has to adapt to be operational (times and investments necessary) and effective during the decision-making processes. Tackling all the aforementioned challenges mainly concerns to the administrations and public research agents (at least in early stages). In this framework, the optimization of workflows in 3D reconstruction based on efficient geophysical methods (in addition to conventional geological and geophysical information) is a keystone for reaching the European Green Deal, especially in those areas with scarce previous subsurface information.

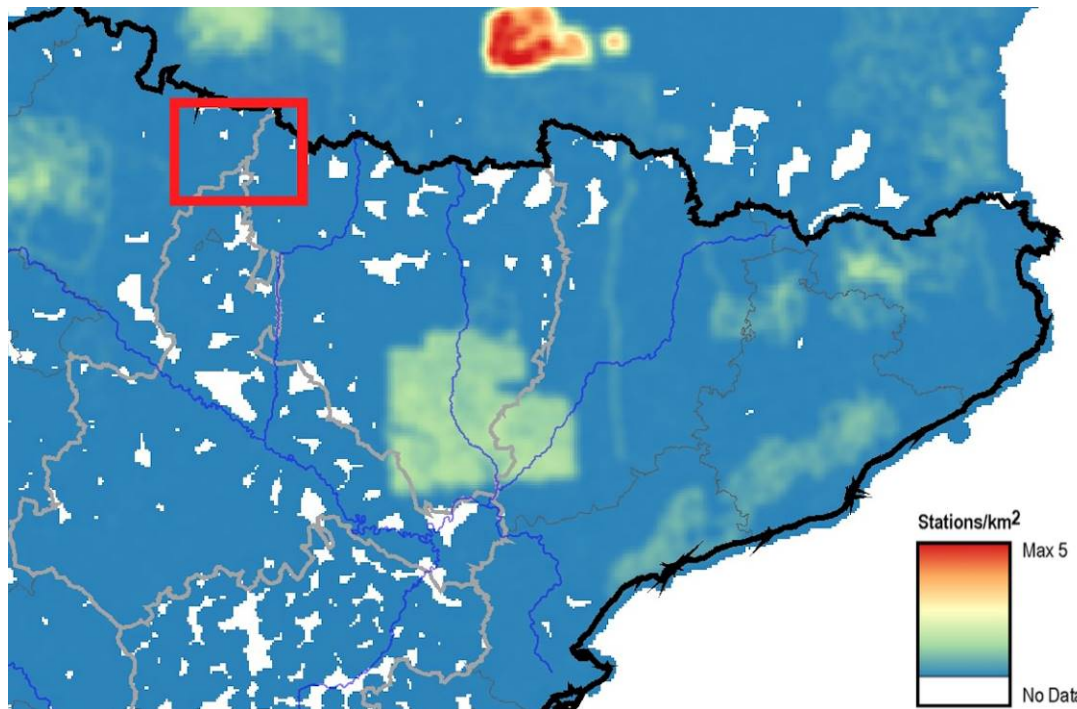
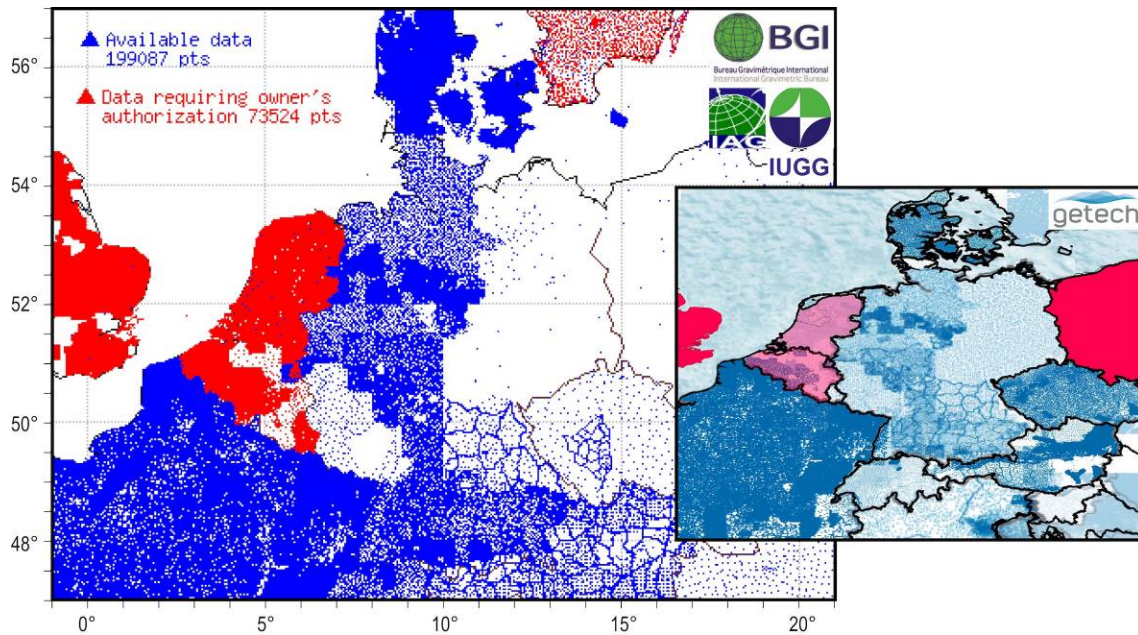


Figure 1.2 Gravimetric coverage approximately equivalent to the maps shown in figure 1. Central European data accessible from the International Gravimetric Bureau (BGI) (Seoane et al., 2018) as well as from the Getech web page. Note some countries do not share gravimetric data with the BGI or under restricted access (red areas). Northeastern Iberia gravimetric coverage (density of gravimetric stations /km<sup>2</sup>) data reprocessed from Ayala et al. (2016).



In this sense, potential field geophysics, gravity and magnetic exploration (Nabighian et al., 2005a& 2005b), may provide important geological and structural subsurface information in a cost effective and resolute way and they are very useful to overcome the lack of (or poor quality) seismic coverage and wells. Gravity and magnetic surveying are able to accurately record the contrast of petrophysical properties (density and magnetic susceptibility and remanence) in lithostratigraphic units of the subsurface. They are particularly effective to identify discontinuities (faults, alignments) and non-outcropping structures. For those reasons, they become essential tools for defining subsurface geology, providing information regarding the extension and internal structure of sedimentary basins and crystalline basement units and, in combination with structural geology, for the identification and characterization of structural styles (salt structures), igneous intrusions, to distinguish between cover and basement units and, in general, to help in understanding regional tectonic frameworks, etc. The main advantage of gravimetric and magnetic exploration is the acquisition of dense and homogeneous networks in an efficient way (fast and cost-effective), something impossible to approach with other geophysical techniques (e.g. reflection seismic). Therefore, potential field geophysics constitutes a robust method to investigate the internal structure, physical properties and lateral extension in subsurface geology and therefore, a valid tool to face the aforementioned challenges of the S. 21<sup>st</sup> and beyond. Gravity networks, for example (Fig. 1.2) are much denser and homogeneous than any other geophysical data (Central European data from the International Gravimetric Bureau; Seoane et al., 2018; NE Iberian data from Ayala et al., 2016).

Potential field geophysical data represent a **bottom-up approach**, the geophysical signal give us insights of the geological bodies at depth. However, the main problem when dealing with potential fields geophysical data is the so-called non-uniqueness solution (Skeels, 1947); the same anomaly and given contrast of the petrophysical property may be described by numerous interpretations by modifying the shape, size and depths of the modelled bodies. Therefore, 2D & 3D reconstructions from gravimetry and/or magnetic data alone represent valid solutions of the subsurface geology but may be, very likely, incorrect. The use of robust petrophysical data to limit the solutions is essential since they are the link between the anomalies, the geological structure and the lithological bodies. *"Petrophysical properties therefore provides a necessary constraint in potential field interpretation thereby considerably reducing the ambiguity in such interpretations"* (Henkel, 1994). Unfortunately, accurate and robust petrophysical data (density, magnetic susceptibility and remanence) with a strong impact in modelling, are not always used (sometimes are simply unavailable). In this work we emphasize and promote an accurate characterization of such data that can be also complemented with databases based on FAIR principles (Wilkinson et al., 2016).

Sharing the same concept, balanced and restored cross sections aim at providing a plausible image of the subsurface from a purely geological (geometrical) point of view independently of the availability of geophysical data. They involve a large variety of datasets: field observations (stratigraphic contacts and thicknesses, bed attitudes, fault surfaces, etc.), interpretative maps and cross-sections and, if available, geophysical data (seismic sections, borehole data, etc.) usually under the light of a structural concept (and its inherent uncertainty; Bond, 2015).



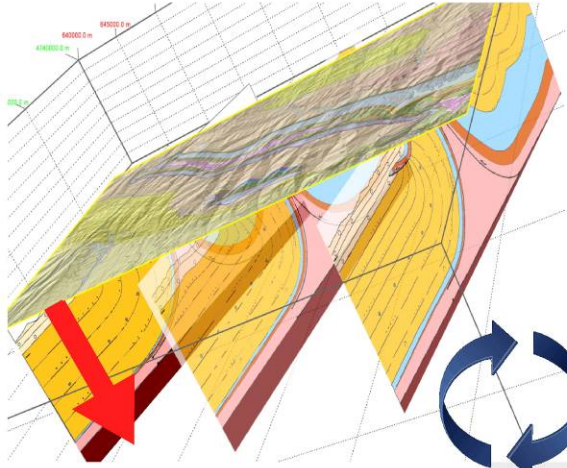
Balancing techniques, strongly driven by the oil industry in the 70's, were designed to characterize the geological structure at depth in areas with scarce and heterogeneous data aiming to help in the decision-making process (Woodward, Boyer and Suppe., 1989; Groshong et al., 2012 and references therein). The classical concept by Chamberline (1910) later on developed by Dahlstrom (1969) and many others is relatively simple; a **top-down approach** that squeezes the surface information (mapping, structural and stratigraphic elements) and extrapolates into the subsurface by honouring simple geometric laws; the conservation of bed lengths and bed thicknesses before and after deformation, which in turn, implies the volume conservation principle (Goguel, 1952) that can be, as a general rule, assume at the higher crustal levels. Cross section balancing (and restoration) techniques have represented an important step further in our understanding of the subsurface.

Both datasets, geology and petrophysics, represent the so-called “a priori information” and the interpretation of the gravimetric signal must be strongly constrained by them. It is worth noticing that, in the absence of seismic data, the geological concept behind serial balanced sections may be not necessarily correct (Judge & Allmendinger, 2011; Bond, 2015) (Fig. 1.3) and thus the gravimetric signal may shed light to re-interpreted the concept during the fruitful feedback process among the three variables.

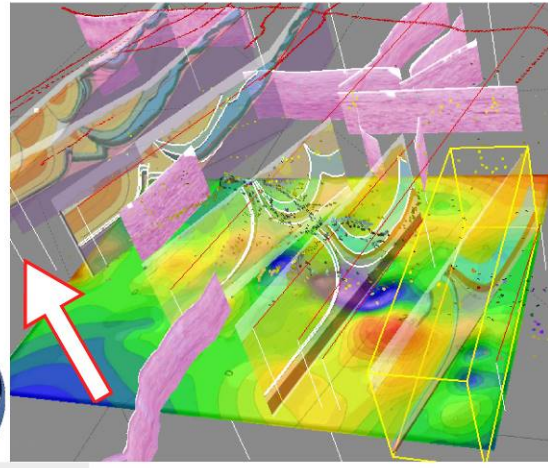
In this report we merge these three main pillars (gravimetry, geology and petrophysics) in an **integrated workflow that aims at obtaining more reliable 3D reconstructions of the subsurface**. We anticipate using serial 2D balanced and restored structural sections when processing the potential field geophysical data together with very robust petrophysical databases will substantially limit the number of possible solutions (3D reconstructions) and will improve our knowledge of the subsurface in regions of scarce oil information. In this work we review and synthesize all these concepts and the subjacent processing procedures in order to propose an optimized workflow for 3D reconstruction. This is supported by the GeoERA networking of European Geological Surveys that represents a fertilized feedback environment involving the experience and skills of 5 institutions (geological surveys and universities) all across Europe. It intends to be a comprehensive instruction's manual for facing future challenges in subsurface exploration.



### Serial Balanced Sections Top to Down



### Gravimetry Bottom up



### Petrophysics



### Integration

Triple balancing of  
geometry, petrophysics  
and gravity signal

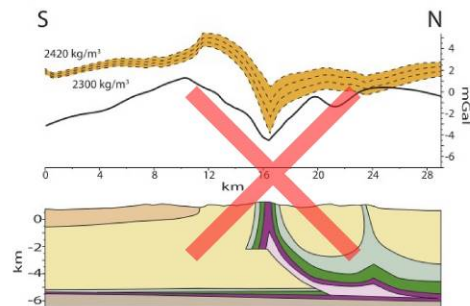
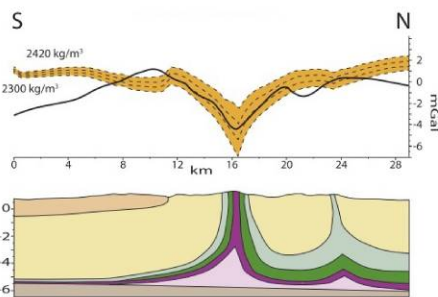


Figure 1.3 Triple integrated compensation of geometry from balanced cross sections (top to down approach), gravimetric data (bottom up approach) and robust petrophysical data in forward modelling. Data from the Southwestern Pyrenees (Calvin et al., 2018) without available seismic sections in the main (steep) structure. The forward modelling allows to identify a detachment fold geometry (right) more suitable than a ramp anticline (left).



## 1.2 Scope of this workflow and overview of the sections

- The workflow for 3D reconstruction introduced in this report is especially **designed for areas of poor or absent seismic and borehole data**. This information is limited, poor-quality (vintage or analogic-only data), does not exist at all or maybe because there is a problem to access the information (no FAIR policies).
- It is also focuses on **inland exploration**, because in case **gravimetric data acquisition** is needed to meet the project goals (improved resolution), then acquisition is more feasible than the most expensive on-shore targets.
- Besides, in-land structures may also allow, depending upon the exposure conditions, the acquisition of **petrophysical data** (outcrops where **hand samples** can be obtained). Certainly, this data could be also complemented with well logs (formation density and gravity) and borehole samples if there exist wells and the access to them is allowed.
- Good-enough exposure conditions allowing for a **trustworthy geological mapping** and for the picking up of structural (dips, etc.) and stratigraphic data are also necessary for the building of consistent **balanced sections**.

The workflow is organized in three levels (sections §) depending upon the degree of the processing and the number of dimensions considered. The first level (top of Fig. 1.4) refers to the raw data needed for the modelling (Subsection 2 in this report). A brief and updated review of theoretical principles, instrumentation and campaign design of gravimetric data (§2.1) is followed by an overview of gravity corrections, common software packages, data formats and databases as well as a succinct analysis on uncertainty sources. Then (§2.2), it follows a review of basic concepts and techniques of cross section balancing and restoration, again followed by an outline of uncertainty sources and common pitfalls in cross section building. In third place we synthesize the field and laboratory procedures involved in the acquisition of petrophysical data from hand samples and well logs, we also review some practical relationships among these variables as well as data formats, databases and, again, a concise analysis on sources of uncertainty. In the three cases (raw data) we do not pretend to do a complete and systematic review of all aforementioned topics, but a kind of practical manual mostly based on common procedures used by some EGS members (and some universities) that are later on illustrated with examples from previous works.

The second level deals with 2D processing of data which can be performed in horizontal surfaces (gravity maps) or in vertical planes (cross sections where all three variables are balanced by forward modelling). First (§3.1), we succinctly review the processing required to obtain the Bouguer, regional and residual maps as well as other enhanced maps (upward continuation, vertical and horizontal derivatives, Euler deconvolution, etc.). Then (§3.2), we review the 2D and 2.5D feedback process (forward modelling) usually done in some common software packages integrating all three main sources of raw data (gravimetric signal, balanced cross sections and density data) until the calculated gravity anomaly consistently match the observations (2D integrated model).

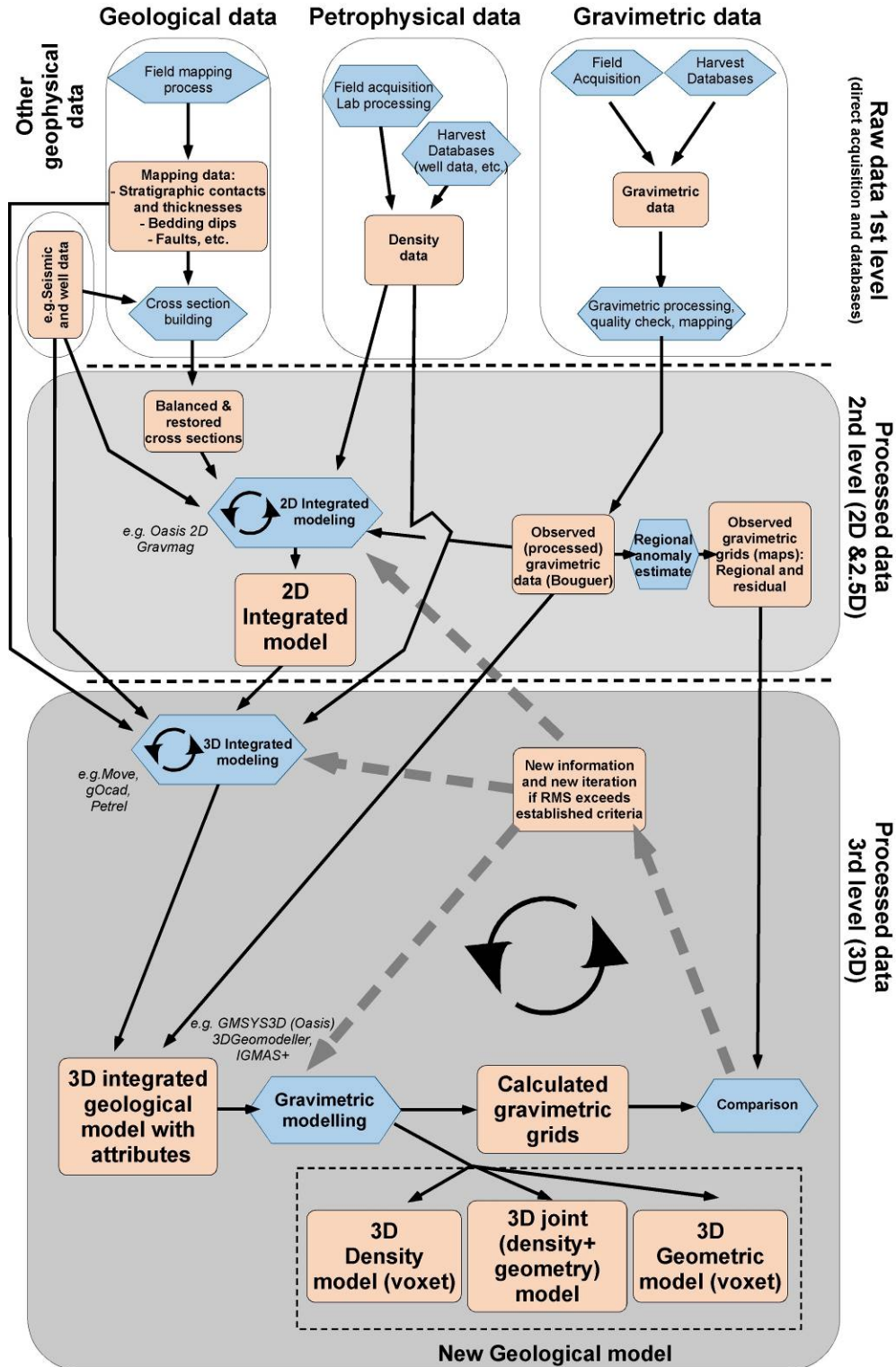


Figure 1.4 Synthetic diagram of the 3D reconstruction workflow based on gravimetric, structural and petrophysical data.



---

Successively or alternatively (the 2D step may be skipped in areas with extensive or at least sufficient subsurface information), in level 3 (§3.2) an integrated 3D structural model is build merging all data together - the petrophysical and geological data (formation and structural trends, bed dips, stratigraphic thicknesses, etc.) together with the measured gravimetric field (areal coverage should have been designed in advance). Besides, robust data from level 2, if available (e.g. 2D sections where all variables have been fitted together), can be here implemented as robust constraints of the model. The combined integration of all data together to obtain a 3D geological model with attributes (and associated uncertainties) can be performed by geophysical inversion in several software platforms during a feedback process that lasts until a reasonable solution is achieved (calculated gravity signal reasonably match the observed one).



---

## 2. Raw data sources (before the modelling)

### 2.1. Gravity data

Exploration geophysics based on potential fields (gravity and magnetism) are among the most efficient and cost-effective methods for imaging the Earth's subsurface at variable depths. The interpretation and potential of the gravity and magnetic data in terms of the location and depth of the geological bodies depends upon the existence of enough contrast in the petrophysical properties: density, magnetic susceptibility and remanence.

Focusing on gravimetric surveying, the **sensitivity** of current portable terrain gravimeters allows measuring relative values with a resolution ranging 10-50 $\mu$ Gal. Future developments in superconducting cryogenic gravimeters and/or micro-electromechanical-system (MEMS) technologies are expected to increase this sensitivity.

**Cost-effectiveness.** Compared to other methods, the advantage of gravimetry is that the gravimeters are affordable, logistics (and derived costs) are in principle more cost-effective and therefore, massive data acquisition can be performed to tackle exploration targets with better **spatial distribution coverage**.

Their **wide applicability** is another advantage in front of other geophysical methods. Gravimetric measurements can be taken almost anywhere (even in rugged terranes) due to the relatively light equipment needed (the gravity meter and the GPS). If the density contrast is high enough to distinguish between the targeted lithologies, it is a useful geophysical method to investigate complex geological environments, regions with steep dips (for example, poorly imaged by seismic reflection), areas with electric lines nearby (which hinders or precludes the use of electromagnetic approaches), etc.

**Satellite data.** Recent satellite missions like CHAMP, GRACE, GRACE-FO, GOCE [or Swarm for magnetic data], have improved their spatial resolution (which depends on the degree and order of the spherical harmonic coefficients, for instance for  $N_{max}=300$ , the half wavelength resolution is 67 km, Barthelmes, 2013 and 14 km when  $N_{max}=1420$ , Shako et al., 2014) and its applications include regional exploration (Visser, 1999; Rebhan et al., 2000). Combination of satellite data with terrestrial or airborne datasets has provided  $\sim 10$  km spatial resolution (Goetze and Pail, 2018) which has allowed to characterize the lithospheric structure of large areas (*e.g.* South America, Africa, passive and active continental margins, etc. Satellite data can be used to define regional gravity anomalies and therefore applicable to perform the regional-residual gravity separation.

For all these reasons, gravimetry is used to tackle exploration challenges and programs almost everywhere independently of the extension of the study area and is one of the main pillars of our workflow for subsurface exploration.



### 2.1.1. Theoretical principles

The gravity method focuses on detecting disturbances and spatial variations in the strength of the Earth gravity field. These are produced by a non-homogeneous composition and density distribution in the Earth interior. Therefore, the gravity method is based on the fact these anomalous variations in the Earth gravity field are caused by rock bodies with a given density that differs from the surrounding rocks. The overall objective of the gravity method in geophysical surveying is to establish or to constrain the shape and position (depth) of the bodies producing the gravity anomaly.

The gravity prospecting method is based on the Newton's Law of Universal Gravitation (Newton, 1726) that states that every particle attracts every other particle in the universe with a force ( $F$ ) which is directly proportional to the product of their masses ( $M_1$  and  $M_2$ ) and inversely proportional to the square of the distance between their centers ( $r$ ):

$$F = \frac{GM_1M_2}{r^2} \quad (1)$$

where  $G$  is the gravitational constant ( $6,673 \times 10^{-11} \text{ N}\cdot\text{m}^2/\text{kg}^2$ ). Focusing on the gravity method, we focus on the gravity acceleration. Considering Force ( $F$ ) = Mass ( $M_1$ ) x acceleration ( $a$ ), we can remove  $M_1$  from (1):

$$a = \frac{GM_2}{r^2} \quad \rightarrow \quad g = \frac{GM}{R^2} \quad (2)$$

where  $g$ , is the gravity acceleration of a body within the Earth gravity field being  $M$  and  $R$ , the mass and the radio of the Earth respectively.

Regardless the scale of work, the gravity method is applied to a study area having X (Longitude), Y (Latitude) and Z (depth) limits. Meaning, it is applied to a constant and specific volume of the Earth. Considering  $M = \rho \cdot V$  in (2), we obtain:

$$g = \frac{GV\rho}{R^2} \quad (3)$$

From this expression, we conclude that  $g$  directly depends on the density ( $\rho$ ). The gravity data reflect the density contrast of subsurface geological bodies. In consequence, the applicability of this method as an indirect study of the Earth interior is contingent on the existence of a certain degree of density contrast between subsurface bodies (Fig.2.1.1).

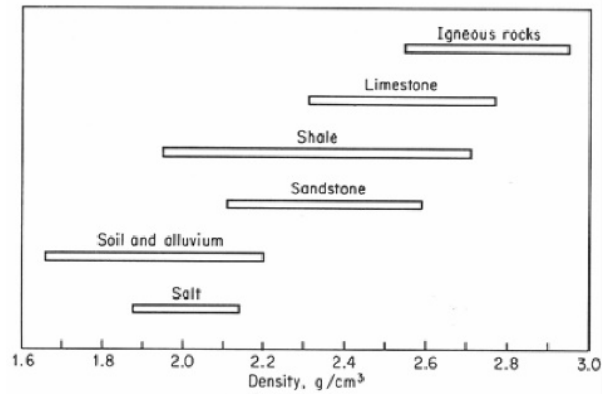


Figure 2.1.1. Density ranges of different types of rocks (Grant and West, 1965).

According to the S.I. (International System) of units,  $g$  is expressed in  $m/s^2$ , which exceeds in several orders of magnitude the range of values measured by a gravimeter. For this reason, the unit used in the S.I. is the gravity unit (g.u.),  $1 \text{ g.u.} = 10^{-6} m/s^2$ , however the most common used units are mGal ( $1 \text{ Gal} = 1 \text{ cm/s}^2$ ; [Gal derived from Galileo]) in c.g.s. units ( $1 \text{ g.u.} = 0,1 \text{ mGal}$ )

## 2.1.2. Instrumentation

### 2.1.2.1 Gravimeters

Since the measurements of Galileo in 1604 and throughout historical gravimetric measurements based on the pendulum principle or other ballistic approaches, a big step forward for relative gravity surveying began in the 1930's with the development of spring-type relative gravimeters. This type of meters can be of two classes: linears and astatics (see historical review by Chapin, 1998; Nabighian et al., 2005; Krynski, 2012; Marson, 2012). The next important step was the arrival of the zero-length spring (LaCoste, 1934). Further developments from the 50s, particularly the use of quartz springs and temperature stabilization systems (LaCoste 1959, 1967), implied a significant step forward in the precision of gravimeters. Superconducting gravimeters (as the GWR) may reach sensitivities of  $10^{-13} \text{ cm}\cdot\text{s}^{-2}$  (one nanogal or less; Imanishi et al., 2004), roughly one trillionth ( $10^{-12}$ ) of the Earth surface gravity, although they are not designed for field acquisition. Future developments and new technological improvements on gravity measuring include micro-electromechanical (MEMS see Tang et al., 2019) or quantum systems (Menoret et al., 2018) and they are expected to reduce costs, weights and considerably increase the sensitivity, resolution and the amount of data acquisition (<http://www.newton-g.eu/>).



Focusing on geophysical investigations, relative gravimeters are the most used for field acquisition. These devices measure the difference of gravity between two places, or the variation of the gravity in the same place over time (Siegel et al., 1995; Kearey et al., 2002).

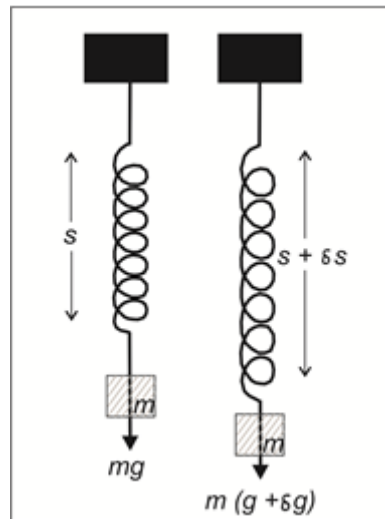


Figure 2.1.2. Principle of relative linear gravimeters

Relative gravimeters are spring balances carrying a constant mass. The variation in gravity causes the variation in the weight of the mass and therefore the length of the spring (Figure 2.1.2). The extension of the spring is proportional to the extending force. Following the Hooke's Law (Hooke, 1618), a spring of initial length has been stretched by an amount  $\delta s$  as a result of an increase in gravity  $\delta g$ , *i.e.* an increase in the weight of the suspended mass  $m$ , thus:

$$\delta s = \frac{m}{k} \delta g$$

Where  $k$  is the elastic spring constant. In practice, the extension of the spring is limited and resolved by optical, mechanical or electronic amplifications. By using the astatic or 'zero-length' spring, which is prestressed during manufacture, the restoring force is proportional to the physical length of the spring rather than its extension, so that instruments can be designed with a very sensitive response over a wide range. By a suitable design of the spring and beam geometry, the instrument works by restoring the beam to the horizontal by altering the vertical location of the spring attachment with a micrometre screw (see Figure 2.1.3). Thermal effects are removed by a battery-powered thermostatic system (Kearey et al., 2002).

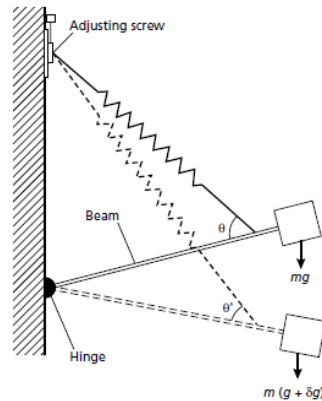


Figure 2.1.3. Simple sketch of the unstable or astatic gravimeter (From Kearey et al., 2002)

### 2.1.2.2 Most common land gravimeters

Since 1939, and over decades, the most used relative gravity meter was the LaCoste&Romberg (model G). Later, in 1989, Scintrex introduced the CG3 relative gravimeter (Hugill, 1990). In 2001, both companies merged to LaCoste&Romberg-Scintrex, Inc. producing over 90% of the world's gravimeters (<https://scintrexltd.com/about/history/>). In 2002, an enhanced version of the CG3 quartz-based gravimeter becomes the new CG5 Autograv<sup>TM</sup>. Recently, in 2016, Scintrex presented the new CG6 Autograv<sup>TM</sup>, introducing the latest technologies and advancements.

Moreover, in 1991, the ZLS company was created in Austin, Texas ([http://zlscorp.com/?page\\_id=46](http://zlscorp.com/?page_id=46)), offering products and services in gravity meters, including the land gravity meter Burris Gravity<sup>TM</sup>, an improved modern version of the LaCoste&Romberg.

The Geological Survey of Spain (IGME) owns a Lacoste&Romberg model G #582 gravimeter since 1985, and a Scintrex CG3 since 1996, updated to CG5 in 2003. In practice, the IGME combines some studies with a ZLS Burris gravimeter from the University of Zaragoza in the frame of the Associated Unit of Earth Sciences IGME/UZ.

#### ***Gravimeters Lacoste & Romberg and ZLS-Burris***

Both gravimeters integrate a zero-length spring, composed by metal parts, having a worldwide range coverage. They have constant thermostatic temperature to avoid metal creep from thermal expansion or contraction.

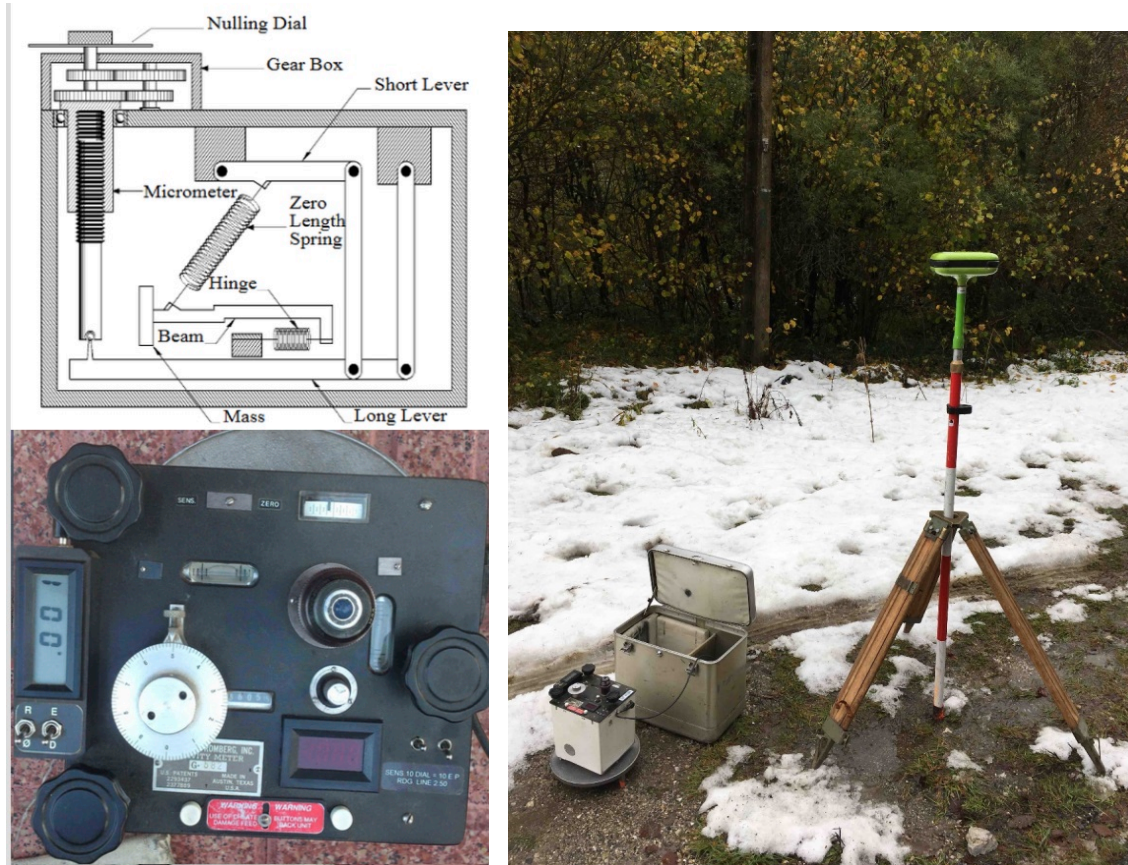


Figure 2.1.4. Up, left) Simplified diagram of the interior of a Lacoste&Romberg gravimeter (From Lacoste and Romberg, 2004). Bottom, left) Top view of the IGME gravimeter (G #582). Right) The Lacoste&Romberg gravimeter during the GeoERA project 3DGeoEU (November 2019).

**The Lacoste&Romberg gravimeter** is a zero-length spring land system whose simplified diagram is shown in figure 2.1.4. It has a single micrometer screw with a range up to 7000 mGal (worldwide). The accuracy is limited primarily by the accuracy of the screw. Readings can be repeated to 0,005 mGal (5  $\mu$ Gal) and over the entire gravity range which indicates an accuracy better than 0,04 mGal (40  $\mu$ Gal). The acquisition drift is mainly due to variations in the gravitational attraction of the sun and the moon (Tidal drift), and of the spring elongation due the use of the meter (instrumental drift). The drift can be of 0,3 mGal in 6 hours, but it is usually lower. During fieldwork this drift is corrected by tables or softwares. When the Tide correction (see 2.1.4 Gravity corrections) is applied, the remaining drift is usually below 0,5 mGal per month. The meters are thermostated to avoid the negligible drift. The calibration factors do not change perceptibly in short periods and thus there is no need for frequent checking calibration. The calibration factors are carefully determined in the laboratory for each gravimeter. These gravity meters are sealed against atmospheric pressure changes in addition to be compensated for pressure changes (LaCoste and Romberg, 2004). For further details, see Table 2.1.1.



**The Burris gravimeter** by ZLS Corporation (<http://zlsCorp.com/>) is a zero-length spring land system, similar to Lacoste&Romberg, but it incorporates the latest advances in digital technology. V-Grav™ control electronics automates the Burris Gravity Meter™ allowing it to be used with  $\mu\text{Gal}$  precision. Main characteristics include: rugged land meter, Earth tide monitoring, real time graphics of beam and levels, 0,1  $\mu\text{Gal}$  Resolution, automatic reading, weather resistant, lightest weight (6 kg including batteries), etc.

A microprocessor-based, automatic reading and data logging system (V-Grav™) controls the meter for blunder-free observations. It takes the reading, applies the calibration factor, corrects for earth tides and off level position, then stores the data and displays the results. V-Grav™ comes installed on an Android tablet for flexibility in the field. The latest versions incorporate wireless technology, which allows the observer to remotely monitor and operate the meter via Bluetooth. Regarding the gravimeter connections, the ZLS Burris gravimeter from the University of Zaragoza and the Associated Unit of Earth Sciences IGME/UZ has not been updated yet.



Figure 2.1.5. Left) the ZLS Burris gravimeter. Right) Measure taken with a Burris gravimeter at Tozal de Guara summit (2008 m) in the External Sierras (Southern Pyrenees)-DR3AM project.

Data have shown that the spring's drift rate improves with age. When new, ZLS springs drift approximately 1,0 mGal per month after aging and when mature, drift is less than 0,3 mGal per month. V-Grav™ provides unsurpassed precision over large ranges and eliminates a class of errors known as circular errors. Calibration values are stable over time as they are determined by a metal micrometer screw. The Burris Gravity Meter™ has consistently yielded standard deviations of 0,003 mGal or better during routine field tests. The Calibrated Screw Burris Gravity



Meter is calibrated every 50 mGal over the entire 7000-mGal meter range. See table 2.1.1 for further details.

### Scintrex Gravimeters

The Autograv Scintrex CG5 is a microprocessor-based automated gravity meter which sensing element is based on a fused quartz elastic system. In this case, the relative value of gravity at the reading site is converted to a digital signal and then transmitted to the instrument's data acquisition system for processing, display and storage. The parameters of the gravity sensor and its electronic circuits are chosen so that the feedback voltage covers a range of over 8000 mGal without resetting. The use of a low-noise electronic design and a highly accurate auto-calibrating analogical to digital converter results in a resolution of 0,001 mGal. The drift is less than 0,02 mGal per day and the rechargeable battery provides sufficient power to operate the Autograv throughout a normal survey day. The protection from ambient temperature changes is provided by locating the quartz elastic system, the analogical to digital converter, the sensitive electronic components and the tilt sensors inside a high-stability, two stages, and thermostatically controlled environment. The fine balancing required to obtain astatication is not needed, as the displacement transducer has sufficient resolution (0,02 nm) to detect the beam position of a non-astatised system, and electronic filtering reduces the effect of seismic noise. The temperature control is also accurate enough for the sensor to operate without mechanical compensation (CG5 Autograv, 2012).

Manufacturer	Model	Type	Abs/Rel	Cont/Discr meas	Resolution $\mu$ Gal	Precision $\mu$ Gal	Drift $\mu$ Gal/mo	Weight kg	Occup. area $m^2$	Power req W	
Scintrex	CG-6	Spring (quartz)	Relative	Discrete	0.1	~5	<600	5	< 1	5.2	100-250 k€
Micro g-LaCoste	gPhoneX	Spring (metal)	Relative	Continuous	0.1	1	<500	58	> 1	100-330	
ZLS	Burriss	Spring (metal)	Relative	Contin./Discrete	1	10	300	6	< 1	~ 5	
GWR	iGrav	Superconducting	Relative	Continuous	< 0.001	0.05	< 1	> 100	2 - 3	1400	
Micro g-LaCoste	FG5-X	Falling Corner cube	Absolute	Discrete	1	1 - 2	n/a	320	3	500	~500 k€
Micro g-LaCoste	A-10	Falling Corner cube	Absolute	Discrete	1	10	n/a	105	> 1	200 - 300	

Table 2.1.1a. Simplified technical specifications of most common gravimeters (by Carbone et al., 2020)



	<b>Autograv CG5 Scintrex</b>	<b>ZLS Burris</b>	<b>Lacoste &amp; Romberg</b>
<b>Institution</b>	IGME,	UNIZAR,	IGME,
<b>Type</b>	Fused Quarz	Metal Zero-Length Spring (Hardened metal micrometre screw)	Metal Zero-Length Spring
<b>Reading resolution</b>	0.001 mGal (1 µGal)	Single Voltaje mode: 0,1 µGal Continuous 22oltaje (filtered): 0,1 µGal	0,005 mGal
<b>Maximun operating range</b>	8000 mGal	7000 mGal	7000 mGal
<b>Residual long-term drift</b>	Less 0.02 mGal/day	1 mGal < 0,3 mGal (mature)	Less than 1mGal per month Less 0,5 mGal per month after aging
<b>Repeatability</b>	0.005 mGal or better	<50 mGal: 5-7 µGal (feedback) >50 mGal: 15 µGal (screw)	0,01 to 0,02 mGal
<b>Accuracy</b>			0,04 mGal or better
<b>Electronic levels Range Resolution</b>		+/- 2 arc minutes 1 arc second	
<b>Precision of Calibrated Points</b>		+/- 0,015 mGal (Calibrated Screw Meters Only)	
<b>Measurement Temperature range</b>		-15 to +50°C; optional low temp up to -45°C	0º to +45º C
<b>Dimensions</b>	336x190x177mm without connectors	267 x 178 x 292 mm	197x178x251
<b>Weight</b>	8,9 Kg	5,9 (with battery)	10 kg (Meter, battery and case)
<b>Batteries</b>	336x215x86mm, 6,4 kg		2,3 kg
<b>Battery Charger</b>		Input 90-260V AC Output: 24V 2.5A AC (60 W)	
<b>Battery life</b>	10 hours	Lithium Bat.at 25° C Standby: 16-18 h Operating: 12-14 h	



<b>Internal battery</b>		Yes
<b>Operative System</b>		Android Tablet
<b>Automated corrections</b>	Tide, Instrument tilt, temperature, advanced noisy Reading rejection, seismic noise filter. Near terrain correction (introducing topographic data).	
<b>Displayed and recorded data</b>	Corrected gravity, Standard deviation, Tilt about the X and Y-axes, Gravity sensor temperature, Tidal correction (Longman), Duration of Measurement, Terrain correction, Time at start of measurement and header information (including date and initialization constants)	
<b>Other specifications</b>	<b>Standard Memory</b> Flash Technology. Standard 12 Mbytes ca. 200000 readings. When row data enabled 6 sample per second digitized simple, capacity depends on read time duration.	<b>V-Grav™ Control System:</b> Type: Pulse width modulated electrostatic nulling system. Feedback range Approximately 50 mGal. Input 23oltaje: 10,5 to 14,0 volts DC

Table 2.1.1b. Technical specifications of most common gravimeters hosted in European Geological Surveys



Figure 2.1.6. Left) Scintrex CG5 on its tripod. Right) view of the CG5 display.

### 2.1.2.3 GNSS receivers

Accurate positioning of the gravimetric stations are required (particularly the elevation, Z coordinate) in any gravimetric survey. The X and the Y coordinate accounts for the latitudinal correction, and its accuracy is not so critical depending the work scale (*UNE 22-611-58*), e.g. in a regular regional survey (a few thousand square kilometres) its impact will be small since most stations will likely have a similar correction. However, the value of the Z coordinate plays an important role in the anomaly calculation. The absolute height of a measurement is a key data since the gravity varies 0,1115 mGal/m, considering a subsurface homogeneous layer of 2,67 g/cm<sup>3</sup> (Hinze, 2003). Therefore, the accurate location of each gravity station (X, Y and Z) yields to an accurately corrected gravity data that will help in better understanding the gravity anomalies and their sources.

Modern GNSS systems have reduced the cost of providing accurate positions and heights comparing to former methods such as optical levelling (Murray and Tracey, 2001) or other classic topographic approaches. Currently, there is a large availability of high technological GNSS equipment that may quickly provide meter accuracy for the X and Y and Z coordinates. However, to attain submetric precision for the total coordinates, specially the Z, differential GPS calculations must be used. Nowadays, accurate differential GPS calculation can be rapidly performed thanks to available public or private absolute networks of GNSS bases offered by companies, communities, and countries. In this section, we overview some GNSS receivers hosted in some European Geological Surveys and Institutes. General specifications of GNSS receivers are shown in table 2.1.2



### *Triumph-1 GNSS receiver*

The TRIUMPH-1 GNSS receiver (Fig. 2.1.7) is the one used by the IGME in gravimetric surveys. It is a fully integrated instrument offering precise and automatic performance. A rugged, light, and hermetically sealed box accommodates everything: the GNSS receiver and modem electronics, antennas, and up to 18 hours-last, rechargeable batteries. The batteries are setup close to the electronic section, which helps to profit the heat, which ensures a better functioning in cold weathers. Batteries can be recharged almost anywhere (power supply from 10-30 volts) including cars, ships and airplanes. The overall device, from the GNSS, UHF, 3.5G UMTS/HSPA/GSM/CDMA2000 to the Bluetooth/WiFi antennas, is hermetically protected. An external antenna can also be used bypassing the internal GNSS one. There are also two SIM/UIM memory cards inside the box, one of them can be easily reached and changed (see more information at: <https://www.javad.com/jgnss/products/receivers/triumph-1.html>). Current web-browser applications also guarantee an easy and quick access to the data (<http://javadgnss.net/jwi/#ui>)

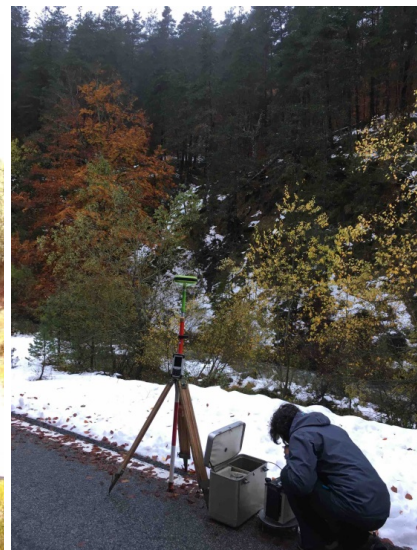


*Figure 2.1.7. Left) Triumph equipment JAVAD. Right) Measurement in the Pyrenees during the GeoERA project.*



	<b>Triumph-1-JAVAD</b>
<b>Institution</b>	IGME
<b>Signal tracked</b>	216 channels: all-in-view (GPS L1/L2/L5, Galileo E1/E5A/E5B, GLONASS L1/L2/LS, QZSS L1/L2/L5, Beidou B1/B2, SBAS L1/L5)
<b>Accuracy</b>	Horizontal: 0.3 cm + 0.1 ppm * base_line_length** Vertical: 0.35 cm + 0.4 ppm * base_line_length
<b>Measurement Temp. range and humidity</b>	-40° C to +60° C 100% condensing
<b>Dimensions</b>	W:178 mm x H:96 mm x D:178 mm
<b>Weight</b>	1700 g (w/o tripod and bar)
<b>Batteries</b>	2 internal Li-Ion batteries (7.4 V, 5.8 Ah each) with internal charger
<b>Batt. Charger</b>	10-30 V
<b>Battery life</b>	Up to 18 h
<b>Operative System</b>	MS Windows Mobile
<b>GNSS Antenna Specifications</b>	Antenna Type Microstrip (Zero Centered) Ground Plane Antenna on a flat ground plane
<b>Radio Specifications</b>	3.5G UMTS/HSPA Module: Global (850/1900/2100)/North America (850/1900/1700-2100AWS)/Euro-pe (900/2100). GSM/GPRS/EDGE Module: Inter-nal GSM/GPRS/EDGE quad-band module, GPRS/EDGE Class 10 CDMA 2000 Module: Internal CDMA2000 dual band module 800/1900MHz UHF Radio Modem Internal 360-470MHz radio transceiver, up to 38.4kbps Base Power Output 1 Watt
<b>I/O specifications</b>	Communication Ports: 2x serial (RS232) up to 460.8 kbps. High speed USB 2.0 device port (480 Mbps). Full-duplex 10BASE-T/100BASE-TX Ethernet port. Wi-Fi (IEEE 802.11b/g). Bluetooth V2.0+EDR Class 2 supporting SPP Slave and Master Profiles Other I/O: Signals 1 PPS synchronized. Event Marker Status Indicator: Six LEDs, two function keys (MinPad)

Table 2.1.2. Technical specifications of some common GNSS receivers used in gravimetric surveying.



### 2.1.3 Gravimetric survey design and control

Several issues must be considered in the design and control of a gravimetric survey. In this section we overview the most important ones dealing with the design of the network of gravity bases, the spatial distribution of stations and the expected resolution (and uncertainty). The control on the quality of the survey based on repetitions and the design of campaigns (including rough terrains) are also reviewed. Other subjects linked to the gravimetric bases (absolute, local, loops, etc.) and the calibration of instruments are assessed in the second half of this section.

#### 2.1.3.1 Networks of gravity bases

Relative gravimeters are widely used in land surveys because its resolution, lightweight and affordability. However, those instruments do not measure the absolute gravity but relative differences of gravity between one specific point and the rest of the zone. These specific points are named as *fundamental bases* or in its short form *Base*, being a place where the absolute gravity value is known.

For example, in Spain, the National Geographic's Institute (Instituto Geográfico Nacional; IGN) is the official institution in charge of building and maintaining the network (<http://www.ign.es/web/recursos/geodesia/visorGeodesia/index.html>) of fundamental gravimetric bases. In 1971, the International Gravity Standardization Net 1971(IGSN-71) was approved and accepted, for historical and technical reasons, the absolute gravity value in the GFZ Potsdam,  $g = 981260,0$  mGal. This international network consists of fundamental stations worldwide: 10 absolute stations, 1200 pendulum measurements, 12000 measurements of Lacoste&Romberg gravity meters and 11700 excentric measurements (Morelli et al.,1972). Focusing on Spain, four stations were included in the fundamental network (Rodríguez-Pujol, 2005 and IGN, 2019):

#10966 ROTA K y P

#14492 MALLORCA J y K

#14503 MADRID A (OAN), B (OAN), C (IGN), J, K, L, M, N

#18012 BARCELONA J, L

From that moment onwards, IGSN71 and the gravity reference system of 1967 were established in Spain. In 1975, the National Fundamental Gravity Bases Network (RGFE-73) was developed by the IGN and tied to the International Gravity Standardization Net (IGSN71). This Spanish Net consists of 101 stations measured with 4 Lacoste&Romberg gravity meters and supported by 2 fixed stations of the IGSN71 in Spain (BARCELONA J, MADRID C) and a third one in Portugal (LISBON A).



Figure 2.1.8. Left) National Fundamental Gravity Bases Network (RGFE 73) (IGN, 2019). Right) Current first order gravimetric bases in Spain (IGN and Rodríguez-Puyol, 2005) with absolute measurements.

In 1975, the IGN designed the Spanish Gravimetric Calibration Line 1975 (LCGE-75), in order to integrate all measurements made with different gravimeters. The LCGE-75 comprises 73 stations and 45 additional derived stations. This Line enables measurements of points of different altitudes (maximum difference of 1200 m), as well as different latitude. Alonso (1975) outlines the complete set of stations of the RGFE-73, including the altitude and gravity, the stations of the Portuguese gravimetric network RGFE-73 and the Bases of the Santander-Málaga Calibration Line (LCGE-75).

### 2.1.3.2 Local Bases

To combine the results with other gravity surveys, absolute gravity values are required, thus at least one easily accessible base station must be available where the absolute gravity is known. The number of base stations depends on the extension of the survey and the stability and drift of the gravimeter. If the location or number of near IGSN stations is not enough, a gravimeter can be used to establish a local base net by measuring the difference in gravity between an IGSN station and the local base. The new local base must be 1) easy to identify and access, 2) durable in time, 3) difficult to be altered, at least during the survey, 3) clearly and permanently marked and 4) accompanied by a drawn sketch with a doubtless and clear sign specifying where the measurement has to be taken.



**Área de Geodesia**  
Subdirección General de Geodesia y Cartografía

20-oct-2018

**Reseña de Señal de Nivelación**

<p><b>Situación Geográfica:</b></p> <p>Número: 16 Nombre: NAP J18* (Jaca) Línea o Ramal: Puntos Nodales</p> <p>Municipio: Jaca Provincia: Huesca Hoja MTN50: 176 Señal: Principal      En posición: Horizontal Señalizada: 01 de noviembre de 1972 Nivelada:</p>	<p><b>Entlaces:</b></p> <p>Anterior: Posterior: Agrupada con: 121001 - NAP 20, 554091 - NAP J19.</p>
<p><b>Datos Geodésicos:</b></p> <p>Altitud ortométrica: 808.8204 m. Geopotencial: 792.3918 u.g.p. Gravedad en superficie: 980143.6 mgal      Calculada Cálculo: 01 de mayo de 2008</p> <p><b>Coordenadas Geográficas ETRS89:</b></p> <p>Longitud: 0° 33' 14.1" Latitud: 42° 34' 01.7" Altitud elipsoidal: Precisión: ± (1 m - 10 m.)</p>	<p>Jaca (Punto Nodal 000 016) NAP J18</p>
<p><b>Reseña:</b></p> <p>Clavo metálico con la inscripción NAP J 18 incrustado aproximadamente en el Km. 283,9 en la margen izquierda de la Carretera N-240 de Pamplona a Jaca, en el cruce con las carreteras a Francia y a Sabiñánigo, en la esquina con la calle de la Infanta Doña Sancha sobre el muro del Instituto de Enseñanza Media, según croquis.</p>	
<p><b>Observaciones:</b></p> <p>- Inicio Línea N° 120 (Jaca - Somport). - Inicio Línea N° 121 (Jaca - Sabiñánigo). - Fin Línea N° 554 (Ludersa - Jaca). Es la antigua señal NAP J 18, folio 1.º de la línea n° 121, Jaca-Sabiñánigo, de 1972.</p> <p>Informe del estado de la Señal en: <a href="http://geodesia.ign.es/uf/infobase/inf971.pdf">http://geodesia.ign.es/uf/infobase/inf971.pdf</a></p>	

**Área de Geofísica y Teledetección**  
Departamento de Investigación y Prospección Geocientífica

26-ag-2019

**Reseña de Señal de Nivelación**

<p><b>Situación Geográfica:</b></p> <p>Número: 554039 - NGV 97 Nombre: Base Isaba Línea o Ramal: Base enlazada de NGV 97</p> <p>Municipio: Isaba Provincia: Navarra Hoja MTN50: 118 (Zurza) Señal: Proada      En posición: Horizontal Señalizada: 26 de agosto de 2019 Nivelada:</p>	<p><b>Entlaces:</b></p> <p>Anterior: 554039 - NGV 97 Posterior: Agrupada con: No está agrupada</p>
<p><b>Datos Geodésicos:</b></p> <p>Altitud ortométrica: xxx.xxx m. Geopotencial: 777.7777 u.g.p. Gravedad en superficie: 980191.421 mGal.      Calculada Cálculo: 26 de agosto de 2019</p> <p><b>Coordenadas Geográficas ETRS89:</b></p> <p>Longitud: 7° 77' 77.7" Latitud: 77° 77' 77.7" Altitud elipsoidal: Precisión: ± (7 cm - 77 cm.)</p>	
<p><b>Reseña:</b></p> <p>Pintadas en el suelo, la situación del gravímetro (CG-5 del IGME) con el que se han hecho las lecturas y la situación del GPS con el que se han medido las coordenadas y altura.</p> <p>La marca del gravímetro está situada enfrente del segundo palo (mirando hacia la pedana, de derecha a izquierda) de la valla y la marca del GPS está situada junto a ésta. A la derecha se ha dibujado una B de Base.</p> <p>Yendo por la carretera NA-137, pasado el km 32 y antes de llegar al km 33, se accede por el desvío a la derecha (puente sobre el río Escas) en el que se ve un indicador hacia el Área de autocaravanas de Isaba. Pasado el puente hay una bifurcación. Hay que ir a la izquierda, dirección Hotel Apartamentos Isaba.</p>	
<p><b>Observaciones:</b></p> <p>Informe del estado de la Señal en: <a href="http://geodesia.ign.es/uf/infobase/inf971.pdf">http://geodesia.ign.es/uf/infobase/inf971.pdf</a></p>	

Figure 2.1.9. Example of gravimetric bases sketches from the GeoERA project. Left) Jaca base from the IGN network. Right) Isaba base, established during the project (IGME).

Since it is not possible to measure, with the same gravimeter and at the same time the local base and the fundamental base (e.g. RGFE-73), a procedure consisting in determining the gravimeter drift between the two bases is used. Considering B1 and B2 bases, a series of readings at each base are made (see figure 2.1.10). The time between the readings must be according to the drift linearity of the gravimeter. In order to construct the drift curves, we measure at least two times at base B2 and three times at B1, these curves should be parallel and allow knowing the values in B1 in the moment that was read in B2 and calculate its difference  $\Delta$ . With the differences at three times  $\Delta_1$ ,  $\Delta_2$  and  $\Delta_3$ , the value  $\Delta_{12}$ , the gravity increment between bases is obtained as:

$$\Delta_{12} = (\Delta_1 + \Delta_2 + \Delta_3) / 3$$

If we need to establish several local bases, we must calculate the closing errors, and compensate the values. Schematically represented, we draw the position of all the bases. In each segment an arrow is pointing to the direction in which the gravity increases, as indicated in the right of figure 2.1.10.

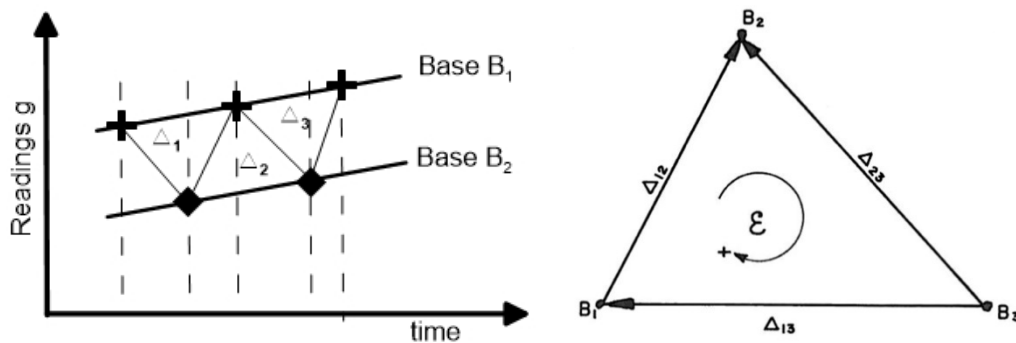


Figure 2.1.10. Left) Scheme of the procedure to establish a local base (see explanation in the text). Right) Diagram showing how to calculate closing error establishing a local base net.

Counter clockwise, the closing error would be:

$$\Delta_{13} + \Delta_{12} - \Delta_{23} = \varepsilon$$

if n is the number of sides of the gravimetric base net.

$$\varepsilon \leq 0,03\sqrt{n}$$

If  $\varepsilon$  is greater than the admissible value, it will be possible to determine on which union the greatest error occurs. Once the closing errors have been determined for each point of the net, they can be compensated throughout the entire network, following usual methods. Once the net has been compensated, the values of each base can be obtained.

### 2.1.3.3 Sampling design and station distribution

A gravimetric survey is a set of gravity observations taken in daily circuits which are planned to open and close in gravimetric bases. Apart from the station spacing (see below), the design of the circuits, the location of the bases, the repeated and tied stations are key for enabling a robust survey (Murray and Tracey, 2001) and the achieving of reliable anomaly maps.

The spatial distribution of gravity stations in a gravity survey depends on the working scale and the survey goals (table 2.1.3). It may range from a few metres (mineral exploration, geotechnical surveys, etc.) to several kilometres in regional surveys. In areas of rapid changes in the gravity field, the density of gravity stations should be increased so that the gravity gradients can be better determined (Kearey et al., 2002).



Working scale	Distribution stations (gravity stations/km <sup>2</sup> )	Distance between stations (in m)	RMS of the observed gravity (in mGal)	RMS of the X and Y coordinates (in m)	RMS of the Z (in m)	RMS of the Bouguer anomaly (in mGal)	Maximum interval between isohipses (in mGal)
1:200.000	0,04-1	5000-1000	± 0,2	± 200	± 2,5	± 0,6	2,0
1:100.000	0,16-4	2500-500	± 0,15	± 100	± 1,2	± 0,3	1,0
1:50.000	1-25	1000-200	± 0,1	± 50	± 0,7	± 0,18	0,5
1:25.000	4-100	500-100	± 0,06	± 25	± 0,35	± 0,1	0,25
1:10.000	25-625	200-40	± 0,06	± 10	± 0,20	± 0,08	0,2
1:5.000	100-2500	100-20	± 0,03	± 5	± 0,10	± 0,04	0,1
1:2.000	625-15625	40-8	± 0,015	± 2	± 0,05	± 0,02	0,05

Table 2.1.3: Working scales, distribution gravity stations recommended, distances among them and associated errors (Source UNE 22-611-58). RMS: root mean square.

The size, depth and density contrast of the involved and assessed bodies will determine the optimum distance between gravity stations. The Nyquist sampling theorem (Nyquist, 1928) provides a prescription for the nominal sampling interval required to avoid aliasing. It may be stated as simply as follows: the sampling frequency should be at least twice the highest frequency contained in the signal. Sampling theorem indicates that the observation spacing should be closer than half the wavelength of the anomaly we are seeking. An observation spacing equal to the dimension (in the measurement direction) of the body (shallow bodies) or twice its dimension (deep-seated bodies) will enable to detect the presence of the body but not to define its shape. Four observations across a body, two just off the edges and two on top of the body (i.e. spacing about a third of the body dimension) will give a reasonable idea of the shape (Murray and Tracey, 2001).

In case of gravimetric cartography or regional studies, the IGME follows the recommendations of the UNE Norm (see table 2.1.3), for example for a 1:50000 scale representation, the distance between station should be 200-1000m, for a 1:100000 scale should be between 500 – 2500 m.



### **Field recommendations**

To ensure a reliable dataset and save time during campaigns some considerations should be taken regarding the characteristics of the gravity station and surroundings. Best-practice manuals (Seigel et al., 1995; Murray and Tracey, 2001) and our own experience allow us to propose some helpful tips **before starting the surveying**:

- **Evaluation of previous anomalies** (gravimetric and/or magnetic), both ground and airborne databases will be very useful together with previous interpretations of the subsurface (balanced sections, wells, seismic lines, etc.) and their possible relationship with outcropping structures (standard geological maps).
- **Station spacing** must be chosen in relation to the resolution needed and the scale of work (Table 2.1.3). Expected petrophysical contrast must be evaluated from databases as well as from the previous knowledge on the subsurface geology (logged wells, depth and wavelength of structures).
- **Define the target area** precisely and add an external frame (at least 25% additional surface) to avoid border problems in further 2D and 3D modelling. This second frame will have a lower gravity station density (higher spacing).
- **Grid design** and station location. The coverage should be as regular as possible in all directions. Opposite to a perfect, orthogonal and homogeneous survey design, some authors (Murray and Tracey, 2001) recommend 30°/60° of obliquity with respect to the main structural grain (trend direction) to improve the structure definition.
- **Plot in a GIS platform** the planned points and gravimetric bases to evaluate terrain difficulties and accesses to the points (roads, dirt roads, etc.), forecast the most efficient daily circuits (logistics and economic impact) and guarantee a homogeneous distribution of stations and repetitions.
- Sometimes, **special permits** (natural preservation areas, private land, etc.) would be necessary and can be anticipated.

Once **during the survey** some other tips should be considered:

- **Safety tips.** Working teams of two people during the field acquisition are safer and practical, usually one oversees the gravimeter and the other the GPS and performs the near topographic correction (manually or operating a drone, etc.)
- **Station location.** A gravity station should fit the designed gravity station network/grid but it is recommendable to leave some degrees of freedom when deciding where to do the gravity measurement. Sometimes it is better to slightly displace the gravity station to a more suitable location with an easier road access. Large buildings and constructions (i.e. dams Reich et al., 2019) must be avoided or their effect must be corrected later on (Nowell, 1999; Dilalos et al., 2018). Similar effects can be expected from large snow accumulations (Breili and Pettersen, 2009).



---

- **Placing the gravimeter.** Try to set it on hard and flat grounds to guarantee a quick and safe leveling of the gravimeter (Fig. 2.1.11 A, B, C), thus avoiding steeps, wet and muddy soils, snow, ice or icy grounds, grasslands, soft sediments, etc. It is important to set the gravimeter carefully. An inadequate and uneven base can be noticed by a slight displacement of the gravimeter levels and/or trendy measurements: a progressive increase or decrease in the measurement is usually related to a small but continuous settlement of the gravimeter. Additionally, and if the tolerance of the network design allows changes in the station location, it is desirable to avoid cliffs and pronounced hollows to minimize the error estimate of the closer topographic correction (Hammer, 1939).

- **Avoiding disturbances.** Levels can be also **disturbed by external factors**. Try to sidestep heavy traffic roads and paths or bridges; do not walk around the gravimeter when it is measuring; avoid windy locations and if it is not possible, cover your gravimeter with some kind of breastwork (Fig. 2.1.11 A and D).

- **GPS antenna tips.** To accelerate and ensure GPS measurements, it is always better to avoid creeks, vertical walls and densely forested areas. Place the GPS always in the same relative location with respect to the gravimeter to guarantee the XYZ location of your gravity station. If it is not possible, at least, try to place the GPS at the same height as the gravimeter (same Z value).

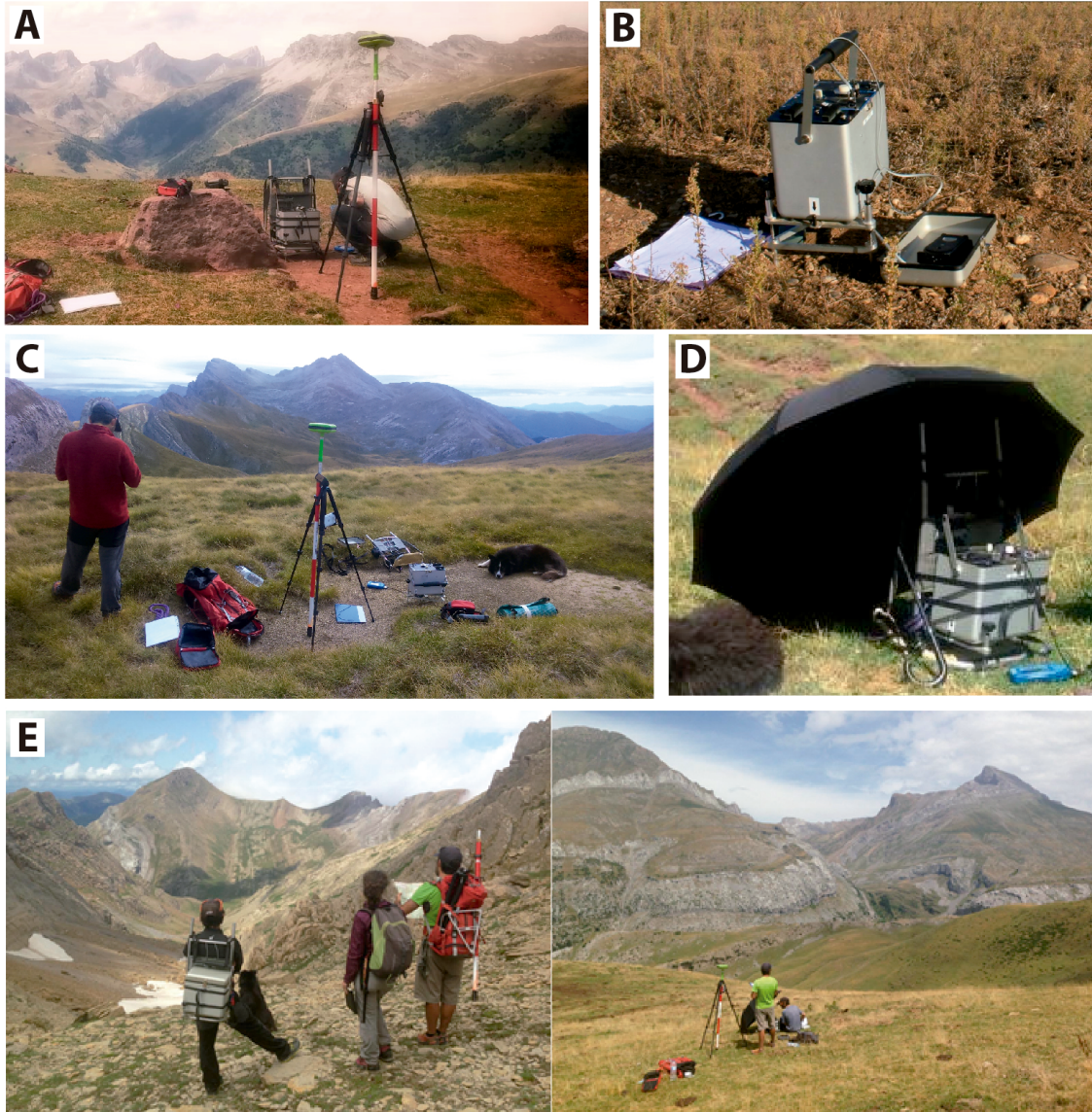


Figure 2.1.11. Some examples of data acquisition in rugged and highly mountainous terrains.

The IGME recent experience in several regional projects (spacing about 1 station/km<sup>2</sup>) comprising the acquisition of thousand(s) points has demonstrated an effectiveness around 20-30 stations/day (including 10% of repetitions). However, this pace may be substantially reduced in orographic terrains, hard weather conditions and, of course, in rugged countries.



### ***Gravimetry in rugged terrains***

During the GeoERA project 3DGeoEU, one of the working packages (WP6) has tackled the acquisition of gravimetric data in the Southwestern Pyrenees. 20% of the target area is in the High Pyrenees at altitudes from 1700m to summits above 2600 m (Bisaurín or Aspe summits). Apart from the very rugged terrain and mountainous orography (very limited accessibility), most part of this portion is also a Natural Preservation Area (Western Valleys Natural Park) with additional mobility restrictions. In this area, the main accesses are hiking paths with strong topographic gradients and additional tips were taken into account:

- **Team of 3 people** (or more) (Fig. 2.1.11 E). In our case, all of them highly trained mountaineers and young geologists (one of them was also Mountain Guide). In the unfortunate case of an accident in such mountainous areas, where communication network signal may be poor, the inevitability of splitting the team is a possibility that must be taken into consideration in advance.
- **Field equipment**, ZLS Burris gravimeter (the lighter in the market) was adapted to a rack backpack that still allows for the tripod setup. The GPS topographic tripod was changed for a robust photography one (much lighter).
- **Loops were closed everyday** this time, sometimes with additional support from vehicles (maybe with helicopters in other cases). Very exceptionally, and according to the continuous control of the drift of our gravimeters (0,064 mGal/day), we could have also considered the closing of some loops after two days (spending one overnight in the mountains) to enhance the effectiveness of the data acquisition. This possibility entails a risk on the determination of the drift and the necessity to carry extra batteries (extra mountain equipment and supplies) to ensure a two-days long sampling loop. A balance between this factor and the efficiency of the loop must be evaluated carefully.
- **Data acquisition efficiency**. Given the special conditions, a maximum acquisition of 11 points/day was achieved (mean of 8/day). It is worth noticing that an average of 1200 m hiking accumulated altitude and 7-9 hours of hiking were necessary per working day in this campaign.

### ***Repetitions control***

Standards and manuals in gravity surveying (Hinze et al., 2005; Murray and Tracey, 2001), including the UNE Norm 22-611-85 for geophysical terrestrial surveying, consider the repetition of stations as a quality control check. For example, the UNE norm 1985 establishes that: “the accuracy of the measurements will be controlled as follows: at least 5% of the stations will be measured twice in the course of different programs”. In the case of regional gravimetric data,



such as the working scale is 1:50.000 to 1:100.000 (that is, 0,16 to 4 stations per km<sup>2</sup>), the value of the mean square error (Ecm) for repetitions of the X and Y coordinates in meters is +/- 200 and for the Z dimension it must be less than 1,2 m. The following formula is used to calculate the mean square error (Ecm):

$$Ecm = \pm \sqrt{\frac{\sum d^2}{2N}}$$

where d is the difference between the first measurement and the repetition and N the number of repeated points.

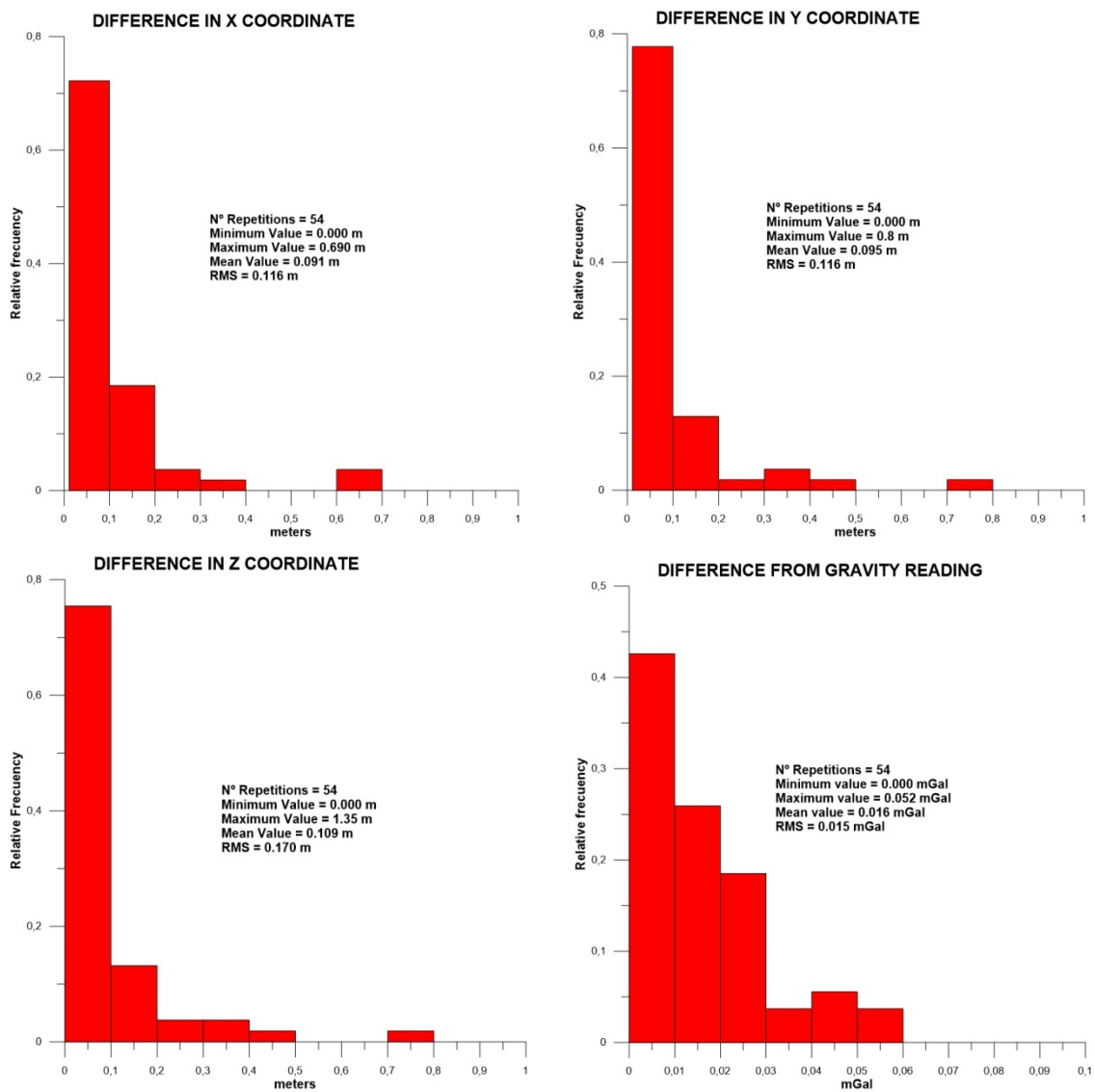


Figure 2.1.12: Graphics of GPS positioning and gravimeter readings control quality (from the IGME survey at Barbastro). Left to right: Plot of differences in m in the repeated points for the X coordinate; Y coordinate; Z coordinate (Orthometric height) and gravimeter readings.



For example, in one of the surveys we have carried out (Santolaria et al., 2020), the number of repetitions was 54, which represent 10% of all measured points. The GPS coordinate mean error was around 10 cm and below 20  $\mu$ Gal for the gravity measurement (Figure 2.1.12; see statistics there).

### 2.1.3.4 Calibration and drift of gravimeters

#### Calibration constant

The accurate calibration of each instrument is initially done by the manufacturer. The calibration constant of gravimeters is used to transform the reading of the screw in gravity values. It is advisable to periodically perform this calibration to control the evolution of the gravimeter constant and to check its proper functioning. In practice, in the IGME, we use some stations of the IGN Calibration Line, near Madrid, with enough difference in elevation to cover a wide range of measurements (Figure 2.1.13) and hence enabling to check the gravimeter constant and control its variation in time. We have calibration data on these IGN stations (we name them Bases) with the IGME's Lacoste&Romberg gravimeter since 1981 and with the Scintrex since 1990 (former CG3). The following tables show the difference in gravity values in mGal observed in these Bases over time. The last column shows the differences indicated by the IGN for the values of these Bases (Table 2.1.4).

Lacoste	May.1987	Mar.1988	Feb.1990	Sep.1994	Abr.1997	Mar.2000	Nov.2009	Dic.2012	Ago.2013	Jul.2018	I.G.N.
<b>Base 20-22</b>	71,87	71,894	71,9	71,895	71,82	71,874				71,884	<b>72,18</b>
<b>Base 20-21</b>	26,839	26,839		26,85	26,78	26,848				26,858	<b>26,95</b>
<b>Base 21-22</b>	45,055	45,0348		45,04	45,07	45,026		45,048	45,04	45,03	<b>45,23</b>
Scintrex CG5	Feb.1990	Sep.1994	Abr.1997	Mar.2000	Dic.2012	Ago.2013	Jul.2018	I.G.N.			
<b>Base 20-22</b>	71,84	71,55	72,12	72,25			72,23	<b>72,18</b>			
<b>Base 20-21</b>		26,73	26,93	27,3			26,99	<b>26,95</b>			
<b>Base 21-22</b>		44,82	45,2	44,88	45,22	45,23	45,24	<b>45,23</b>			

Table 2.1.4. Calibration values obtained with the IGME gravimeters (top) Lacoste&Romberg #582 since 1987 (bottom) Scintrex CG3 and CG5 since 1990.



The gravity observations obtained over time varies very little, which indicates the stability of the gravimeters. The values of the Scintrex gravimeter are very similar to those of the IGN bases, while a difference is observed between the values obtained by Lacoste&Romberg and those indicated by the IGN, approximately 0.4% lower in the Lacoste&Romberg. This difference does not represent any significant drawback if only this gravimeter is used in a survey but must be taken carefully into consideration if other gravimeters are used or if we want to combine our data with external datasets.

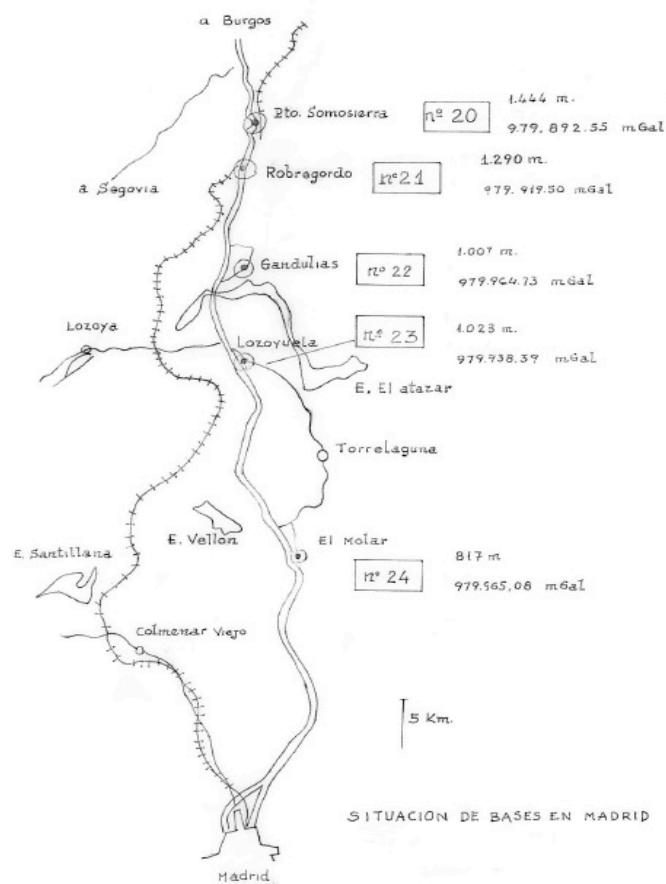


Figure 2.1.13. Simple sketch of the gravity calibration line near Madrid. The name, gravity value and orthometric elevation for these gravimetric bases are also shown.



### Drift correction

Gravimeters are instruments of very high sensitivity whose reading may vary with time, what is known as drift. Knowing and controlling the source of this drift is essential to ensure the quality of the gravity measurements. There are different types of controls or drifts. If the gravimeter is working in static mode, taken readings at the same point, it is called “static drift”, and gives an idea of the static behaviour of the instrument. If the gravimeter is working in dynamic mode, taking readings at different stations during a measurement program, it is called “working drift”.

A low and lineal static drift ensures a reliable in situ measurement during field campaign and give an idea about the behaviour of the meter. In figure 2.1.14 examples of the IGME gravimeters, Lacoste & Romberg and Scintrex CG5 static drifts curves are shown. These values guarantee the gravimeters are suitable for field campaigns designed with a single opening and a closing Base.

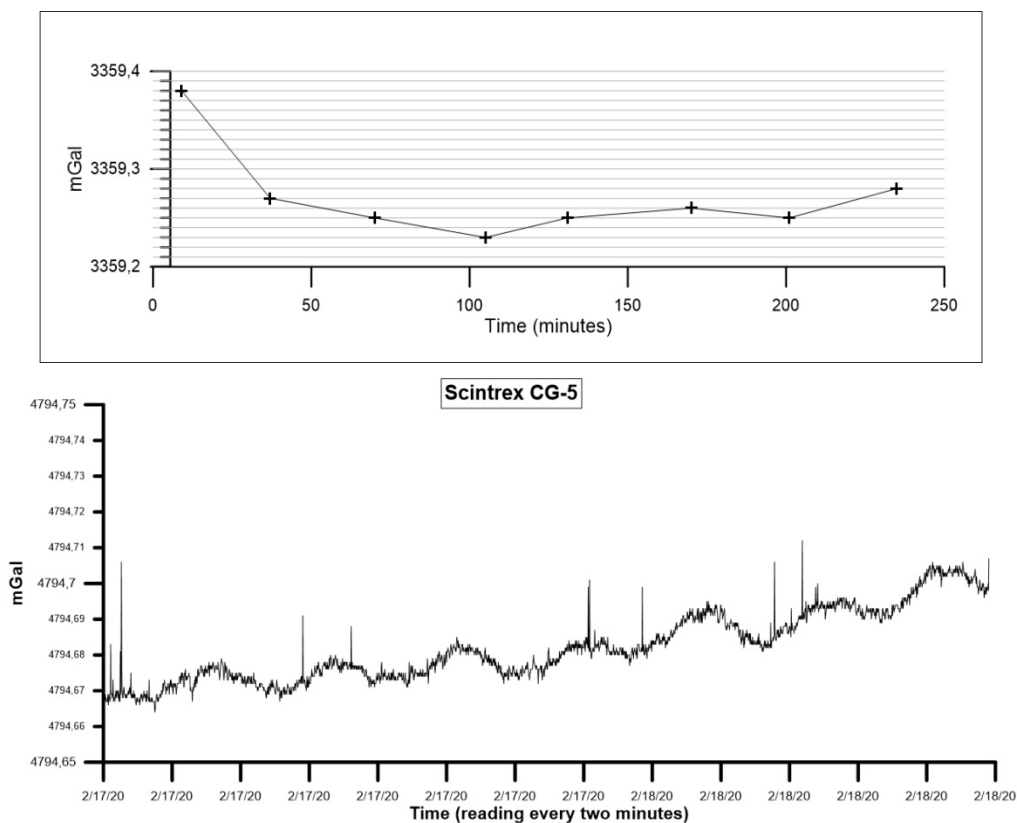


Figure 2.1.14. Lacoste & Romberg (#582) (Top) and Scintrex CG5 (Bottom) static drift graphs are shown. The measurements were taken at a fix location placed in the IGME headquarters (Tres Cantos village, near Madrid).



Concerning the working drift, its main purpose is to correct the gravimeter readings variations that, due to mechanical and thermal effects, may have happened during a daily loop, that is, from the measure at a Base at the beginning of the day, until the closing of the loop at the same Base at the end of the day. This drift is assumed to follow a linear function. The drift correction is about correcting the variation “D” with respect to an initial moment; this (initial base) is assigned drift 0. At the final measurement (final base) the drift can be calculated by the expression:

$D = L_{Bi} - L_{Bf}$  ( $L_{Bi}$  and  $L_{Bf}$  are the opening and closing readings at the base after the tide correction)

For each station, n read at time  $t_n$ , the drift, assuming a linear variation, will be:

$$D_n = D \frac{t_n - t_{Bi}}{t_{Bf} - t_{Bi}}$$

for this purpose, (among others), the time of each reading must be written down usually in universal (solar) time.

After drift and tidal corrections (see section 2.1.4 for further details, the difference in gravity between an observation point and the base is obtained by multiplying the difference in the reading by the calibration factor of the gravimeter.

$$\delta_{in} = (l_n - l_{Bi})k + LS_n - LS_{Bi} + D_n$$

$\delta_{in}$  = difference in gravity between point n and base  $B_i$

$l_n$  and  $l_{Bi}$  readings at point n and Base i

$LS_n$  and  $LS_{Bi}$  tidal correction at point n and Base i

$D_n$  = drift correction at point n

Knowing this difference in gravity, the absolute gravity at the observation point  $g_{obs}$  can be computed from the known value of gravity at the base  $g_b$ .

$$g_{obs} = \delta_{in} + g_b$$

Alternatively, readings can be related to an arbitrary datum, but this practice is not desirable, as the results from different surveys cannot then be tied together.

### 2.1.3.5 Coordinate acquisition using GNSS

The calculation of the gravity anomalies (i.e. the Bouguer gravity anomaly, see section 2.1.4.3) requires an accurate positioning of the gravimetric stations, particularly the elevation (Z



coordinate). This need, in a regional gravimetric campaign, has historically meant a significant limitation for the acquisition of quality gravimetric data, especially in areas of difficult access, since it is necessary to combine two teams in the field, one of them in charge of the gravimetric data and another one carrying out the high precision topographic data. The need of topographic equipment makes the campaign more expensive by employing more personnel, more means and more time.

The arrival of topographic equipment based on the global satellite navigation system (GNSS), enables the measure of topographic data simultaneously with the gravimeter, lowering the cost, reducing acquisition times and making the data collection easier in areas with difficult access (Davis et al. 1989; Fairhead et al., 2003; Hinze et al., 2013; Kearey et al., 2002; Berné et al., 2014).

### ***Global navigation satellite system (GNSS)***

A Global Navigation Satellite System (**GNSS**) is a constellation of satellites that transmits several signal frequencies and are used for geo-positioning anywhere on the surface of the Globe, whether on land, sea or air. These systems allow determining the geographical location (XY horizontal coordinates and the altitude Z) of a given point using the signal received from constellations of artificial satellites of the Earth for different purposes; navigation, transportation, geodetic, hydrographic, agricultural, and other related activities (Hofmann-Wellenhof et al., 2007; Seeber 2003; Leick 2004; Berné et al., 2014; Kaplan and Hegarty 2017).

Common GNSS Systems are GPS (USA), GLONASS (Russia), Galileo (Europe), Beidou (China) and other country systems. The advantage of having access to multiple satellites is the accuracy, redundancy and data availability at any time. Though satellite systems do not often malfunction; if one fails, GNSS receivers can pick up signals from other systems. Besides, if the line of sight is obstructed, having access to multiple satellites is also an advantage.



System	BeiDou	Galileo	GLONASS	GPS	NavIC	QZSS
<b>Owner</b>	China	European Union	Russia	United States	India	Japan
<b>Coverage</b>	Global	Global	Global	Global	Regional	Regional
<b>Coding</b>	CDMA	CDMA	FDMA & CDMA	CDMA	CDMA	CDMA
<b>Altitude</b>	21,150 km (13,140 mi)	23,222 km (14,429 mi)	19,130 km (11,890 mi)	20,180 km (12,540 mi)	36,000 km (22,000 mi)	32,600 km (20,300 mi) – 39,000 km (24,000 mi) <sup>[33]</sup>
<b>Period</b>	12.63 h (12 h 38 min)	14.08 h (14 h 5 min)	11.26 h (11 h 16 min)	11.97 h (11 h 58 min)	23.93 h (23 h 56 min)	23.93 h (23 h 56 min)
<b>Rev./S. day</b>	17/9 (1.888...)	17/10 (1.7)	17/8 (2.125)	2	1	1
<b>Satellites</b>	BeiDou-3: 28 operational (24 MEO 3 IGSO 1 GSO) 5 in orbit validation 2 GSO planned 20H1 BeiDou-2: 15 operational 1 in commissioning	26 in orbit 22 operational 6 to be launched <sup>[34]</sup>	24 by design 24 operational 1 commissioning 1 in flight tests <sup>[35]</sup>	30, <sup>[36]</sup> 24 by design	3 GEO, 5 GSO MEO	4 operational (3 GSO, 1 GEO) 7 in the future
<b>Frequency</b>	1.561098 GHz (B1) 1.589742 GHz (B1-2) 1.20714 GHz (B2) 1.26852 GHz (B3)	1.559–1.592 GHz (E1) 1.164–1.215 GHz (E5a/b) 1.260–1.300 GHz (E6)	1.593–1.610 GHz (G1) 1.237–1.254 GHz (G2) 1.189–1.214 GHz (G3)	1.563–1.587 GHz (L1) 1.215–1.2396 GHz (L2) 1.164–1.189 GHz (L5)	1176.45 MHz(L5) 2492.028 MHz (S)	1575.42MHz (L1C/A,L1C,L1S) 1227.60MHz (L2C) 1176.45MHz (L5,L5S) 1278.75MHz (L6) <sup>[37]</sup>
<b>Status</b>	Basic nav. service by 2018 end to be completed by H1 2020 <sup>[34]</sup>	Operating since 2016 2020 completion <sup>[34]</sup>	Operational	Operational	7 operational	Operational
<b>Precision</b>	10m (Public) 0.1m (Encrypted)	1m (Public) 0.01m (Encrypted)	4.5m – 7.4m	5m (no DGPS or WAAS)	10m (Public) 0.1m (Encrypted)	1m (Public) 0.1m (Encrypted)

Table 2.1.5. Technical specifications of current GNSS satellite constellations used for navigation (source; [https://en.wikipedia.org/wiki/Satellite\\_navigation#Global\\_navigation\\_satellite\\_systems](https://en.wikipedia.org/wiki/Satellite_navigation#Global_navigation_satellite_systems)

Creative commons licence).

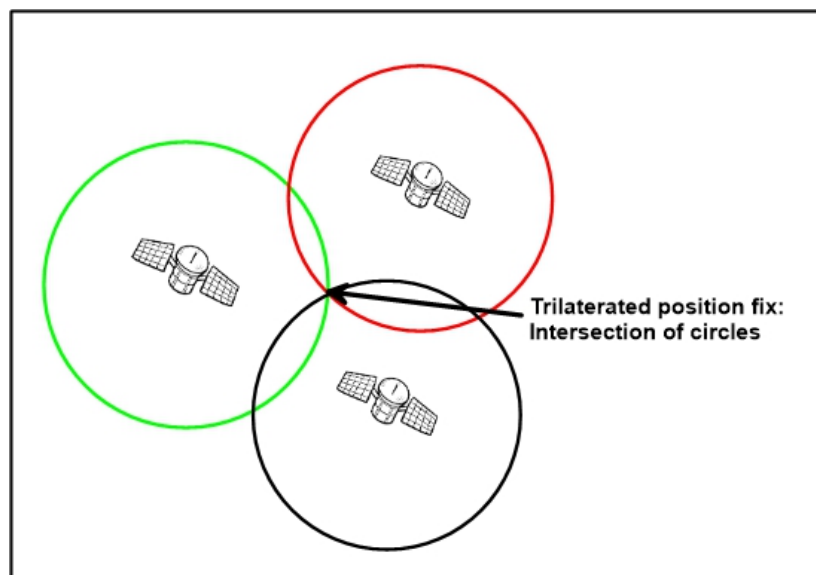


Figure 2.1.15. Sphere intersection to determine the XYZ position. A fourth satellite is used to compensate the error on measuring the time.



The pioneer GPS consists of up to 32 medium Earth orbit satellites in six different orbital planes, with the exact number of satellites varying as older satellites are removed and replaced. Operational since 1978 and globally available since 1994, GPS is currently the world's most commonly utilized satellite navigation system.

The basis for determining the position of a GNSS receiver is trilateration from the reference provided by satellites in space. To carry out the trilateration process, the GPS receiver calculates the distance to the satellite by measuring the time it takes for a given signal with known frequency to arrive. For this calculation, GNSS needs a very precise system to measure time (in some cases measurements can be 0,067 seconds). To solve this problem, transmitters and receivers use a method called "Pseudo-Random Code" or PRC. In addition, it is necessary to know the exact position of the satellite. Finally, the received signal must be corrected to eliminate the delays caused by atmospheric effects. Once the GPS receiver collects the position of at least four satellites and knows the distance to each of them, it can determine its own position by superimposing the imaginary spheres generated and centred on each satellite whose radius is the calculated distance (Leica, 1999).

### Differential GPS

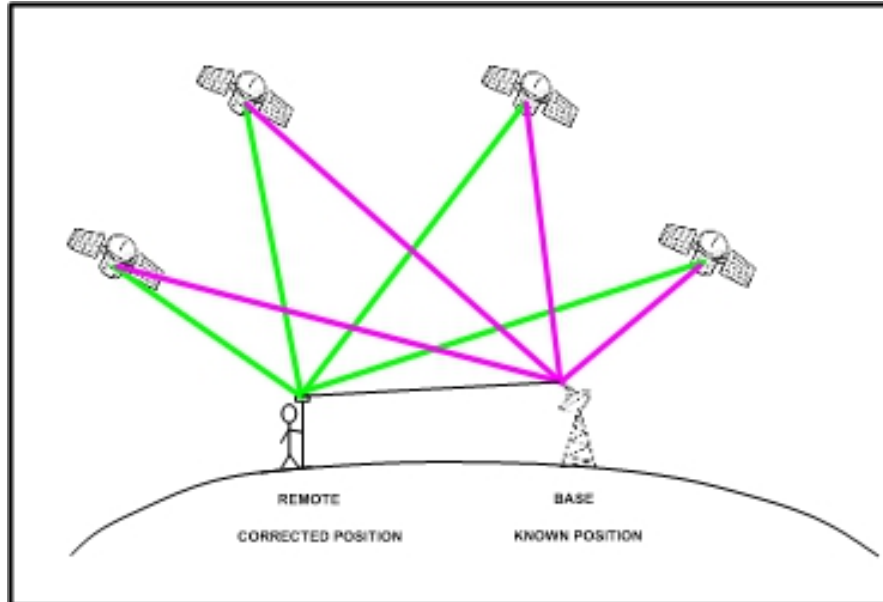


Figure 2.1.16. Simple scheme of the differential GPS correction.

Differential GPS was developed mainly following the drawback caused by the limited and selected availability of the positioning data, or unwanted limitations of the precision related to military reasons, which has already disappeared since the beginning of the 21st century. Differential GPS is a procedure to improve the accuracy obtained through the GNSS system. The



rationale behind lies in the fact that the errors produced by the GPS system affect the receivers located close to each other in the same way (Seeber 2003; Berné et al., 2014). Besides, differential GPS solves an important problem in gravimetric surveying; the accuracy in the Z coordinate.

Assuming that a static receiver is very accurately located (by means of other techniques) and receives the position given by the GNSS system, it will be able to estimate the errors produced by the system. If this receiver corrects and transmits the error to other receivers near it, they can also correct the errors produced by the system. In the differential system, a receiver is placed on a Base, a fixed station with a highly precise and accurate set position. In this station, two types of corrections are made:

- A correction directly applied to the position. This has the disadvantage that both, the user and the monitoring station, must use the same satellites.
- A correction applied to the pseudorange of each of the visible satellites. In this case, the user can make the correction with the 4 satellites with better signal/noise ratio. This correction is more flexible.



Figure 2.1.17. EUREF Permanent GNSS Network. Example of location of stations providing real-time data (source <http://epncb.oma.be/>).



---

These corrections can be transmitted via radio or GSM to a mobile receiver and this receiver will perform the real-time differential correction. In areas where communication between the Base receiver and the mobile device has difficulties (poor coverage), or there is no transmission between the receivers, a post-processing correction will be applied in the office. Noticeably, to perform an accurately differential correction, both in real time or post-processing, the measurement of the receivers must be simultaneous and with at least four common satellites. Since 1994, the International GNSS Service (IGS), formed by more than 200 agencies around the world, is working in GNSS data and generates products inside the International Association of Geodesy (IAG). The IGS network is formed by more than 300 permanent stations. In Europe the EUREF permanent GNSS Network (EPN) (<http://euref.eu/>), operate under the IGS and consist of:

- a network of continuously operating GNSS (Global Navigation Satellite Systems, such as GPS, GLONASS, Galileo, Beidou, ...) reference stations,
- data centres providing access to the station data,
- analysis centres that analyse the GNSS data,
- product centres or coordinators that generate the EPN products,
- and a Central Bureau that is responsible for the daily monitoring and management of the EPN.

In Spain, the ERGNSS network have more than 100 permanent stations (GPS/GNSS) distributed throughout the territory (that belong either to National Geographic Institute or to the different regional networks) where some of them belong to the EUREF network. These permanent stations are used as Base receivers. Besides this national network, there are regional networks that complement the Spanish network, as for example the one used in this project is the ARAGEA network (Aragón network) and one Base from the IGN network. The standard procedure of the IGME is to perform the differential correction during post-processing in the office.



Figure 2.1.18 ERGNSS network (source Spanish Geographical Institute-IGN)



Figure 2.1.19 (next page). Regional ARAGEA network ( <https://gnss.aragon.es/> ) and technical details of one of the Bases (Sabiñánigo) near the 3DGeoEu project target area.



---

## ***Coordinate system in Gravimetry***

The GPS system provides coordinates in the global system WGS84 (World Geodetic System of the year 1984) associated with the ellipsoid of the year 1984.

In Spain, for example, the Royal Decree 1071/2007 of July 27, regulates the official reference geodetic system, and states that the official reference geodetic system in Spain becomes the ETRS89 (European Terrestrial Reference System 89) since 2015. In most surveys, for the required accuracies, the error using the WGS84 instead of the ETRS89 is negligible (decimetric level, <https://www.icgc.cat/es/Administracion-y-empresa/Herramientas/Transforma-coordenadas-y-formatos/ETRS89/Aspectos-geodesicos-del-ETRS89>), therefore, the coordinates obtained with the GPS receivers are assumed as valid. The ETRS89 is the reference GNSS coordinate system throughout Europe. This system is supported by EuroGeographics (<https://eurogeographics.org>) and endorsed by the INSPIRE Directive (2007/2/EC, in the D2.8.1 1 Data Specification on coordinates reference system-Technical guidelines of 2014-04-17). The access to the system is provided by the EPN. The ETRS89 forms the backbone for geolocation data on the European territory, both on a national and on an international level.

In the case of gravimetric data, the normal gravity value (latitude gravity) is established from the reference surface or geoid (approximated to a revolution ellipsoid) at sea level and depends on the geographical latitude. The adoption of different ellipsoids gives rise to different reference systems for gravimetric surveys. In Spain, the UNE Norm 22-611-85, Terrestrial Geophysical Survey, gravimetric method, established the GRS67 geodetic system for the calculation of normal gravity (latitude gravity). Currently, the Bouguer anomaly maps are calculated in the GRS80 geodetic reference system, being most appropriate to follow the new standardization proposed by Hinze et al (2005) in their article “New standards for reducing gravity data: The North American gravity database”.

The orthometric height,  $H$ , is referred to the geoid (nearly equivalent to the average sea level; Alicante as a reference in Spain), while the ellipsoidal height,  $h$ , is the height referred to the ellipsoid. The height measured with GPS provides the ellipsoidal height referred to the international ellipsoid WGS84. To convert ellipsoidal heights to orthometric heights it is necessary to know the height of the geoid  $N$  (separation between the geoid and the ellipsoid), so that:

$$H = h - N$$

The surface of the geoid is usually not well known, and its calculation is constantly updated (Fairhead et al., 2003). The currently used geoid model is the Global Geoid model EGM08 (Pavlis et al., 2008 and 2012). Usually, heights are expressed in meters. For our calculations in the Iberian peninsula, we used the EGM08REDNAP which is the universal geoid model improved with the station elevations Net established by the IGN (<ftp://ftp.geodesia.ign.es/documentos/EL%20NUEVO%20MODELO%20DE%20GEOIDE%20PARA%20ESPAÑA%20EGM08-REDNAP.pdf>). For the calculation of gravity corrections (in the GRS80 geodetic system), coordinates referred to WGS84 and orthometric heights must be used, since the currently available digital terrain models have been obtained from orthometric heights.



### 2.1.4 Gravity Corrections

This section is devoted to the reduction of gravity data to anomalies, that is, the gravity corrections. After gathering the gravity measurement in the field, the subsequent gravity processing aims: i) to isolate the “geological” signal that contributes to the gravity acceleration (Observed Gravity) and ii) to obtain the gravity anomaly found between the Observed Gravity and the Theoretical Gravity (Bouguer anomaly).

i)  $\text{Bouguer anomaly} = \text{Observed Gravity} - \text{Theoretical Gravity}$

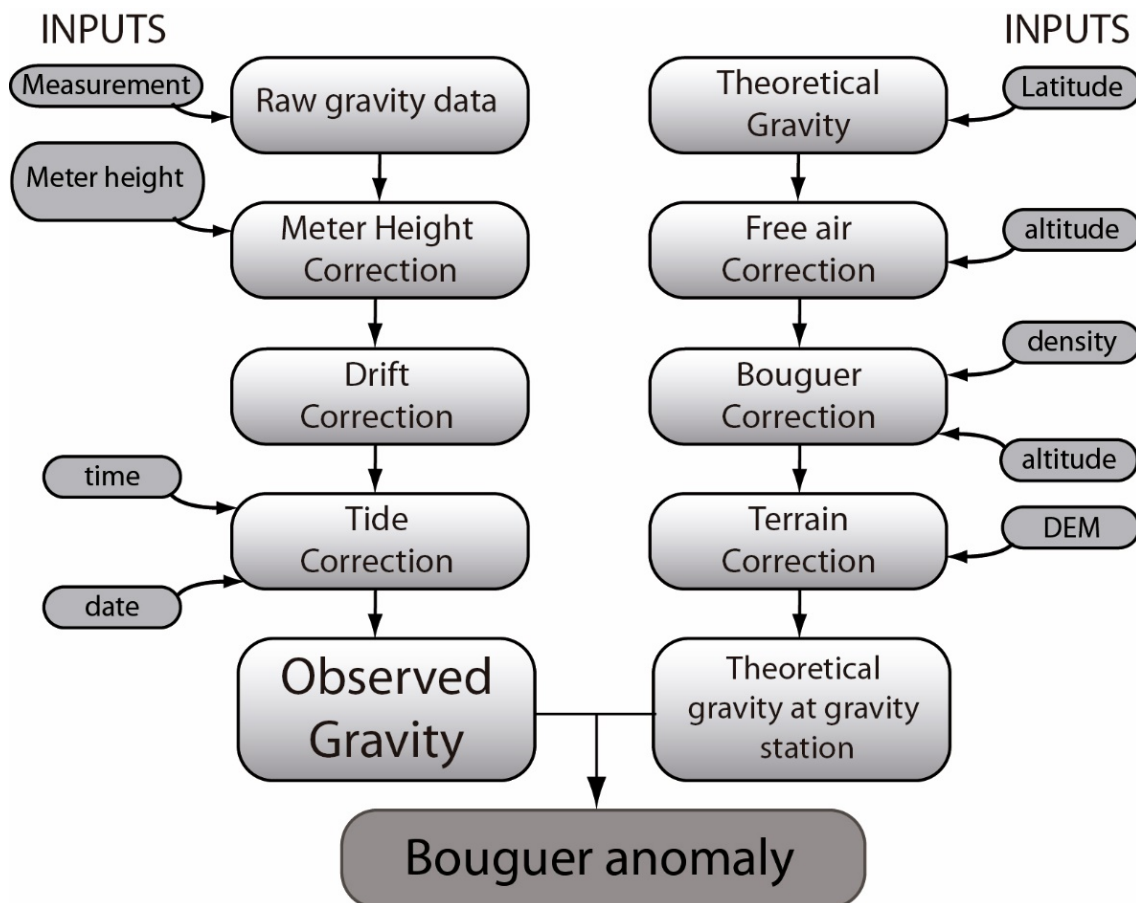


Figure 2.1.20. Flow diagram summarizing the gravity processing workflow used to obtain the Bouguer anomaly of a specific gravity station. Modified after Santolaria, 2015.

Gravity data processing workflow includes, on one hand, the computation of the field raw gravity data and, on the other hand, the calculation of the Theoretical Gravity value at the



gravity station (Fig. 2.1.20). These involve a series of corrections which are here detailed. Despite the mathematical procedures are known as “correction”, this is a historically accepted term that actually refers to the reduction of gravity data to isolate the required component of the gravity field used to perform geological interpretations.

#### **2.1.4.1 Observed Gravity**

The raw relative gravity data taken in the field must be reduced to the absolute gravity value by means of the connection between gravity station and an absolute gravity base. Apart from the density of the rocks underneath the gravity station, there are some other factors that contribute to the obtained absolute gravity data. These out-of-the-target factors may mask the true geological source of the gravity anomaly and must be removed from the absolute gravity data to obtain what is named as Observed Gravity. Therefore, the observed value is a conversion of the raw and relative gravity measurement to the absolute gravity at the station after applying the following corrections: the tide, drift and meter height corrections. As we have seen before, relative gravity measurements are usually tie to the International Gravity Standardization Net (IGSN71) of absolute gravity stations.

The *Tide Correction ( $T_dC$ )* compensates the gravity attraction of the Sun and the Moon. The relative position of the Earth with respect the Sun and the Moon fits to a time-dependent function. This is a wave function including several periods: 12 h, 24 h, 12 days and 6 months. The maximum variation rate is about 0,3 mGal in 6 hours. The input data is the date and time (solar time) of the gravity measurement.

The *Drift correction (DC)* is, as previously explained, associated with the instrumental drift of the gravimeter during the surveys. The instrumental drift is easily controlled by systematically and daily repeating the measurement in specific gravity stations. Drift is considered to behave linearly among base measurements, and this is normally supported by punctual checks of the instrument used (short periods of continuous measurement) (for further details see Section 2.1.3).

Finally, the *Meter Height correction (MHC)* is specific of each gravimeter and considers the height between the meter and the Earth surface (input data). This correction aims to eliminate the influence of the meter height in the gravity measurement.

The Tide correction and the Meter Height correction are already implemented in the internal software of some gravimeters (*e.g.* Burris, Scintrex) and therefore the output reading is already corrected.

Thus, considering these corrections, the Observed Gravity of a station is;

$$\text{Observed Gravity} = \text{Raw absolute instrumental data} \pm T_dC \pm DC + \text{MHC}$$



#### 2.1.4.2 Theoretical gravity

The theoretical gravity corresponds to a mathematical model of the Earth gravity field. This model assumes i) an ellipsoidal Earth whose radius is maximum in the Equator and minimum in the poles, ii) that the Earth rotation creates a linear acceleration at the surface which is maxima in the Equator and minima in the poles, iii) that the mass accumulation between the center of the Earth and the equator is higher than between the center of the Earth and the poles and iv) that the internal Earth layering and its tectonic anisotropy is obviated.

The latest ellipsoid recommended by the International Union of Geodesy and Geophysics is the 1980 Geodetic Reference System (GRS80) (Moritz, 1980) (Hinze et al., 2005). The Somigliana's closed-form formula (Somigliana, 1930) for the theoretical gravity ( $g_T$ ) is:

$$g_T = (g_e) \frac{1+0.001931851353\sin^2(\varphi)}{\sqrt{1-0.0066943800229\sin^2(\varphi)}} \text{ mGal}$$

where  $\varphi$  is the latitude and  $g_e$  is the normal gravity at the equator, 978032,67715 mGal. The 1980 Geodetic Reference System (GRS80) (Moritz, 1980) includes the atmospheric effect on the Earth gravity field and therefore the atmosphere gravity correction ( $\delta$ ) is needed; its value corresponds to (Wenzel, 1985):

$$\delta = 0,874 - 9,9 \cdot 10^{-5}h + 3,56 \cdot 10^{-9}h^2$$

where  $h$  is the gravity station height. New standardizations (Hinze et al., 2005) recommend the use of the International Terrestrial Reference Frame (1980 Geodetic Reference System ellipsoid) as datum.

This Earth model implies some simplifications: i) the gravity acceleration value is located at the datum, ii) the Earth interior is homogeneous in terms of density and iii) the Earth surface is regular and represented by the GRS80 ellipsoid (Moritz, 1980) (Hinze et al., 2005). To calculate the Theoretical Gravity at the gravity station ( $g_\varphi$ ), the *Height correction* must be applied. This correction involved three different steps: The *Free air*, the *Bouguer* and the *Terrain corrections* (Fig. 2.1.21).

The *Free air correction* (FAC) represents the decrease of the gravity acceleration as the distance between the center of the Earth and the gravity station increases. Therefore, since the gravity station is not located at the datum, this correction depends on the Earth gravity field gradient (0,3086 mGal/m) and the gravity station height ( $h$ ). The FAC is expressed as (LaFehr, 1991):

$$FAC = 0,3086 \cdot h$$

Hinze et al. (2005, 2013) recommend a more precise function proposed by Heiskanen and Moritz (1969) that considers the GRS80 ellipsoid:

$$FAC = \frac{-2g_e}{a} \left[ 1 + f + m + \left( -3f + \frac{5}{2}m \right) \sin^2\varphi \right] h + \frac{3g_e h^2}{a^2} \quad (8)$$

The GRS80 ellipsoid has the following parameter values:  $a$ , the semimajor axis, is 6378137 m;  $b$ , the semiminor axis, is 6356752,3141 m;  $f$ , flattening, is 0,003352810681;  $g_e$  is 9,7803267715 m/s<sup>2</sup>; and  $m$ , which is  $\omega^2 a^2 b^2 / GM$ , is 0,00344978600308, where  $\omega$  is angular velocity (7292115



$\times 10^{-11}$  radians/s) and GM is a geocentric gravitational constant ( $3986005 \times 10^8 \text{ m}^3/\text{s}^2$ ). The FAC is negative or positive if the gravity station is above or below the datum, respectively.

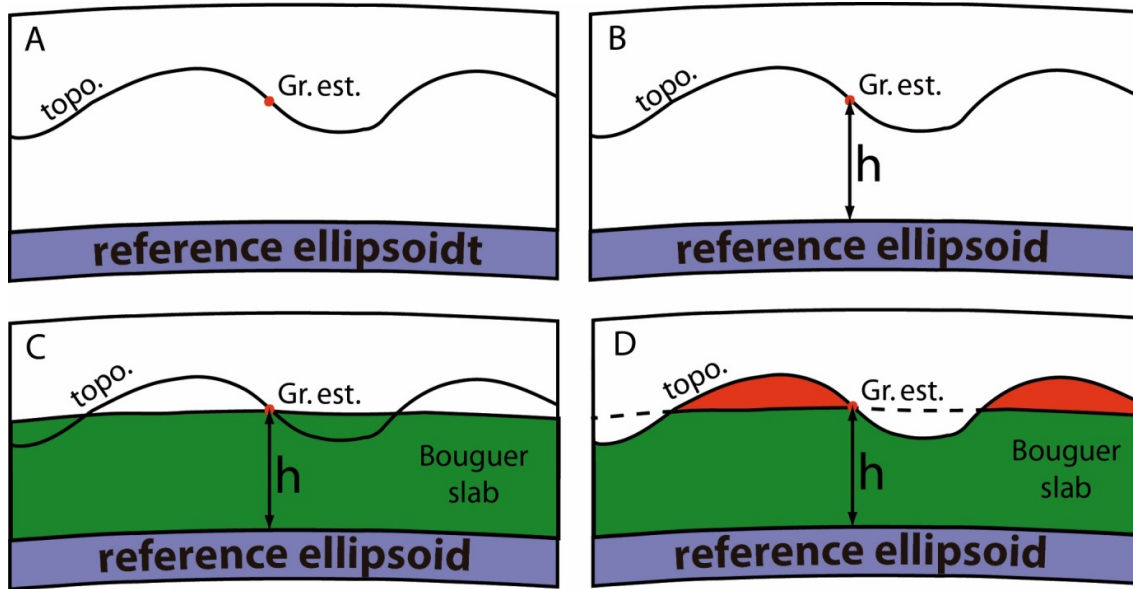


Figure 2.1.21. Simple sketches illustrating the step-by-step procedure to obtain the Theoretical gravity value of a gravity station (Gr. Est.) (A) Raw theoretical gravity value; (B) Free air correction (FAC); (C) Bouguer correction (BC); (D) Terrain correction (TC). Modified after Santolaria (2015).

The *Bouguer correction* (BC): Its rationale considers that between the modeled Earth surface and the gravity station, a horizontal and infinite slab exists. This slab is characterized by a given density (Reduction density,  $\rho_r$ ) and a thickness that equals the height of the gravity station above the reference ellipsoid. The BC value is expressed as:

$$BC = 2\pi G \rho_r h$$

considering  $G = 6,673 \times 10^{-11} \text{ N}\cdot\text{m}^2/\text{kg}^2$

then  $BC = 0,04193 \rho_r h$

$h$  in m,  $\rho_r$  in  $\text{g}/\text{cm}^3$  and BC in mGal. The Bouguer correction represents the attraction caused by the Bouguer slab and therefore is positive.

There are several mathematical approaches to calculate the reduction density aiming to minimize the correlation between the Bouguer anomaly and the topography (Nettleton, 1939, 1976; Rikitake et al., 1965; Parasnis, 1952, 1979; Fukao et al., 1981, Murata, 1990, 1993; Yamamoto, 1999). Regional studies tend to use a standard value of  $2,67 \text{ g}/\text{cm}^3$  (Chapin, 1996; Hinze, 2003) but, ideally, a different density reduction should be used for each station (Hackney



and Featherstone, 2003; Hinze, 2003). Latter implies a previous knowledge of the geology at depth and, if not it may represent a circular reasoning. Other works (e.g. Santolaria et al., 2016) and new standardizations (Hinze et al., 2005) use and recommend, respectively, a reduction density calculate from the mean density of outcropping rocks, assuming that this mean is the most representative value of the Bouguer slab density. For the sake of simplicity when merging different surveys, a common procedure is to use the standard reduction gravity of  $2,67 \text{ g/cm}^3$ .

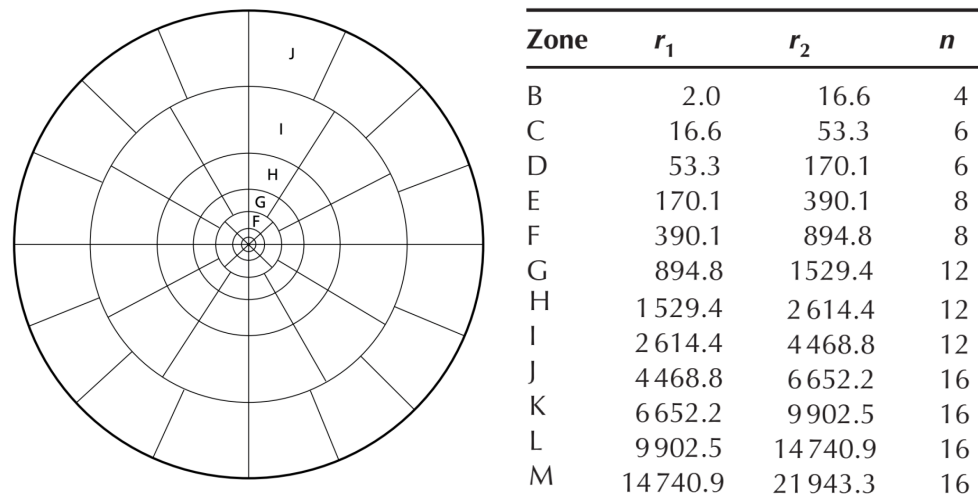


Figure 2.1.22. The Hammer's net (Hammer, 1939; taken from Kearey et al., 2002).

Finally, the *Terrain correction* (TC) considers the influence of the uneven topography of the Earth surface and its subsequent effect on the gravity measurement in a given station. The terrain/topography correction represents the deviations from the uniform slab of the Bouguer correction. The Terrain correction is negative: either because a topographic high (over the gravity station) counteracts the Earth gravity attraction or a depression (below the gravity station) does not add any effect. The terrain correction is a three steps correction based on the Hammer's net (Hammer, 1939); a ring-based template (Fig. 2.1.22), centered in the gravity station, where zones are defined by the distance to the gravity station and are characterized by the mean altitude difference between the gravity station and the specific zone. Generally, a single density is used for terrain corrections. Methods using variable surface density models have been proposed by Vajk (1956) and Grant and Elsharty (1962). The *near terrain* correction applies from the gravity station (0 m) up to 53,3 m away and it is done in-situ by the data operator. It can be done by using high resolution topographic maps, laser measurements (Schivone et al., 2009), etc. But, in most cases is based on eye-ball estimations, there is always a subjective visual component when trying to find out the mean height difference. For this reason, it is highly recommendable that the same operator performs the near terrain correction during the gravity surveys. However, some recent drone applications (photogrammetry, LiDAR or the combination of standard and emerging sensors etc.; Dering et al., 2019) have a promising future in estimating high precision (less than 0,01 m) DEMs for the near (inner)-terrain



correction (Porzucek et al., 2017; Kaub et al., 2018) in open landscapes and thus, reducing the uncertainty of classic approaches.

The second and third portions of the Terrain corrections, also based on the Hammer's net, use local to regional high resolution digital elevation models to compute the terrain effects (e.g. Godson and Plouff, 1988). The more precise is the elevation model the more accurate will be the terrain correction (Tziavos et al., 2010) but computational time increases. The IGME uses the software CCT, developed by the geophysical group in 1991, and updated in 2014 (Plata, 1991, 2014). The software makes use of data from digital elevation models, usually from the IGN, and the calculation is based in the Hammer's method and the Neumann Interpolation algorithm (Hammer, 1939; Neumann, 1963). In a gravimetric survey, the protocol followed by the IGME is: the station must be placed in flat terrain (if it is possible), at least 2 m around the reading point; the near correction till 150 m is made by direct estimation in the field (prospector). Medium and far corrections for Hammer sector's E to M (from 150 m to around 22km) are calculated by the software updated version of 2014 that allows to extend the correction up to sector Q (around 167 km). The Terrain correction may be critical in high mountain areas whose magnitude can exceed 30 mGal (Nabighian et al., 2005).

Theoretical gravity of the station ( $g_{\phi}$ ) equals:

$$g_{\phi} = g_t - FAC + BC - TC$$

and therefore the Bouguer anomaly formula is obtained by

$$BA = g_{obs} - g_{\phi} = g_{obs} - g_t + FAC - BC + TC$$

#### **2.1.4.3 Bouguer, Regional and Residual anomalies**

As mentioned in the beginning of the previous section, the Bouguer anomaly equals the difference between the Observed and Theoretical gravity. The Bouguer gravity anomaly reflects the deviation of the actual Earth gravity field with respect to the modelled Earth gravity field. This deviation reflects, in turn, the mass heterogeneities of the Earth interior. The Bouguer anomaly includes short to long wavelength gravity anomalies which are associated to shallow and deep-seated mass heterogeneities respectively. Once the Bouguer anomaly for each gravity station has been calculated, several interpolation methods are used to elaborate the Bouguer anomaly contour map. The more recommended ones being the minimum curvature (Briggs, 1974), gradient enhance minimum curvature (O'Connell et al., 2005) or kriging (Hansen, 1993).

The Bouguer anomaly can be used to interpret and model the geometry and density variations within the mid-crust to the mantle. Thus, it is useful to assess large scale, geodynamic settings.

Conversely, if the geological target is located at shallower levels, its signal may be superposed on the regional gravity field associated to a larger and deeper heterogeneity. In this situation, it is needed to isolate the gravity signal related to these shallow bodies, procedure known as regional-residual separation. This is a critical step on gravity data interpretation. The main objective is to isolate the short wavelength anomalies (Residual anomaly) from the long wavelength anomaly (Regional anomaly) by removing this latter from the Bouguer anomaly. A



broad range of methods has been applied to separate the regional and residual gravity signals, either by using a simple graphical approach based on profile data and, eventually, gridded data or by means of mathematical methods. Some of the mathematical methods used to calculate the regional field are the second vertical derivative (Henderson and Zietz, 1949 and Roy, 1985 after Griffin, 1949), the least-squares fit (Agocs, 1951), gravity modelling (Hammer, 1963), 2D linear-wavelength filtering with filters of different cutoff wavelengths (Zurflueh, 1967; Agarwal and Kanasewich, 1971), spectral analysis (Spector and Grant, 1970; Guspi and Introcaso, 2000) or others (Syberg, 1972; Pawlowski and Hansen, 1990).

Despite the regional-residual separation is a historical problem, there is not yet a single right answer and the applied method should be based on, or at least check against if possible, the geological knowledge of the target area and surroundings (Nabighian et al., 2005). Sometimes it is recommendable to extend your regional gravity farther out of the studied area to have a broader overview of the long wavelength signal and prevent for boundary effects. Estimation of regional gravity anomaly maps from airborne surveys (Olesen, 2002) or satellite data (like GOCE) may be also a choice (Eicker et al., 2014; Bouman et al., 2015).

Once the regional field has been extracted from the Bouguer anomaly (Figure 2.1.23), the remaining Residual anomaly (Figure 2.1.24) may appear as an untrendy contour map where anomalies stand out over a “flat” background. But, this is not always the rule since in some situation “regional” but shallow-seated density trends may appear. In any case, the Residual anomaly reflects the signal of the geological bodies located relatively close to the surface having different densities, shape, lateral extent and emplacement depth (Hamdi-Nasr et al., 2010).

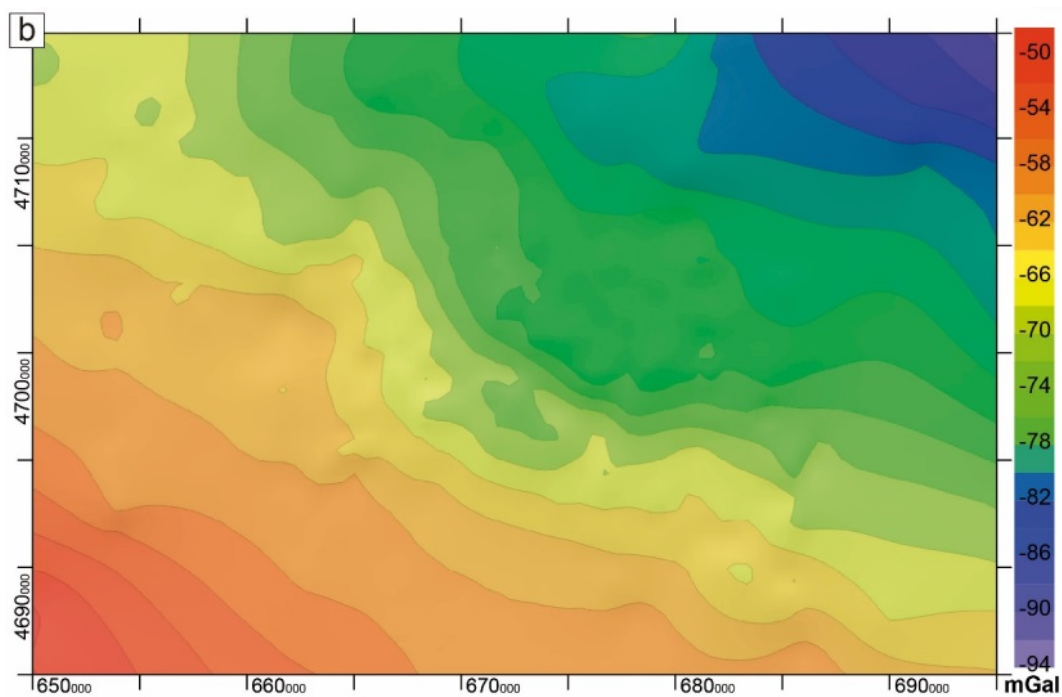


Figure 2.1.23. Bouguer anomaly map from the Western External Sierras (Southern Pyrenees)

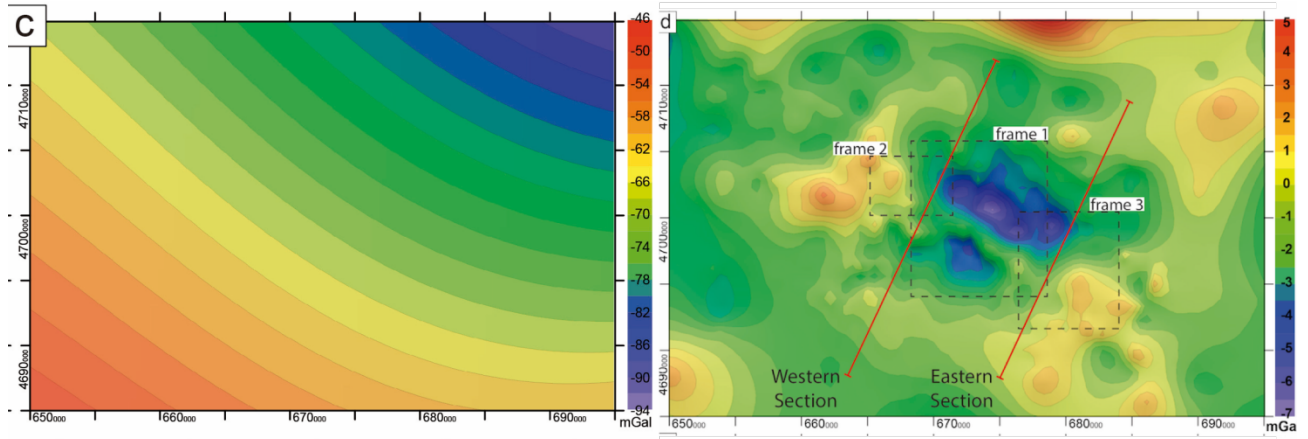


Figure 2.1.24. Regional and residual anomaly maps from the same region (Pueyo et al., 2021).

### 2.1.5 Gravimetric data model and databases

There are several international and national standards for gravimetric data both for absolute measurements (e.g. Boedecker, 2002; Vitushkin, 2011; Wziontek et al., 2012) or land, airborne (Hinze et al., 2005; Tracey et al 2007) and satellite data (van der Meijde et al., 2015). Besides, there are some standardized protocols for gravity surveys (Murray & Tracey, 2001; Hinze et al., 2005). The acquisition of gravimetric data, specifically the criteria and parameters involved in geophysical surveys as we perform in the IGME, are based on the Norm UNE 22-611-85. This Norm is dated November 1985, and therefore some aspects must be updated, specifically the new World References Systems, both topographic and geodetic (see annex). Other geological surveys and institutes across Europe have their own standards. In short, gravimetric data has been standardized in several countries (Hinze et al., 2005 in the US; Tracey et al 2007 in Australia, etc...) and, accordingly, several data models and data schemes exist which are not always accessible or interoperable. This section of the report aims to overview what has been done so far in gravimetric data management.

In Europe, the INSPIRE directive (<https://inspire.ec.europa.eu/>), particularly in the Data Specification on Geology – Technical Guidelines (<https://inspire.ec.europa.eu/id/document/tg/ge/>) and partially in the Data Specification on Mineral Resources – Technical Guidelines (<https://inspire.ec.europa.eu/id/document/tg/mr/>), has defined very few geophysical data descriptors (Ayala, 2013) in its thesaurus (e.g. GE.GeophStation). Therefore, many details on gravimetric data, metadata and data models are still to be outlined to define standard gravimetric databases ruled by FAIR principles in alignment with current trends of public data repositories. FAIR data, data models and databases are those which meet the principles of findability, accessibility, interoperability, and reusability (<https://www.go-fair.org/fair-principles/>) (Wilkinson et al., 2016). There are some ongoing ambitious European efforts (EPOS [<https://www.epos-ip.org/>]) and EGDI [[D6.4 Workflow 3D - 55 of 264](http://www.europe-</a></p></div><div data-bbox=)



---

[geology.eu/](http://geology.eu/)] data repositories) that could remediate the situation regarding the gravimetric data. However, they have not yet defined the data model for gravimetric data.

On one side, and sponsored by the International Association of Geodesy (IAG), the International Gravity Field Service (IGFS):

- (i) coordinates collection, validation, archiving and dissemination of gravity field related data,
- (ii) coordinates workshops, information materials and general public outreach related to the Earth's gravity field,
- (iii) and unifies gravity products for the needs of GGOS – the Global Geodetic Observing System.

The IGFS also coordinates the servicing of the geodetic and geophysical community with gravity field-related data, software and information. The combined data of the IGFS entities include both satellite-derived and combined global models, time-variable gravity models, terrestrial, airborne, satellite and marine gravity observations, Earth tide data, GPS leveling data, digital models of terrain and bathymetry, ocean gravity field and geoid from satellite altimetry. The IGFS collects, through its services, gravity, geoid, GEM, COST-G, DEM, SG raw, and tidal products for use in a wide range of geodetic, geophysical, and oceanographic works. These datasets are used by the geodetic community and the IGFS services members, SGs, JWGs, to generate the data products which are made available to interested users through this website: <http://igfs.topo.auth.gr/>. Moreover, the IGFS has developed and provides online applications for the creation of metadata for gravity and geoid data. Human readable formats are available as well as search functions.

On the other side, the International Gravimetric Bureau (BGI) was created in 1951 by decision of the International Union of Geodesy and Geophysics (IUGG). It is one of the services of the International Association of Geodesy (IAG) and of its International Gravity Field Service (IGFS); <http://igfs.topo.auth.gr/>, which coordinates since 2001 the servicing of the geodetic and geophysical community with gravity field-related data, software and information. It is also recognized as one of the services of the Federation of Astronomical and Geophysical Data Analysis Services (FAGS) that operates under the auspices of the International Council for Science (ICSU). The FAGS Services was incorporated into the new World Data System (WDS) of ICSU in 2009-2010.

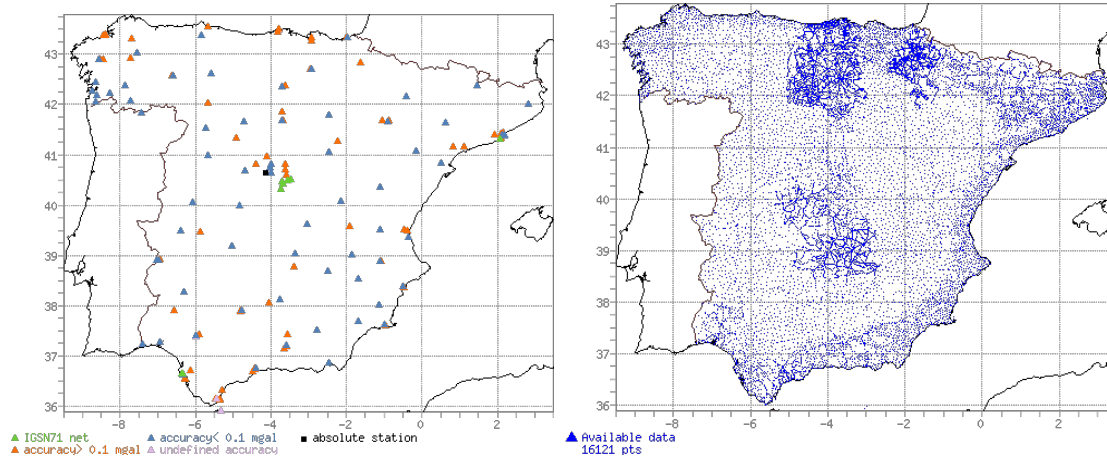


Figure 2.1.25. Gravimetric bases and available gravimetric data in Spain from the BGI web page (data are provided upon request).

The BGI central office is located in Toulouse, France, in the premises of the Observatoire Midi-Pyrénées (OMP). In France, it is supported by national agencies and educational and research laboratories which directly contribute to the BGI activities in various fields (service, research and education). The BGI is recognized in France as the Service d’Observation CNRS/INSU (Service “Gravimétrie-Géodésie”). It has also contributions from the Groupe de Recherche en Géodésie Spatiale (GRGS). <http://bgi.omp.obs-mip.fr/>

Different institutions offer public (not always free of charge) gravimetric datasets: the British Geological Survey (BGS) has the GB Land Gravity Survey. It comprises 165000 gravity observations (1,6 per km<sup>2</sup>). Most of the surveys were carried out by the BGS but the database includes data originally acquired by other organizations. This was subsequently given to the BGS and integrated into a consistent dataset that became a national archive. (<https://www.bgs.ac.uk/products/geophysics/landGravity.html>). The national geological service of France, the BRGM, offers the BD-Gravi, a database with around 410000 gravimetric stations measured in French territory, [https://www.brgm.eu/sites/default/files/plaquette\\_gravimetrie.pdf](https://www.brgm.eu/sites/default/files/plaquette_gravimetrie.pdf). There are also private initiatives (<https://getech.com/gravity-magnetic/>) (Fig. 2.1.26) that have harmonized thousands of data worldwide, but whose data schemes are not public and data access is subjected to fees.

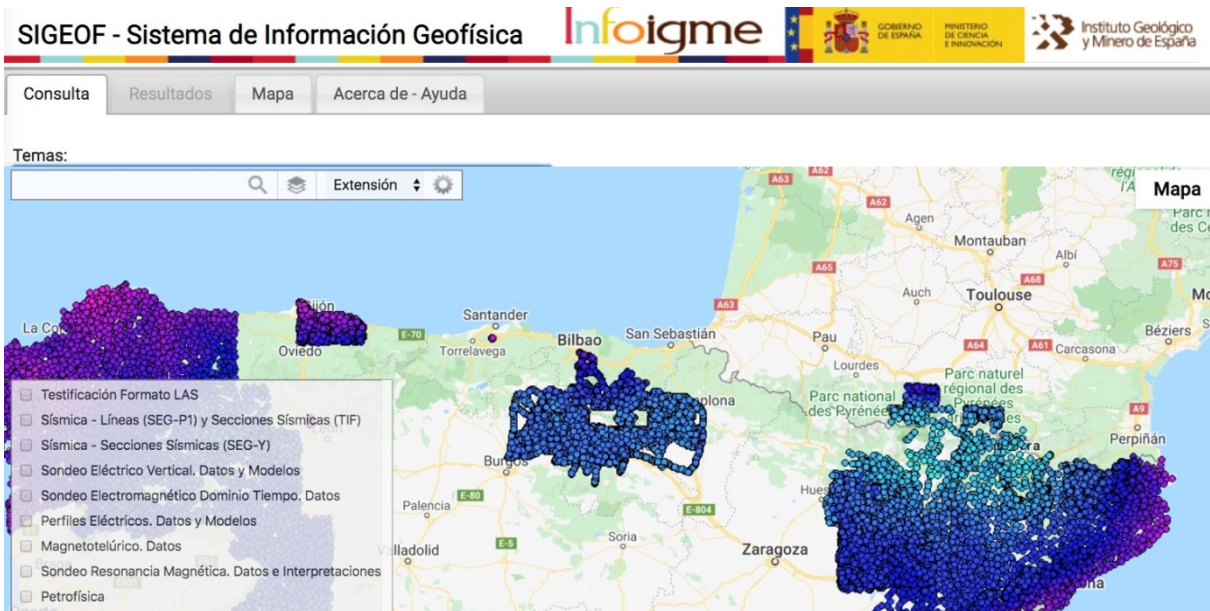
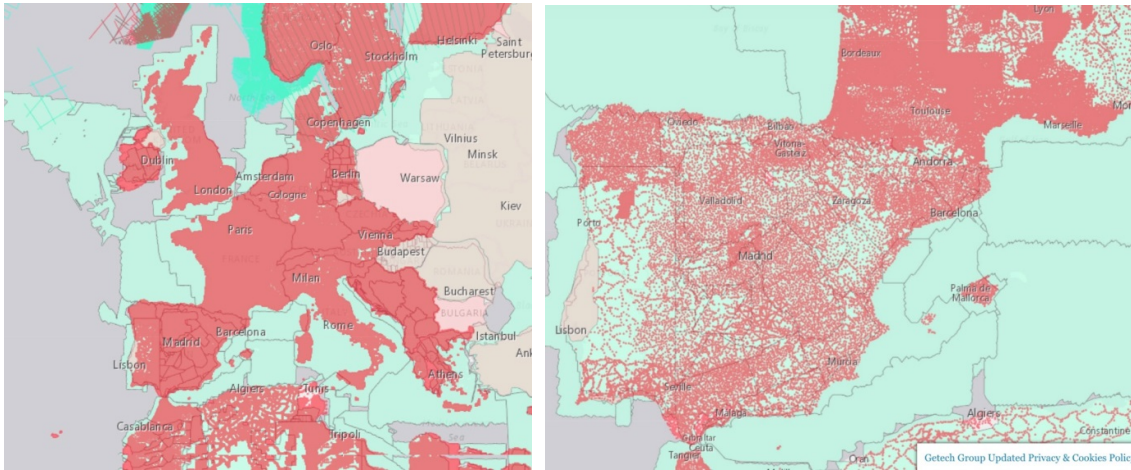


Figure 2.1.26. The Getech private (top) and the public Spanish Sigeof (bottom) gravimetric databases.

In Spain and framed on the TOPOIBERIA project, the SITOP database includes a compilation and harmonization of more than 210,000 gravimetric stations of the Iberian peninsula (Ayala et al., 2016). These data are stored in an IGME server (<http://cuarzo.igme.es/sitopo/> not operative at the time of writing this report). Besides, the IGME Geophysical information system (SIGEOF) compiles the geophysical data measured or harvested by the IGME (<http://info.igme.es/SIGEOF/>). The SIGEOF (Fig. 2.1.26, not fully updated for the gravimetric information) is guided by FAIR principles and incorporates specific datasets (gravimetric, magnetic, seismic sections, well data, petrophysics, etc.) throughout the territory from multiple surveys accessible through a browser based on subjects, e.g. gravimetry. The searching machine allows copying the results to the clipboard and pasting them elsewhere. It also may provide an excel or a CSV format file. The SIGEOF also provides the gravimetric information as ESRI shape



file format. This format is readable by multiple software products, some of them are open-access, e.g. QGIS software. The shape files contain point-based geometric entities (Coordinate system EPSG: 4326, Geographic Coordinates WGS84), with additional identification attributes (sequential No., recognition No., etc.), calculated measurements and corrections (Table 2.1.6).

FIELD	CONTENT (SUBJET)	FORMAT	
ID	Sequential identifier	Number	*
IDTR	Identifier of the work	Number	*
WORK	Location and work information or recognition	Text	
COORDX	X coordinate (EPSG: 25830; ETRS89 / UTM 30N)	Number	*
COORDY	Y coordinate (EPSG: 25830; ETRS89 / UTM 30N)	Number	*
GRABS	Gravity measured decreased by 979000 (mGal)	Number	*
CORTP	Near terrain correction (mGal) (density 2.0)	Number	*
CORTT	Complete terrain correction (mGal) (density 2.0)	Number	*
A1	Bouguer anomaly (density 2.67 (mGal) )	Number	*
COORDZ	High (m)	Number	*
IE	Code of the work (*)	Number	*
NH50K	Sheet number 1:50.000	Number	*

*Table 2.1.6. Data descriptors for gravimetric data in the SIGEOF database. Most fields (those with an asterisk) can be exported to Excel, CSV or copied to the clipboard. The output will also include an extra field "TITLE" that refers to the name of the IGME Documentation Report, Geophysics Area Report, Project, Article, etc. (2020, April).*

The IDTR or WORK attributes allow identifying the work, project, survey or campaign program where the gravity value was collected.

Note: In the processing of gravimetric data compiled in the SIGEOF database, latitude gravity was calculated using the GRS80 system formula, based on the WGS84 ellipsoid, adopting a reduction density of  $2.67 \text{ gr/cm}^3$ . The coordinates for the calculation of normal (theoretical) gravity are referred to the ETRS89 reference system. Terrain correction is calculated till sector "m" of Hammer ( $\approx 22 \text{ km}$ ).

In conclusion, many efforts are still to be done to standardize gravimetric data (data models and metadata schemes). Besides, gravimetric data must be fully compiled and updated to ensure the achieving of FAIR principles. In this frame, EPOS and/or EGDI leading initiatives should fulfill these gaps and lacks on gravimetric information in Europe.



### 2.1.6 Common software used in gravity surveys

Throughout a gravimetric survey, various types of software can be used (table 2.1.7). During the last years, partially due to the increasing computer performance capabilities, several software packages have been launched being part of them free licensed. A first group of software is specifically designed for some gravimeters to control the data acquisition and some corrections (CG3TOOL for the Scintrex by Gabalda et al., 2003 or AGES© for the Burris by Schulz, 2018). Other universal packages allow gravimetric corrections and even reduction for any kind of data source; Grav Process (Cattin et al, 2015), pyGrav (Hector & Hinderer, 2016), Gsolve (McCubbine et al., 2018), etc. A third group is focused on the reduction of gravity data (and beyond) to obtain the Bouguer anomaly, as well as further processing for obtaining regional and residual maps, or derived products: continuations, vertical derivative, Euler's solutions, etc. Part of this last group also allows the application of more advanced techniques of forward modelling and inversion: Oasis Montaj, IGMAS+ (Schmidt et al., 2010), 3D Geomodeller (Calcagno et al., 2006) (see also section 3.2).

Processing – Software	Data acquisition (gravity meter)	Tide correction	Drift Correction	GPS acquisition	GPS processing	Terrain Correction	Mapping/Gridding	Complete Calculations: From data acquisition to Bouguer anomaly; Mapping and gridding	References/url
CG3-Tools	x (Scintrex)								Gabalda et al., 2003
AGES©	x (Burris)								Schulz, 2018
QuickTide Pro		x							MicrogLaCoste product software
CCT						x			In house (Plata, 1991,2004)
TCP				x					<a href="https://www.aplitop.com/software/tcp-gps-windows">https://www.aplitop.com/software/tcp-gps-windows</a>
Justin					x				<a href="http://javad.com/jgnss/products/software/justin.html">http://javad.com/jgnss/products/software/justin.html</a>
SURFER							x		<a href="https://www.goldensoftware.com/products/surfer">https://www.goldensoftware.com/products/surfer</a>
GravProcess		x	x			x		x	Cattin et al., 2015
pyGrav		x	x						Hector & Hinderer. (2016). (Microgravity)
Gsolve								x	McCubbine et al., 2018
INTREPID Geophysics								x	<a href="https://docs.intrepid-geophysics.com/intrepid/topics/Tool-References.html">https://docs.intrepid-geophysics.com/intrepid/topics/Tool-References.html</a>
OasisMontaj								x	<a href="https://www.seequent.com/es/productos-y-soluciones/geosoft-oasis-montaj/">https://www.seequent.com/es/productos-y-soluciones/geosoft-oasis-montaj/</a>
IGMAS+								x	<a href="https://www.seequent.com/es/productos-y-soluciones/geosoft-oasis-montaj/">https://www.seequent.com/es/productos-y-soluciones/geosoft-oasis-montaj/</a>

Table 2.1.7 Overview of software packages and programs used in our surveys. Red colour, other software that can be used for calculations and processing for different processes involved in gravimetric surveying.

During the field surveys, gravimeters and GPS receivers used by the IGME integrate their own operating software. In the case of the CG5 and Burris gravimeters, the instruments incorporate all the factory software for measurement management: tilt control, temperature control, tidal correction calculation, etc. Although the device creates files with the data that can be downloaded, in many cases we only use these files as a backup of the data. Other vintage gravimeters (Lacoste and Romberg) are totally analogic. During the field survey, the operators



---

fill in paper sheets the data and upload them to an in-house designed excel sheets. For further corrections, we also use in-house software for calculate some of corrections (CCT for terrain correction) but usually some commercial softwares are run for the different steps of the processing of the gravimetric data.

### 2.1.7 Uncertainty Sources in gravimetric data

The interpretation of gravimetric data itself contains uncertainties at different levels. Some of them related to the acquisition of the data itself (imprecision of the measurement process, positioning of the stations), and others related to the processing of gravity data to obtain the observed gravity anomaly that not always are calculated using the same standard or taking into account the same parameters (Siegel, 1995; Hinze et al., 2005). The semiquantitative interpretation of the gravity data (Euler solutions, derivatives, etc.) and the gravity modelling (either forward or inversion) also contain uncertainties that are difficult to assess.

Besides, different levels of accuracy are required for surveys with different objectives (i.e. regional studies versus microgravimetric surveys). The level of precision required will determine the field procedure and the level of accuracy of the corrections that are pertinent. Focusing on a given survey, instrumental errors and the data reduction procedures will require a post-processing to estimate the associated uncertainties that propagate and accumulate into the final data. For example, Cattin et al., (2015) have developed a MATLAB software that allows processing the gravity data and obtain the uncertainties at the same time. At IGME we estimate the uncertainty by repeating a 10% of the survey and calculating the standard deviation of the differences between pairs of repeated measurements. However, before any joint interpretation, we must bear in mind that the uncertainty level of the raw gravimetric data is significantly lower than other raw data sources (geological or petrophysical data).



**Uncertainty sources in gravimetric exploration**

	Source	Brief explanation (more details in text) ***	Raw data	Type	code*5	level*4	Impact*	table 1 of 7 y/n/!	Reference(s) **	Comments
G R A V I M E T R Y	<b>Type of make the reading</b>	Some instruments (Scintrex and Burns) have automated reading. Others have optical reading and depend on the operator (S&R old instrument).	Grav	Human, Instrumental	3,4	Data acquisition	Low	Y	Instruments manual	Current portable equipments have enough resolution for regional studies. Old gravimeters are not appropriate for microgravimetric studies.
	<b>Calibration factor</b>	Adjusted by manufacturer and controlled by the user using calibration lines		Human, Instrumental	3,4	Data acquisition	Large, important		Instrument manual Seigel et al. 1995 Torge 1989 Ludmer 2009 Murray and Tracey 2001	Some gravimeter tables with calibration values and gravity are manually calculated. Modern gravimeters give directly the gravity value.
	<b>Temperature control</b>	Effects of temperature shocks		Instrumental	3,4	Data acquisition	Critical		Instrument manual Seigel et al. 1995 Torge 1989 Ludmer 2009 Murray and Tracey 2001	
	<b>Elastic relaxation</b>	Change in the position of the proof mass from its null position		Instrumental	3,4	Data acquisition	Large		Instrument manual Seigel et al. 1995 Torge 1989 Ludmer 2009 Murray and Tracey 2001	
	<b>Leveling</b>	Affect to the precision of the measurement		Human, Instrumental		Data acquisition	Large, important		Seigel et al. 1995 Murray and Tracey 2001	Some gravimeters correct leveling errors automatically
	<b>External factors</b>	Vibrations, wind, rough conditions, etc		Human, Instrumental		Data acquisition	Important		Seigel et al. 1995 Murray and Tracey 2001	Some gravimeters implement software and correction systems for some of these effects.
M E A S U R E M E N T	<b>Bases establishment</b>	Level bases are needed to control the quality and duration of daily usage	Grav	Human, Instrumental	3,4,5,7	Data acquisition	Critical		Seigel et al. 1995 Murray and Tracey 2001	
	<b>Stations locations</b>	Appropriate locations of the station: flat terrain, minimum external factors, etc.		Human	2,4	Data acquisition	Medium		Seigel et al. 1995 Murray and Tracey 2001	
	<b>Duration of the readings</b>	Depend on the scale, more time on repetitions for micro than for regional (p.4.)		Human	3,4	Data acquisition	Large		Seigel et al. 1995 Murray and Tracey 2001	
M E A S U R E M E N T	<b>Elevation station estimation</b>	Currently obtained by GPS. In campaigns where high precision is required (mm) it is done with an optical level	Grav	Human, Instrumental	3,4	Data acquisition	Large			precision and precision of the correction depend on satellite coverage and quality of GNSS static stations. Very important is also the measurement time, distance to the reference base, type of the correction differential (RTK, Offloc, etc.)
	<b>Latitude, Longitude estimation</b>	Currently obtained by GPS surveys	Grav	Human, Instrumental	3,4	Data acquisition	Large			Precision depends on satellite coverage and quality of GNSS static stations and of measurement time, distance to the reference base, type of the correction differential (RTK, Offloc, etc.)
M E A S U R E M E N T	<b>Drift instrumental</b>	Instrumental drift is assumed to be linear	Grav	Conceptual	4,5	Data processing	High		Seigel et al. 1995 Murray and Tracey 2001	Continuous drift control on gravimeters allow assuming the linearity. In any case the impact is usually very small (DATA)
	<b>Tidal corrections</b>	Calculated by software	Grav	Calculation	4,5	Data acquisition and processing	Medium		Hop 1983 Longman 1959	
	<b>Pressure estimation</b>	Measured or collected from base station	Grav	Human, Instrumental	3,4	Data acquisition			Seigel et al. 1995 Murray and Tracey 2001	important in high definition and/or microgravimetric surveys
M E A S U R E M E N T	<b>Density reduction</b>	Value adopted to minimize the topographic effect. A value is usually taken for the entire study area, in regional studies it is normal to take 2.67 g/cm <sup>3</sup>	Grav	Human, Conceptual	5,6	Data processing	Large		(Bartlett, 1976)	
	<b>Topographic correction</b>	The Hammer method is usually used. The linear correction is made by the operator in the field and the rest of the sectors (medium and fort) by means of digital elevation models.	Grav	Human calculation	3,5	Data processing	Medium		Oliver, 1981 Module Terrain Correction Oassil (Montaj) Powell 1999	
	<b>Gridding of bouguer data</b>		Grav	Calculation	5	Data processing	Medium		Juffer Manual Oassil Montaj manual	
	<b>Separation residual-regional</b>		Grav	Calculation	5	Data processing	Large		Oassil Montaj manual	
	<b>Processed data</b>	Calculation of vertical and horizontal derivatives, continuations up or down, gradients, Euler's solutions, filters	Grav	Calculation	5	Data processing	Large		Oassil Montaj manual	

Table 2.1.8 Overview of uncertainty sources in gravimetric data acquisition, processing, reduction and initial interpretation of anomaly maps



## 2.2. Balanced and Restored cross-sections

### 2.2.1. Introduction

The method for evaluating and validating a geological cross-section consists of checking its “retro-deformability”. In other words, if a section can be restored to an unstrained state, it is a viable cross-section (Woodward et al., 1989). Restoration is a fundamental test to validate and interpret. Moreover, when bed-lengths, angular relationships, or cross-section areas are equal in both the deformed and the undeformed states, then the retro-deformable cross-section is called balanced cross-section. By definition, a balanced cross-section is both viable and admissible, and satisfies a larger number of reasonable constraints than an unbalanced cross-section. Therefore, it is more likely to be correct (Woodward et al., 1989) and always represents a lower risk solution in decision-making processes. On the contrary, a cross section which does not restore and is not balanced cannot be a valid representation of reality. For this reason, an integrated modelling of gravimetric (or magnetic) data must necessarily be supported in 2D (chapter 3) and 3D (chapter 4) by balanced and restored cross sections.

In this chapter a review of the following aspects related to geological cross-sections is presented. This review is focused on cross-section construction, methods, techniques and software of 2D and 3D restoration and balancing, and includes an assessment of uncertainty sources and some examples of case studies. In cases where standard subsurface information is absent, scarce or poor-quality, balanced cross sections represent a keystone to model the gravimetric signal in combination with robust petrophysical data.

### 2.2.2. Background

Restoration of cross-sections represents a well-established technique used in structural geology since the 1950s and 1960s. The pioneering works were carried out by the petroleum industry in the Canadian Rockies (Bally et al., 1966, Dahlstrom, 1969), though the first works using this technique dealt with schematic evolutionary models of the Jura Mountains (Buxtorf, 1916) and depth-to-detachment calculations (Chamberlin, 1910; Laubscher, 1961; see Fig. 2.2.1). The basic geometric foundations of most of these pioneer works were based on the 2D simplification of the principle of volume conservation that can be applied in the upper crustal levels (Goguel, 1954). These first studies were made in compressional terranes although the cross-section restoration concept was soon extended to others tectonic contexts: extensional areas (e.g., Gibbs, 1983; Davison, 1986; White et al., 1986), inverted terranes (e.g., Butler, 1989; Chapman, 1989; Bishop and Buchanan, 1995) and salt tectonics areas (e.g., Worrall and Snelson, 1989;



Rowan, 1993, 1994, 1996; Hossack, 1994, 1995).

Originally, 2D restorations were carried out manually using different geometric techniques: the equal area method (Chamberlin, 1910), the line-length method (Dahlstrom, 1969), or a combination of both (Mitra and Namson, 1989). Subsequently, other techniques were developed depending on particular tectonic contexts (e.g., flexural slip method in extensional contexts; Davison, 1986). Because of the accuracy needed in hydrocarbon exploration, these restoration techniques were rapidly implemented in computer programs which used various methods to restore cross-sections (e.g., Kligfield et al., 1986; Moretti & Larrère, 1989; Geiser et al., 1988). In the early 21st century, the increasing computer performance (even beyond Moore's law [1965]) has greatly influenced the way cross-section construction and structural balancing are approached. New technologies allow us to integrate numerous and heterogeneous data and other elements of the Earth's complex system to interpret subsurface structures and to develop reconstruction methods of geological models directly in 3D.

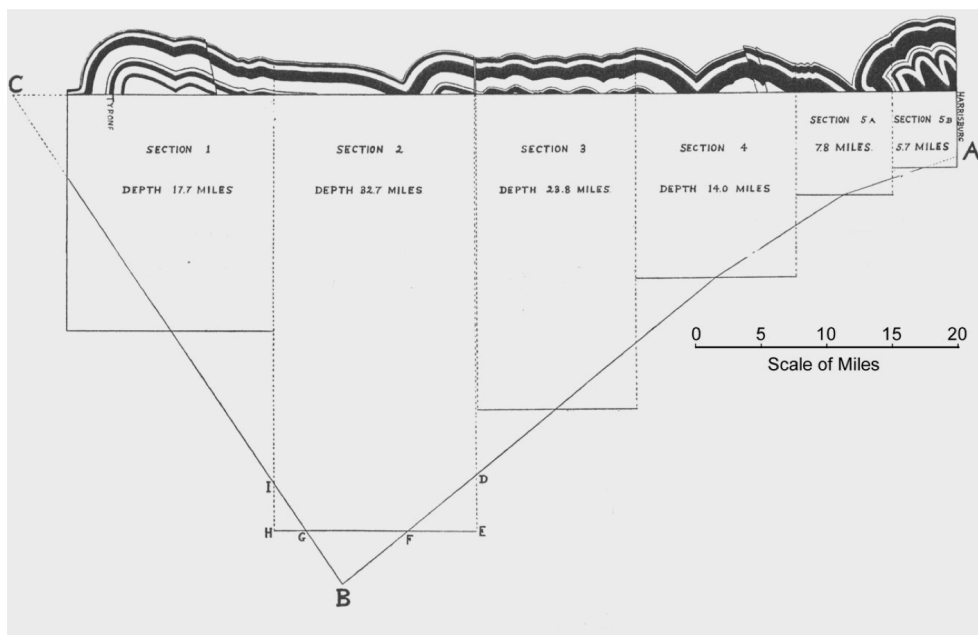


Figure 2.2.1. Cross-sections and calculated depth-to-decollement (Chamberlin, 1910). Modified from Wiltchko & Groshong (2012).

### 2.2.3. Cross-section construction

Cross-sections represent the projection of data extracted from a geological map and from the interpretation of subsurface data (e.g., borehole, seismic sections, gravity, and other geophysical data) onto a vertical plane showing the geology above and below the Earth's surface



(e.g. Davis et al., 2012; López-Mir, 2019). Cross-sections are valuable tools for visualizing structures.

The building of cross-sections based on geological maps and subsurface information consists mainly of three basic processes (López-Mir, 2019): (i) cross-section design, (ii) data projection to the selected cross-section plane and (iii) interpretation of the structure (i.e., interpretation of the geometrical relationship between the structural and stratigraphic elements previously projected to the cross-section trace).

### 2.2.3.1 Cross-section design

It is desirable that cross-section lines go through areas with abundance of data, but when the purpose of the cross-sections is to give a structural interpretation, they should be designed as straight lines perpendicular to the main structural trend (Fig. 2.2.2a). The aim of this orientation is to get the most illustrative view of the geometry of the studied areas (Groshong, 2006) and to honour the out-of-plane assumption (see section 2.2.5.3). In cross-section lines that are perpendicular to the structures, *true* dips and *true* sedimentary thicknesses are used which are necessary to achieve a realistic reconstruction of the structures. Sometimes, available dip or thickness data are oblique to the cross-section trace and should be depicted as *apparent* dips or *apparent* thicknesses when projected to the section plane. Apparent dips and thicknesses can be calculated using trigonometric algebra (Cooper, 1983; Rowland et al. 2007; López-Mir, 2019).

Discrete cross sections are appropriate for the geometrical interpretation of cylindrical structures. Nevertheless, when structural studies are carried out in areas showing along-strike structural variations, serial cross-sections should be used instead. They are of key importance as a first approach to the actual 3D understanding of the subsurface. The spacing between serial cross-sections should be the appropriate one to capture the lateral relay and geometrical changes in the main structures and it will thus change in every specific case study. In particular, the construction of serial cross-sections is recommended when significant variations in the amount of shortening along-strike are expected (Dixon, 1982). This applies to many geological settings affected by lateral transference of deformation (oblique structures, laterally changing structural inheritance, thrust and fold relays, lateral termination or rheological changes in the main décollements, non-linear salt structures...). In these cases, serial sections are usually designed radially across the structural grain, keeping cross-section traces perpendicular to the main structures although not necessarily parallel to the shortening direction (e.g. Dixon, 1982 in the Wyoming salient). As it will be shown later (section 3.2), in these scenarios, serial sections are essential during the 2D interpretation of potential-field geophysical data and represent the basis for their robust 3D inversion.



### 2.2.3.2 Data projection

This process implies transferring data from the geological map (topographic height, geological contacts, dip data, etc.) or other sources of subsurface information (horizons from seismic sections, stratigraphic boundaries or dipmeter data from wells, etc.) to the cross-section, taking into account that the scale of the cross-section must be the same as that of the geological map. The whole process requires:

- (1) Transferring the topographic height by marking the intersection of each topographic contour line with the cross-section line to construct the topographic profile (Fig. 2.2.2b).
- (2) Transferring the geological contacts (stratigraphic horizons and faults) from the geological map to the topographic profile. Firstly, it is necessary to mark the intersection of each contact, fault, unconformity, etc... with the cross-section plane. Then, the location of each marked intersection is transferred to the topographic profile (Fig. 2.2.2b).
- (3) Projecting dip data onto the cross-section plane. Dip data in a narrow band along either side of the cross-section line (i.e. at a short distance from the cross-section) should be preferentially used. These data are projected onto the cross-section plane using projection vectors that are parallel to the strike of the layers and the fold axes (Fig. 2.2.2b). Depending on the orientation of fold axes and the height at which dip data are located, dips will be projected on, below or above the topography across the section plane. When the projected data are apparent dips, the true dip should be calculated for avoiding interpretation errors (Fig. 2.2.2b).
- (4) Including and projecting all the available subsurface data to the cross-section trace (well data, geophysical information) in order to constraint the possible interpretations. Well tops (i.e. boundaries between the main stratigraphic units) from boreholes located on or close to the section trace will be preferentially considered. Well tops should be projected following the main structural trend in the study area (ideally, dip meter data can be used if available). Regarding seismic data, cross-section traces should be adapted as much as possible to seismic line traces to avoid projection from long distances. If this projection is anyway required, it must be done following the general structural trend. Alternatively, if 2D seismic data are abundant or 3D seismic data are available, 3D seismic horizons can be constructed and their intersection with the section trace can be considered for cross-section construction.

### 2.2.3.3 Interpretation of the structure

The interpretation of the rock arrangement consists of interpolating all the available surface and subsurface data. Some basic principles should be taken into account (<https://geo.illinoisstate.edu/field-camp/documents>; (i) uniform layer thickness unless there is evidence of thickness variations (e.g. growth strata), and (ii) dip angles projected from a short



distance. In many cases data are scattered and the geological structure can be complex. Therefore, in order to build a geological cross-section, the application of all the knowledge of the geological features of the region is necessary (Fig. 2.2.2c). This regional knowledge allows to choose the suitable structural techniques to reconstruct folds and faults according to the geological regional context: (i) folds, (ii) folds and faults in contractional contexts, (iii) folds and faults in extensional contexts or (iv) tectonic inversion (Poblet, 2006). These geometrical techniques (partly summarized in Table 1) reduce the degree of interpretation of the rock arrangement at depth.

In the case of fault-related folds, three different geometrical models are usually considered: fault-bend folding, fault-propagation folding and detachment folding (see references in Table 1). These models impose certain geometrical relationships between fold limb dips, detachment depth and fault geometries and help thus constraining fault geometries at depth from surface dip data at their hangingwalls. Methods and techniques used for the reconstruction of structures in different geological contexts (Poblet, 2006) are shown in Table 1.

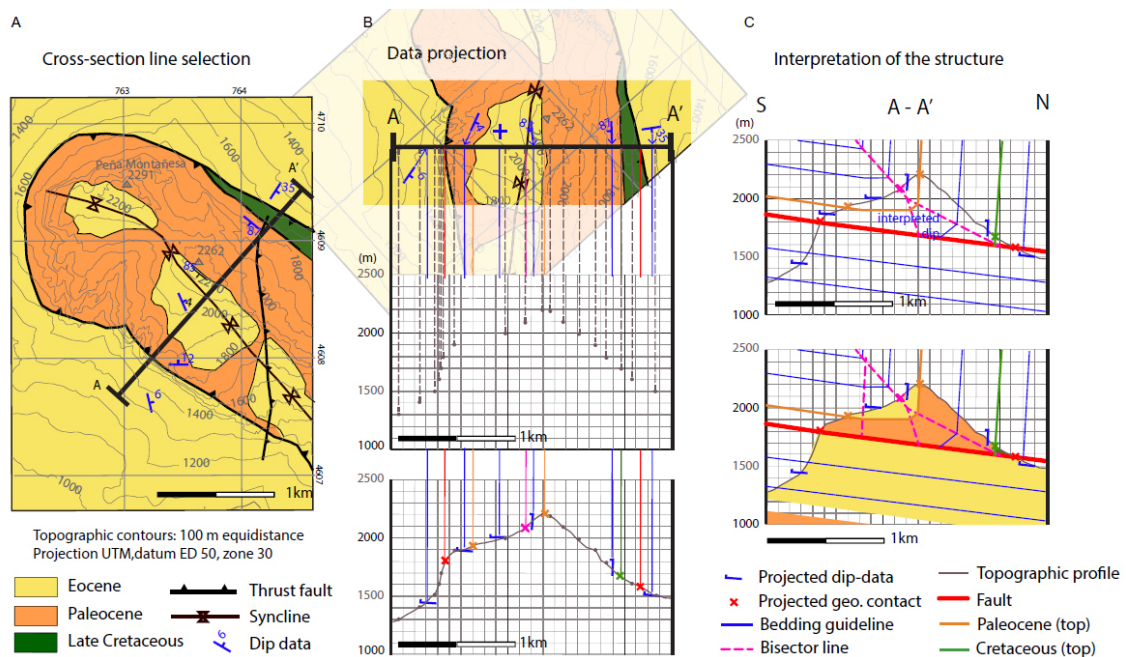


Figure 2.2.2. (A) Cross-section line selection perpendicular to the main structural trend. (B) Data projection from the map onto the vertical section. (Above) Projection of the topographic contour intersections with the cross-section line. (Below) Projection of the geological intersections with the topographic profile and of the dip data. (C) Interpretation of the structure. The geometry of the strata is interpolated following the kink Method. (Taken from López-Mir, 2019).



Regions	Structures	Methods		Authors	
1 Folded regions	Folds	Involute-evolutes	Busk method, or tangent-arc method	Busk (1929)	
			Busk-Mertie method	Busk (1929); Mertie (1940)	
			Arc method combined with free-hand	Badgley (1959)	
			Layer-thickness method	Roberts (1982)	
		Dip domains	Boundary ray method	Coates (1945), Gill (1953)	
			Dip domain method or Kink method	Suppe (1983)	
		Isogones	Isogones (surfaces) method	Phillips & Byrne (1969)	
			Isogones (lines) method	Ramsay & Huber (1987)	
2 Folds and faults in contractional contexts	2.1 Detachment depth calculation	Excess/lost area	Excess/lost area	Chamberlin (1910)	
			Chevron detachment folding	Jamison (1987)	
		Detachment depth-shortening profile	Mitra & Namson (1989)		
		Lost area diagram	Epard & Groshong (1993)		
		Variable detachment depth	Homza & Wallace (1995)		
		Best-fit detachment-depth graph	Bulnes & Poblet (1999)		
		2.2 Reconstruction of beds geometry and thrust geometry	Projecting faults to depth		Roeder et al. (1978)
	Thrust trajectory projection		Geiser et al. (1988)		
	Deformed state cross-section – Forward modelling		Fault bend folds		Suppe (1985), Jamison (1987), Marshak & Mitra (1988)
			Fault-propagation folds		Suppe & Medwedeff (1990), Jamison (1987), Marshak & Mitra (1988)
			Detachment folds		Jamison (1987), Poblet & McClay (1996)
			Trishear folds		Allmendinger (1998)
			Transported folds		Jamison (1987)



			Hybrid fault-propagation detachment folds	Marret & Benthm (1997)	
			Shear fault-bend folds	Suppe et al. (2004)	
		Dip spectral analysis		Suppe (1985)	
		Lost area diagram		Epard & Groshong (1993)	
3 Folds and faults in extensional contexts	3.1 Detachment depth calculation	Excess/lost area		Chamberlin (1910)	
		Inclined shear		White (1987)	
		Bed-length and displacement conservation		Williams & Vann (1987)	
		Block rotation along circular faults		Moretti et al. (1988)	
		Lost area diagram		Groshong (1994, 1996)	
		Requisite strain equation		Groshong (1994, 1996)	
		Best-fit detachment-depth graph		Bulnes & Poblet (1999)	
	3.2 Reconstruction of the normal fault geometry	Vertical shear	chevron construction or constant heave		Verrall (1981)
			Fault construction		Rowan & Kligfield (1989)
		Constant displacement			Gibbs (1985)
		Flexural slip	Flexural slip		Davison (1986)
			Flexural slip with subsidiary faults		Davison (1986)
			Thrust trajectory projection		Geiser et al. (1988); Rowan & Kligfield (1989)
		Inclined shear	Inclined shear -antithetic or synthetic-		White et al. (1986)
			60° method		Faure & Chermette (1989)
Fault construction			Rowan & Kligfield (1989)		
Inclined shear bed-to-fault model			Dula (1991)		
Inclined shear bed-to-fault model with subsidiary faults			Song & Cawood (2001)		
Slip-line			Williams & Vann (1987)		
Oblique simple-shear using layer-parallel strain			Groshong (1990)		



	3.3 Reconstruction of beds geometry from normal fault	Constant-thickness deformation		Morris & Ferrill (1999)
		Inclined-vertical shear	Inclined shear	White et al. (1986)
			60° method	Faure & Chermette (1989)
			Inclined shear fault-to-bed construction	Dula (1991)
		Block rotation along circular faults		Moretti et al. (1988)
		Half-graben extensional faults-bend fold		Groshong (1989)
		Finite difference method		Waltham (1989, 1990)
		Oblique-simple shear using layer-parallel strain		Groshong (1990)
		Bed-length balanced grabens		Keller (1990)
		Coulomb collapse theory		Tearpock & Bischke (1991)
		Extensional fault-bend fold		Xiao & Suppe (1992)
		Constant-thickness deformation		Morris & Ferrill (1999)

Table 2.2.1. Restoration methods used for different tectonic contexts (Synthetized and modified from Poblet, 2006).

## 2.2.4. 2D restoration and balancing

### 2.2.4.1. Concept

The validity of a cross-section depends on (e.g. Groshong, 2006; Rowland et al., 2007; López-Mir, 2019): (1) its consistency with the available data and with known geological concepts (admissible cross-section), (2) its valid retro-deformation (i.e. it must be recomposed into a plausible pre-deformational geometry or restored cross-section) and, (3) its valid balancing (i.e. there is no gain or loss of material between the deformed and restored states) (balanced cross-section). Despite the actual solution can be different, an admissible, retro-deformable and balanced cross-section would be a valid interpretation of the subsurface geometry consistent with the available data (e.g. Groshong et al., 2012). In this chapter we go deeper into the concepts of restoration and balancing of geological cross-sections.



**Restoration** of geological cross-sections represents the process of reversing deformation to the undeformed state in one or multiple steps (sequential restorations, e.g. Rowan and Ratliff, 2012) (Fig. 2.2.3). Originally, restoration was used to test and validate the subsurface interpreted geometry of cross-sections and interpreted seismic profiles. But its power is much broader, and it can be used, for example, to (e.g. Bulnes and McClay, 1999; Rowan and Ratliff, 2012): (1) determine the original position and dip of the structures and illustrate their structural evolution, (2) calculate the amount and rates of deformation (i.e. finite displacement, rotation and internal deformation fields in terms of Rouby et al., 1993) or other geometrical variables (i.e. normal and Gaussian curvatures), (3) quantify the timing of basin formation and evolution, (4) analyze the kinematic evolution of deformed rocks, (5) determine the original spatial relationships between sedimentary facies and the interplay between deformation and sedimentation, and (6) constrain models of thermal maturation and hydrocarbon migration.

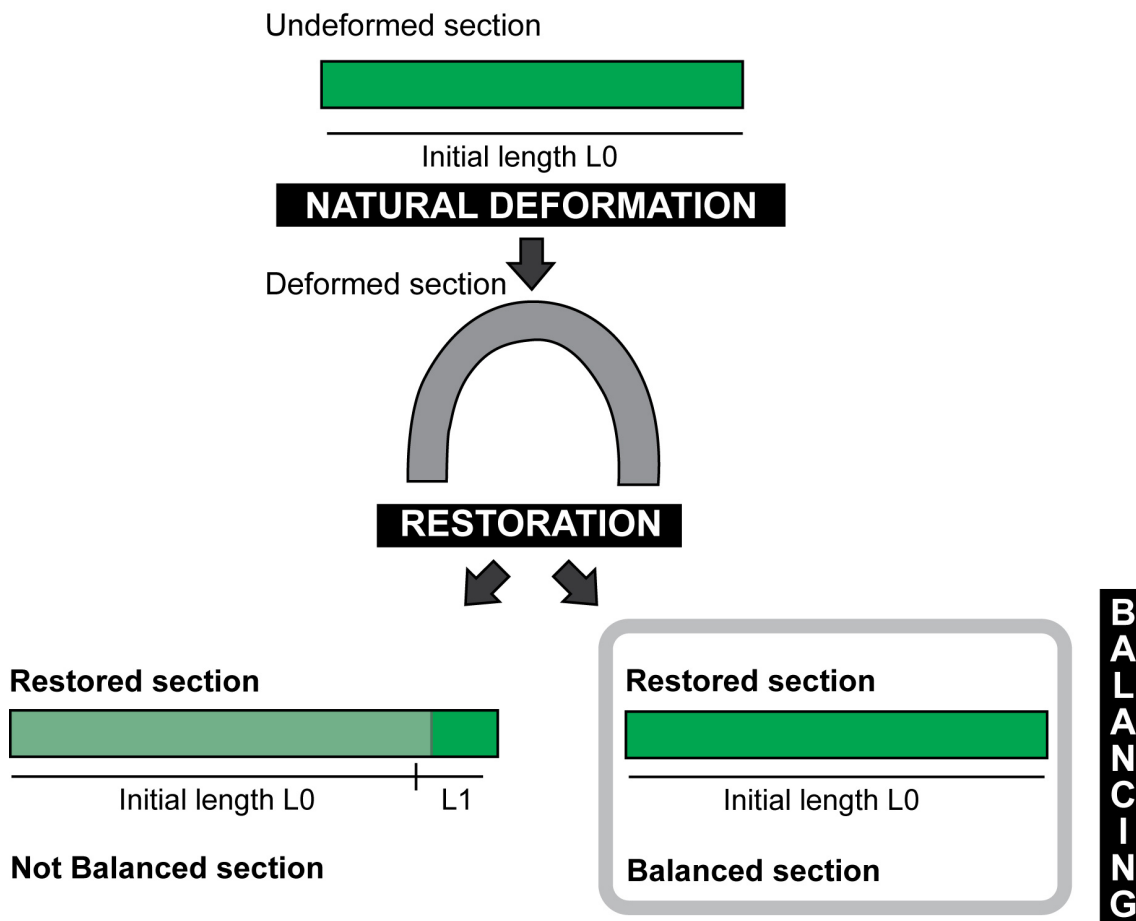


Figure 2.2.3. Simple schematic illustration showing the concept of restoration and balancing in structural geology.



**Balancing** of geological cross-sections is needed to guarantee the validity of an interpreted geometry. The fundamental assumption of balancing is that material remains constant (i.e., no gain or loss of material) during deformation, thus honouring the volume conservation principle by Goguel (1954). This implies that rock volumes remain constant during deformation both in space and time pointing to a rock volume redistribution when metamorphism, compaction or whatever process related to deformation occurs (López-Mir, 2019).

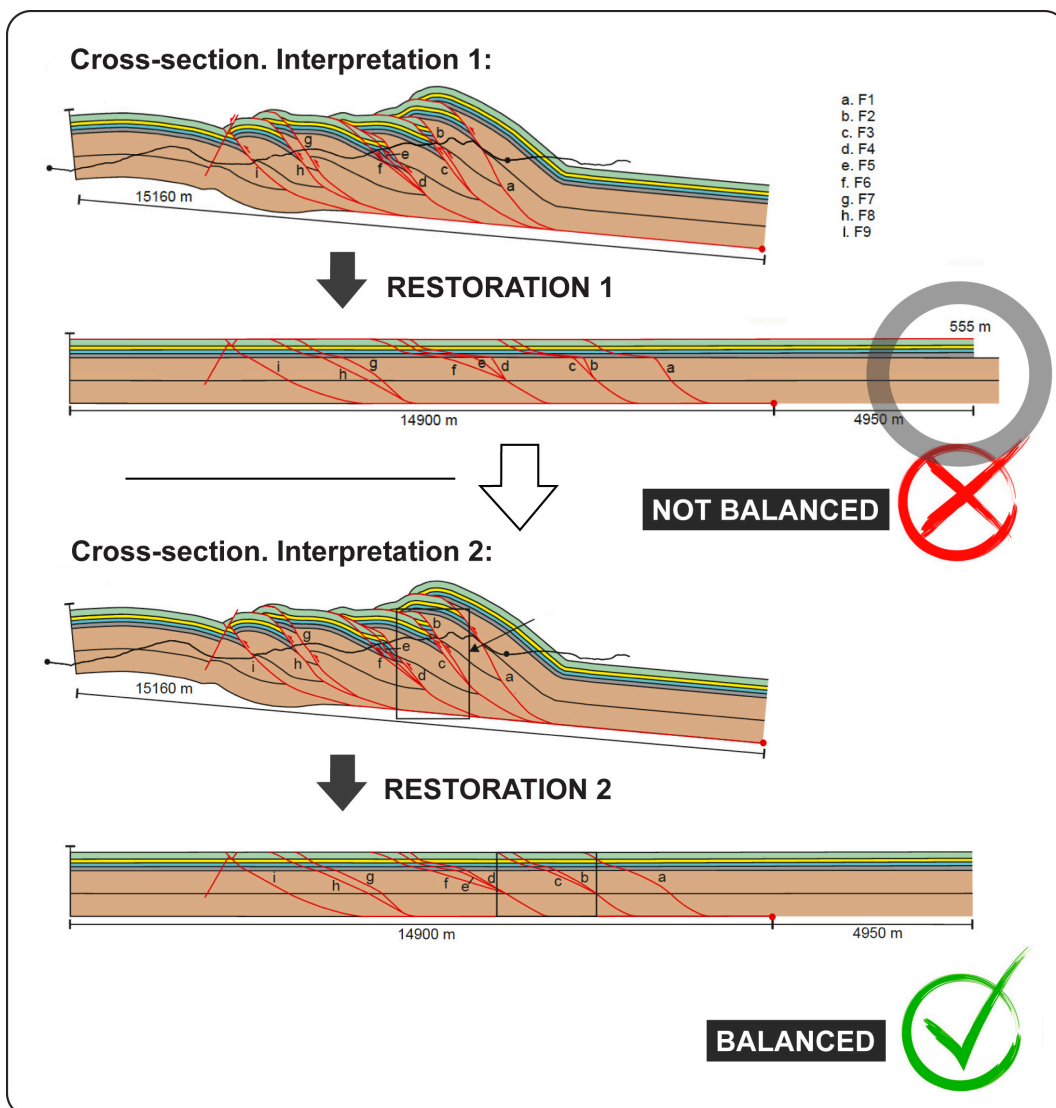


Figure 2.2.4. The first interpreted subsurface geometry represents cross-section 1. Restoration 1 consists of line-length restoration of cross-section 1 and indicates a minor length imbalance (i.e., a non-balanced cross-section). Taken this into account, cross-section 2 is done with changes in fold and thrust geometries to achieve a second interpreted subsurface geometry. Restoration 2 consists of line length restoration of cross-section 2 and it is balanced. Cross-sections and restored cross-sections modified from Watkins et al. (2014)



The standard workflow to validate an interpreted geometry is shown in Fig. 2.2.4. Once the cross-section is constructed, it is restored (i.e., the current structure is returned to a plausible pre-deformation geometry) and then checked that it is balanced (i.e., the volume of rocks remains constant between the deformed cross-section and the restored state). If this restoration confirms an imbalance between units, then a second cross-section should be constructed taking this into account. This process is repeated until a balanced cross-section is achieved. Wilkerson and Dicken (2001) have proposed some tips for detecting and preventing common errors during the construction of balanced and restored cross sections in contractional settings.

#### 2.2.4.2. Assumptions and methods

The fundamental assumptions for restoring and balancing cross-sections are described below (e.g. Woodward et al., 1985; Allmendinger, 2015). (1) Deformation is plane strain, i.e., there is no movement of material into or out of the section plane (Hossack, 1979). This assumption implies that the cross-section must be oriented parallel to the overall transport direction which is very often implicitly assumed to be straight and constant with time. Shortening estimates in oblique sections can be corrected (Cooper, 1983) although their restoration is uncertain and they should be avoided. (2) The area of individual stratigraphic levels does not change during deformation. This is typically achieved using several graphical restoration algorithms and/or finite-element modelling (e.g., Rowan and Kligfield, 1989; Nunns, 1991; Schultz-Ela, 1992; Maerten and Maerten, 2006; Rowan and Ratliff, 2012):

- a. Bed-length restoration or line-length balancing. It preserves the line length, thickness and angles between horizons.
- b. Vertical-simple shear and inclined simple shear. They maintain the lengths of vertical or inclined lines, respectively.
- c. Fault-parallel slip. It keeps imaginary lines parallel to a given fault at a constant length.
- d. Rigid-body rotation. It maintains the exact shape and size of fault blocks.
- e. Area restoration. Its only condition is to preserve unit area relaxing other constraints (i.e. internal deformation).

To date, bed-length and area balancing are the most used techniques when restoring and balancing cross-sections (Allmendinger, 2015).

Bed-length balancing assumes that the length, thickness, and angles between horizons remain constant between the deformed and the restored states. Despite this method is simple, it generally allows to immediately rule out many incoherent geometries (Moretti, 2008). Historically done with a curvimeter and nowadays with computer aided tools, it is possible to measure the length of the folded horizons between faults before and after deformation. The comparison of those lengths is the core of the bed- or line-length balancing technique (e.g., Moretti, 2008) and allows the estimation of the horizontal shortening values required to reach the deformed state. Bed-length restorations were developed and have been largely used in fold



and thrust belts (e.g., Dahlstrom, 1969; Hossack, 1979; Elliott, 1983). Bed-length balancing is restricted to parallel folds (i.e., folding occurs via shear parallel to bedding, Fig. 2.2.5). When shear oblique to layering occurs, the preservation of the bed-length assumption is not achieved (Allmendinger, 2015). Bed-length consistency can be determined by analysing the restored shape of the loose line (e.g., Marshak and Woodward, 1988) (see Fig. 2.2.6). Shortening values obtained from the application of line-length balancing are minimum estimates: they must consider minimum displacement options for the structures that are reconstructed above the topography and do not take into account deformation at scales that are smaller than the section resolution (see section 2.2.5).



Figure 2.2.5. Bed-length balancing in a parallel fold. Taken from López-Mir (2019).

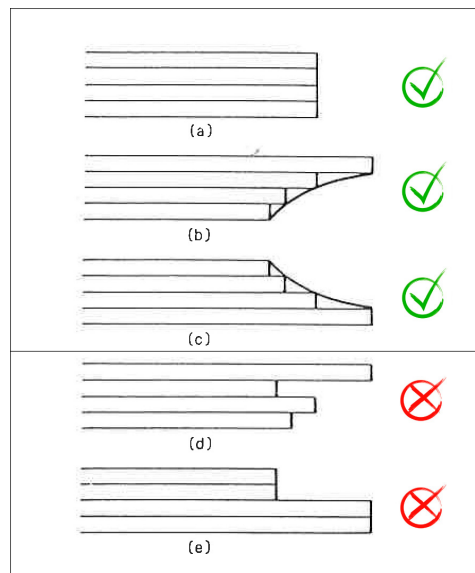


Figure 2.2.6. Examples of restored loose-line geometries. Green symbols indicate an admissible restoration and balancing whereas red symbols indicate a non-admissible restoration and balancing. Modified from Marshak and Woodward (1988). The total lengths of each layer in a sequence depicted in a restored cross-section should be nearly the same or should vary in a consistent manner. This consistency does not require the restored loose line to be exactly perpendicular to bedding in the restored and deformed-state cross-sections (Marshak and Woodward, 1988).



Area balancing assumes that the initial and deformed areas remain equal. Area balancing techniques are subdivided into two methods (Mitra and Namson, 1989; see López-Mir, 2019 for further explanations): (1) equal-area restoration and, (2) excess-area restoration. Area balancing also assumes that deformation is plane strain, i.e., that there is no movement of material into or out of the plane of the cross-section (Fig. 2.2.7) (e.g., Allmendinger, 2015).

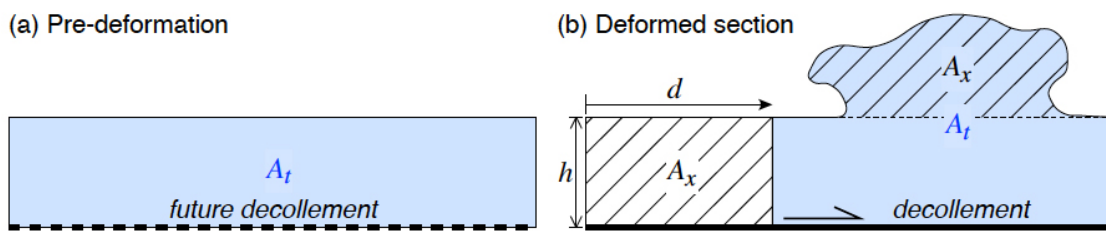


Figure 2.2.7. Area balancing considering excess-area restoration. Taken from Allmendinger (2015).

The general tectonic features in which line length and area balancing assumptions cannot be accomplished are (Allmendinger, 2015): (i) Volume changes (due to compaction during deformation, which is particularly important in accretionary prisms and foreland basins, to sediment accumulation during faulting, to pressure solution processes [cleavage fronts], or to intrusive magmatism and salt tectonics) and, (ii) Non-plane strain (strike-slip faults and/or lateral ramps leading to out-of-plane deformation). The occurrence of vertical axis rotations (often witnessed by paleomagnetic analysis) is usually related to local or regional gradients of shortening (McCaig and McClelland, 1992; Allerton, 1998; Sussman et al., 2012) and also imply that the plane-strain assumption is not met. They have received much less attention (Pueyo et al., 2016; Ramón et al., 2016a and references therein). Uncertainties related to these different scenarios are described below.

### 2.2.4.3. Forward modelling

In complex tectonic scenarios or in data-poor studies, the forward modelling (Fossen and Tikoff, 1997; Fossen and Hesthammer, 1998) represents a very useful technique to achieve a valid geological cross-section which is difficult to obtain using the traditional 2D restoration techniques. The forward modelling consists of generating a plausible structural evolution, compatible and contrasted with actual field and subsurface data, from a pre-tectonic situation (Fig. 2.2.8) (Válcarcel, 2015; Nussbaum et al., 2017). Forward modelling consists of an iterative process summarized in the workflow of Figure 2.2.9.

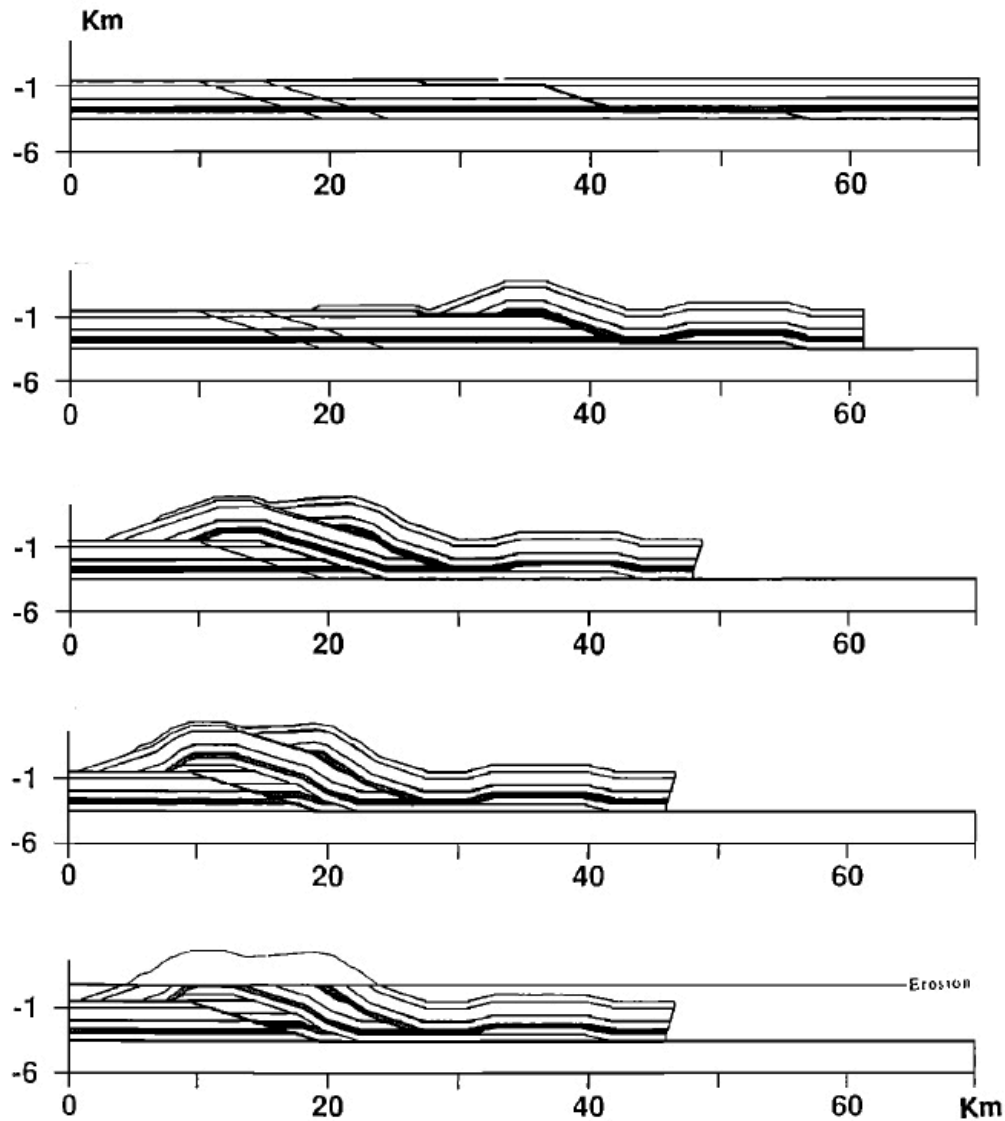


Figure 2.2.8. Example of kinematic forward modelling. Taken from Endignoux and Mugnier (1990).

Forward modelling overcomes the traditional bed-length and area balancing methods because of it can be implemented with different kinematic and geomechanical constraints depending on the deformation style (Nussbaum et al., 2017). The power of forward modelling resides on its capacity to predict the strain throughout structures (Allmendinger, 1998). Forward modelling employs the same kinematic algorithms used for restoration that are available in some commercial reconstruction tools (e.g. Move by Midland Valley Exploration Ltd.).

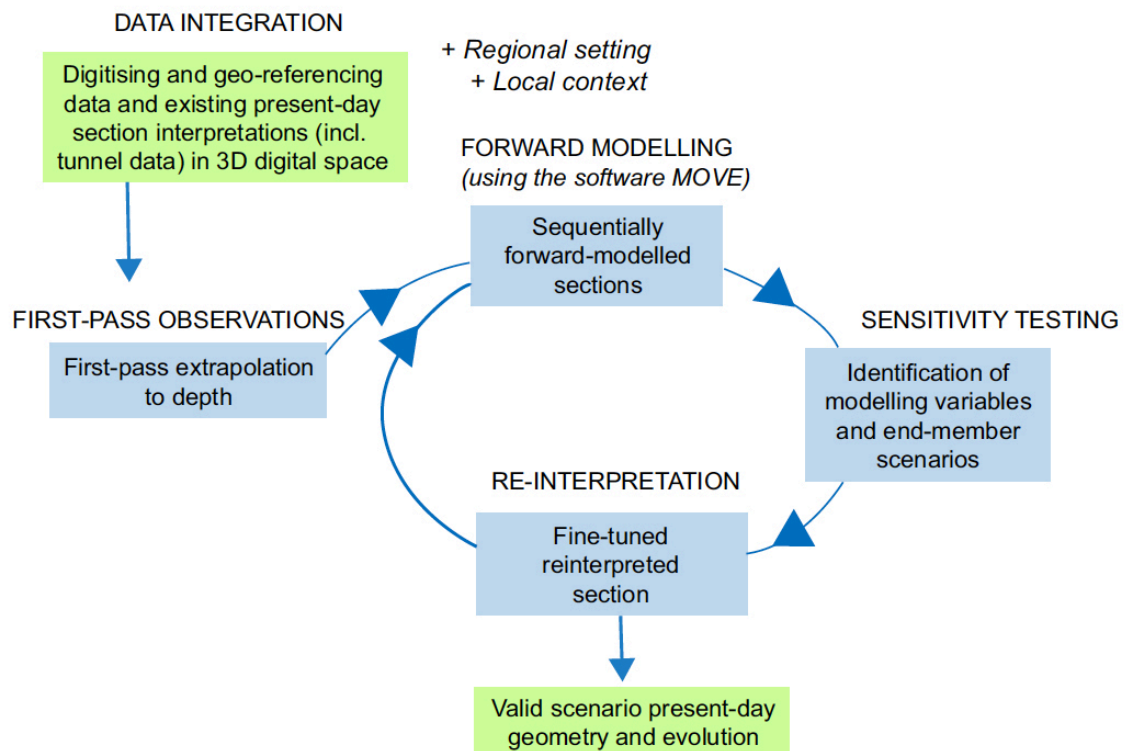


Figure 2.2.9. Kinematic forward modelling workflow taken from Nussbaum et al. (2017).

### 2.2.5. Uncertainties and pitfalls in balanced & restored cross sections.

Uncertainty is an inherent element on the measurement, calculation or interpretation of any geological data (Mann, 1993; Bardossy and Fodor, 2011; Bond, 2015) that has to be considered when cross section construction and balancing techniques are applied. Uncertainty is defined (Bardossy and Fodor, 2011), in its broader sense, as *‘the recognition that the results of our measurements and observations may deviate more or less from the natural reality’*. Its quantification requires the estimation of the error, understood as *‘the difference between a true value and an estimate of that value’*. This uncertainty, although rarely reported in geological maps or cross sections can be handle using traditional and new mathematical methods, taking into account that they have specific limitations when applied to geological case studies (see Bardossy and Fodor, 2011 for a review; Woodward, 2012).



### 2.2.5.1. Data uncertainties (geological and geophysical data)

Uncertainty sources in geology are variable and can derive from the data acquisition, data processing or data interpretation process. The main types of uncertainties in geology (following the classification of Mann, 1993 and Bardossy and Fodor, 2011) are: (1) the inherent natural variability of geological objects, (2) the sampling error (i.e., limitations in sampling geological objects in time and space), (3) the observation error (generally dependent on outcrop conditions), (4) the measurement error (i.e., imperfection of the measurements due to the instrument, the applied measurement method and the human factor) and (5) errors on the mathematical evaluation of geological data (insufficient number of samples or incorrect statistical analysis). Apart from these errors, mostly related to the geological objects and the way we observe, measure and quantify them, it is also important to consider two additional uncertainty sources: (6) the conceptual and model uncertainty (i.e., application of pre-existing conceptual ideas that may be wrong) and (7) the propagation of errors.

From these seven types of uncertainty sources, only the natural variability and the limitations of sampling (exposure conditions) of geological objects are independent on us. All the other types are part of the geological investigation process and should be considered in the specific field of cross section construction and structural modelling. Cross-section constructions are usually based on the combination of datasets from different sources (field and borehole data, seismic imagery, potential fields geophysics...) that have a limited resolution and spatial distribution as well as their own uncertainty sources. The exposure of geological elements is normally incomplete (Jones et al., 2004; Keffer, 2007; Lindsay et al., 2012) and certainly limits the subsequent interpretation as well as conditions the associated uncertainty. For example, when dealing with shortening estimates from 2D sections, eroded or unknown subsurface cutoffs (exposure conditions) constitute a major source of uncertainty as well as the occurrence of inherited extensional faults or salt structures later reactivated (Bulnes and McClay, 1999; Judge and Allmendinger 2011; Groshong et al., 2012). Likewise happens when internal deformation is ignored (Mitra, 1994; Sans et al., 2000; Moretti and Callot, 2012) or when out of plane motions in the cross section are obviated (Pueyo et al., 2004; Sussman et al., 2012).

Other necessary data, such as borehole or surface structural data (when outcrops are available), are relatively well-constrained and their related uncertainties are defined by the accuracy and sensitivity of measuring tools and georeferencing instruments (compass, GPS, drilling sensors) or the skills and background of the person doing the outcrop measurement or interpreting the well (Randle et al., 2018). On the other hand, geophysical data such as seismic images or potential fields geophysical data (gravimetric and magnetic) have their own sources of uncertainty (for a further analysis on the uncertainty of gravimetric data and processing see also sections 2.1 and 3 as well as the deliverable D4.2 “Sources of uncertainty in 3D geological modeling” by Zehner et al). The use of geophysical data usually needs an initial processing that requires the geophysicist in charge to make certain assumptions (for the stacking of seismic data, the interpolation of potential fields geophysical data, the separation of deep regional and shallow residual anomaly sources in gravimetry, etc.) that will have an impact on the derived final structural models. For example, in the specific case of seismic data, an additional and important source of uncertainty is defined by the need of converting the time-based vertical



scale of seismic images to the depth-based scale of borehole data. This requires the use of time-depth relationships discretely defined in a certain number of (sometimes limited) boreholes and their extrapolation to wider areas, which adds uncertainties to the position of the stratigraphic horizons derived from seismic interpretation. Another source of uncertainty in seismic-based stratigraphic horizons is the fact that seismic reflections in deformed areas surrounding faults, folds and salt structures are usually perturbed (Sibson, 1977), adding uncertainty to seismic interpretation (Iacopini and Butler, 2011). In these scenarios, seismic interpretation requires assumptions to be made by the modeler that, as the processing step assumptions made by the geophysicist, will have implications for the final cross-sections and structural models.

The interpretations done by geoscientists rely upon their previous experience and the geological concepts they apply. This translates into the well-known human bias or ‘conceptual uncertainty’ inherent to seismic and structural interpretation that has been revealed to be significant (Bond et al., 2007; Bond, 2015). The application of incorrect geological models when building cross sections (or 3D models) in areas with scarce and heterogeneous datasets can turn into totally erroneous interpretations. However, when these “wrong” models or sections are used to compute the potential field it is likely that the match to the measured potential field is worse than if the sections (or 3D model) were correct. To minimize this human bias, different methodologies (Maerten and Maerten, 2015; Eichelberger et al., 2015) including computer-aided restorations and forward modelling have been developed in order to guide interpreters towards optimal geometrical solutions that reduce uncertainty in 2D geological interpretations.

Nevertheless, the spatial uncertainties on the source data and their interpretation are generally small when compared with the interpretational space where the source ‘hard’ data (surface, well or seismic data) are extrapolated to create a 3D model. Geologists extrapolate observations over significant distances and this uncertainty space is much greater than the data uncertainty itself (Bond, 2015). In this sense, two main uncertainty sources should be considered. The first one derives from the selection of appropriate axis to project surface and borehole data to cross-sections. For the projection of surface data, the more and better distributed source bedding data, the more accurately the projection axis will be defined. Besides, the longer the projection distance, the higher will be the uncertainty in the position of the projected data. The second source of uncertainty derives from how the source data are connected through space. In this sense, the use of geometrical models and balancing techniques will reduce the degree of uncertainty (Lopez-Mir, 2019). Geometrical models (Suppe, 1983, Jamison, 1987, Suppe and Medwedeff, 1990) for fault-related folding allow predicting fault geometry (dip, location of fault ramps and flats) and décollements depths from overlying fold geometries that can be usually constrained from surface data. In active settings, the use of well georeferenced focal mechanisms can also help in reducing the uncertainty in the location, geometry and kinematics of deep faults. Part of these uncertainties and related errors are efficiently reduced by using digital geological mapping and computer-assisted cross-section construction tools (Jones et al., 2004; Lingrey and Vidal-Royo, 2015). They allow a more accurate positioning of the raw data and incorporate structural tools to define bedding average values, projection axis, line lengths



---

and sedimentary thicknesses as well as algorithms for the application of cross section construction and balancing techniques.

As a general conclusion, it can be stated that, unfortunately, most sources of uncertainty related to the building of balanced and restored cross sections have been partially studied but very little quantified in previous works (see e.g. overviews by Judge and Allmendinger, 2011; Woodward, 2012; Lingrey and Vidal-Royo, 2015). In the next subsections we also review common pitfalls in the construction of balanced sections.

#### **2.2.5.2. Matrix and meso-scale internal deformation**

Cross-sections in fold-and-thrust systems have been classically restored using line length and/or area balancing techniques (Dahlstrom, 1969; Elliott, 1983). As previously described, these techniques consider that either the length or the area of beds is preserved in the plane of the cross-section between the deformed and the undeformed stages (Woodward et al., 1989; Mitra and Namson, 1989). This assumption implies that deformation is fully absorbed by flexural-slip for line length balancing and plane strain for area balancing which clearly breaks down in the internal parts of fold-and-thrust systems where beds are penetratively deformed (Mitra, 1978; Boyer and Mitra, 1988; Yonkee, 1992). Besides, it also fails in the external parts (including foreland basins) where internal deformation of beds might not be related to the development of clear meso-scale features, but significant percentages of shortening can be absorbed at the matrix-scale by, for example, layer parallel shortening (Holl and Anastasio, 1995; Sans et al., 2003).

In this scenario, the accurate restoration of fold-and-thrust systems requires the inclusion of internal deformation in the shortening estimates done for individual macro-scale folds and thrusts (Mitra, 1994; Sans et al; 2003; Parés, 2015). Cross-sections must then be balanced by removing the displacement on faults, unfolding the folded horizons at the large scale and summing up the internal strain that can be calculated for the different portions of the fold-and-thrust system from field strain markers (Fig. 2.2.10).

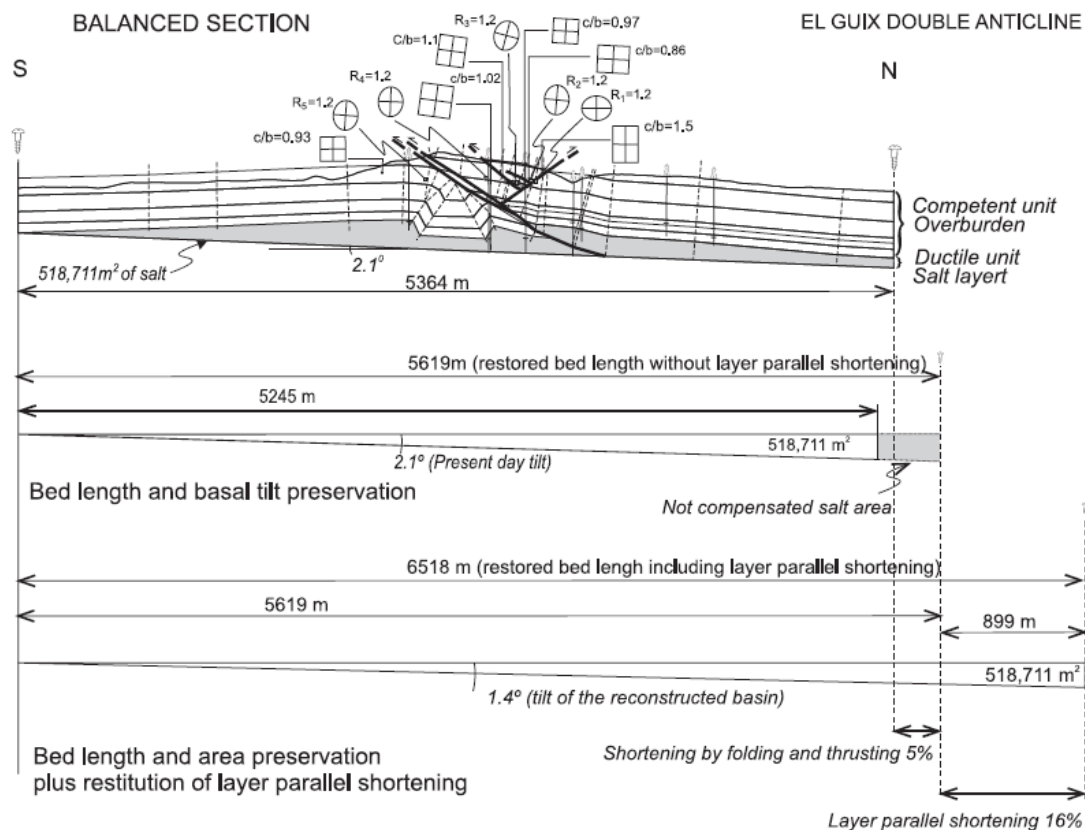


Figure 2.2.10. Restoration of “el Guix anticline” in the external part of the Eastern Pyrenees. The restoration in the central part of the figure is based on the line length balancing method whereas the restoration in the lower part considers internal deformation resulting from layer parallel shortening. Note the underestimation of shortening derived by the use of only line length methods (Sans et al., 2003).

The contribution of internal deformation to the total shortening becomes evident when meso-scale contractional features such as foliation (e.g. cleavage) or stylolites are recognized in the field. These features can develop either prior, coevally or after macro-scale folding. Syn-folding cleavage in strained sedimentary rocks has been reported to absorb up to 50-59% of shortening in the direction of the Z axis of the strain ellipsoid and 29 to 42% tectonic volume loss (Beutner and Charles, 1985). Similarly, high shortening values in the Z direction (up to 60%) have been also defined in low metamorphic grade units affected by pre-folding cleavage where a 40-60% of volume loss is estimated (Wright and Henderson, 1992). The non-consideration of these values would result in a considerable underestimation of the shortening amount if only the line length or area balancing methods are used (Fig. 2.2.10).

The absence of macroscopic cleavage or stylolite sets in the field (a common situation in the external part of fold-and-thrust systems) does not necessarily mean that internal deformation is negligible. Early shortening in fold-and-thrust systems is generally accommodated at the matrix-scale through the mechanical reorientation of mineral grains and the reduction of porosity without producing visible meso-scale structures (i.e. layer parallel shortening). These



consolidation and porosity loss can attain up to 60-75% of the horizontal shortening in young sediments deformed in accretionary wedges (Moore et al., 2011), although these values are lower in partly or fully consolidated sediments. Studies in un-cleaved or weakly cleaved areas in fold-and-thrust systems indicate shortening along the Z axis can range from <5% at distances of 1-2 km from the macroscopic cleavage front (Holl and Anastasio, 1985) up to 16-23% of shortening in external areas affected by subtle cleavage (Sans et al., 2003, Fig. 2.2.10). These values are relatively low in absolute terms but can double or triple the shortening values calculated from the restoration of folding and thrusting (i.e. line-length balancing; Fig. 2.2.10).

### 2.2.5.3. Uncertainties related to the determination of line lengths and areas

Line-length balancing techniques have been tested in sandbox models (Koyi, 1995; Koyi et al, 2003; Groshong et al. 2012; Schlische et al., 2014; Burberry, 2015; Lathrop and Burberry, 2016) that systematically show that bed lengths after compression are shorter than the undeformed beds. This line-length misfit mostly results from an area-constant thickening accompanying shortening (i.e., bed thickness increases and line length decreases but the area of beds remains essentially constant through deformation, Moretti and Callot, 2012; Groshong, 2019). This phenomenon of line-length reduction is analogous to the internal deformation effect in nature described in the previous section. To correct shortening estimates from bed-length reduction, Moretti and Callot (2012) experimentally defined from sandbox experiments the following equation:

$$\text{Length} = \text{current length} \times (1 + \text{computed shortening})$$

This relationship can be applied in natural case studies where field evidences indicate volume and area conservation during deformation and where strain markers are absent.

This drawback of bed-length reduction can also be avoided using the area-balancing method. Nevertheless, this method also has inherent uncertainties (Judge and Allmendinger, 2011) that are related to the uncertainties in the position of the vertexes defining the area to be restored. This uncertainty encompasses those associated with (i) the reconstruction of hanging-wall cut-offs above the topography (the minimum shortening option should be considered) and (ii) the definition of the basal décollement depth. An analytical solution to estimate these uncertainties was proposed by Judge and Allmendinger (2011).



### 2.2.5.3. Out-of-plane deformation

The 2D restoration has a very important limitation; it does not allow out-of-plane deformation and therefore it does not consider possible vertical-axis rotations, thrust transport directions oblique to the cross-section plane and/or out-of-plane movement of evaporitic decollements (mostly salt) in detachment folding or salt tectonics scenarios. The restoration into 2D uses 2D references (bedding surface) and therefore cannot resolve 'out of plane' motions, a classic drawback already identified in the early studies focused on cross-section balancing techniques (Dahlstrom 1969; Elliott 1976).

During the last decade, several authors are working in the incorporation of palaeomagnetic constraints in restoration methods to reduce the uncertainty of vertical axis rotations because such constraints can be applied both before and after deformation (Pueyo et al., 2004; Arriagada et al., 2008; Ramón et al., 2016a and references therein). Besides, the obliquity between structures and thrust transport directions (i.e., strike-slip tectonics or oblique thrusting) can also lead to significant shortening underestimations when cross sections are constructed perpendicular to the structures but oblique to the tectonic transport direction. Shortening underestimates caused by this effect can be calculated and corrected from Cooper (1983) formulations, using the expression ' $S_{real} = S_{perp} / \sin \alpha$ ' where  $\alpha$  is the angle between the strike of the main faults and the shortening direction,  $S_{real}$  is the actual shortening and  $S_{perp}$  is the shortening measured perpendicularly to the structures. Similarly, Sussman et al (2012) have estimated the impact of vertical axis rotations in shortening estimates;  $\%Error = [1 - (S/S_m)] \times 100 = \{1 - [\beta\pi/180 \tan(\beta)]\} \times 100$ . Where  $S$  is the actual shortening,  $S_m$  is the calculated shortening and  $\beta$  is the vertical axis rotation angle. In any case and despite shortening can be corrected, any out of plane movement across the section may turn into unrealistic 2D reconstructions of the subsurface and these scenarios must be reconstructed, balanced and restored only in 3D.

### 2.2.5.4. Extensional faults

The inverted extensional faults, their features and their deformational history are study goals in inverted basins. Different techniques originally used to restore extensional faults (Gibbs, 1983, 1985) have been used to restore cross-sections involving inverted faults (Bulnes and McClay, 1999 and references therein). The limitations of these techniques and models have been analysed in Bulnes and McClay (1999) and Yamaha and McClay (2003). The former concluded that the flexural slip technique appears to be the best method for restoring physical experiments of inverted extensional faults to their pre-inversion stage. On the contrary, the latter considered that the hanging wall deformation can be best approximated by inclined simple shearing. On the other hand, both works found some reasons that could be source of uncertainties and,



therefore, the models should be applied with caution to natural examples. These uncertainties can be related with:

1. The master faults shape (listric or planar), geometrical parameters like, i.e., their dip, the detachment dip,
2. When series of faults or small-scale faults are involved, the restored bed lengths and fault shapes may be incorrect because the movement along each fault assumes that it is restored multiples times.
3. Using a single method of restoration applied to one deformation mechanism because in nature more than one mechanism may occur.
4. Considering that the footwall remains completely undeformed which is unlikely in nature.
5. Slip vectors may not be uniform over all the section
6. Assuming that the volume (or area on 2D sections) of the hanging wall is preserved during deformation while tectonic/load compaction occurs in the nature.

Moreover, in many cases the extensional basins undergo transpressional and strike-slip inversion mechanisms joined to erosion and subsequent deposition. All this makes necessary the use of additional techniques such as vitrinite reflectance (paleo temperature estimation), fission tracks analysis (exhumation and burial kinematics) and 3D restoration tools that help constraining the amount of denudation and the timing of inversion and erosion (Hill and Cooper, 1996).

### 2.2.5.5. Salt tectonics

Restoration of cross-sections including one or more layers of salt is not easy because the fundamental assumptions as bed-length and area balancing (see above) are usually invalid.

The special problems inherent to the restoration of salt-related structures are the following (Rowan and Ratliff, 2012): (1) Salt usually flows in 3D. Salt may flow laterally into different salt-related structures (diapirs, detachment folds, minibasins) implying that the plane strain assumption is not honoured. (2) Even if salt does not flow laterally, it can flow into or off the limits of the cross-section. (3) Salt can be dissolved. This would entail that conservation of rock volume assumption is not valid. (4) If vertical-axis rotations above salt are present, the plane-strain assumption would not be valid to the overburden.

Despite all these concerns, restoration of salt structures is possible, and it is still a valid and essential structural tool. However, several general guidelines must be applied to achieve useful results (see Rowan and Ratliff, 2012 for further details) (Fig. 2.2.11). Among them, the determination at regional scale of 3D salt flow patterns and their timing can help in predicting

the distribution of cross-section domains where a 2D salt area increase or decrease has to be considered.

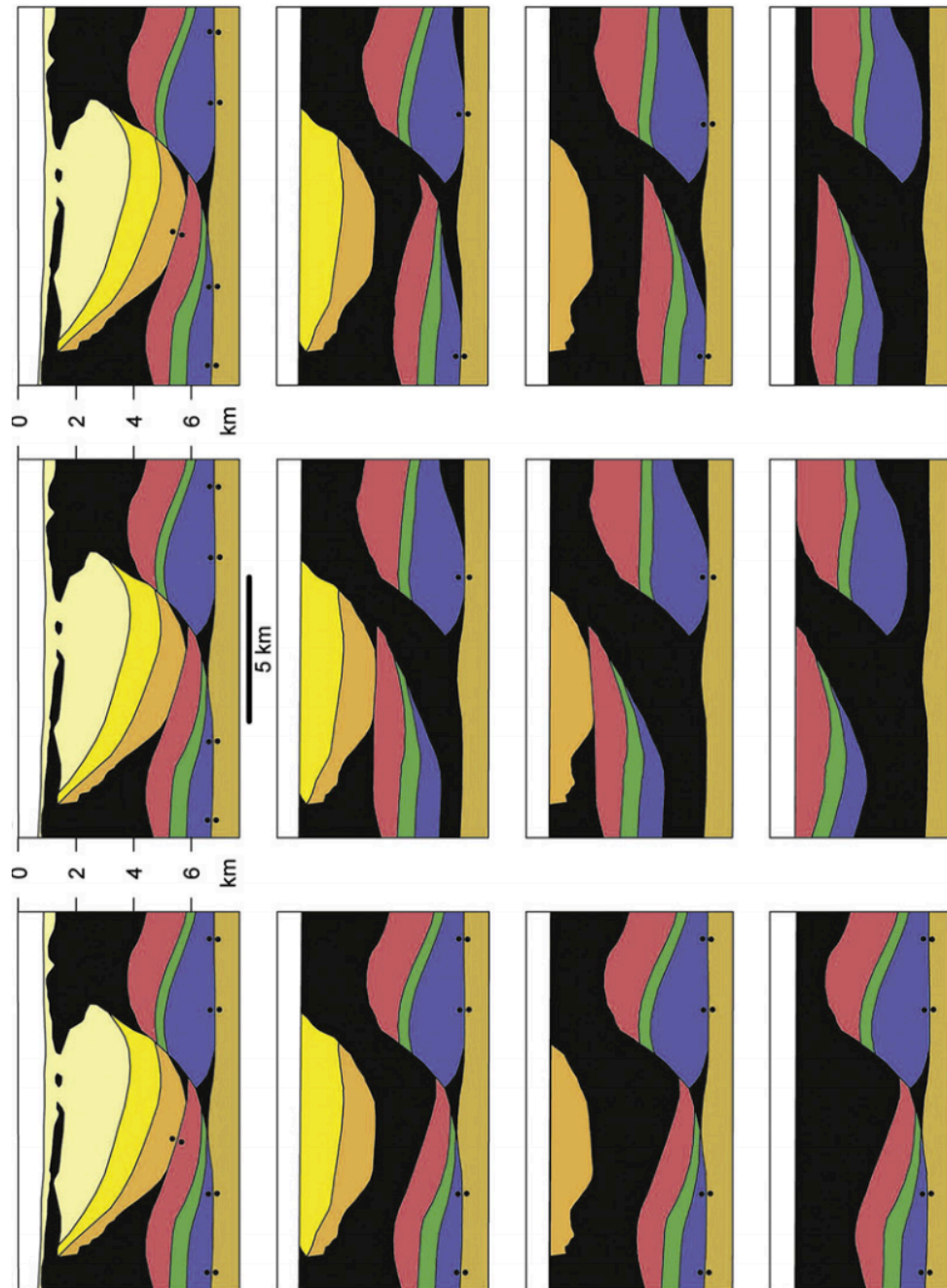


Figure 2.2.11. Restoration of a portion of a minibasin floored by a salt weld (taken from Rowan and Ratliff, 2012). The reconstructed salt thickness must be deduced applying adequate corrections (see Rowan and Ratliff, 2012 for further explanations). Salt in black, weld indicated by pairs of dots.



	Source	Brief explanation (more details in text) ***	Raw data	Type	code <sup>5</sup>	level <sup>4</sup>	Impact <sup>2</sup>	tackled <sup>1</sup> ? Y/N	References <sup>2</sup> **	Comments
1	Bedding data	Every compass has its own resolution (between 1.0° or more). Besides, So is often not flat and operator may also chose an inappropriate surface...	Cross section	Instrumental/human	3.4	DATA ACQUISITION	10% ???	Y	Mann, C. J. (1989), Bickley, C., & Fodor, J. (2007), Keeler, D.A., Mann, C. J. (1989), Keeler, D.A., Fodor, J. (2007), Goshong, R.H. (2006), Bond, C. E., et al. (2007), Goshong, R. H., et al. (2012), Bond, C. E., et al. (2015), Jones, R. et al. 2004, Goshong, R.H. 2006, Keeler, D.A. 2007, Lindsey, M.D et al., Gill, 1953; Fernández, O., et al., 2003; Moretti, L., & Callet, J. P. (2012); Ungrey, S., & Vidal-Royo, O. (2015); Rowan, M. G., & Balluffi, R.A. (2012); Bulnes, M., & McCaig, K.R. (1999); Judge, P. A., & Altmendinger, R. W. (2011); Goshong Jr, R. H., et al (2012); Ungrey, S., & Vidal-Royo, O. (2015); Woodward, N. B. (2012); Ungrey, S., & Vidal-Royo, O. (2015).	This source generally dependent both human factor as on outcrop conditions
2	Dip domain	Robustness of a dip domain depends on number of data	Cross section	Sampling quality	2	ACQUISITION	small	Y		Both amount as spatial distribution of data affects to the recognition of dip domain. The cross section reconstruction are generally based on non-uniform data set, which can cause uncertainty by recognizing the actual features of these domains.
C	Horizontality assumption	Some beds were inclined at the time of formation, although they are assumed to be horizontal during restoration	Cross section	Conceptual	6	DATA INTERPRETATION	variable	Y		The exposure of the geological contacts is normally incomplete, although the topography, surface which depends usually of the subsurface geology can be useful to contact locations. In the last years digital geological mapping and computer-assisted are helping to better location of the contacts.
R	Geological contacts	Mistakes or imprecision in mapping of geological contacts	Cross section	Human	3	ACQUISITION	large	Y		The constant-thickness style has been often used when constructing dip-domain cross sections, but pre-tectonic thicknesses can vary along- and across-strike. Thickness changes during deformation are very common in salt tectonics. When considering thicknesses constant during deformation, geometries could be restorable but often will be erroneous, due to both diachronic deformation and internal deformation of layers.
O	Thickness changes	(S.1) Stratigraphic piles may significantly vary, data are usually scarce. (S.2) If cross section is not perpendicular to beds and structures, the same unit may have different apparent thicknesses. (S.3) Thickness changes can also occur during deformation which imparts uncertainty in cross section balancing and restoration	Cross section	Instrumental/human	1.3	DATA ACQUISITION AND INTERPRETATION	variable	Y		
S	Faults	(G.1) Restoration of a fault needs both, the hanging and footwall cutoffs. Erosion or unknown subsurface cutoffs impart a large uncertainty in cross section balancing and restoration. (G.2) Unknown amount of inversion in inverted extensional faults	Cross section	Natural	1	DATA INTERPRETATION	large	Y		
S	Conceptual models	Application of erroneous structural concepts	Cross section	Conceptual	6	DATA ACQUISITION AND INTERPRETATION	very large	Y		Eroded or unknown subsurface cutoffs constitute a major source of shortening magnitude uncertainty. The presence of previous extensional faults later inverted also constitutes a source of shortening magnitude uncertainty.
S	Internal deformation	Shortening accommodated at the matrix- and the meso-scale is normally not estimated and not considered in line-length and area-balancing cross-section restorations	Cross section	Natural	1.3	DATA INTERPRETATION	variable	Y		The use of geological reasoning and rules can help decrease interpretation uncertainty. The choice of inappropriate algorithms could impart large uncertainties.
S	Out-of-plane deformation	Depth conversion requires the use of individual well velocity data (when available) and their expansion to the area covered by seismic data. Seismic velocities are usually considered as constant along the strike of the units but significant velocity changes can occur if lateral facies changes take place.	Cross section	Natural	1.3	DATA INTERPRETATION	variable	Y		Matrix-scale horizontal shortening can be estimated from field strain markers and these values incorporated in macro-scale cross-section restorations
E	Derived from seismic exploration: Time to depth conversion	Tying well and seismic data requires the use of time-depth correlations, normally based in scarce velocity data	Seismic and well data	Conceptual		DATA INTERPRETATION	variable	Y		
C	Poor seismic imaging	Some geometries (vertical and steeply-dipping bedding, sub-salt or deeply-buried structures, horizons close to faults) are normally poorly imaged by seismicities	Seismic data	Instrumental		DATA PROCESSING AND INTERPRETATION	variable	Y		These gaps in the seismic imaging can be "filled" using surface structural data when they occur in the uppermost levels. Deeper levels require a good regional geological knowledge or the extrapolation of surface observations to depth.
T	Human Bias in Seismic Interpretation	The seismic interpretations done by geoscientists rely upon their previous experience and the geological concepts they apply. This translates into a "conceptual uncertainty" inherent to seismic interpretation that has been revealed to be significant.	Seismic Data	Human	5.6	DATA PROCESSING AND INTERPRETATION	large	Y		To minimize this human bias, different methodologies including computer-aided restorations and forward modelling have been developed in order to guide interpreters towards optimal geometrical solutions

Table 2.2.2 Uncertainty Sources in Cross Section



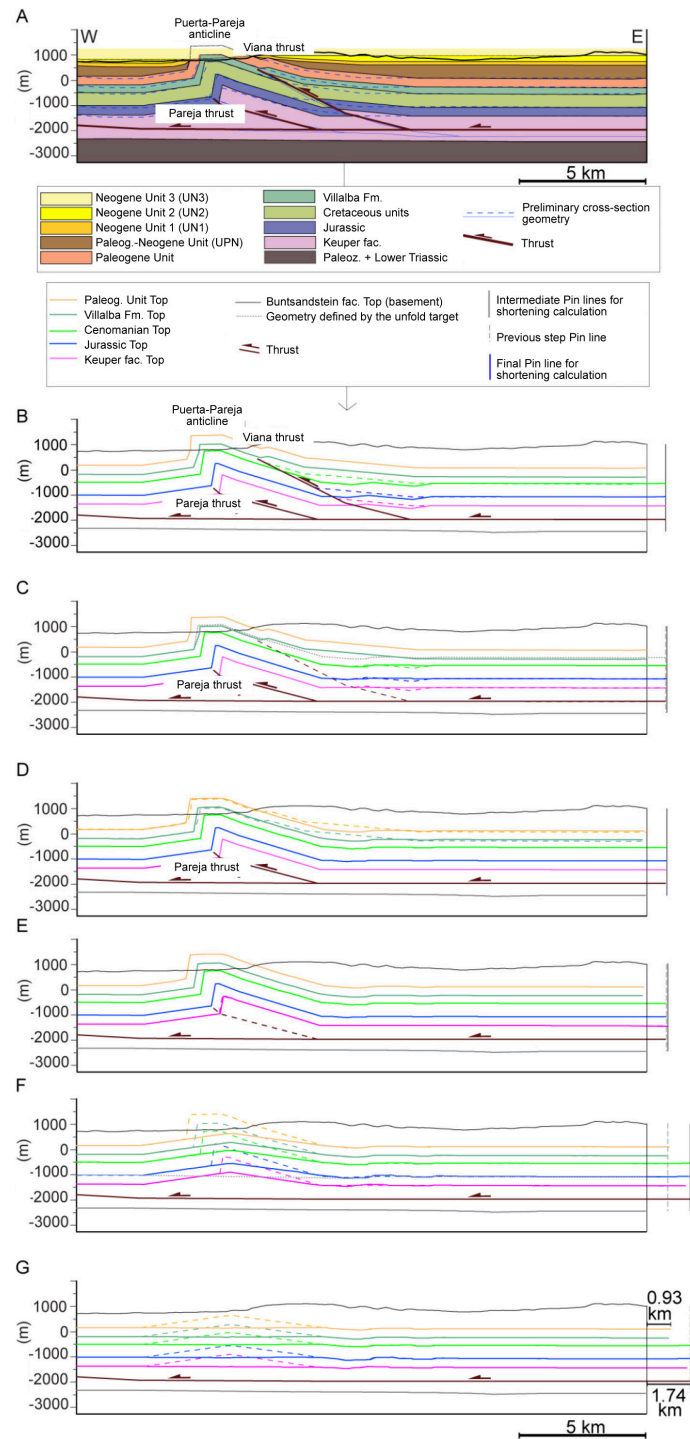


Figure 2.2.13. Steps in the restoration of the geological cross-section of Puerta-Pareja anticline (location of cross-section on Fig. 2.2.12) using the following algorithms included in the software Move 2011.1 (Midland Valley Exploration): flexural-slip for folds and fault-parallel flow for thrusts. From Valcárcel (2015).



The Loranca basin and Altomira Range represent the SW deformation front of the Iberian Chain at this latitudinal portion. The Iberian chain formed by the tectonic inversion of previous Permo-Triassic and Upper Jurassic–Cretaceous basins during the Alpine Orogeny (e.g., De Vicente et al. 2009). Structures belonging to the Loranca basin and Altomira Range are oblique with respect to the general NW–SE trend of the Iberian Chain. They are oriented N-S at its central portion, NNE–SSW at its northern sector and N-S to NNW–SSE at its southern sector, therefore tracing a subtle arc convex towards the west. Deformation in the Loranca basin and Altomira Range did not occur simultaneously both across- and along-strike.

At its northern and central sector where the Puerta-Pareja structure is located, the Altomira Range structures formed firstly during Eocene–Late Oligocene time (Gómez et al. 1996) with a westwards transport direction. Their formation individualized the Loranca basin, an inward piggyback basin, also containing approximately north–south-aligned west-verging thrust-related folds as the Puerta-Pareja anticline, formed later during Late Oligocene–Early Miocene time (Díaz Molina et al. 1995), in an out-of- sequence thrusting with respect to the Altomira’s structures (Gómez et al. 1996). Both the Altomira and Loranca structures affect a Mesozoic-Cenozoic cover detached over a regional décollement level formed by Middle–Upper Triassic evaporites and clays (e.g., Gómez et al. 1996; Muñoz-Martín and De Vicente 1998). A major portion of the Puerta-Pareja structure does not crop out, but it can be roughly identifiable from seismic profiles (Querol 1989; ITGE 1990; Valcárcel et al., 2016).

Restoration of a preliminary cross-section of the Puerta-Pareja anticline (see Valcárcel, 2015 for further details) can be seen in figure 2.2.13. The different shortening obtained in this restoration for the older units with respect to the younger ones has been interpreted as differential internal deformation between those units (Valcárcel, 2015).

#### **2.2.6.2. Linking Zone**

The Linking Zone is located in the north-eastern part of the Iberian plate, at the transition between the Iberian and the Catalan Coastal ranges. As mentioned in the previous example, this fold-and-thrust system results from the inversion during Cenozoic times of early extensional basins developed during two main rifting stages (Permo-Triassic and Late Jurassic–Early Cretaceous). The thrust system formed under a general N-S to NNE-SSW shortening direction (Guimerà, 1988; Casas-Sainz et al., 1992; De Vicente et al, 2009) and presently displays a curved pattern in map view (Fig. 2.2.14). Its geometry is strongly controlled by the inversion of Mesozoic inherited structures but also by the areal distribution of Triassic weak décollements which conditions the structural style (thick versus thin-skinned tectonics).



Outcrop conditions in the Linking Zone are excellent but its deep structure is poorly constrained because of a general lack of sub-surface information; no seismic surveys and scarce wells are available. This situation, common in other regions, is due to the lack of interest in oil exploration in shallow basins (insufficient thickness of the cover rocks to mature organic matter). Despite that, the Linking Zone was selected as a potential reservoir for CO<sub>2</sub> storage and an evaluation of the deep structure in the zone was requested to the IGME.

In this framework, and to better constrain the deep structure of the interest area, a combined and integrated structural, geophysical and petrophysical study was carried out. New gravity data (938 stations) and density determinations (827 samples) were acquired and combined with previous existing databases (1953 and 643 respectively) to obtain the Bouguer anomaly and residual Bouguer anomaly maps. Besides, surface outcrop and well data were used to construct seven serial (radial) and balanced cross-sections whose depth geometries were constrained through their 2.5D gravity modelling and the 3D gravity inversion in the whole zone (Fig. 2.2.15). The result of this workflow was the accomplishment of a set of seven geometrically correct and gravity-constrained cross-sections in the study area (Izquierdo-Llavall et al., 2019). Comparison between the constructed cross-sections before and after the 2.5D gravity modelling revealed an initial mislocation of target horizons (relevant to CO<sub>2</sub> storage) of up to 0.8 km in depth that was effectively resolved thanks to the gravity modelling (Pueyo et al., 2015) with significant implications in farther processes of decision making.

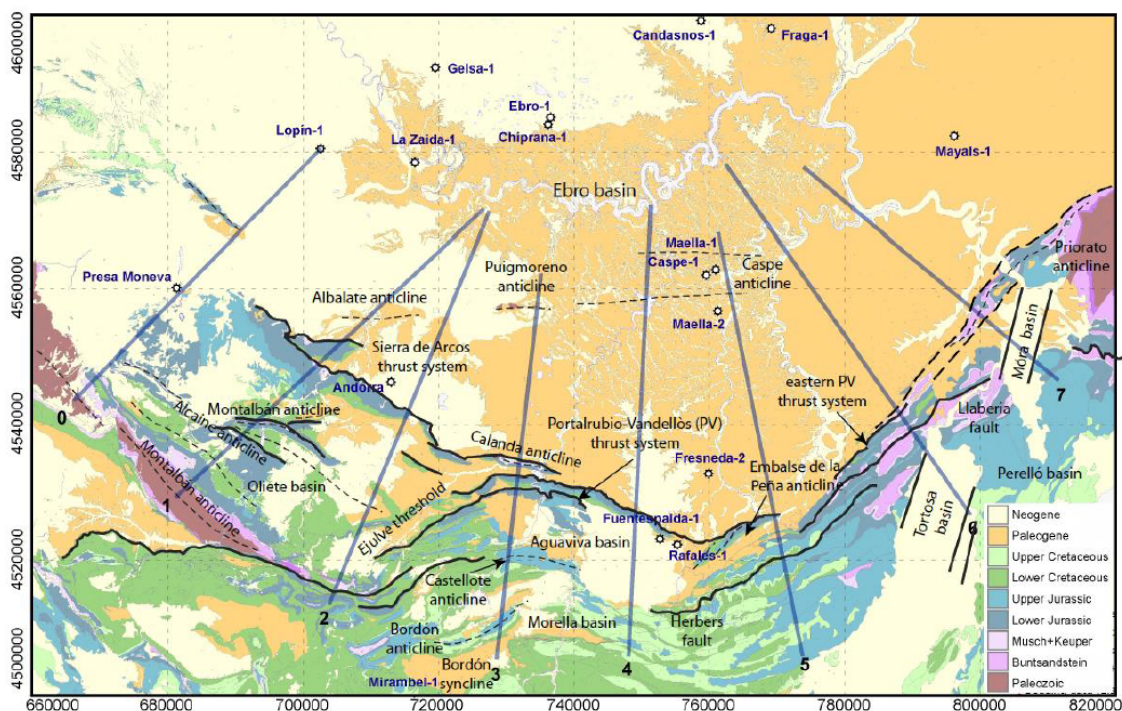


Figure 2.2.14. Geological map of the study area with location of the seven constructed cross-sections.



The cross-sections run perpendicular to the main structures and describe a radial pattern, being parallel to the main shortening direction in the central part but slightly to considerably oblique in the West and the East, respectively (Fig. 2.2.14). They define the main geometries across the study area and, combined with studies on thrust transport directions (that may vary through time, Simón and Liesa, 2011), allow investigating the kinematics of the fold-and-thrust system. These cross-sections evidence that the structure in the eastern and western domains is controlled by the inversion of inherited extensional faults whereas thin-skinned structures, detached in the Triassic weak layers, are mostly concentrated in the northern part of the central area (Fig. 2.2.14).

The comparison between present-day geometries (Fig. 2.2.15) and the cross-sections restored to the end of the Cretaceous (Fig. 2.2.16) enabled the estimation of shortening values. These values are extremely variable in the West (sections 1 and 2) but approximately constant in the central area (sections 3, 4 and 5). In the East (sections 6 and 7), shortening estimates were much lower because of the obliquity between the main structures and the shortening direction. Up to 50% of the total shortening occurred out of the plane of the selected cross-sections in this area.

Apart from this general structural information, the 3D gravity inversion (see more details in §3.2.5 Modelling case studies) allowed to better constrain the geometry of the basement in the study area (maximum uncertainty of 0.15 km; Pueyo et al., 2015). From this better definition of basement geometries, we could reject a potential reservoir for CO<sub>2</sub> storage previously prospected in the front of the Linking Zone.

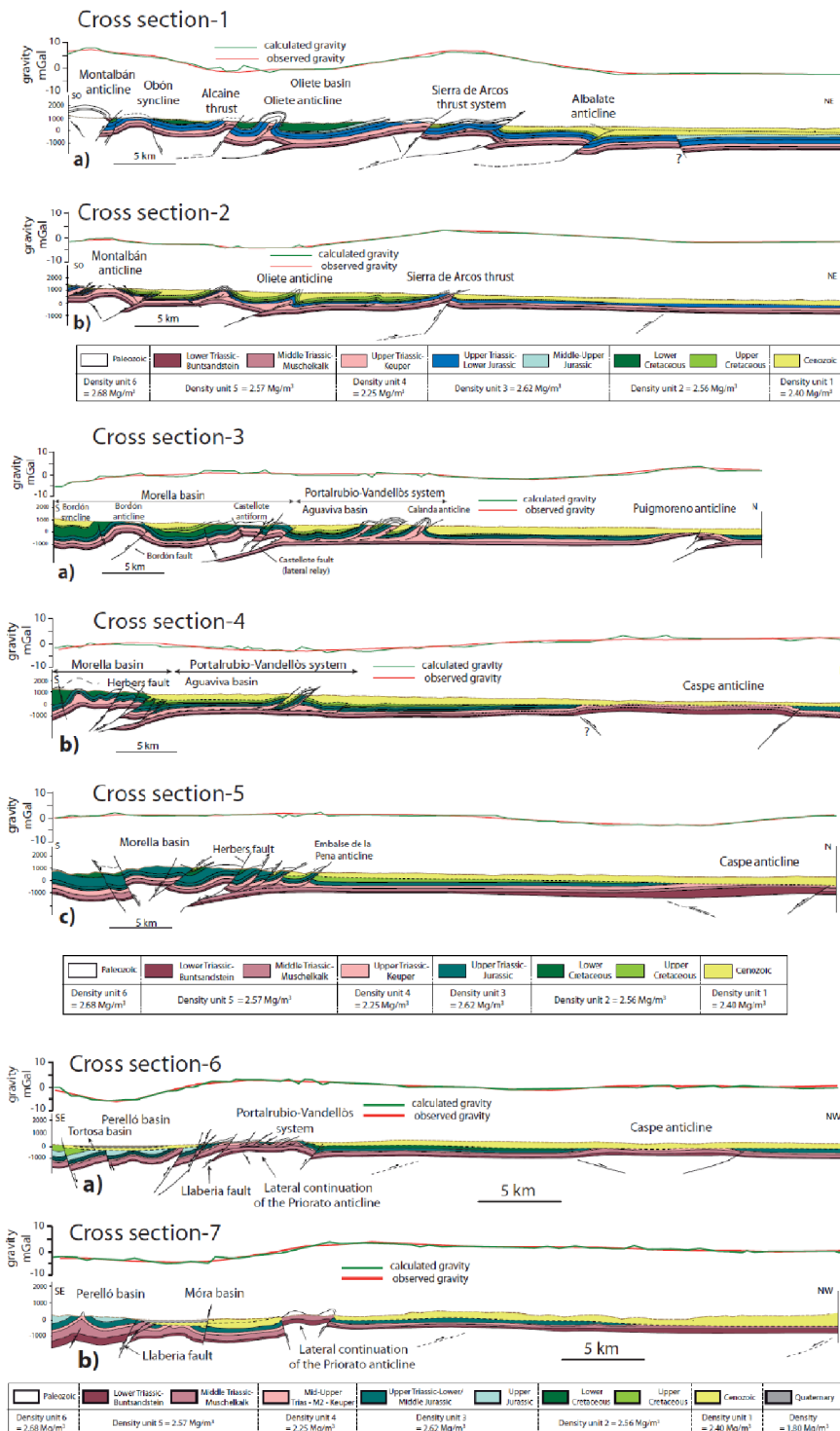


Figure 2.2.15. Gravity constrained cross-sections. Observed and calculated gravity anomalies are indicated in the upper part. Considered densities are shown in the legend.

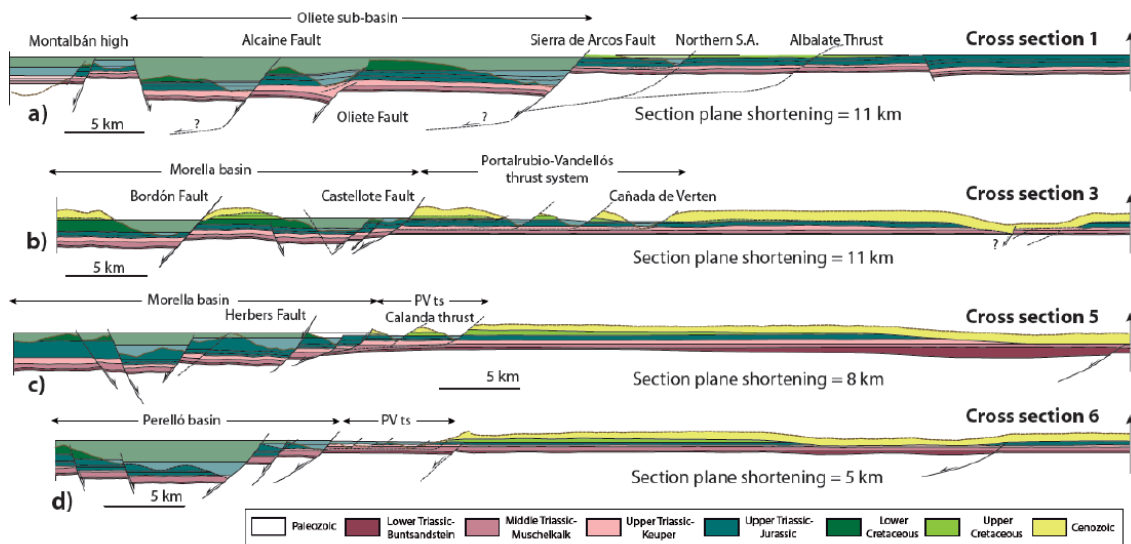


Figure 2.2.16. Restored cross-sections.

### 2.2.7. 3D restoration

Working in 3D represents a powerful tool capable of integrating all available data (e.g., field data, 2D and 3D seismic, wells, gravimetry, resistivity, etc..) in the same georeferenced framework (Fig. 2.2.17). The advantages of working in 3D are the better visualization and better understanding of the geometry and property distribution of geological structures (see Vidal-Royo et al., 2012). Besides, part of the assumptions needed in 2D can be overcome in 3D (out-of-plane deformation). Beyond 3D reconstructions, research into 3D restoration has been very active for the last three decades since the pioneer papers by Gratier et al (1991). However, there are still many drawbacks:

- (1) when working in complex structural zones (e.g., non-cylindrical geometries, non-coaxial superposition of deformation and/or areas with vertical-axis rotations): stratigraphic horizons represent a 2D indicator (paleohorizontal) and are often ambiguous to reproduce the actual 3D location.
- (2) in the choice of adequate algorithms. Current 3D restoration software packages; Unfold by Gratier et al. (1991) Move by MVE (Egan et al., 1997), Kine3D by gOcad (Moretti et al., 2005), Dynel3D by Schlumberger (Maerten and Maerten, 2006) or



Pmag3Drest by Ramón (2013) are very limited from their initial assumptions (part of them based upon extrapolation of 2D concepts to 3D) and/or

- (3) considering that computer capabilities are limited when working with 3D meshes (Moretti, 2008), although the continuous improvement of computer performance nowadays overcomes this issue.

Available geometric and kinematic 3D restoration algorithms present a major weakness: ad hoc kinematics must be assumed to perform the restoration (see also Valcárcel, 2015). In order to solve this limitation, geomechanical or physical-based restorations do not consider kinematics. They perform a mechanically stable restoration using measurable rock parameters such as density, Young modulus and Poisson's ratio (see Vidal-Royo et al., 2012 for further details). These methods are especially useful when the kinematics is unknown and/or difficult to quantify in tectonically complex areas. 3D geomechanical restorations have also the advantage of reproducing the stress and strain fields associated with the development of structures, and to predict the distribution and orientation of mesoscopic structures such as fractures (e.g., Vidal-Royo et al., 2012).

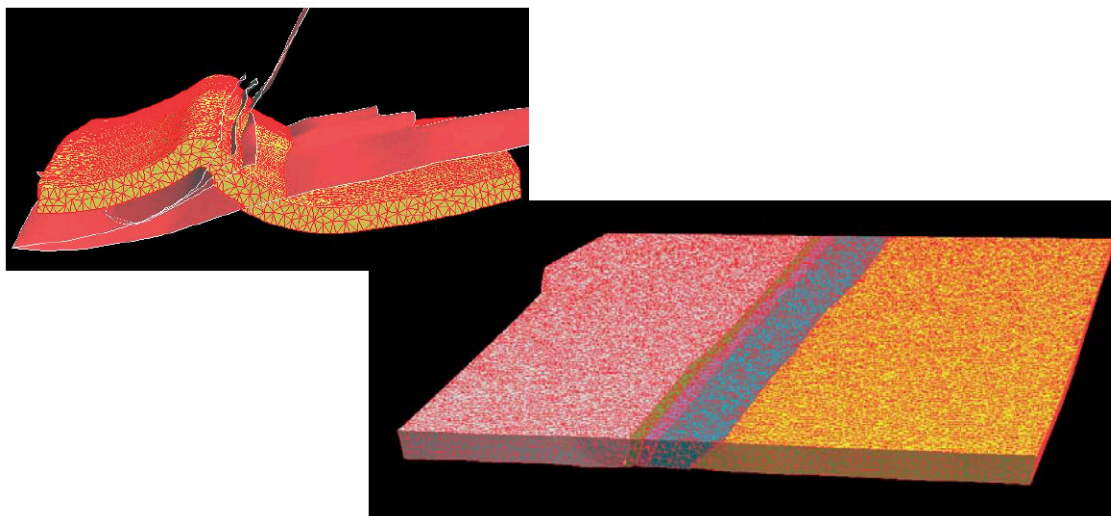


Figure 2.2.17. 3D restoration of a fold. Taken from Moretti et al. (2006).

Some solutions have been also proposed to overcome the 3D reference system problem. Ramón et al. (2012) first introduced the use of primary paleomagnetic vectors (those recorded at the rock formation time) in a 3D restoration algorithm based on piecewise discretization of complexly folded surfaces (conical folds and superposed folding). Because this method (Ramón et al., 2016b) as well as UNFOLD (Gratier and Guiller, 1993) or the one by Williams et al. (1997) were very sensitive to the mesh geometry and other factors (pin elements), a parametric



approach (in the sense of Mallet, 1992) was later on successfully launched (Ramón et al., 2016). Palaeomagnetism was used as the initial gradient of one of the parametric systems of the folded surface and the obtained restoration results were much better than other commercial tools (Move, Kine3D or Dynel3D). These authors used analogue models where the 3D deformation patterns were fully known at both, the deformed and undeformed stages to test the restoration outputs. Despite the current limitations, the implementation of palaeomagnetic vectors must be a keystone in the development of future and reliable 3D restoration methods.

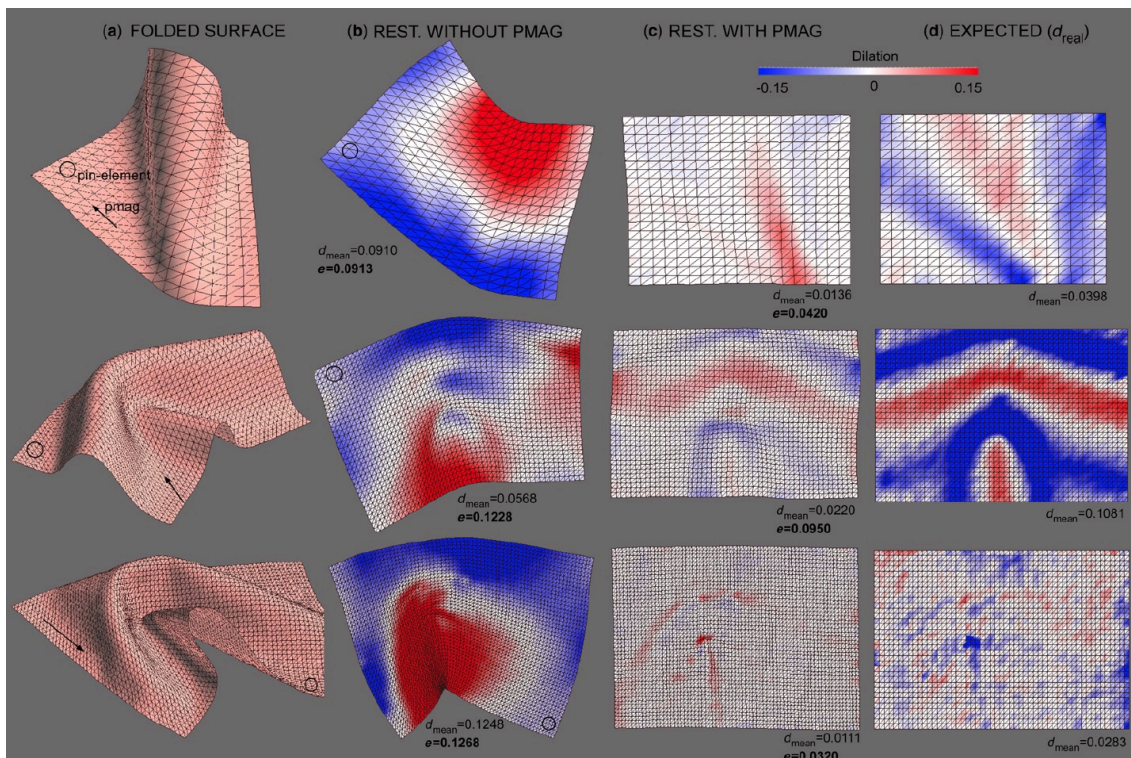


Figure 2.2.18. 3D Restoration of three analogue models of complex folds (3D surfaces) with and without taken into account palaeomagnetic data. (a) Folded surface with the pin-element and pin-vector orientation displayed. (b) Restored surface without palaeomagnetism (Kine3D solution). (c) Restored surface with palaeomagnetism (Pmag3Drest). Restored surfaces are plotted together with their dilation values. (d) Initial horizontal surface displaying the real (expected) dilation ( $d_{real}$ ) (Taken from Ramón et al., 2016a).



## 2.2.8. Backstripping

Backstripping is a technique that allows carrying out a detailed analysis of subsidence and sedimentation of a basin, with the main purpose of revealing tectonic driving mechanisms of basin subsidence (Miall, 2010). The analysis consists of sequentially removing of the sedimentary cover load, correcting parameters such as the compaction, paleobathymetry and sea level changes. Two models can be applied in order to fit the sedimentary load: air-type or flexural isostatic model, while the residual subsidence is related to thermal subsidence (lithospheric thermal behaviour).

Compaction assumes that porosity decreases with increasing depth. Different algorithms can be applied to investigate compaction (Fig. 2.2.19). The most common ones are Slater and Christie (1980), Baldwin and Butler (1985) and Dickinson (1953). These algorithms are commonly used in reverse model decompaction during the backstripping technique.

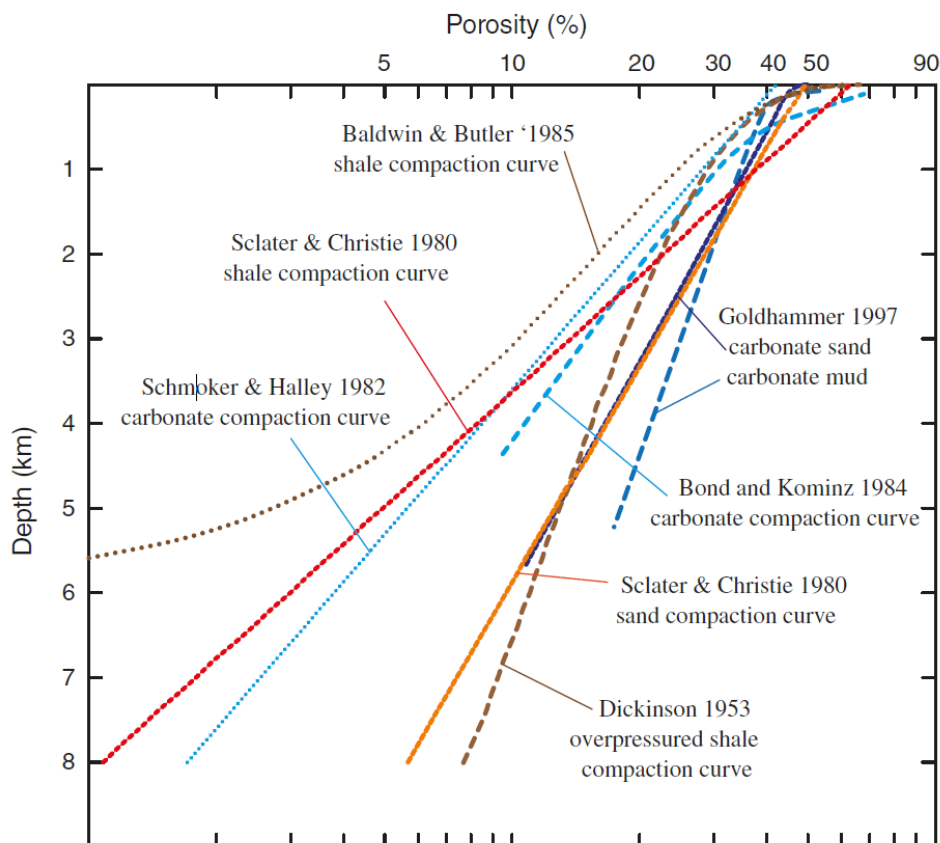


Figure 2.2.19. Empirical compaction curves from the literature showing porosity reduction as a function of burial depth for a variety of sedimentary lithologies (taken from Lingrey and Vidal-Royo, 2015).



The decompaction process takes place once a stratigraphic horizon has been restored and backstripped, the porosity lost during compaction is returned to the underlying strata. At this stage, some aspects have to be considered: 1) surface geometries change as the beds expand (thickness increase); 2) removal of the differential compaction effects; 3) the effect of crustal loading can be removed using flexural or airy isostasy model.

On a regional scale, the crust is deformed when applying loading. This effect can be solved applying the two aforementioned methods. The Airy Isostasy assumes a flexural model where a brittle crust (tectonic plate with no strength) is floating on a fluid layer (mantle) (Fig. 2.2.20a), being unable to support its own weight (Burov and Diament, 1995). This produces a vertical movement and is best suited to loads with little lateral variation. Airy Isostasy is local, and there is no lateral effect of loading/unloading. Therefore, it is recommended when dealing with loads without significant thickness lateral variations, and during restoration of salt. The Flexural Isostasy assumes that the lithosphere has an inherent strength and rigidity, causing it to flex when a load is applied (Fig. 2.2.20b). The local load changes can be related to tectonic contraction and extension or erosion and are not compensated locally, however they are spread regionally. The flexural properties of the lithosphere determine the extent to which the loads are spread. Flexural Isostasy may influence on fault geometry, sequence thickness, rate and spatial distribution of rock uplift and erosion across the region.

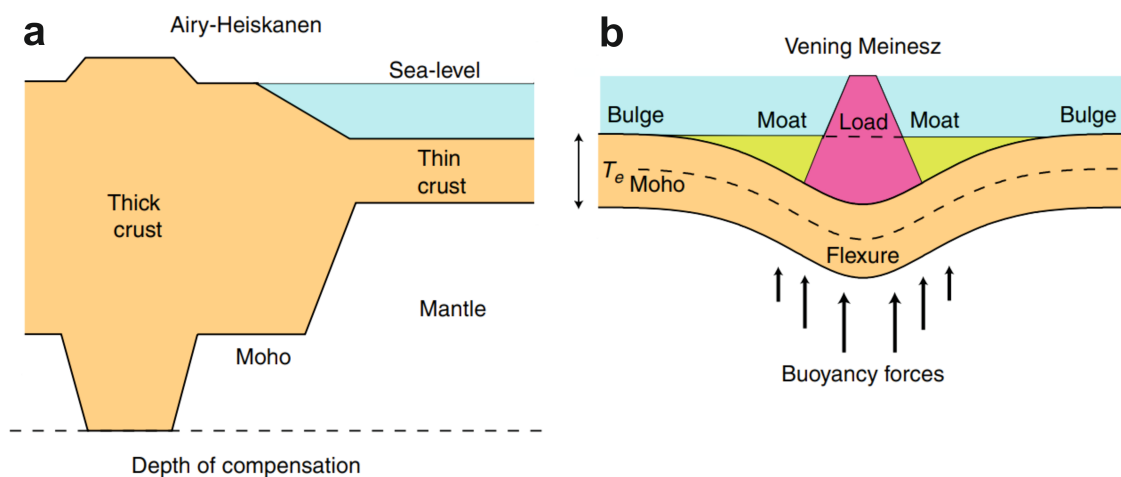


Figure 2.2.20. Isostasy models. a) Airy isostatic compensation to varying loads; b) Flexural response of the crust to a load e.g., a seamount. Adapted from Watts (2001).



Flexural Isostasy is defined by several parameters: 1) Young's Modulus (E); 2) Flexural Rigidity (D); 3) Density of the Bulk Load; 4) Density of the Mantle and; 5) Effective Elastic Thickness (Te). Te is equivalent to the thickness of a theoretical, perfectly elastic and isotropic layer with the same flexural strength as the lithosphere (Roberts et al., 1998). Te is a function of Young's Modulus (E) and the thickness and curvature of the crust. E varies with rock density and temperature.

Isostasy is also influenced by the thermal subsidence, which takes place when initial sedimentary basin is produced by the stretching of continental crust (initial subsidence: Si), becoming thinner and allowing the asthenosphere to fill in the gap (Fig. 2.2.21). Over time, this increase in temperature falls, causing thermal subsidence (St). The total subsidence will be the combined effect of Si + St. Different models for thermal subsidence are available, although the most common is based on the work by McKenzie (1978).

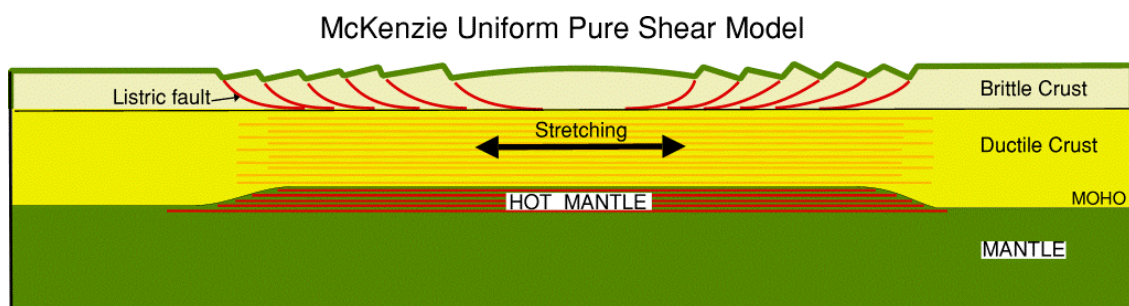


Figure 2.2.21. Uniform stretching model of crust and mantle (after McKenzie, 1978 and Tarney, 1998)

The types of structures and geometries formed depend on the amounts of stretching involved. The stretching is generally measured using the  $\beta$  parameter called beta factor, where:

$$\beta = \frac{t_0}{t_1} \quad \begin{array}{l} t_0 : \text{initial crustal thickness} \\ t_1 : \text{final crustal thickness} \end{array}$$

Low beta factor values are located in areas where there is a relatively low extension of the crust, and the characteristic structures are extensional faults of large to moderate angles, with associated half grabens and tilted fault blocks, e.g., proximal domains of continental margins. High beta factors take place in high-extension areas of the crust, where the individual extensional faults may rotate to a too low dip to remain active, and then a new set of faults is generated, e.g., distal domains of extended passive margins.



### 2.2.9. Example of backstripping

This example is extracted from Bell et al. (2014). The Halten Terrace represents the eastern margin of the Vøring Basin, located on the mid-Norwegian continental shelf (Fig. 2.2.22). The area is characterized by multiple rift events that started in the Devonian (e.g., Doré et al., 1997). Permo-Triassic rifting was followed by the deposition of a thick sequence of Triassic evaporites, resulting in the formation of a range of rift- and halokinesis-related structural styles (e.g., Elliott et al., 2012; Pascoe et al., 1999). The major rifting phase occurred in the Late Jurassic to Early Cretaceous times (Roberts et al., 2009), which resulted in the formation of large extensional faults and rotated fault blocks (Fig. 2.2.22b). Further rifting took place in the mid-Norwegian margin during the Early Cenozoic (Roberts et al., 2009), leading to continental break-up and opening of the NE Atlantic Ocean (e.g., Scheck-Wenderoth et al., 2007). Bell et al. (2014) unravel the Late Jurassic–Early Cretaceous geometry of the southern Halten Terrace, poorly understood before. The understanding of the geometry of a rift basin through time is crucial for resolving the dynamics of continental rifting and in assessing the prospectivity for hydrocarbon or energy/CO<sub>2</sub> storage of such basins.

In order to resolve the magnitude and distribution of extension that occurred during Late Jurassic–Early Cretaceous rifting in the Halten Terrace area, Bell et al. (2014) restored the Late Jurassic–Early Cretaceous margin geometry through 2D seismic reflection profiles using a combination of sedimentology, seismic stratigraphy and reverse post-rift thermal subsidence modelling. Sedimentological data from wells (lithology, near-surface porosity, decay constant and matrix density) and seismic-stratigraphic observations provide important constraints on palaeobathymetry in the Late Jurassic and Early Cretaceous.  $\beta$  and  $T_e$  parameter pairings that can restore palaeobathymetry to comply with all of these constraints are restricted between  $T_e$ 's of 3–13 km and  $\beta$  profiles ranging from  $\beta = 1$  to 1.2 and 1 to 1.6 from east to west (Fig. 2.2.23).

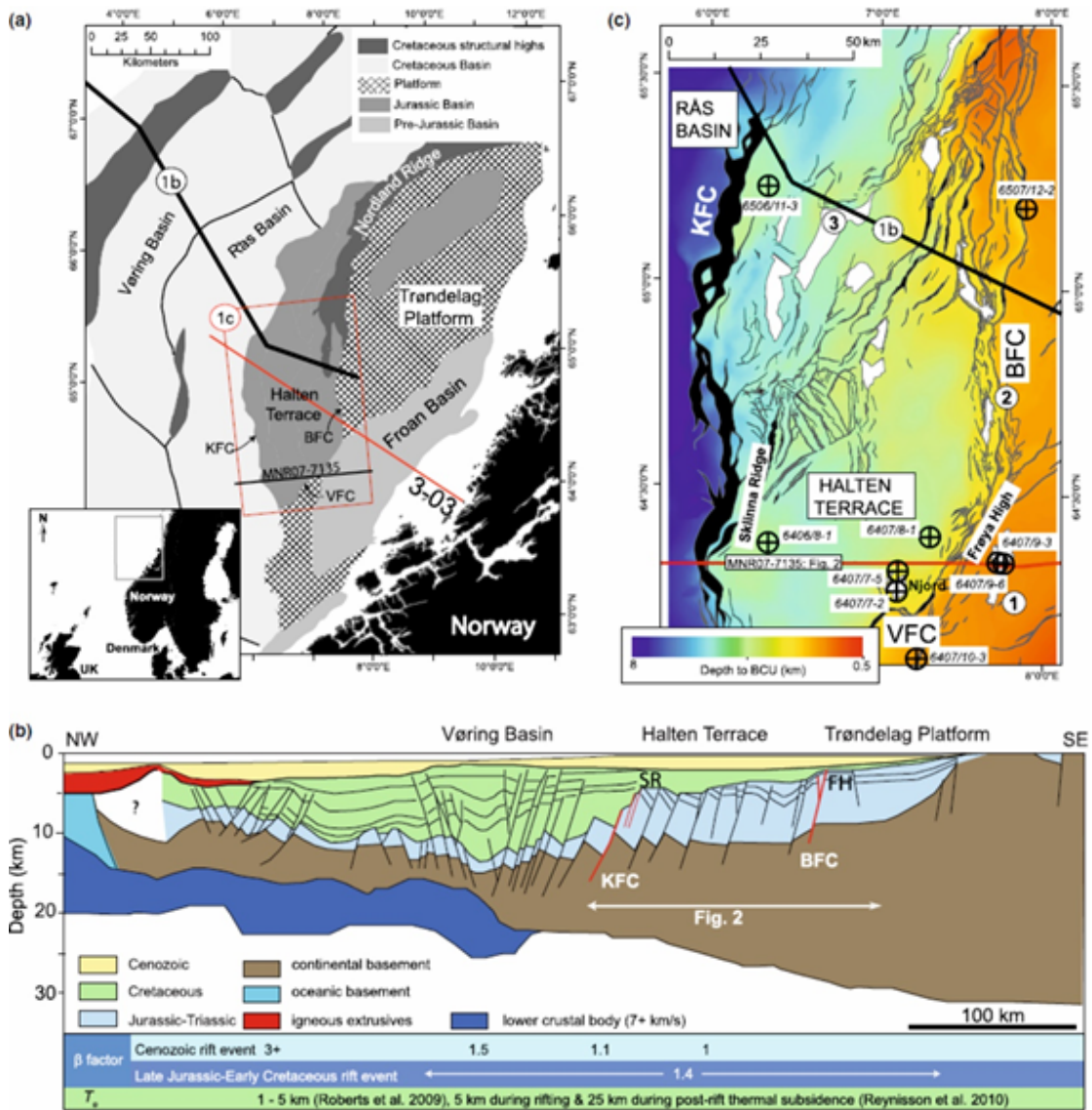


Figure 2.2.22. (a) Simplified geological map of the mid-Norwegian Shelf. (b) Regional cross section across the Halten Terrace and Vøring margin. (c) Map displaying the depth to the Base Cretaceous Unconformity in the Halten Terrace region, together with fault polygons. Taken from Bell et al. (2014). See the reference for further explanation.

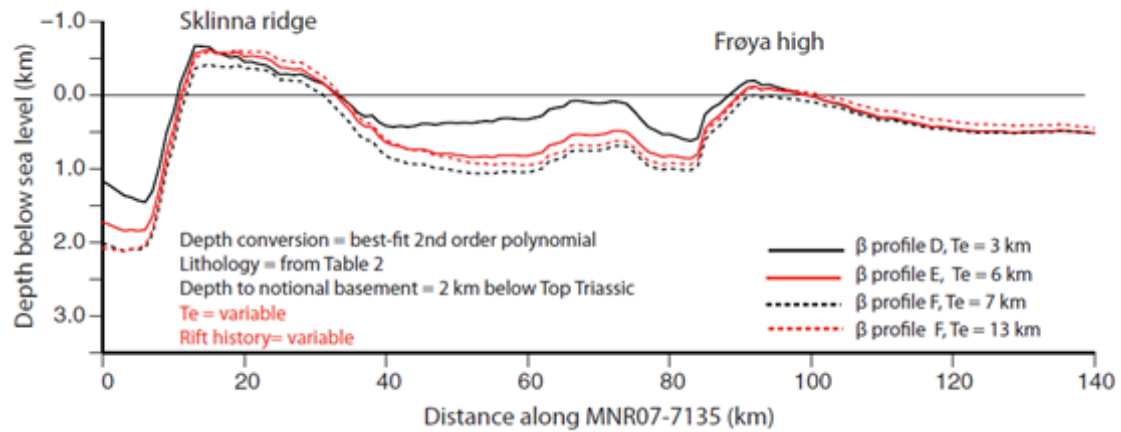


Figure 2.2.23. Reconstructed Late Jurassic–Early Cretaceous seafloor geometries for the full range of possible  $T_e$  and  $\beta$  profile values (taken from Bell et al. 2014).

With sediment compaction, flexural loading and thermal subsidence being considered, instead of using simple horizon flattening techniques, the results of the backstripping restoration show that the late syn-rift geometry of the Halten Terrace in the Late Jurassic–Early Cretaceous involved a series of isolated depocentres between footwall islands, which were not connected into a single subsiding depocentre until the Coniacian (Fig. 2.2.24). Cretaceous sediments were deposited in a single, relatively unconfined basin in water depths of 1–1.5 km (Fig. 2.2.24c). Bel et al. (2014) also concluded from restoration process that the amount of upper-crustal stretching during the Late Jurassic–Early Cretaceous rift phase is comparable to the total amount of lithospheric stretching, supporting a uniform pure-shear stretching model.

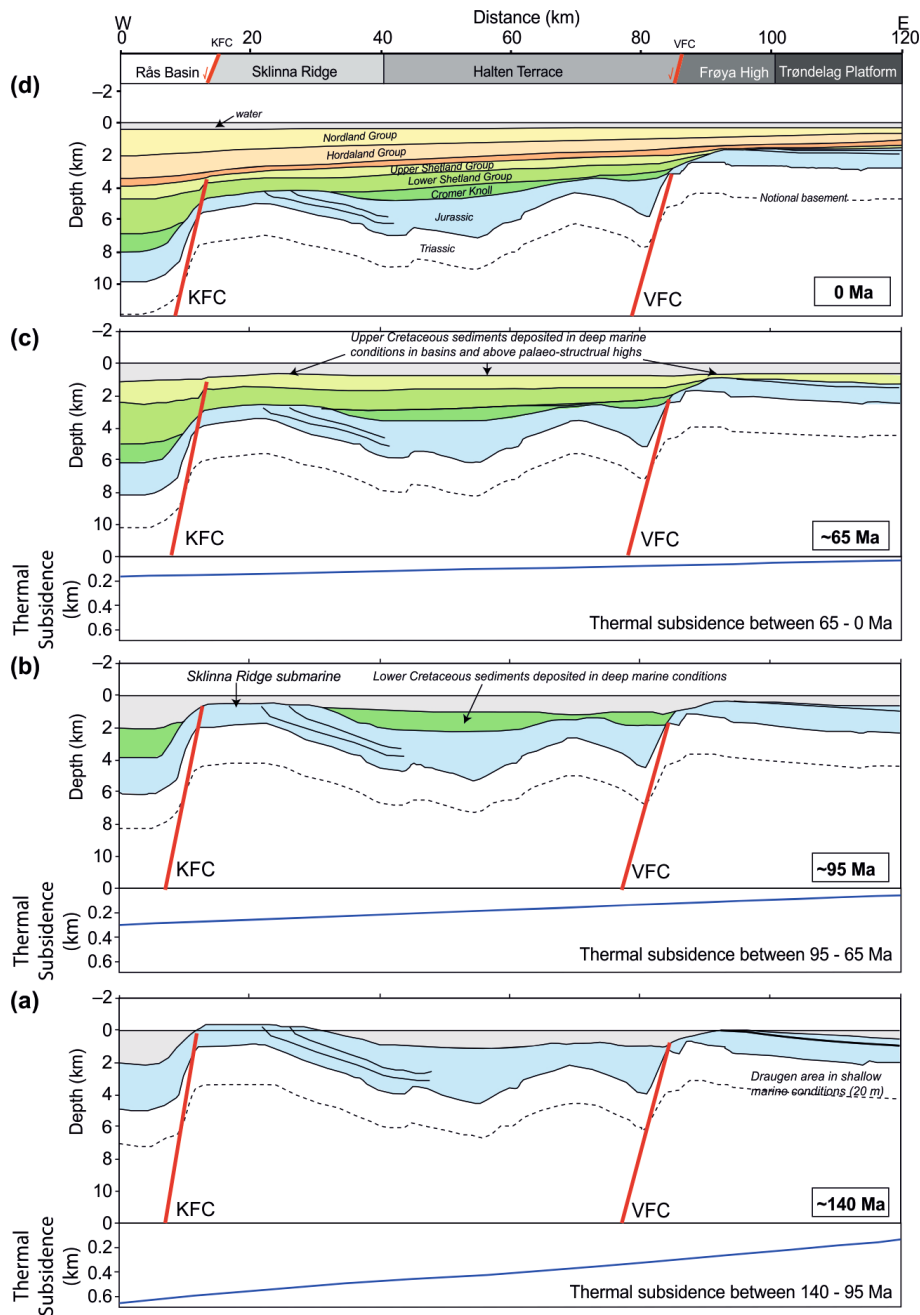


Figure 2.2.24. Restoration of line MNR07-7135 back to the Late Jurassic–Early Cretaceous syn-rift geometry using the backstripping technique. The inset graphs in Fig. 2.2.24a, b and c show the magnitude of thermal subsidence during the period 140–95 Ma, 95–65 Ma and 65–0 Ma respectively. See Fig. 2.2.22 for location. Taken from Bell et al. (2014).



## 2.3 Petrophysics

### 2.3.1 Introduction

Petrophysical data related to gravity and magnetic interpretation (rock density, rock magnetic susceptibility and natural remanent magnetization [NRM]) are one of the three keystones in this workflow for 3D modeling based on potential-field geophysical data. In all modelling programs (see section 3), rock volumes have to be characterized by their petrophysical properties. In this chapter, we mainly focus on density, but magnetic variables (especially susceptibility) are also described because of its coupling relationships with density (see section 2.3.4 for more details). Beyond formation density and gravimetric logging, indirect relationships between bulk density and other variables (e.g. seismic velocity logs) are treated secondarily.

The density of a substance (also referred as volumetric mass density and as specific mass) is defined as the mass divided by the volume. In the International System (SI) the unit for density is  $\text{kg/m}^3$ , but CGS unit ( $\text{g/cm}^3$ ) is still commonly used. The bulk density of a rock is determined by the summation of the density of its constituents (mineral and mineral aggregates; also known as grain density), the density due to the pore space (actual porosity) and the density of fluids and gases. In petrophysics different density definitions can be used depending upon the fluid considered and the rock porosity (actual or effective) but most common terms are; dry bulk density (weight of grains/ bulk sample volume [grain+pores volume]), saturated bulk density ([weight of grains + weight of pores saturated in water]/ bulk sample volume), natural bulk density (weight of grains + weight of pores saturated in natural fluid{e.g. oil}/ bulk sample volume) (see additional definitions in Olhoeft & Johnson, 1989).

The density of a mineral depends upon its chemical elements (composition) but also on the crystallographic habit (shape and crystallographic form) as well as the internal bonding and structure. Currently, there are many mineralogical databases where the density magnitudes of thousands of minerals can be found (<http://webmineral.com/>, <https://www.mindat.org/> or as the aforementioned work by Olhoeft & Johnson, 1989). In any case, the density of most common rock forming minerals ranges from 2.2 to 3.5  $\text{g/cm}^3$  and many ore minerals range between 4.0 and 8.0  $\text{g/cm}^3$  (Schön, 2015) (Fig. 2.3.1).

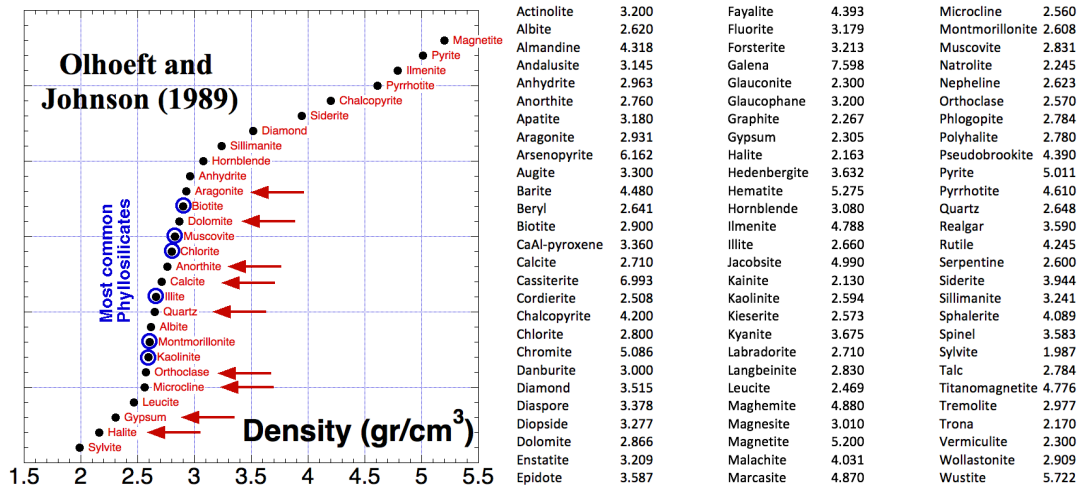


Figure 2.3.1. Density values ( $\text{g/cm}^3$ ) of most common rock forming minerals and ores (red arrows for top-most common minerals and blue circles for phyllosilicates). Extracted from the compilation by Olhoeft and Johnson (1989).

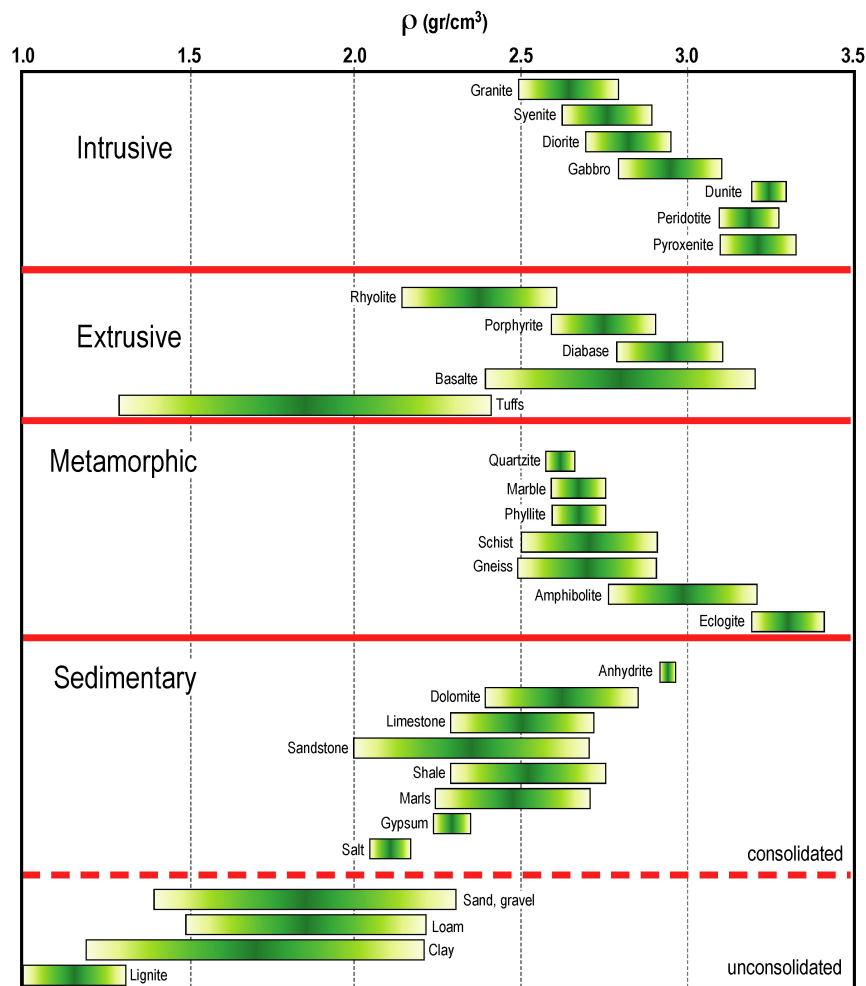


Figure 2.3.2. Density values ( $\text{g/cm}^3$ ) of most common rocks (redrawn from the compilation by Schön, 2015).



The variability found in the density of common rock types is much larger and it may follow two simple trends (Schön, 2015) (Fig. 2.3.2) igneous intrusive rocks exhibit an increase of density from felsic to mafic affinities (this also happens to a lesser extent in extrusive ones), and 2) sedimentary porous rocks show a density decrease with increasing porosity and decreasing water saturation. Although, the factors controlling the variability of the rock density are much more complex, some interesting applications in petrophysical analysis that focuses on gravimetric interpretation are derived from the first relationship, as we will see later (section 2.3.4).

Unfortunately, petrophysical information is often obviated in many workflows, sometimes is poorly described in technical reports or scientific papers (e.g. only frequency diagrams are shown) and, as a general rule, it is usually scattered, scarce and many times opaque, restricted or with difficult access. Very often, theoretical data (as those from figure 2.3.2, Carmichael, 1982; Kobranova, 1990; Schön, 2015) are assigned to rock formations during the balancing of the observed gravimetric/magnetic signal. In this way, the feedback between the geometry and petrophysical data for a given rock formation becomes an important source of uncertainty since we can reduce the thickness or depth of the target formation or, alternately, we can also modify its density.

In fact, this uncertainty is straightly related to the ambiguity problem in gravimetric interpretation (also known as the non-uniqueness solution, which can be extended to all geophysical methods). This is a well-known problem in the geophysical literature since the pioneer works by Skeels (1947), Roy (1962) and many others: *“for a given anomaly and a given density contrast a wide range of possible interpretations can be made, at various depths, and that whereas there is a maximum depth for the solution the minimum depth is zero”* (Skeels, 1947) (Fig. 2.3.3). Actually, the density contrast may vary as well, so the number of solutions is much larger, that is, the possible locations of given bodies with a certain geometry and density. However, Saltus and Blakely (2011) has pointed out that *“the rigorous mathematical label of non-uniqueness can lead to the erroneous impression that no single interpretation is better in a geologic sense than any other”* and they have highlighted the importance of *“a priori”* geological information to produce significant, robust, and definitive results.

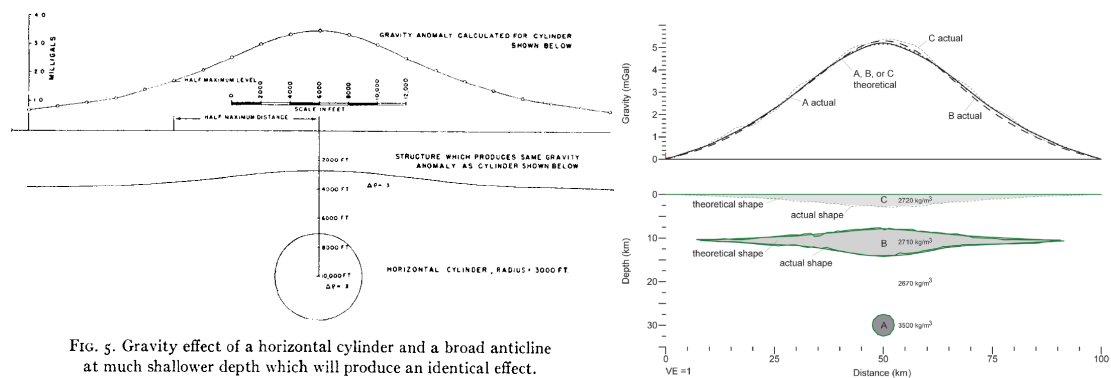


FIG. 5. Gravity effect of a horizontal cylinder and a broad anticline at much shallower depth which will produce an identical effect.

Figure 2.3.3. Reproduction of classic figures to show the ambiguity problem in gravimetric analysis. Different bodies with different densities at different depths may approximately produce the same gravity anomaly. Left one by Skeels (1947) and right one by Saltus and Blakely (2011).

We claim here in agreement with recent works (Enkin et al., 2020; Dentith et al., 2020) that petrophysical data play a decisive role in reducing the number of possible solutions and optimizing geophysical exploration. Therefore, and to avoid this ambiguity (at least in part), we consider the petrophysical information as primary and crucial data in our workflow proposal. Numerous data for characterizing the target formations have to be acquired directly from outcrops or harvested from databases (rock samples or well logging). The final goal is to build robust histograms for every modelled volume to constraint the mean density and its variability (both at surface and at depth) in order to be able to quantify a much more bracketed uncertainty.

*The rock physical properties represent the link between geophysical anomalies of potential fields and geology in terms of structure and lithology. Knowledge of the petrophysical properties therefore provides a necessary constraint in potential field interpretation thereby considerably reducing the ambiguity in such interpretations (Henkel, 1994).*

In this section we review the different petrophysical data used in gravimetry (and magnetism) the most common field, acquisition and laboratory procedures, some useful relationships among variables and the related uncertainty. At the end we list some open problems and itemize some useful lessons to be learnt.



## 2.3.2 Field and laboratory procedures for density and magnetic susceptibility determinations

### 2.3.2.1 Field data and field measurements

The standard procedure is, as simple as taking fresh (unaltered and non-fractured) hand samples with enough volume (about 1-2 dm<sup>3</sup> or more, that is, about 3-5 kg) directly from the outcrops (not always a simple game). It is desirable, although not always possible, that some few samples (2-3 or more) are taken in every outcrop to obtain a robust mean of that sampling point. Besides, the size of individual samples must guarantee the estimation of a few density measurements from every hand sample. Additionally, an accurate positioning (GPS coordinates), bedding/foliation data (if possible) and petrological and geological data description (lithology, stratigraphic formation and age), must be accomplished. Blocks could be also oriented in the field with solar or magnetic compasses if natural remanent magnetization is later on needed (Plata, 2009; García-Lobón et al., 2014).



Figure 2.3.4. Petrophysical hand sampling in the outcrop. All pictures; sampling igneous rocks in the Pyrenees, except for the bottom right one; hand samples from the Iberian Range (Pueyo et al., 2016a).



Some measurements can be taken directly in the field. Modern portable magnetic susceptibilimeters (SM20 by GF Instruments [<http://www.gfinstruments.cz/>], SM30 by ZH Instruments [<http://www.zhinstruments.com/>], KT20 by Terraplus - Geomatrix Earth Science Ltd; <https://www.geomatrix.co.uk/land-products/electromagnetic/kt20/>) or a large variety of Bartington coils using the MS3 measurement unit (MS2D, E and F coils) (<https://www.bartington.com/ms2-ms3/>) as well as the RT-1 (formerly by Fugro and by CorMaGeo) can register many measurements in a short time gap (Hroudá et al., 2009) (Fig. 2.3.5 and Table 2.3.1). In fact, the KT20 even allows estimation of density in the field (Archimedes principle, see later). Even if the study is only focused on gravity interpretation, magnetic measurements should be also taken to compare the density vs susceptibility trends in the Henkel's (1976 and 1994) diagram (see later). Both data together have an added value identifying petrological processes and they can be implemented together in databases being reusable in future studies (v.g. Enkin, 2018 and Enkin et al., 2020).

	<b>SM20</b>	<b>SM30</b>	<b>KT10</b>	<b>KT20</b>	<b>RT-1</b>	<b>MS3+MS2D</b>
	GF Instruments	ZH Instruments	Terraplus	Terraplus/Geomatrix	CorMaGeo/Bartington	Bartington
<b>Launching year</b>		2016				
<b>Units</b>	SI	SI	SI	SI	SI and cgs	SI and cgs
<b>Sensitivity</b>	1 x 10 <sup>-6</sup>	1 x 10 <sup>-7</sup>	1 x 10 <sup>-6</sup>	1 x 10 <sup>-7</sup>	1 x 10 <sup>-5</sup>	1 x 10 <sup>-6</sup>
<b>Measurement range</b>	1 x 10 <sup>-6</sup> - 1 SI		1 x 10 <sup>-6</sup> - 10 SI	1 x 10 <sup>-7</sup> - 20 SI	1 x 10 <sup>-5</sup> - 1 SI	1 x 10 <sup>-6</sup> to 26 SI
<b>Operating frequency (kHz)</b>	10	8	10	1/10/100	0,75	0,95+/-0,06
<b>Measurement frequency</b>	1 ms/sg	12 ms/sg	20 times per second		1 ms/sg	up to 0,1 ms/sg
<b>Measuring modes</b>	single/continuous				Single and continuous	Single and continuous
<b>Graphic Display</b>	LCD (just ms)	4 digits LCD	LCD 104 x 88 pixels	400 x 240 pixels	LSD 55x28 mm	requires PC
<b>Memory</b>	120 ms	250 ms	3000 ms	16 Gb	9800	depends on external PC/PDA
<b>Water resistance</b>	?	?	?	?	IP65	?
<b>Control</b>	button	button	buttons	buttons	buttons	Software on PC/PDA
<b>Connectivity</b>	RS 232C/USB	RS232C	USB, Bluetooth	USB, Bluetooth	Bluetooth	Hirose HR10-7R-6P
<b>Power Supply</b>	3 V cells CR 2032	2 lithium CR2430	1AA Batteries	2 x Li-Ion Batteries	3 x 1.5V AA	depends on external PC/PDA
<b>Battery life</b>	100 hr	80 hr	Up to 4000 single readings	??	25 hr	depends on external PC/PDA
<b>Operating temperature</b>	from -10 to +60 °C	from -20 °C to 50 °C	-20 °C to 60 °C	-20°C to 60°C	- +50°C (storage: -40°C - +6	-10°C to +40°C
<b>Dimensions (mm)</b>	100 x 65 x 25	100 x 65 x 25	200 x 57 x 30	260 x 72 x 60	155 x 84 x 34	208 x 208 x 104
<b>Coil Diameter (mm)</b>	50	56	65 max (elliptic)	66 max	18 x 40 (elliptic)	185
<b>Penetration</b>	90% at 20 mm	90% at 20 mm	?	?	90% at 30 mm	50% at 15mm, 10% at 60 mm
<b>Coil material</b>	?	?	?	?	Ferrite	?
<b>Averaged volume (cm<sup>3</sup>)</b>	<b>35</b>	<b>40-45</b>	≈	≈ <b>50-60</b>	≈ <b>60</b>	<b>200</b>
<b>Weight (kg)</b>	0,127	0,18	0,3	0,6	0,35	0,13 (ms unit) + 0,5 (coil)
<b>GPS</b>	NO	NO	YES	SBAS (WAAS, EGNOS, MSAS)	NO	NO
<b>GPS accuracy (m)</b>	----	----	?	2	----	----
<b>Camera</b>	NO	NO	NO	YES (2Mp)	NO	NO
<b>Voice recording</b>	NO	NO	YES	YES	YES	NO
<b>Density measurements</b>	NO	NO	NO	YES	NO	NO
<b>Sample weight (kg)</b>	----	----	----	1	----	----

Table 2.3.1. Specifications of most common portable susceptometers



Special attention and cautions must be taken during susceptibility measurements. First of them is the selection of appropriate outcrop surfaces, as a general rule, joints are flat and usually more regular than bedding surfaces and are always available (even in igneous rocks). Second, the outcrop surface to be measured should be representative for the rock type, and readings should be evenly distributed in, let say so, 10-25 m<sup>2</sup>. Very few studies have tackled this point, except for granitic outcrops (Olivier et al., 1997). Moreover, an important point to keep in mind is that susceptibility is an anisotropic property, and therefore readings must be taken in different orientations with respect to bedding and structural features of rocks to ensure a representative value. While sampling in roads, combustion dust can be strongly magnetic (Boyko et al., 2004; Petrovsky & Ellwood, 1999), thus these outcrops must be washed up or avoided. Hand ornamental jewellery (rings, pins, arm rings, etc.) may have a significant impact in the measurements (Fig. 2.3.6), and they should be removed during the measuring. Rock hammers and some metal and technical instruments may also affect the readings if they are not far enough from the coils.

Moreover, some issues are not fully solved with regard of the sampling of field susceptibility:

- 1) The **number of data per outcrop** is not fixed, but susceptibility may significantly vary at the outcrop scale (10-25 m<sup>2</sup>). We do not have a guarantee that the minerals responsible for the susceptibility are evenly distributed throughout the rock, especially in igneous rocks such as basalts, the distribution of susceptibility can be very uneven, where magnetite can appear in pockets. In the example below (Maladeta granite), susceptibility in single outcrops may oscillate more than 200 10<sup>-6</sup> SI units in less than 10-15 m<sup>2</sup> (Fig 2.3.6 and Table 2.3.2). The effect of the number of readings was also evaluated (site GM03): mean and mode values were relatively stable from 10 measurements onwards, although the entire range of variability was reached with more than 60 data. Similarly, other statistical parameters were pretty constant as well (standard deviation and error, variance and RMS) except for those related to the geometry of the distribution (skewness and kurtosis indexes) that seem to reach a more stable pattern after 40 readings. This kind of analysis should we performed in a larger outcrop collection considering several lithologies and a wider range of susceptibilities (including the ferromagnetic domain). Meanwhile, and due to the quickness of data acquisition, more than



50 readings are desirable per outcrop. The number of observations can be reduced if larger coils are used since they averaged out a larger rock volume and thus are more robust. In smaller devices (SM20, SM30, KT20 meters) the coils are 5-6 cm in diameter, and averaged out between 35-60 cm<sup>3</sup> of rock volume per measurement but the Bartington's MS2D coil (Ø 19 cm) may average close to 200 cm<sup>3</sup> per measurement (Fig. 2.3.5 and table 2.3.1).



Figure 2.3.5. Some portable magnetic susceptibility meters available in the market. From up left to downright: KT10 and KT20 by Terraplus (this last one with the density upgrade), SM20 by GF Instruments, SM30 by ZH Instruments, RT-1 (former by Fugro and by CorMaGeo) now by Bartington and the MS3 multi sensor susceptibility unit with a MS2D surface coil by Bartington.



**Maladeta granite susceptibility measurements; Statistics per outcrop**

Site	n	Min	Max	Mean	Median	RMS	Std Dev	Variance	Std Error	Skewness	Kurtosis
GM-01	42	12	205	106,38	96,00	114,09	41,72	1740,44	6,44	0,41	-0,21
GM-02	60	2	190	95,13	100,00	106,12	47,42	2248,90	6,12	-0,19	-0,81
GM-03	93	41	318	196,04	197,00	207,55	68,52	4695,24	7,11	-0,36	-0,63
GM-04	44	125	315	240,02	238,50	243,46	41,25	1701,51	6,22	-0,49	-0,08
GM4-Ring	28	4	193	56,50	45,00	72,69	46,57	2169,07	8,80	1,58	2,00
GM-05	35	61	267	182,97	183,00	188,31	45,16	2039,26	7,63	-0,28	-0,14
GM-06	68	47	263	144,07	143,50	150,84	45,01	2026,25	5,46	0,12	-0,20
GM,07	56	34	212	117,16	120,00	123,72	40,11	1609,08	5,36	-0,22	-0,38
GM-08	34	63	262	131,18	125,00	138,93	46,44	2156,94	7,96	0,60	0,30
GM-09	46	25	211	116,93	116,50	124,22	42,38	1795,93	6,25	-0,12	-0,38
GM-10	53	38	297	172,23	170,00	185,15	68,60	4705,72	9,42	-0,10	-0,79
GM10-Hammer	54	43	302	169,94	159,00	183,74	70,50	4970,02	9,59	0,25	-1,01
GM-11	70	23	4100	705,09	351,00	1102,65	853,88	729103,67	102,06	2,01	4,00
GM-12	67	2	203	65,88	57,00	79,59	45,00	2025,32	5,50	1,08	0,91

Table 2.3.2. Statistics of granite outcrops (Maladeta massif). Data taken with a SM20 susceptometer.

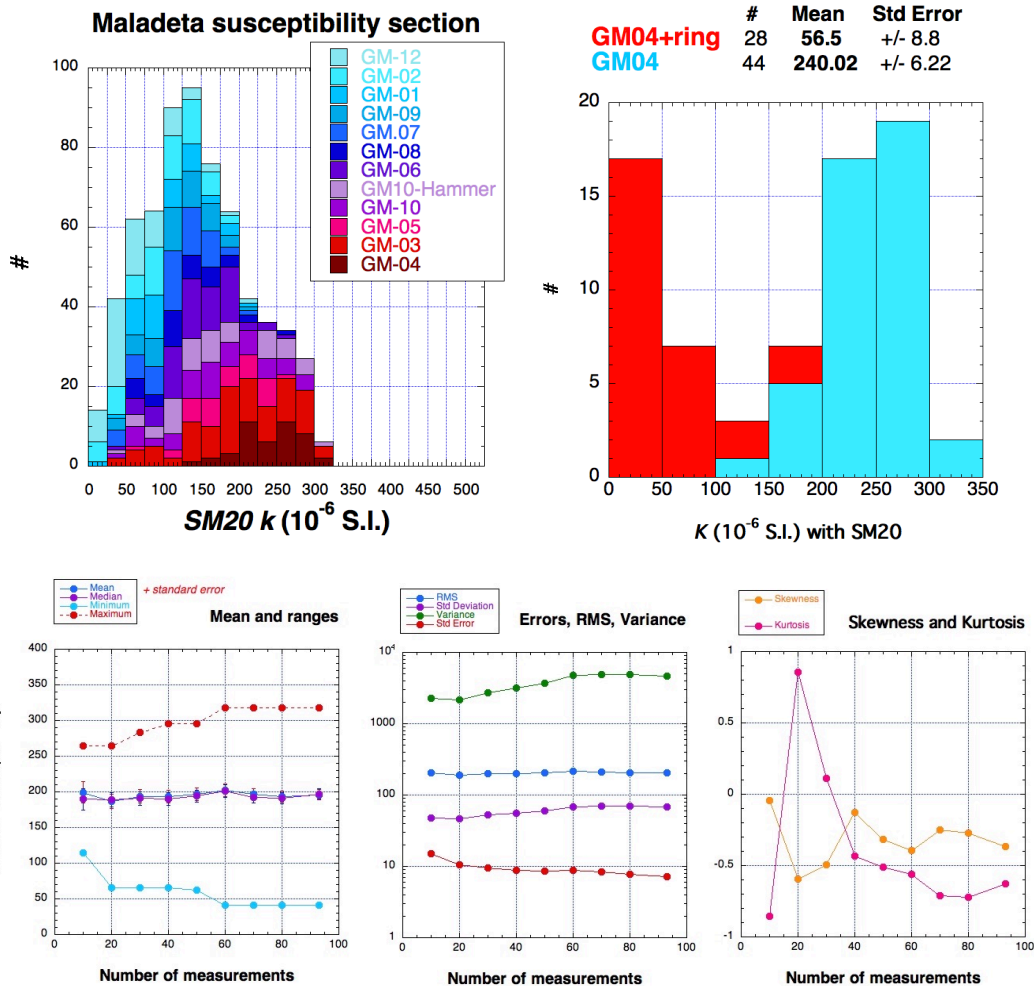


Figure 2.3.6. Natural magnetic susceptibility variability at the outcrop scale. In the Maladeta granite 12 outcrops were densely measured with a SM20 meter and more than 50 measurements were taken in average (and up to 90 in some cases). All measurements fell in the paramagnetic domain ( $< 300 \cdot 10^{-6} \text{ SI}$ ). Individual sites may easily cover a wide range about  $200 \cdot 10^{-6} \text{ SI}$ . Right plot- Same outcrop (GM04) using and not ornamental jewellery (golden ring). Lower row: evolution of statistical parameters as a function of the number of measurements (site GM03).



2) Comparison of data coming from different instruments is not straightforward (Fig. 2.3.7) and therefore, calibration with standard and widely used laboratory instruments (for example the Bartington installed in the Geotek system (<https://www.geotek.co.uk/products/mscl-s/>) or the very common AGICO susceptibilimeters (<https://www.agico.com/>) must be done providing the same frequency conditions. Susceptibility may be a function of measurement frequency depending upon the occurrence of superparamagnetic minerals and not all the portable devices measure at the same value (Table 3.3.1 and Fig. 2.3.5), thus this issue must be always kept in mind. Similarly, and for the same reason, an intercalibration of portable devices must be also done if different susceptometers were used in the same project.

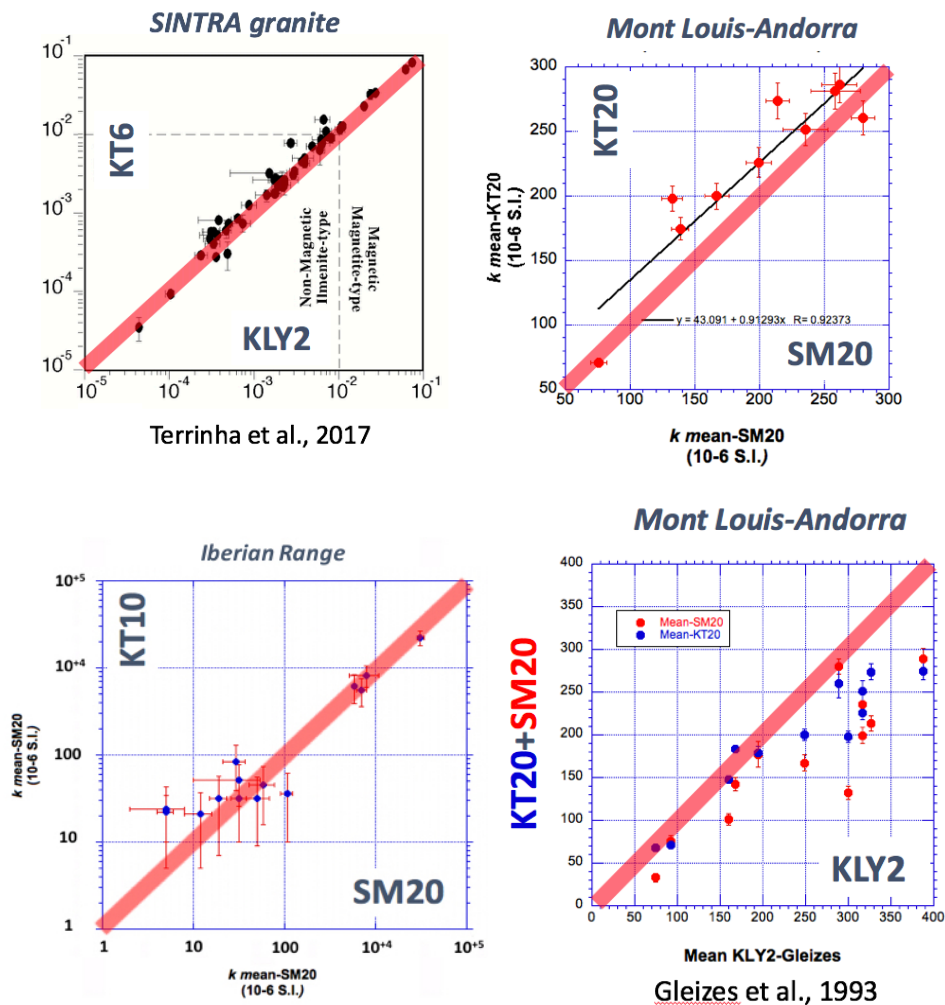


Figure 2.3.7. Intercalibration of susceptibility measurements taken from different portable devices in Iberian granites (Sintra by Terrinha et al., 2018; Mont Louis Andorra by Gleizes et al., 1993; Pueyo et al., 2021) and in the Iberian Ranges (right; data by Izquierdo-Llavall et al., 2019).



### 2.3.2.2 Laboratory procedures

#### Density estimation by Archimedes principle:

Standard density estimates in the laboratory can be determined by several methods (Olhoeft and Johnson, 1989) but most utilized ones are the liquid displacement and buoyancy methods based on the Archimedes's principle (On Floating Bodies, c. 246 BC). "An object immersed in a fluid experiences a buoyant force that is equal in magnitude to the force of gravity on the displaced fluid".

The apparent sample density ( $\rho$ ) is defined as sample mass ( $m$ )/sample volume ( $v$ ). The simplest procedure starts drying and weighting the sample ( $m_1$ ), thus we first need to estimate the last variable; the sample volume. A common procedure for estimating the dry bulk density usually will coat the sample surface with paraffin to avoid the water penetration during the immersion due to the, never negligible, rock effective porosity. Therefore, to know the actual volume of the samples three weighings are necessary:

$m_1$ : sample weight,

$m_2$ : weight of sample+ paraffin and

$m_3$ : sample weight after the immersion in water.

Then, the paraffin weight in the sample is  $m_2 - m_1$

and the paraffin volume = paraffin mass / paraffin density ( $\rho_p$ )

where the paraffin density ( $\rho_p$ ) must be known from technical specifications or estimated by weighing a known volume (usually around  $0.80 \text{ gr} / \text{cm}^3$ )

On the other hand, the weight of the dislodged water is =  $m_2 - m_3$

(distilled water has a known density in standard ambient conditions =  $1 \text{ gr} / \text{cm}^3$ )

The volume of dislodged water =  $(m_2 - m_3) / 1$

and the sample + paraffin volume =  $m_2 - m_3$

Thus, the sample volume = paraffin sample volume - paraffin volume

and therefore:  $\rho = m_1 / ((m_2 - m_3) - [(m_2 - m_1) / \rho_p])$



Figure 2.3.8. Density calculation using the Archimedes principle in the laboratory (Geotransfer Research Group UZ/IGME Associated Unit). A) fragments of different types rocks to be measured, B) Kappabridge KLY-3S (AGICO Inc., Czech Republic), C) Precision scale (COBOS) and device for submerged weighing, D) Samples at the time of waxing. The advantage of these sample sizes is the later fitting in the sample beaker of the AGICO susceptibilimeter (around 90 cm<sup>3</sup>). Similarly happens with standard paleomagnetic specimens (see next section) or with borehole core samples (Andersen et al., 2013).



Figure 2.3.8 (cont). Cutting hand samples and pressurized chamber at IGME laboratories (Madrid).



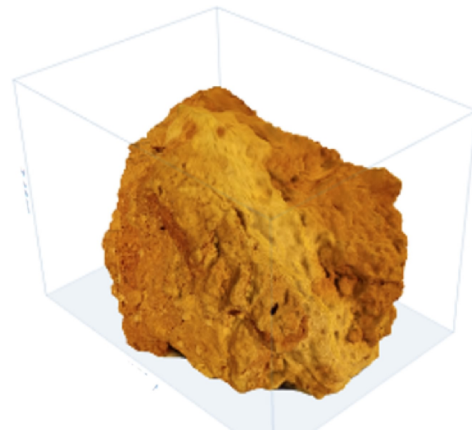
This simple procedure can be applied almost to any size of hand sample (Fig. 2.3.8.). However, regular samples may help to alternatively estimate the rock volumes and more refined procedures are defined and normalized. Apparent density estimations at IGME laboratories (Tres Cantos, Madrid) follow the standard norm UNE-EN 1936: 2007 (equivalent to the European standard UNE EN 1936:2006 Natural stone test methods - Determination of real density and apparent density, and of total and open porosity [CEN/TC 246 - Natural stones; CEN/TC 246/WG 2 - Test methods]) with some minor variations: irregular specimens may be also measured, although regular cubes or cylinders are very often used (0.3 and 0.6 kg). There is no minimum of six specimens per sample/outcrop. Rounding at 10 kg / m<sup>3</sup> is not considered. The specimens must have an apparent minimum volume of 60 ml, and their surface/volume ratio must range between 0.08 and 0.20 mm<sup>-1</sup> (although this is difficult to estimate in irregular samples).

In the laboratory, the specimens are first dried in an oven at 70 ± 5°C until a constant mass ( $m_D$ ) is achieved, the difference between two consecutive weighing carried out after 24 hours must be lower than 0.1% of the initial mass (this mass will allow also obtaining the dry bulk density). Then, the specimens are subjected to a vacuum of 2.0 (± 0.7 kPa) for 2 (± 0.2) hours. Demineralized water is added without losing the vacuum slowly, so that the samples are submerged more than 15 minutes. The water temperature should be 20 ± 5 ° C. Atmospheric pressure is slowly restored and the samples are left 24 (± 2) additional hours in water. Then, we proceed to the weighing of the specimens immersed in a hydrostatic balance ( $m_H$ ) and subsequently dried with a damp cloth, and its saturated mass is determined ( $m_S$ ).

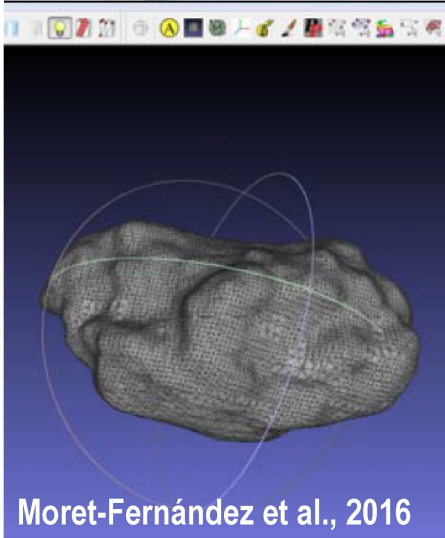
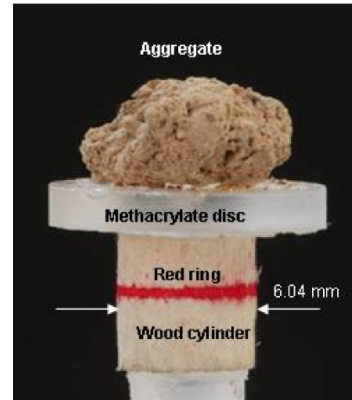
Then the apparent (saturated) density is:

$$\rho = \rho_W \cdot m_D / ([m_S - m_H])$$

where  $\rho_W$  is the density of distilled water at 20°C: 988 kg/m<sup>3</sup>



Whiting et al., 2020



Moret-Fernández et al., 2016

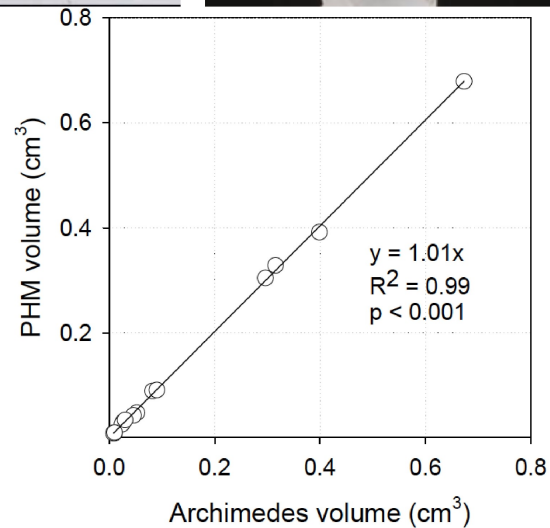


Figure 2.3.9. Volume estimation by photogrammetric methods (Moret-Fernández et al., 2016 and Whiting et al., 2020). Comparison of density determinations (bottom right) between the photogrammetric method and that of Archimedes (Moret-Fernández et al., 2016).



---

### **Volume estimation by photogrammetric and laser-scan techniques:**

On the other hand, during the past few years, some smart solutions have recently been launched that allow the determination of the volume of irregular samples using photogrammetric and laser scanning techniques. These applications, which can even be implemented in smart-phones, have been developed by soil science (Stewart et al., 2012; Moret-Fernández et al., 2016; Whiting et al., 2020) and could be easily adaptable to petrophysics focused on the modeling of the gravimetric signal. The degree of correlation between the volumes obtained photogrammetrically and those derived from the application of the Archimedes method is excellent (Figure 2.3.9) and the apparent disadvantage of the small volume could be easily solvable by including a larger number of samples. The great advantage of these techniques is their speed in determining density, which could open up the possibility of mass data acquisition.

### **Magnetic susceptibility and natural remanence estimations:**

Magnetic susceptibility ( $\kappa$ ) is the ratio between the induced magnetization ( $M$ ) and the external magnetic field ( $H$ ). It is a tensorial property of the matter (usually represented by the three principal axes of the ellipsoid) and it is dimensionless in the S.I. system ( $\kappa = M/H = A/m/A/m$ ). There is a large variety of susceptibilimeters, although most common ones for rock samples hosted in paleomagnetic, magnetic fabrics and petrophysical laboratories are manufactured by the AGICO, Bartington companies. The KLY-x family (started by Geophysika Brno with models 1 to 3, and then by AGICO Ltd.), is likely the most popular laboratory instrument for measuring the magnetic susceptibility in standard paleomagnetic samples (Fig, 2.3.10).

The main advantage of these instruments, especially the latest models by AGICO (KLY5 and MFK2 models measuring at 1,22 kHz) is the larger resolution and sensitivity up to  $2 \times 10^{-8}$  SI (for field 400 A/m) and measuring range up to 1 SI. The lower range is very critical when measuring in the diamagnetic/paramagnetic boundary. The main drawback is the volume limitation (maximum  $40 \text{ cm}^3$  for bulk susceptibility in the beaker holder). The MS3 Bartington sensor has a lower sensitivity (resolution to  $2 \times 10^{-6}$  SI) but a higher range (up to 26 SI) which affects very seldom to ferromagnetic rocks.



*Figure 2.3.10. Magnetic susceptibility meters for the laboratory. KLY3 at Magnetic fabrics laboratory (U. Zaragoza). The recent KLY-5 and MFK2 models, all of them by AGICO. The Geotek Multi-Sensor Core Logger (MSCL-S) can be equipped with a loop sensor (MS2C, enlarged) and a point sensor (MS2E) that are paired to the Bartington MS3 meter with a measuring range of 26 SI.*

### 2.3.2.3 Paleomagnetic samples

Paleomagnetic sampling is very often performed using drilling machines to sample the rock cores that are later oriented with a special compass (Butler, 1992) (Fig. 2.3.11). There are many different sampling strategies depending upon the project goal, but very frequently, tectonic studies used to define sites/localities in outcrops of few squared meters. Sites usually consist in an even distribution of 10-15 cylindrical cores (2,5 cm  $\varnothing$  and 5-10 cm in length) spread out along an outcrop, or slightly less in AMS studies of igneous rocks (Pueyo et al., 2004 and 2016b).



The outcrop is lithologically homogeneous in a variable surface, but typically comprises 10-15 meter of stratigraphic sections or about 20-40 m<sup>2</sup> in igneous rocks (Fig. 2.3.12) (Olivier et al., 1997), although depending on the outcrop and vegetation conditions of the area, sometimes you have to settle for less, prioritizing in these cases a regular spatial distribution of the sampling sites. Cores are cut in standard samples ( $\approx 10 \text{ cm}^3$ ; 2.1-2.2 cm height and  $\varnothing 2.5 \text{ cm}$ , Fig. 2.3.13) in the laboratory and the natural remanent magnetization (NRM) and magnetic susceptibility ( $k$ ) is normally measured in all of them. Similarly, it may happen with core samples from boreholes, independently if they are used for paleomagnetism (Bleakly et al., 1985) or other purposes (Andersen et al., 2013)



Figure 2.3.11. Paleomagnetic sampling and orientation of samples (cores) with a solar and magnetic compass.



These samples have a high added value for petrophysical investigations (Enkin, 2014 & 2018; Enkin et al., 2007, 2012, 2020) since density can be rapidly obtained (geometrically and/or by Archimedes principle), and the final set of specimens includes a large collection of 15-20 samples (sometimes more) representing the outcrop natural variability and comprising all three main variables needed in potential field geophysics investigations; natural remanent magnetization (NRM), magnetic susceptibility ( $k$ ) and density ( $\rho$ ). The Canadian Petrophysical database (Enkin, 2014 & 2018) has been significantly enriched by the measurement of the large collection of samples available in the Paleomagnetism and Petrophysics Laboratory archive that were collected for paleomagnetic studies since the 70's.



*Figure 2.3.12. Typical paleomagnetic outcrops in tectonic studies. Standard paleomagnetic cores are 2,5 cm in diameter ( $\emptyset$ ).*

In the case of southwestern Pyrenees, the Marboré calcarenite and the Zuriza marls Fms. are Upper Cretaceous (Maestrichtian) rocks from the Internal Sierras. There have been several paleomagnetic studies in these rocks to characterize both the rotational kinematics of this structural unit (Larra system) but also because of the occurrence of a pervasive remagnetization caused by progressive burial diagenesis (Oliva-Urcia et al., 2008; Izquierdo-Llavall et al., 2015). In the following example we illustrated the potential of paleomagnetic samples to derived robust averages of all the petrophysical variables involved in potential field exploration (NRM,  $\kappa$  and  $\rho$ ).



Figure 2.3.13. Paleomagnetic cores, standard specimens and orientation convention (Bouchez, 1997). Cores sampled in a standard paleomagnetic site. Granite standard specimens (25 mm  $\varnothing$  and 22 mm in height).

Some outcrops were densely sampled for a detailed magnetic sub-fabrics study (Oliva-Urcia et al., 2009) and allow us to illustrate the variability of Marboré Fm, and its usefulness to derive the three main petrophysical variables in potential field geophysics (Figure 2.3.12 and table 2.3.3). Density (geometric volume determination) and magnetic susceptibility (KLY-2 in the laboratory) were measured in more than 25 specimens per site; an averaged out density (nine sites) of  $2.651 \pm 0.142 \text{ g/cm}^3$  ( $\approx 5\%$ ) and susceptibility of  $218.5 \pm 49.8 \cdot 10^{-6} \text{ S.I.}$  ( $\approx 22\%$ ), within the paramagnetic domain (Pueyo Anchuela et al., 2013a), although at the site scale (table 2.3.3) the standard deviation hardly exceed 4% for the density, and is usually below 15% for the susceptibility. The NRM displayed a slightly lower variability than the susceptibility ( $251 \pm 8.1 \cdot 10^{-6} \text{ A/m}$ ;  $\approx 3\%$ ).

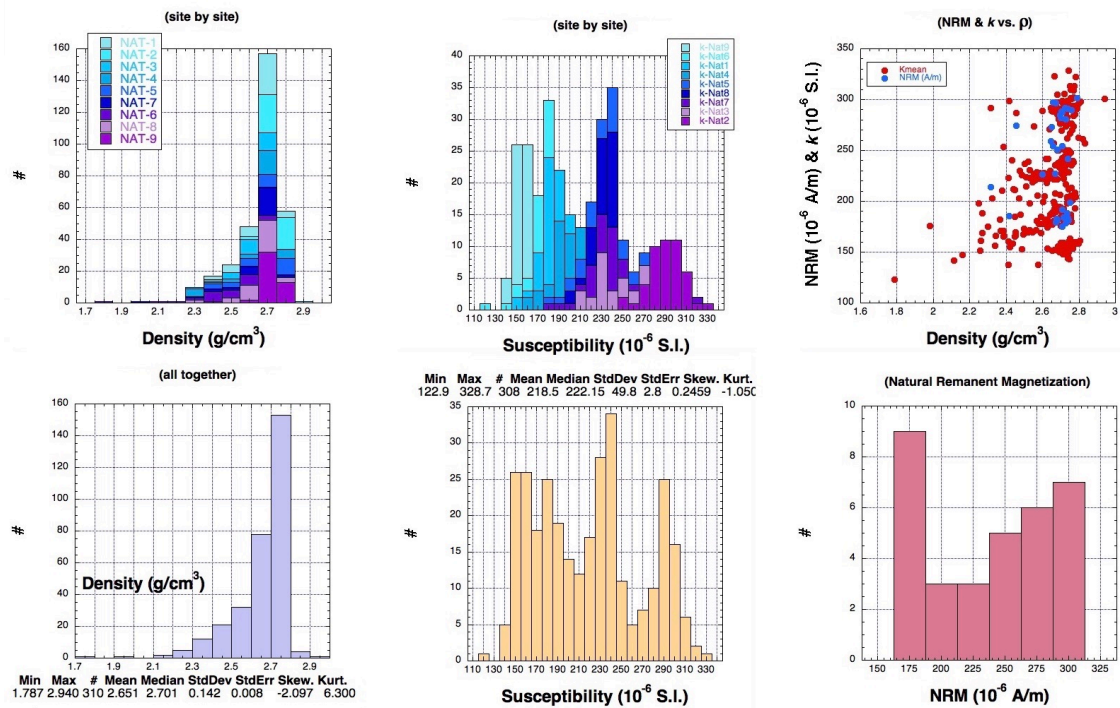


Figure 2.3.14. Petrophysical data in nine paleomagnetic and AMS sites of the Western Pyrenees. Data belong to the Marboré calcarenite Fm. and Zuriza marls Fm. (Oliva-Urcia et al., 2009). Upper pictures correspond to sites NAT1, 2 and 3 (left) and site NAT-5 (right). All petrophysical variables were profusely characterized in all sites; NRM,  $\kappa$  and  $\rho$ .

Density determination from paleomagnetic samples are very often based on the measuring of the geometry of the standard cylindrical specimens. For that purpose, only regular (cylindrical sections) and complete samples (whole, unbroken, etc.) can be used. Any broken, incomplete, irregular or cracked specimen must be ruled out. Apart from the weighting of the sample (m),



the maximum and minimum diameters ( $\varnothing$ ) and heights of the specimen (H) are measured with a Vernier caliper. Afterwards both measurements are averaged out ( $\varnothing_m$  and  $H_m$ ). Thus, the volume can be rapidly calculated:  $V = \pi (\varnothing_m / 2)^2 \cdot H_m$ , as well as the density  $\rho = m / (\pi [\varnothing_m / 2]^2 \cdot H_m)$

Site	Variable	n	Min	Max	$\Delta$	Mean	Median	RMS	Std Dev	Variance	Std Error	Skewness	Kurtosis
NAT1	$\rho$	42	2,416	2,78	0,364	2,659	2,691	2,66	0,099	0,01	0,015	-1,081	0,082
	$\kappa$	40	153,1	298,5	145,4	210,5	183,3	216,7	51,8	2687,3	8,2	0,876	-0,930
	NRM	12	175,2	198,9	23,7	184,3	183,2	184,4	6,4	40,8	1,8	0,928	0,454
NAT2	$\rho$	47	2,385	2,94	0,555	2,730	2,738	2,731	0,076	0,006	0,011	-1,857	8,693
	$\kappa$	47	249,9	328,7	78,8	289,8	288,5	290,3	16,3	266,4	2,4	-0,051	0,154
	NRM	11	280,4	301,6	21,2	290,0	289,3	290,0	6,5	42,8	2,0	0,254	-0,835
NAT3	$\rho$	25	2,316	2,738	0,422	2,604	2,623	2,606	0,104	0,011	0,021	-0,939	0,481
	$\kappa$	25	205,3	292,0	86,7	254,8	243,7	256,7	32,0	1023,9	6,4	0,054	-1,702
	NRM	10	213,7	274,6	60,9	247,5	252,5	248,2	20,1	404,7	6,4	-0,260	-1,012
All 9	$\rho$	310	1,787	2,94	1,153	2,651	2,701	2,655	0,142	0,02	0,008	-2,097	6,300
	$\kappa$	308	122,9	328,7	205,8	218,5	222,2	224,1	49,8	2483,3	2,8	0,246	-1,050
	NRM	33	175,2	301,6	126,4	238,7	251,0	243,0	46,7	2179,3	8,1	-0,113	-1,647

Table 2.3.3. Statistics of petrophysical variable of Marboré calcarenites (data compiled and reworked from Oliva-Urcia et al., 2008 & 2009). Units; NRM in  $10^{-6}$  A/m,  $\kappa$  in  $10^{-6}$  S.I. and  $\rho$  in  $g/cm^3$ .

	$\rho$	Min	Max	Mean	Median	RMS	Std Dev	Variance	Std Error	Skewness	Kurtosis
Archimedes	2.435	2.974	<b>2.709</b>	2.709	2.709	<b>0.046</b>	0.002	0.002	0.005	-0.256	25.854
Geometry	2.466	3.249	<b>2.674</b>	2.672	2.675	<b>0.079</b>	0.006	0.006	0.009	4.757	33.849
Difference	-0.530	0.362	<b>0.035</b>	0.038	0.097	<b>0.090</b>	0.008	0.008	0.010	-2.705	20.083

Table 2.3.4. Statistics of mean petrophysical density data of the Hecho Group turbidites without using paraffin and based on the geometric determination of the rock volume of AMS samples (units  $\rho$  in  $g/cm^3$ ).

However, a note of caution must be stated. In those samples in which standard procedures (Archimedes with and without paraffin) and geometric determinations of the sample volume were performed, an underestimation of the density was obtained from the geometric method. South of the Internal Sierras, in the Jaca Turbiditic Basin, 82 samples from 22 different paleomagnetic sites (flysch facies) were measured in the laboratory with geometric and Archimedes methods (without paraffin) (Table 2.3.4 and figure 2.3.15). The mean difference between both densities is 1.3% +/-3%, which certainly can be assumed during the modeling. However extreme values were also found; between - 20% and +13%. In any case, the sharpness



of the distributions (high Kurtosis positive values) allow us to be confident if a large collection of samples is measured independently of the method.

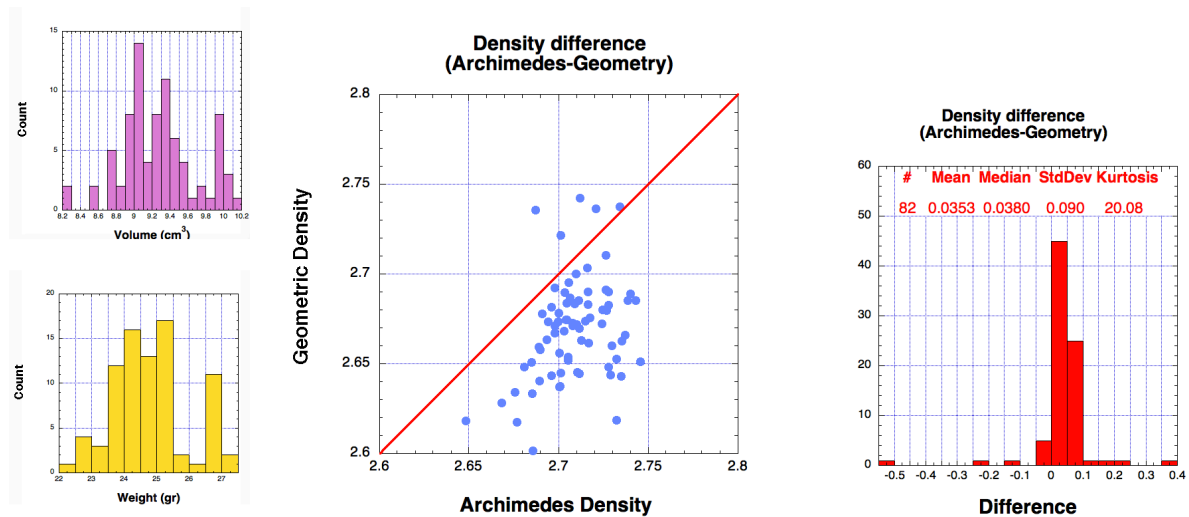


Figure 2.3.15. Comparison of density determinations by Archimedes's principle and by geometric measurements of standard paleomagnetic samples (cylinders).

$\rho$	Min	Max	Mean	Median	RMS	Std Dev	Variance	Std Error	Skew	Kurtosis
W/o Paraff.	2.605	2.973	<b>2.707</b>	2.698	2.708	<b>0.074</b>	0.005	0.007	1.495	2.789
With Paraff.	2.577	2.946	<b>2.693</b>	2.689	2.694	<b>0.074</b>	0.005	0.007	1.218	2.023
$\Delta w$ & w/o	-0.052	0.048	<b>-0.014</b>	-0.014	0.019	<b>0.012</b>	0.000	0.001	0.593	7.582
Geometric	2.474	2.880	<b>2.651</b>	2.655	2.652	<b>0.078</b>	0.006	0.007	0.448	0.464
$\Delta w$ & G	0.002	0.189	<b>0.042</b>	0.035	0.051	<b>0.028</b>	0.001	0.003	1.969	6.278
$\kappa$ 10-6 S.I.	27.0	535.0	<b>231.5</b>	227.0	263.4	<b>126.2</b>	15932	12.260	0.264	-0.730

Table 2.3.5. Statistics of mean petrophysical density data of the Marimanha granite (Loi et al., 2019) without and with using paraffin as well as the geometric determination of the rock volume of AMS specimens (units  $\rho$  in  $g/cm^3$ ).

A more complete analysis was carried out by Loi et al. (2019) in the Marimanha calc-alkaline Carboniferous granites from the Pyrenean Axial Zone (Antolín et al., 2009; Oliva-Urcia et al., 2012) to the North of the Internal Sierras, also in the Western Pyrenees (Table 2.3.5 and Figure 2.3.16). Density measurements were carried out using the three procedures; Archimedes with and without paraffin and also the geometric method in “perfect” samples. In total 111 specimens were measured. Again, the geometric method seems to underestimate the rock



density by <2%. The use or not of paraffin implies differences below 1% but this is very likely caused by the very low effective porosity of the granites.

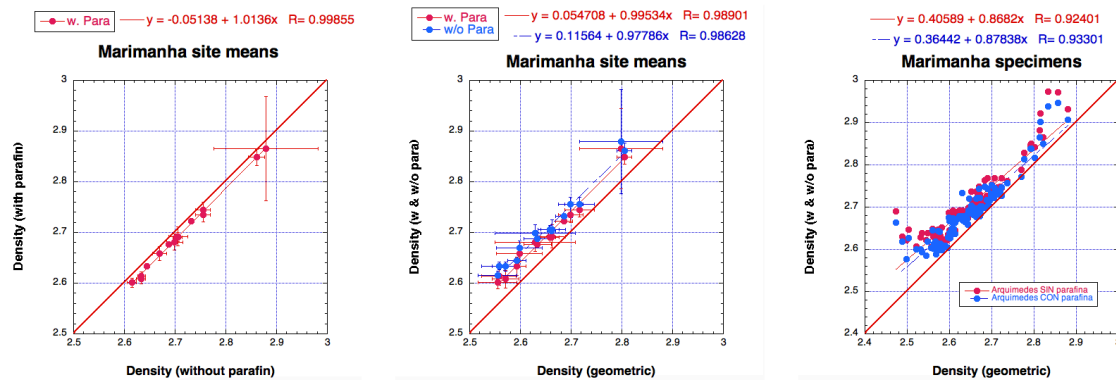


Figure 2.3.16. Comparison of density determinations by Archimedes' principle and by geometric measurements of standard paleomagnetic samples (cylinders)- Marimanha granite (data reworked from Loi et al., 2019).

In all introduced examples, as well as in similar cases from the bibliography (Enkin, 2018), the use of paleomagnetic standard specimens is a very suitable way to obtain petrophysical data in a quick and cost effective manner. The handicap of the small sample volume is clearly compensated by the large number of samples normally available in paleomagnetic sites. Besides, all three key petrophysical variables used for the modelling of potential field geophysics are obtained in the same rock volume with very robust statistical parameters.

### 2.3.2.4 Data representation and characterization

Petrophysical data are usually described and characterized in some scientific papers and technical reports as distribution histograms and/or tables displaying the statistical information (which should be as complete as possible; Fig 2.3.17). Dentith et al. (2020) encourage the publication of the frequency histograms and the probability density curves as well as the box-and-whisker plots. Respect to the numerical data, apart from the mean and median as well as classic scattering parameters (standard error and deviation, variance and RMS), parameters on the shape (geometry) of the distribution (for example Skewness and Kurtosis) should be provided for further evaluation of the petrophysical data.

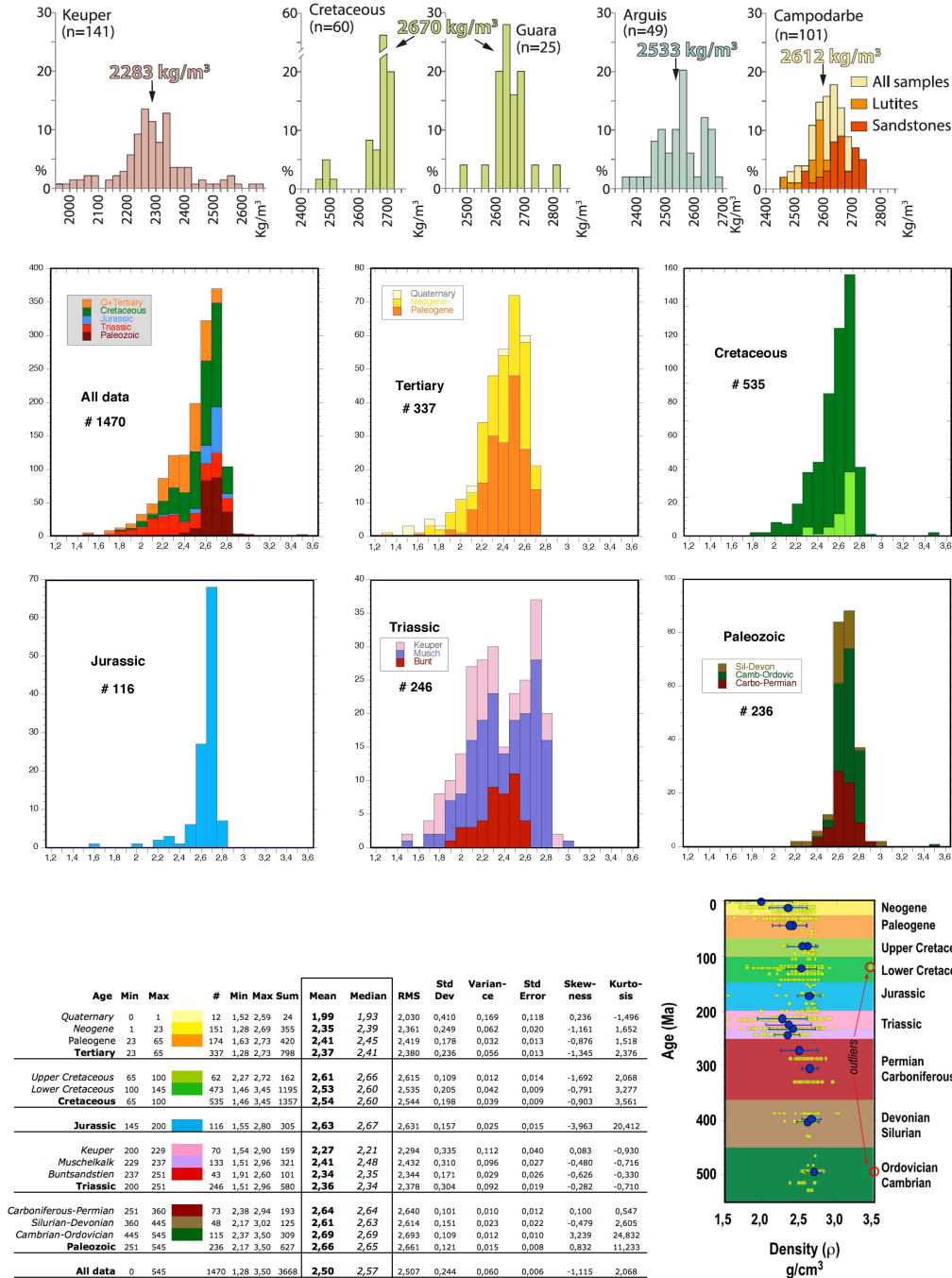


Figure 2.3.17. Density data characterization. Upper row; data from the Santo Domingo Anticline (Southwestern Pyrenees) where lithologies (formations) were treated separately (Calvin et al., 2018). The rest of data in this figure belong to the Iberian Range and southern Ebro Basin database (Pueyo et al., 2016a) and only an age grouping was possible considering the large variability of lithologies considered.



Skewness informs about the symmetry and measures the relative size of the two tails of the distribution. A normal distribution (perfectly symmetrical) displays a null (0) skewness index. Any positive skewness indicates an unbalancing of the right-handed part of the distribution which is larger than the left one and the other way around for negative indexes. Density data distributions are typically negative for this index (but not only). On the other hand, the Kurtosis parameter measures the peakedness or flatness of the distribution and thus the relative influence of the two tails. A normal distribution displays a value = 3; then, Kurtosis > 3, implies a sharp distribution with longer tails and accordingly Kurtosis < 3, shorter tails (less in the tails). The magnitude of the Skewness and Kurtosis indexes are strongly dependent upon the number of measurements and thus, they must be taken with caution.

All statistical parameters are critical to evaluate the petrophysical information during the modelling and to constrain the density values assigned to the rock volumes (e.g. mean or mode and their assumed variability; standard deviation). As long as we have a sufficient (large) number of data, the density for a given rock type and age very often displays a pseudo-normal probability distribution. However, meteorization uses to reduce the density of surficial rock and it is responsible for a pretty typical asymmetry of the histogram and a negative skewness index (see some examples in fig. 2.3.17) and this must be taken into account.

The degree of grouping of the data and how this grouping is carried out depend upon the project goals. Therefore, sometimes the data are merged by lithology and/or age, sometimes the entire data from a modelled volume may integrate all data together independently of ages and lithologies. Ideally, the data should be divided considering both criteria but an equilibrium between the number of data and data representativeness must be matched, and unfortunately, only very detailed information can be currently provided from very advanced databases (Enkin, 2018). Apart from the density versus depth data derived from borehole logging (see section 2.3.4.2), the construction of artificial pseudo-logs plotting all available data are very informative and are not infrequent (Fig 2.3.17).



### 2.3.3 Well Logging data

As in all geophysical methods, well logging techniques are based on physical principles and a number of assumptions necessary for the processing and interpretation of the actual nature of the formation rocks (following the reservoir semantics) from the data received in well sensors. For rock bulk density determination there are two main “direct” methods, the formation density log and the gravimetric log. We also consider here density determination using dual-CT (Computer Tomography) scanning of core samples. Other density values, like the apparent matrix density, can be also indirectly derived from other logs (sonic log, neutron logs, etc.) if some assumptions are taken and some theoretical and/or empirical functions are applied (v.g. Gardner et al., 1974), but are not here considered. For further readings of updated overviews, we here refer to classic works (Asquith and Gibson, 1982; Glover, 2000; Asquith et al., 2004; Zinszner & Pellerin, 2007), or recent petrophysical manuals (Cannon, 2015; Tiab & Donaldson, 2016; Yang & Wei, 2017; Liu, 2017).

#### 2.3.3.1 Formation density log

The *formation density* log (FDL), also known as gamma-gamma log ( $\gamma$ - $\gamma$ ) or bulk density log, estimates the bulk density of the formation, that is the actual density of the rock volume. Since this volume also contains fluids and gases it can be useful to derive the total porosity of the formation, the occurrence of gas and fluids, etc. For practical reasons, the direct calculation of the formation density from the gamma-gamma ray log is a perfect estimate for gravimetric modeling. FDL uses a radioactive source to emit the gamma rays, unlike the gamma log alone that measures natural radioactivity of the formation rocks (gamma rays coming from natural decay of K, U and Th radioactive isotopes present in the rocks).

**Gamma-rays** have the shortest wave lengths ( $10^{-11}$ ,  $10^{-12}$  m) and the highest frequencies and energy ( $11^{19}$ - $10^{20}$  Hz) of the electromagnetic spectrum and therefore, the highest penetration in matter (but also the highest absorption). Gamma radiation ionizes matter via three processes: The Compton scattering (after Compton, 1923), the photoelectric effect and the pair production. Gamma-ray scattering and absorption as a function of the rock bulk density are used in density logging by the oil industry since the 50’s (see very early reviews by Pickell & Heacock, 1960; Wahl et al., 1964 and Tittman & Wahl, 1965). The basic concept is bombarding the formation



with a stream of gamma rays (either from  $^{60}\text{Co}$  or from  $^{137}\text{Cs}$  [being this last one more sensitive to borehole temperature]), and measuring the intensity of the back-scattered radiation (the rest would be absorbed by the formation). This kind of interaction (the one it can be measured) is the Compton scattering, represents the interaction with electrons and thus, is proportional to the electron density of the rock formation ( $\rho$ ). In a material of atomic number  $Z$ , atomic weight  $A$  and density  $\rho$ , the number of electrons per volume is equal to  $N(Z/A) \rho$ , being  $N$  the Avogadro's number. Since in most common rock forming elements, the  $Z/A$  ratio can be considered constant (0.5) then, the so called Compton scattering is a direct function of the rock (bulk) density. The practical interpretation of gamma ray logs actually follows the reverse relationship; the greater the degree of Compton scattering implies a higher density of the formation but the lower response at the detector. The other two kind of interactions (photoelectric absorption and pair production) are considered negligible (or corrected) in most cases.

$$n_e = \frac{N Z}{A} \rho_b$$

The electron number density is:

where:  $n_e$  = density of electrons in the substance (number of electrons/cm<sup>3</sup>)

$N$  = Avogadro's number ( $6.022 \cdot 10^{23}$ )

$Z$  = Atomic number (no units)

$A$  = Atomic weight (g/mole)

$\rho_b$  = the bulk density of the material (g/cm<sup>3</sup>).

Element	Z/A ratio	Na	0.47845	S	0.499
H	0.99215	Mg	0.4936	Cl	0.4795
C	0.4995	Al	0.4818	K	0.4859
O	0.5	Si	0.49845	Ca	0.499

Table 2.3.6. Z/A ratios of most frequent rock forming chemical elements.

Main sources of errors and uncertainty related to the estimation of rock density from gamma rays were early identified (Pickell and Heacock, 1969), and they have to do with:

- 1) The instrument calibration with known samples,
- 2) The borehole roughness (because it produces variations of the drilling mud thickness),



3) The occurrence of natural gamma radiation of some rock type (usually affecting less than 2% of cases),

Mineral	Composition	Actual rock		Effective Electron density $\rho_e$	Apparent bulk density		Error $\rho_b - \rho_a$	Error %
		density $\rho_b$	Z/A		$\rho_a$			
Quartz	SiO <sub>2</sub>	2,654	0,999	2,650	2,648	0,006	0,23	
Calcite	CaCO <sub>3</sub>	2,710	0,999	2,708	2,710	0,000	0,00	
Dolomite	CaCO <sub>3</sub> ,MgCO <sub>3</sub>	2,870	0,998	2,863	2,876	-0,006	-0,21	
Anhydrite	CaSO <sub>4</sub>	2,960	0,999	2,957	2,977	-0,017	-0,57	
Sylvite	KCL	1,984	0,966	1,916	1,863	0,121	6,10	*
Halite	NaCl	2,165	0,958	2,074	2,032	0,133	6,14	*
Gypsum	CaSO <sub>4</sub> ,2H <sub>2</sub> O	2,320	1,022	2,372	2,351	-0,031	-1,34	
Anthracite-low		1,400	1,030	1,442	1,355	0,045	3,21	
Anthracite-high		1,800	1,030	1,852	1,796	0,004	0,22	
Coal-bituminous		1,200	1,060	1,272	1,173	0,027	2,25	
Coal		1,500	1,060	1,590	1,514	-0,014	-0,93	
Pure Water	H <sub>2</sub> O	1,000	1,110	1,110	1,000	0,000	0,00	
Salt Water	NaCl	1,146	1,080	1,237	1,135	0,011	0,96	
Oil	(CH <sub>2</sub> ) <sub>n</sub>	0,850	1,141	0,970	0,850	0,000	0,00	
Methane	CH <sub>4</sub> <sub>rm</sub>	1,247	1,247 <sub>rm</sub>	1,335 <sub>rm</sub>	0,188	1,059	84,92	*
Gas	C <sub>1,1</sub> H <sub>4,2</sub> <sub>rg</sub>	1,238	1,238 <sub>rg</sub>	1,325 <sub>rg</sub>	0,188	1,050	84,81	*

Table 2.3.7. Comparison of apparent bulk and actual rock densities from most common rock forming minerals Z/A ratios. Errors and % of error are also shown (modified from Glover, 2000).

- 4) The occurrence of minerals where the ratio of the atomic number to atomic weight (Z/A) is non-significant (those containing Hydrogen),
- 5) The logging speed; originally had to be below ≈0,1 m/sg nowadays can be faster,
- 6) The actual volume of the mud cake whose thickness is unknown (but for a long time it is common practice to compensate for the mudcake by using two or more detectors at different spacing's) and,
- 7) Other rock formation properties may influence the final estimate of rock density; formation fluid content; % of saturation, salinity, gas %, oil%. They may account for significant errors in density estimation as a function of rock actual porosity (less porosity -> less influence)

Most of these sources have been amended with technical and methodological developments during the last decades (Fig. 2.3.18). Even the occurrence of Hydrogen bearing minerals (factors 4 and 7), which can be a major cause of deviation of the actual rock density, can be reasonably corrected in combination with neutron logs, reducing this source of uncertainty (Glover, 2000; Cannon, 2015 among others). (See an example of density log in Fig. 2.3.19).

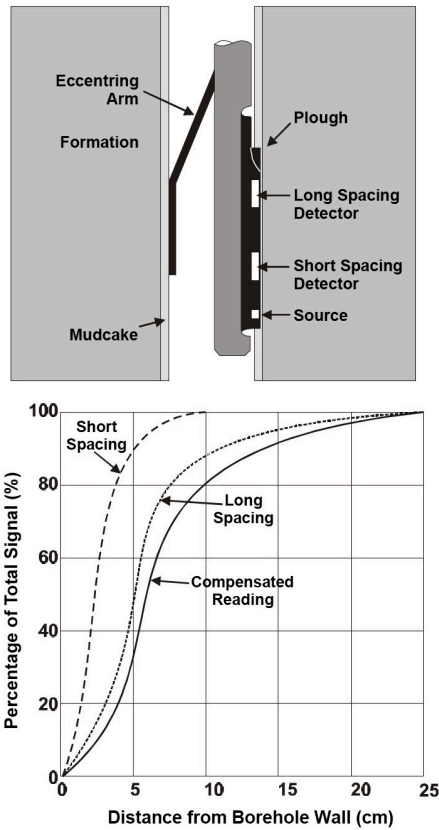


Figure 2.3.18. Schematic diagram of a formation density tool (taken from Glover, 2000)-Compensated formation density logs, an example of which is Schlumberger’s FDC (formation density compensated) tool.

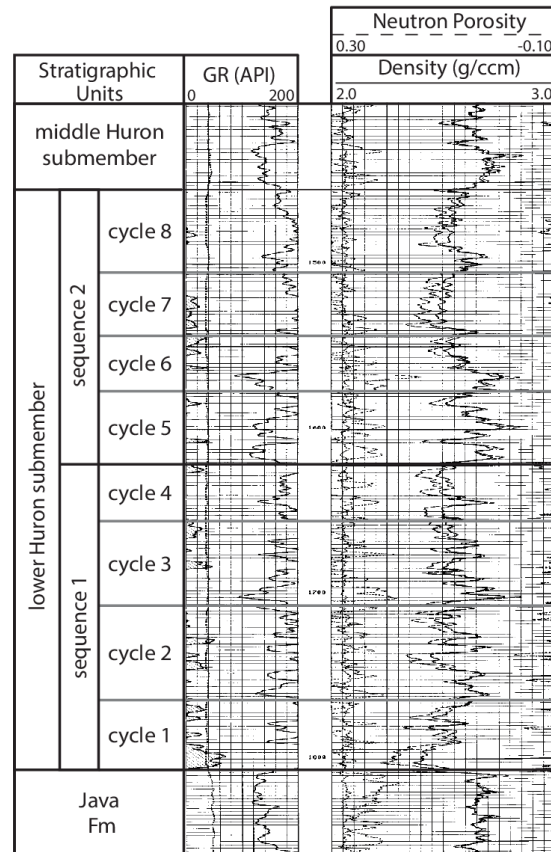


Figure 2.3.19. Example gamma-ray (RG in API), neutron porosity, and bulk density log (g/cm<sup>3</sup>) for the lower Huron sub-member (taken from Waid, 2018).

Another interesting issue is the calibration of density estimates derived from formation density logs and those obtained from core samples following standard laboratory procedures (Fig. 2.3.20). This calibration was very early applied by the oil industry. In fact, densities derived from core samples are not necessarily an absolute standard, basically, and apart from laboratory accuracy (uncertainty is very limited), because of pressure and temperature changes (from in-situ to laboratory conditions) that will probably result in changes of sample density. However; already pioneer studies (Pickell & Heacock, 1960) depicted average deviations of only about 0.03 g/cm<sup>3</sup> (maximum deviations of 0.05 g/cm<sup>3</sup>), and real data rarely exceeds 0.04 g/cm<sup>3</sup> (Minette et al., 1988)

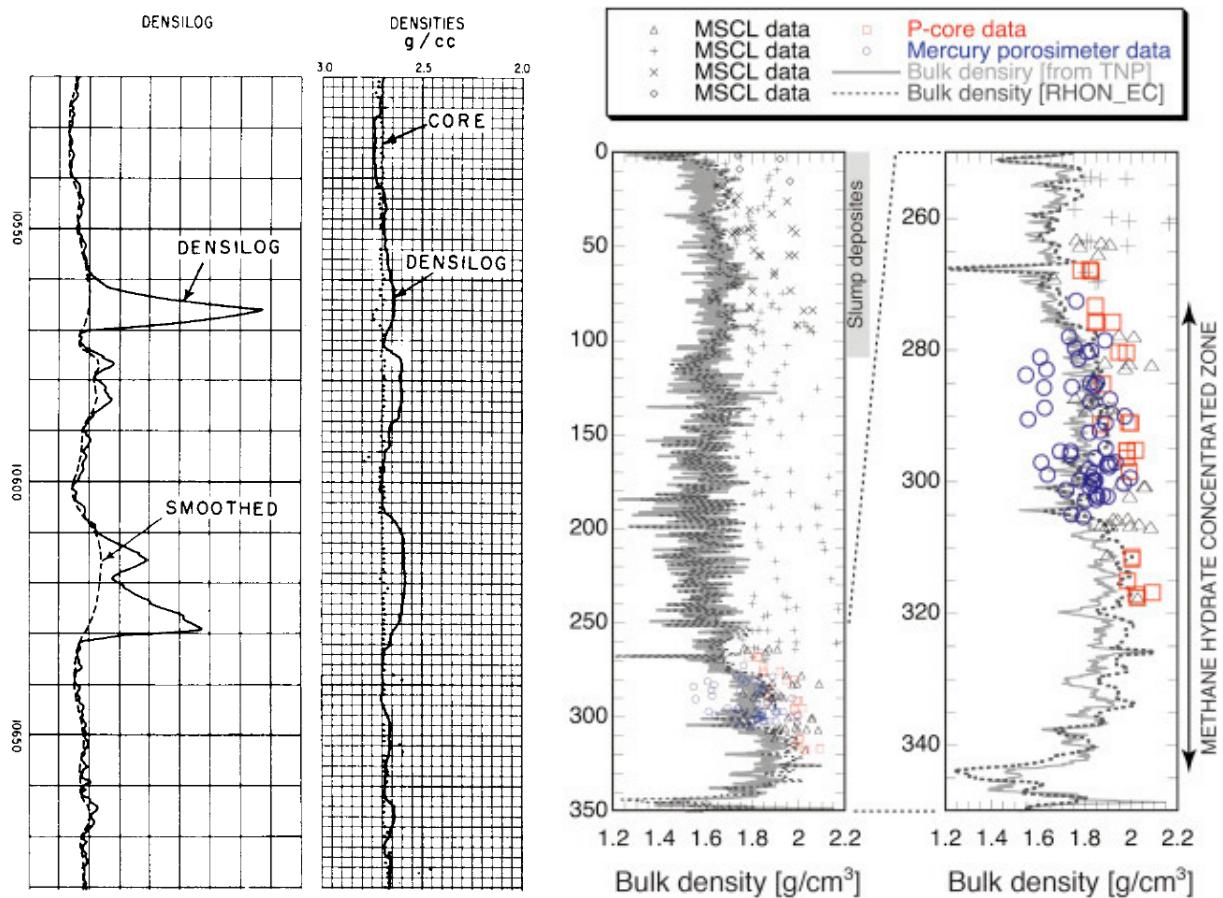


Figure 2.3.20. Comparison of density logs with densities derived from core samples. Left) Pioneer paper by Pickell and Heacock (1960). Right) data in a well from the Nakai Trough (Suzuki et al., 2015).

### 2.3.3.2 Borehole Gravimetry (BHGM)

Another direct measurement of the formation “apparent density” is based on borehole gravimetric measurements (BHGM). This technique basically inserts an especially designed gravimeter in the borehole to obtain gravity readings (formerly with 1 mGal resolution, nowadays close to the  $\mu\text{Gal}$ ) and transform them in averaged (apparent) density data. It was proposed in the 1950’s (Hammer 1950, 1965; Smith, 1950; Goodell and Fay, 1964; Howell et al., 1966), even earlier than the development of currently common logging techniques (Fig. 2.3.21); see also an early review by Robbins (1989). The principle behind this technique is, as in gravity surveying, the gravitational attraction between two bodies which is a function of



their masses and the distance between them. The derivation of the apparent density follows this equation:

$$\rho = [F - (\Delta g / \Delta z)] / 4\pi G$$

where F is the free-air gradient,  $\Delta g$  is the difference of consecutive gravity readings separated at a  $\Delta z$  distance and G the universal gravitational constant

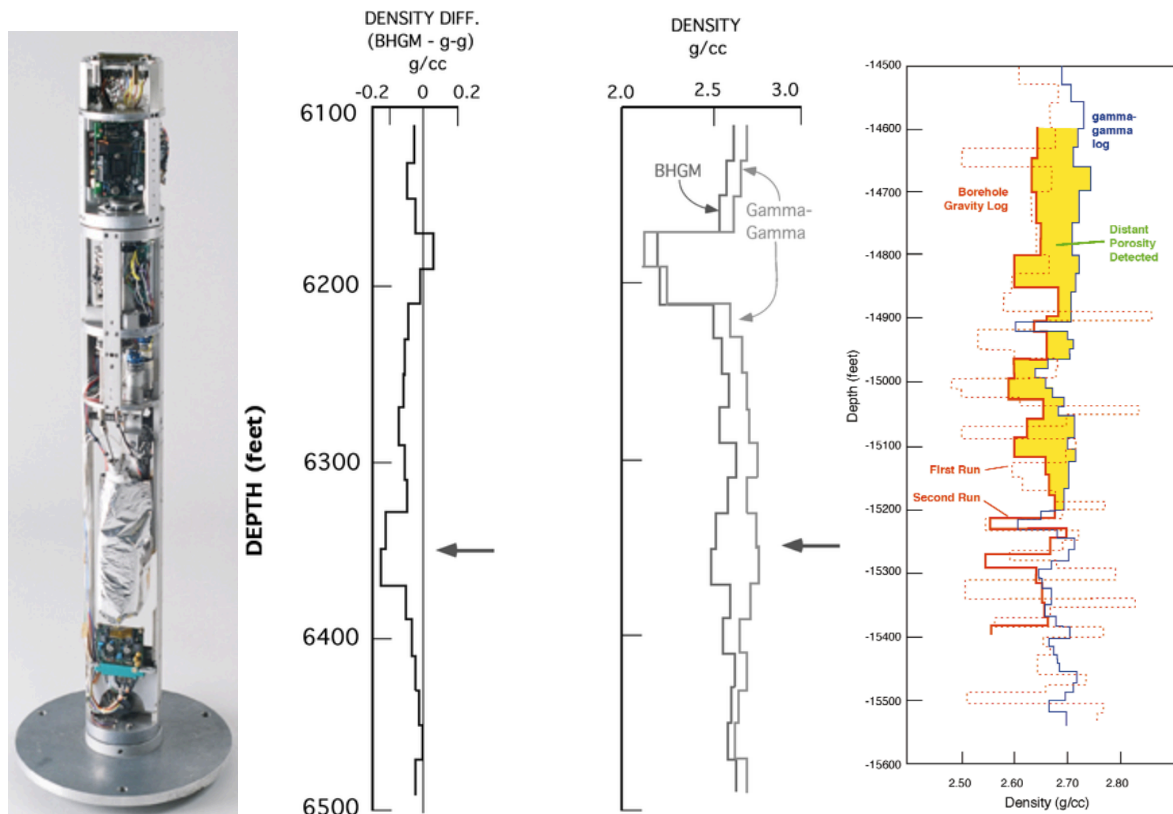


Figure 2.3.21. Borehole gravimeters (former Lacoste and Romberg probe) and BHGM data comparisons to standard formation density logs (Rasmussen, 1975 [center]; Chapin and Ander, 1999[right]).

LaFehr (1983) established some needed assumptions for conducting density determinations from borehole gravity: 1) the well crosses beds which are horizontal. 2) These beds infinitely extended laterally. 3) They must display a uniform thickness and 4) their densities are constant. In many cases, these assumptions can be met, and earlier comparisons of core density data, formation density (gamma-gamma) and gravity logging (Fig. 2.3.21) have confirmed the applicability of the method (Heintz & Alexander, 1979), but also the existence of significant differences (Schmoker, 1977). In any case, the occurrence nearby the well of masses with anomalous densities (or, for example, sudden changes caused by faults), may



produce significant deviations from those recorded by the formation bulk density logging, which certainly has additional applications in subsurface exploration.

Given the high resolution of modern borehole gravimeters (5 to 20  $\mu\text{Gal}$ ) like the Gravilog by Scientrex (<https://scintrexltd.com/product/gravilog-slim-hole-gravity-probe/>) or the L&R BHGM, the density measured is highly precise but averaged out a much larger rock volume and, of course, is highly dependent on the 3D distribution of nearby rock bodies. Other advantages of BHGM are (Robbins, 1989; Nabighian et al., 2005a): 1) They are not harmful (non-radioactive) as the FDL, 2) Borehole gravity measurements go beyond casing, mud, cement, hole rugosity and formation damages, and 3) Is the only logging tool measuring average density at tens of meters from a well and therefore its measurements are more reliable and representative of the formation than gamma-gamma ones (Chapin and Ander, 1999; Chapin and Mann, 1999). Some disadvantages are: 1) They are very costly, 2) manufacturing times are very long, 3) Sensitive to high temperatures (and thus depths), usually operate until 125°C, 4) Large well casings are needed (> 5 1/2-in  $\emptyset$ ), and, 5) They are only operative in pseudo vertical settings (up to 10-12° from vertical), although the development of vector gravity techniques has overcome this problem (Rim & Li, 2015)

Currently, the application of inversion method on BHGM signals (MacQueen, 2007; Krahenbuhl and Li, 2012) together with the development of vector gravimeters (Rim and Li, 2012, 2015) have improved the logging resolution and data consistency and have opened new applications such as 4D monitoring and surveillance of oil and gas reservoirs, CO<sub>2</sub> storages (Gasperikova & Hoversten, 2008), etc. Other kind of energy storages (Hydrogen), geothermal reservoirs, deep water reserves, are also expected to generate new demands for this technology due to its efficiency and reliability to track fluids in the subsurface (Rim and Li, 2012, 2015).



### 2.3.3.3 Computer Tomography determination of density from borehole cores

Another interesting source of density data is coming during the past few years from the CT scanning of borehole core samples (Andersen et al., 2013). Dual-energy CT scanning is used as an evaluating tool of petrophysical properties in the oil industry since the late 1980's (Wellington and Vinegar, 1987). The samples (core portions) are scanned two times with different X-ray energies each time. One image (above 100 kV) accounts for the Compton scattering and is proportional only to bulk density. The other (well below 100 kV) controls the effect of the Photoelectric absorption and then to the atomic number. Therefore, this technique is able to generate CT slices showing density and atomic number variations at the same time (Fig. 2.3.22).

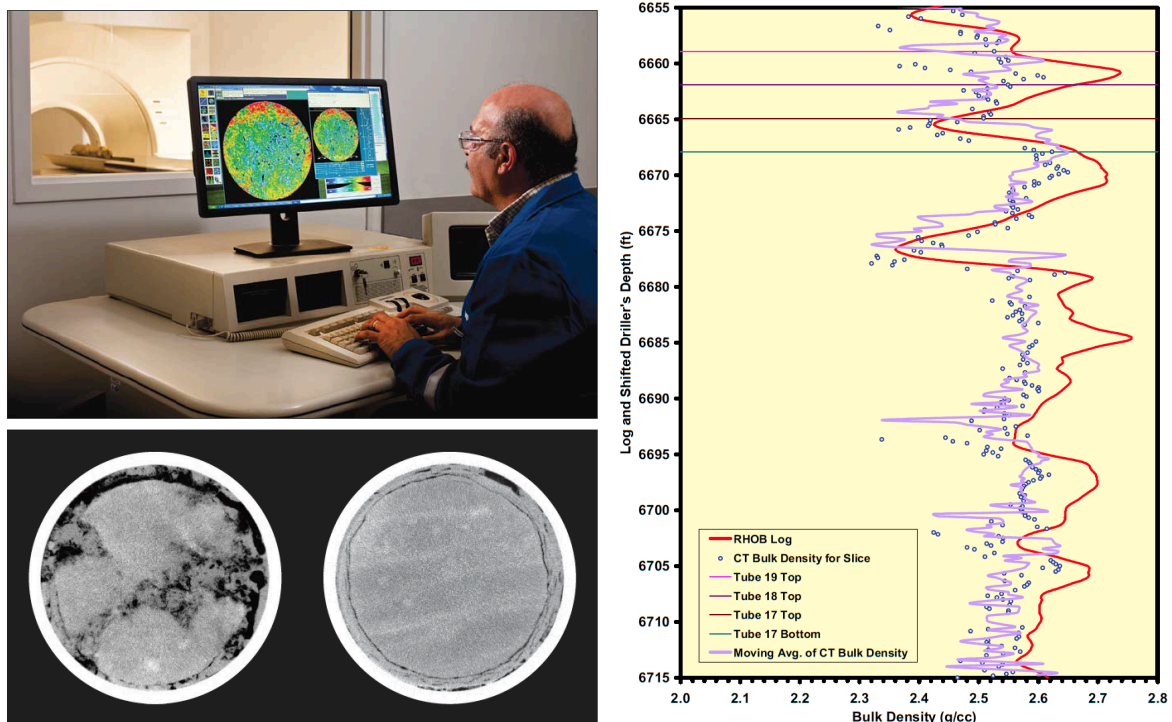


Figure 2.3.22. Dual energy CT scan for density determinations (taken from Andersen et al., 2013) and comparison with formation density (RHOB) logs (Siddiqui & Khamees, 2004).



On the other side, X-ray  $\mu$ -tomographic (XMT) methods with a higher range of energies are more versatile and have opened a large variety of applications (Moreno-Atanasio et al., 2010). Once the software processing and technical procedures needed to generate the bulk density and atomic number images were solved (Siddiqui & Khamees, 2004; Paziresh, et al., 2016), the dual-energy, or multi energy (Jussiani & Appoloni, 2015) scanning techniques are currently used to get a better characterization of the reservoir rocks, and it has been very useful for validation purposes of standard formation density logs (small samples of known petrophysical properties from laboratory essays).

## 2.3.4 Petrophysical relationships

### 2.3.4.1 Magnetic and density relationships

#### Henkel plot

The relationship between the two main petrophysical properties in potential field geophysics, density and magnetic susceptibility, plotted in bivariate diagrams (Fig. 2.3.23) was long ago recognized as a powerful approach to understand some petrological/geochemical differences and to identify distinct patterns in local and regional processes; this is the so-called Henkel's plot (after Henkel, 1976). Besides, and due to the usual proportionality (or pseudo proportionality) of magnetite content of a rock and its magnetic susceptibility, it has an important impact in the interpretation of magnetic anomalies (Clark, 1983; 1997). In these cases, the remanence is also considered together with the Q-ratios, that is, the fraction between the remanent and the induced magnetization of a rock (Koenigsberger, 1938). Therefore, the covariation of density and susceptibility can be used as an additional classifying tool, as well as allowing the natural occurring distributions to be related to a few general trends typical for specific minerals or to processes changing these minerals. Besides, the Henkel's diagram also displays the contrasts and variation ranges of key parameters in potential field interpretations (both at the same time; gravimetrics and magnetics).

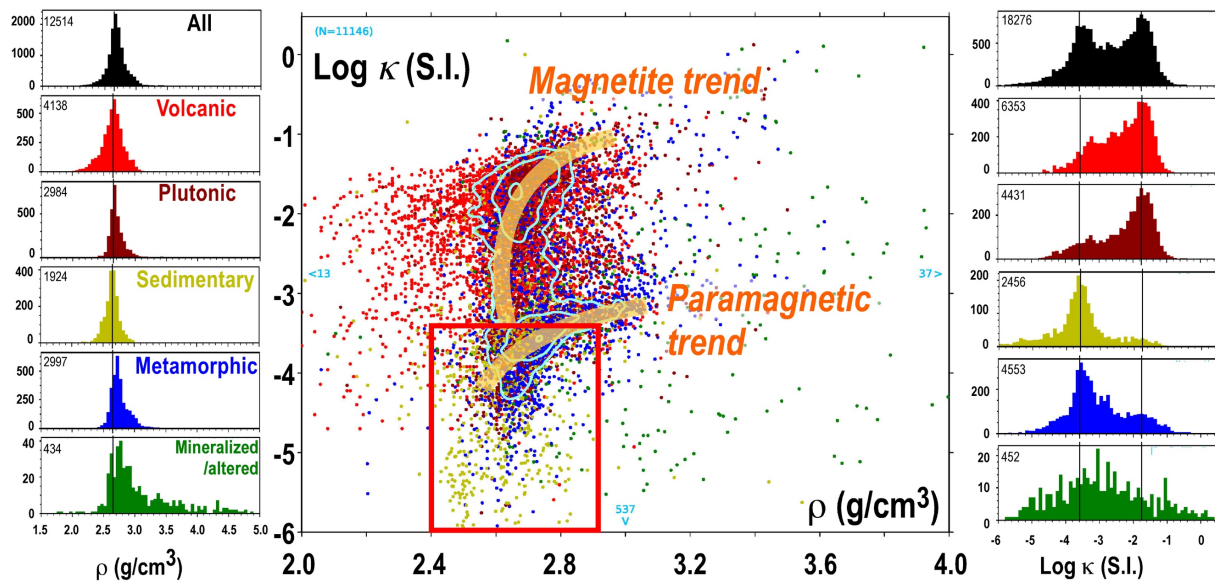


Figure 2.3.23. The Henkel's plot of the Canadian database (> 18,000 data, redrawn from Enkin, 2018, Geological Survey of Canada Open File 8460). Red box represents the plotted area in figure 2.3.24.

This diagram has been very useful to classify rocks with distinct trends in cratonic shields where thousands of samples were measured and where ample ranges of susceptibilities were found (Henkel, 1991 and 1994; Clark and Emmerson, 1991; Clark, 1997; Enkin, 2018). Recently Enkin et al. (2020), have gone beyond and distinguished a “magnetite trend” or a “paramagnetic trend” (as formerly done by Ishihara, 1977 and Clark, 1999 in igneous rocks) in relation to quantitative mineralogical/petrological standard diagrams (quartz-feldspar-calcite, ferromagnesian silicates or magnetite content) but focuses on understanding petrological processes able to alter these mixtures. This quantitative analysis represents a new turn on the screw and provides a new vision to integrate petrological (geological) processes in the interpretation of potential field geophysics surveys, very useful in ore exploration.

### Linear relationships in the paramagnetic domain

Beyond mineral exploration applications, based on the density and susceptibility relationships located in the ferromagnetic domain ( $k > 300-500 \cdot 10^{-5}$  S.I. Rochette, 1987; Pueyo-Anchuela et al., 2013a) or magnetite trend (Enkin et al., 2020), some other applications of the density and magnetic susceptibility cross-plot may take place in the paramagnetic domain (paramagnetic trend by Enkin et al., 2020).



Burial diagenesis is the main mechanism driving the organic matter maturation and the formation of oil and gas in sedimentary basins and orogenic wedges worldwide. Burial is also claimed for explaining pervasive remagnetizations in the same geological settings. It involves authigenic formation (e.g. chemical remagnetization) of magnetic minerals in response to progressively enhanced temperature conditions at deep basinal positions (Katz et al., 1998; Elmore et al., 2001 and Aubourg et al., 2012), which in turn implies an increase of susceptibility from shallow to deep conditions. The parallelism between the two processes, oil maturation and remagnetization of rocks, has turned magnetic surveying in a powerful exploration technique (Perroud et al., 1995; Schumacher, 1996; Aldana et al., 2003; Costanzo-Álvarez et al., 2012).

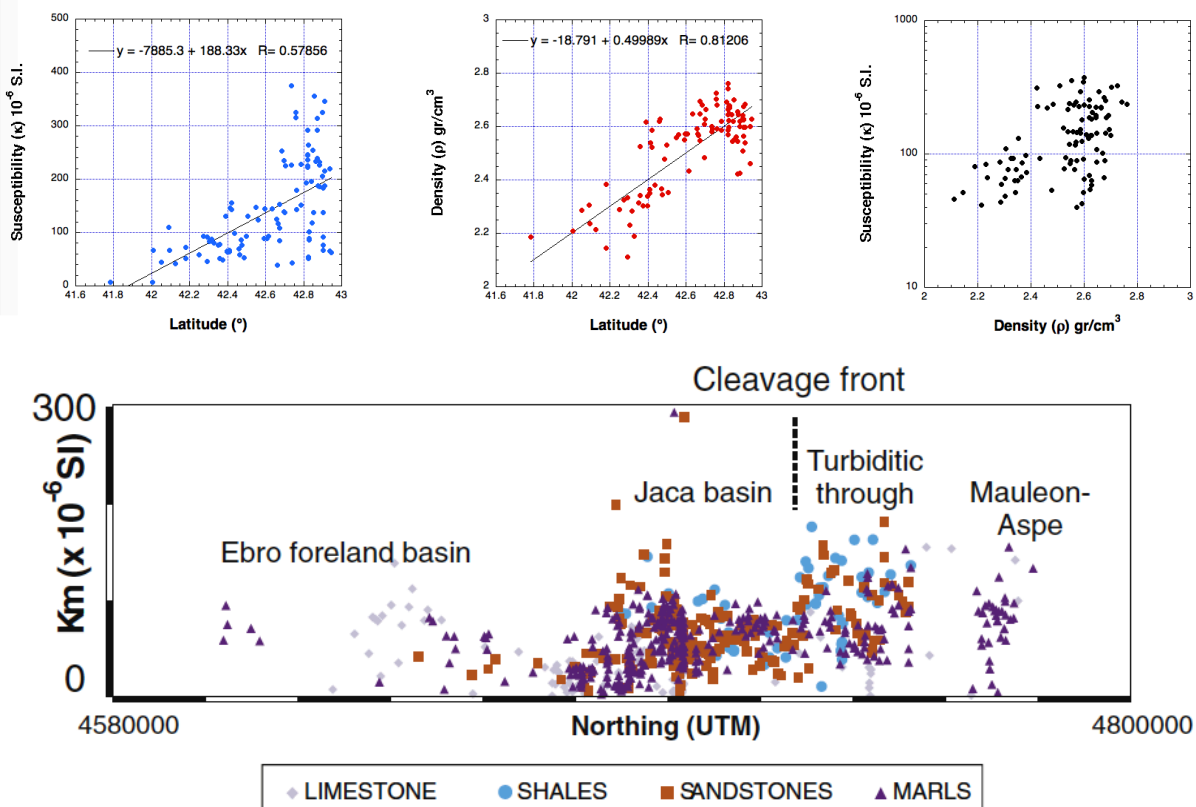


Figure 2.3.24. The Henkel's plot of western Pyrenean turbiditic facies (Pueyo-Anchuela et al., 2010 and 2013b; Pocoví et al., 2014). Density and magnetic susceptibility have been separately plotted against Latitude (S-N) to observe these relationships in an orogenic perspective (northern position are deeper in the orogenic wedge). Lower figure plots the susceptibility of different lithologies along the structural position (N-S section)



Besides, an increase of the density is often observed when focusing on given lithological types (Fig. 2.3.24). This can be seen in the northern Jaca Basin and the turbiditic facies (Hecho group) in a section crossing the cleavage front (Pocoví et al., 2014). The mudstones of the Arguis Fm and the shales (E levels) and silty-sandstones (levels A to D) from the flysch facies display a clear increase of density in deeper structural positions that run parallel to the increase of magnetic susceptibility as well as many other magnetic properties (NRM, AARM, etc.; Pueyo Anchuela et al., 2010 and 2013b). Logically, this relation will reach a maximum value for the density, when porosity is lost but magnetic properties (depended on the thermal history) may still increase.

With regards to intrusive igneous rocks, several works have already demonstrated that  $\delta^{18}\text{O}$  or  $[\text{SiO}_2]$  display a negative correlation to density and/or to magnetic susceptibility (Ellwood and Werner, 1981; Criss and Champion, 1984; Bourne, 1993, Ameglio et al., 1997). These relationships are particularly stable (and linear) in the so-called “non-magnetic”, ilmenite-type, granites (susceptibilities falling within the paramagnetic range; between 0 and  $500 \cdot 10^{-6}$  S.I.; Kanaya and Ishihara, 1973; Ishihara, 1977; Bouchez, 1997), and usually coincident with calc-alkaline (CA) compositions (very common in Variscan domains).

In some variscan granites from Iberia (mostly located in the Pyrenean Axial Zone), density and magnetic susceptibility were plotted together (Fig. 2.3.25). Data come from previous papers (Mont Louis-Andorra by Gleizes et al., 1993; Veiga by Román et al., 1995; Marimaha by Loi et al., 2019) as well as data here reported from the Maladeta and Mont Louis-Andorra batholiths. Petrophysical hand-samples and standard specimens from previous AMS studies were plotted together in the Henkel’s diagram.

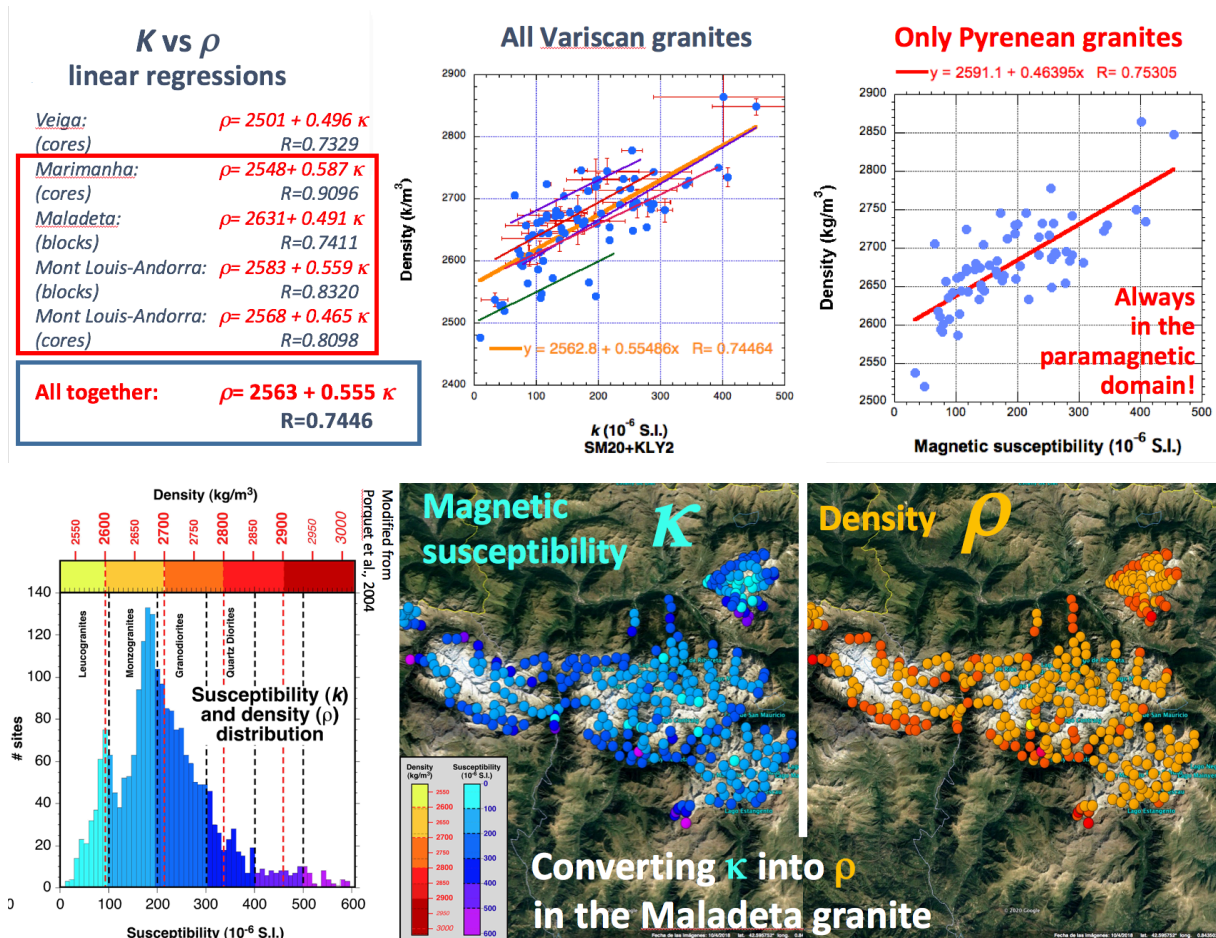


Figure 2.3.25. Density and susceptibility cross-plot for Variscan granites and regressions obtained. The relationship between petrologic facies with magnetic susceptibility (Gleizes et al., 1993) as well as with density (Pueyo et al., 2021) allow to convert the vast Pyrenean AMS dataset (Porquet et al., 2017) in density values.

Regressions were derived for every granite body and they typically follow a linear function similar to:  $\rho = 2600 \text{ kg/m}^3 + (0.5 * k * [10^{-6} \text{ S.I.]}$ ). This relationship is only valid in CA and paramagnetic granites, where iron is mostly fractioned in iron-bearing phyllosilicates (biotite), in ilmenite, and the occurrence of magnetite is negligible (or at least its contribution to the bulk susceptibility). Given the large amount of AMS measurements focused on the internal characterization of plutonic rocks, (only in the Pyrenees there are more than 2200 studied sites; > 10,000 individual measurements; Porquet et al., 2017), these relationships allow transforming magnetic susceptibility data into density data helping in the 3D modelling of the gravimetric signal when density data from rock samples are scarce. The large amount of AMS studies worldwide (very often in paramagnetic rocks), together with the quickness and cost-effectiveness of susceptibility measurements with portable devices, allow densifying and



homogenizing the petrophysical dataset with this methodology, when modelling granite rock volumes based on both magnetic and gravimetric signals (Pueyo et al., 2021).

### 2.3.4.2 Density at depth

The general increase of density (and decrease of porosity) with depth was very early recognized in sedimentary rocks by the oil industry as a consequence of burial (increased geostatic pressure) and subsequent rock compaction (Athy 1930, Hedberg 1936, Terzaghi, 1940; Jones, 1944; Eaton, 1969; Maxant 1980) (Fig. 2.3.24). The seminal paper by Athy (1930), with a profound impact in later research on the topic, proposed an empirical formulation to explain the change of density of Permian and Pennsylvanian shales in Oklahoma:

$$\rho_z = \rho_s + \Delta\rho_{\max}(1-e^{-bz})$$

where:  $\rho_z$  is the density as a function of Z

Z is the depth

$\rho_s$  is the density at the surface

$\Delta\rho_{\max}$  is the maximum increment of density

b is a constant characterizing the compressibility of the sediment.

However, this exponential behavior, always observed in density logging of wells, does not follow a unique mathematical function because of the enormous 3D (and 4D) variability of lithologies with different porosities and responses to compaction as well as distinct effects of diagenesis and tectonic and thermal histories (Cordell, 1973; Granser, 1987). These last authors were among the first who investigated the effect of density increase with depth on the gravimetric signal. Cordell (1973) proposed an empirical function to estimate the decrease of density contrast (sedimentary vs basement rocks) with depth as  $-0.2 \text{ g/cm}^3/\text{km}$ . Granser (1987) estimated the increase of density in the Pannonian Basin rocks as:  $\rho_z = -0.45 e^{-0.65 \cdot Z}$ . This means that the density increase is almost negligible below 5 to 6 km (or so) once the basinal rocks have reached the maximum compaction and their densities cannot increase anymore. On the other hand, recent compilation of numerous sites of the Deep Sea Drilling Project (DSDP) has estimated the decreasing density trend for marine sediments in  $-0.05 \text{ g/cm}^3$  per 1 km (Tenzer and Gladkikh, 2014).



In any case and due to the large variability of this relationship and considering the modelling point of view of cover and basement configurations, the estimation of an empirical function for the modeled rocks is always desirable. This information is rapidly derived from the formation density logs (gamma-gamma logs) in areas where intense oil and gas exploration has taken place (Fig. 2.3.26). Unfortunately, this is not always the case and alternative solutions and/or assumptions have to be taken.

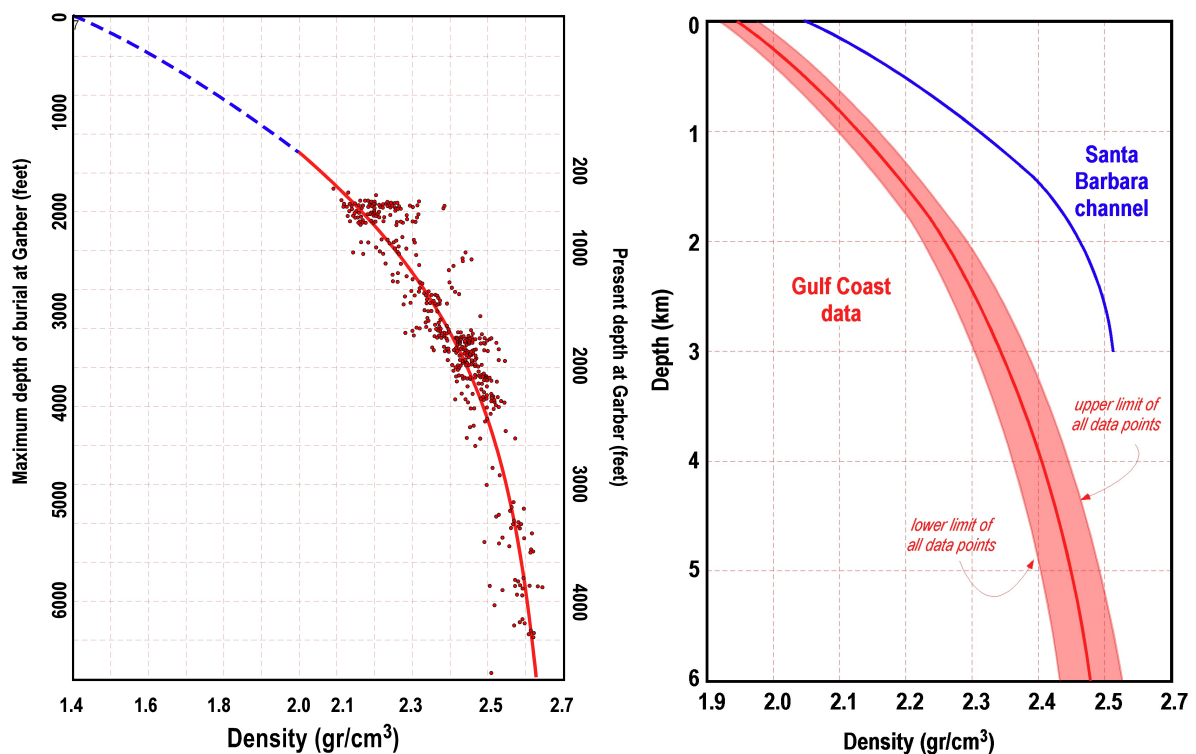


Figure 2.3.26. Classic examples of the variation of density at depth. Left) Redrawn from the pioneer paper by Athy (1930), data from Oklahoma shales. Right) Data from the Gulf Coast wells and including the Santa Barbara channel (redrawn from Eaton, 1969).

The modelling and interpretation of gravimetric signals has taken into consideration many types of relationships between density and density contrast at depth: linear, exponential, quadratic, hyperbolic, parabolic etc. (Cordell, 1973, Chai and Hinze, 1988, Rao et al, 1986; see the review by Silva et al., 2006). They are always geologically more reasonable than those models (and software programs) implementing constant densities, and they represent the more reliable way for modeling complex basins (Silva et al., 2006). Unfortunately, some commonly used processing packages does not allow for the implementation of density-depth functions.



### 2.3.4.3 Density and other variables

Density can be also estimated considering the relationships with other variables. Very often density is derived from seismic velocity data (sonic logs), in particular with the P wave velocity because of the empirical and simple relationship observed among them in many sedimentary rocks. This is physically explained by the Gassmann's theory (1951) that relates elastic constants, density and P-wave velocity in porous rocks. However, and despite the systematic empirical relationships found in many sedimentary logs and witnessed by plentiful data (typically valid until up to 7-8 km in depth), achieving an absolute estimation of this function is seldom possible and a universal solution cannot be established since several interrelated variables play a key role in the system at the same time and modified the elastic properties: rock and mineral composition and fabric (porosity, cementation, microcracks, etc.), content and nature of fluids as well as lithostatic and hydrostatic pressures (Gardner et al., 1974). This is why P wave velocity and density cross-plots usually display a noisy behavior (Fig. 2.3.27) where a large variability of density can be observed for given velocity.

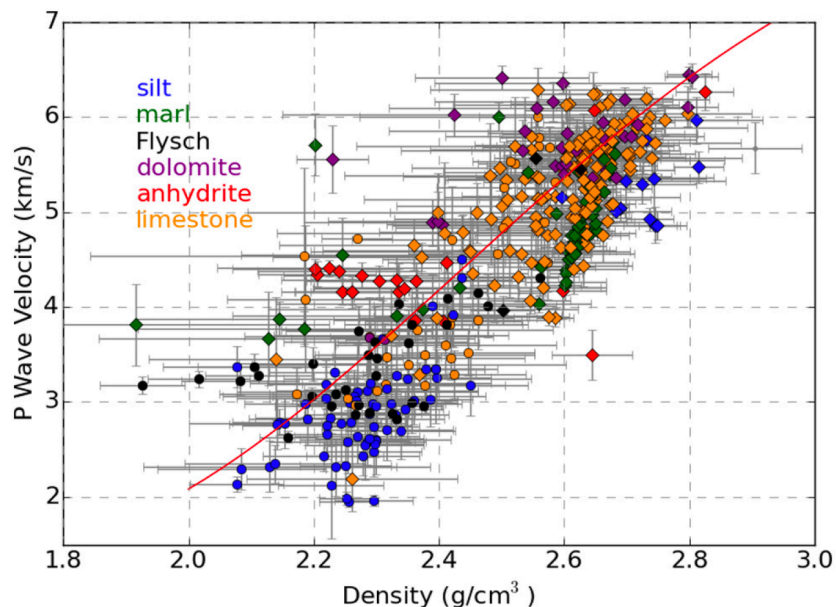


Figure 2.3.27. Mean densities and P-wave velocities from well-logging in the North Pyrenean Foreland Basin (Aquitaine). Lithologies are shown with different colors and ages in different shaped-symbols. Diamonds: Mesozoic, circles: Cenozoic. This relation allows to describe the structure of the Aquitania basin by two main layers; Mesozoic and Cenozoic, exhibiting a diffuse boundary of their physical properties around 2.4 g/cm<sup>3</sup> and 3.5 km/s (Wehr et al., 2018).



Therefore, in the absence of FDL (direct density observation) or BHGM (Borehole Gravimetry) data, we here recommend not using density data from sonic logs for the building of petrophysical databases to be used in the modelling of gravimetric data because of the inherent (large) uncertainty.

### 2.3.5 Petrophysical data models and databases

Several papers have implicitly established data schemes for the compilation of petrophysical properties in certain regions (v.g. Rybakov et al., 1999; García-Lobón et al., 2006; Tenzer et al., 2011; Yang et al., 2013; Pueyo et al., 2016 among many others). When the data are properly published (georeferenced, fully described, etc.) and specially when they meet FAIR principles (findability, accessibility, interoperability, and reusability, after Wilkinson et al., 2016), these databases, are very useful in forthcoming studies since the petrophysical information can be harvested, re-used, enlarged and improved.

One step forward has been done in larger regions with a historic development of mining activities, like those in Minnesota (<https://conservancy.umn.edu/handle/11299/175581>) (Chandler and Lively, 2015) with more than 9,000 data entries, or in British Columbia (<https://catalogue.data.gov.bc.ca/dataset/rock-properties-database>), later on expanded to whole Canada, with almost 20,000 entries (Enkin, 2018), or like the Australian government on line application that is able to serve countless geoscience data (<http://www.ga.gov.au/explorer-web/rock-properties.html>) (Barlow, 2019; Fig. 2.3.28).

The Geological and Mining Institute of Spain (IGME) has already established some basic criteria, and methodological protocols to build a petrophysical database (Plata, 2009). IGME has also developed since 2001 its own geophysical database that met the FAIR principles (Plata et al., 2008); the SIGEOF portal (<https://info.igme.es/SIGEOF/>) has already defined simple and operative data models for petrophysical and gravimetric data (among many other) that are easy searchable and downloadable (Fig. 2.3.29).

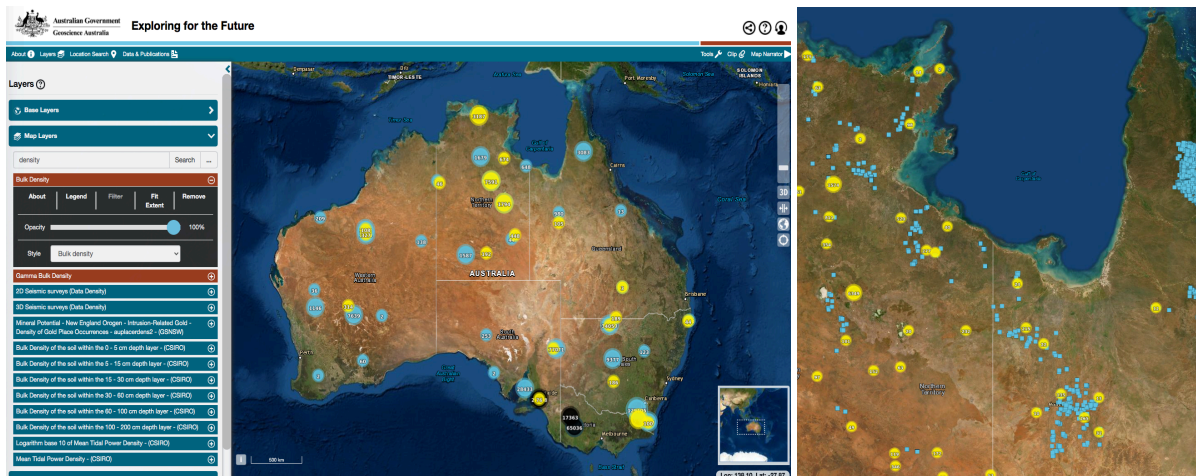


Figure 2.3.28. The Australian online database *Exploring for the future* (<https://portal.ga.gov.au/persona/eftf>) showing density and magnetic susceptibility data. The right map is an enlargement for the Northern and Queensland territories. Yellow dots (or point clouds) are density data, while blue ones are magnetic susceptibility entries.

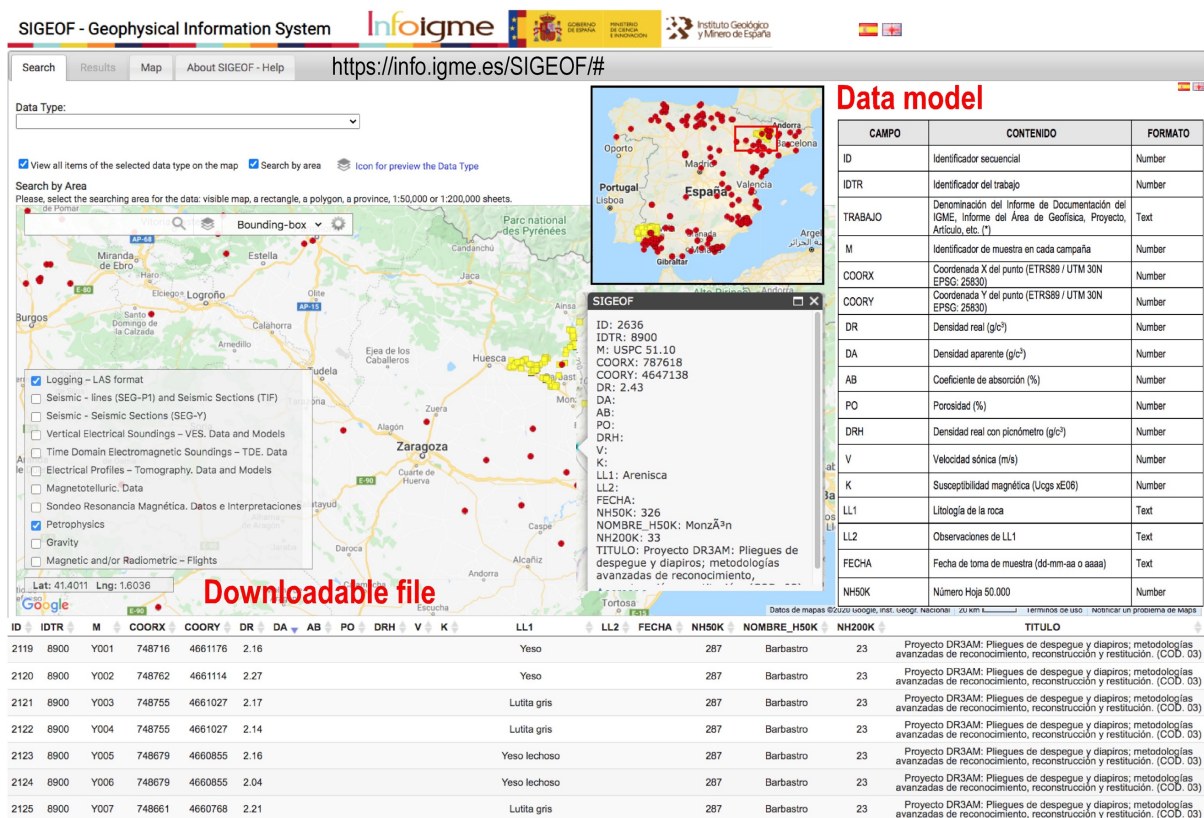


Figure 2.3.29. The SIGEOF portal showing the petrophysical data model and an example of NE Spain.



Recently and in the frame of the European project IMAGE, that is focused on the exploration of geothermal resources (<http://www.image-fp7.fr/>), there have been more ambitious initiatives to build an integrated and international PetroPhysical Property Database (P<sup>3</sup>) (Bär et al., 2020). Beyond standard sample/site information (ID, location, sample, petrologic, chronologic, stratigraphic items, etc.) that could be harvested from other databases through the metadata scheme, the database also contains information relevant for geothermal exploration and characterization, namely hydraulic, petrophysical [density and porosity], thermophysical, mechanical properties and electrical resistivity and magnetic susceptibility, as well as a quality control on some parameters and measurement conditions. This data model (Fig. 2.3.30) is, therefore, fully compatible with a petrophysical database focused on gravimetric and magnetic exploration (except for the absence of magnetic remanence and the Q index data). So far P<sup>3</sup> has compiled information in more than 75,000 points all over the world and its accessibility is granted in the GFZ data repository (Bär et al., 2019), but the interoperability, and reusability of the data is limited in the present format. Besides, the harvesting of additional data in P3 is also under question since the IMAGE project life is over.

<b>Sample Information</b> <i>sample ID</i> <i>reference</i> primary reference secondary reference date of input editor <i>sampling location</i> loc. type (area, outcrop, well) loc. name loc. country loc. state/region loc. longitude loc. latitude loc. elevation (m a.s.l.) radius of uncertainty (km) <i>sample information</i> original sample ID int. geo sample no. (IGSN) sample type (drillcore, etc.) sample length (m) sample height (m) sample width (m) sample diameter (m) sample longitude sample latitude sample elevation (m a.s.l.) sample depth (m b.g.l.) <i>Petrography</i> petrographic ID petrographic parent ID pet. term (simplified) petrography (in detail) sample texture sample homogeneity sample layering direction of measurement sample consolidation remarks on sample <i>Stratigraphy</i> stratigraphic ID stratigraphic parent ID chronostratigraphic unit local stratigraphic unit	<b>Thermophysical Properties</b> <i>bulk thermal conductivity</i> <i>[W/(m·K)]</i> value standard deviation minimum maximum inhomogeneity number of measurements measuring type remarks <i>matrix thermal conductivity</i> <i>[W/(m·K)]</i> <i>specific heat capacity</i> <i>[J/(kg·K)]</i> <i>volumetric heat capacity</i> <i>[J/(m³K)]</i> <i>thermal diffusivity [m²/s]</i> <i>radiogenic heat production</i> <i>[W/m³]</i>	<b>Mechanical Properties</b> <i>p-wave velocity [m/s]</i> <i>s-wave velocity [m/s]</i> <i>Youngs modulus: dynamic</i> <i>[MPa]</i> <i>Youngs modulus: static</i> <i>[MPa]</i> <i>shear modulus: static</i> <i>[GPa]</i> <i>bulk modulus: static</i> <i>[GPa]</i> <i>Lamé's first parameter</i> <i>Lamé's second parameter</i> <i>Cohesion [MPa]</i> <i>Coefficient of friction [-]</i> <i>Poisson ratio [-]</i> <i>Uniaxial compressive strength</i> <i>[MPa]</i> <i>tensile strength [MPa]</i>	<b>Quality control</b> <b>Quality indices</b> q, geographic uncertainty q, petrography q, stratigraphy q, measurement conditions q, property mean value quality index (mean) quality class remarks on quality <b>measurement conditions</b> temperature (K) pressure (Pa) saturating fluid degree of saturation (%) $\sigma_1$ (MPa) $\sigma_2$ (MPa) $\sigma_3$ (MPa) pore pressure (MPa)
	<b>Petrophysical Properties</b> <i>grain density [kg/m³]</i> value standard deviation minimum maximum number of measurements measuring method remarks <i>bulk density [kg/m³]</i> <i>total porosity [%]</i>	<b>Electrical Properties</b> rock conductivity [S/m] fluid conductivity [S/m] formation resistivity factor [-] standard deviation minimum maximum number of measurements measuring type remarks	
	<b>Hydraulic Properties</b> <i>effective porosity [%]</i> <i>apparent permeability [m²]</i> <i>intrinsic permeability [m²]</i> <i>hydraulic conductivity [m/s]</i>	<b>Magnetic susceptibility</b> value standard deviation minimum maximum number of measurements measuring type remarks	

Figure 2.3.30. The data scheme of the PetroPhysical Property Database (P<sup>3</sup>) (Bär et al., 2020).



These problems may be solved in the mid-term under the frame of the European Plate Observing System a (European Research Infrastructure Consortium). EPOS-ERIC initiative (<https://www.epos-eu.org/>) (Bailo et al., 2015) is a long-term plan to facilitate the use of integrated data, data products, and facilities from distributed research infrastructures for solid Earth science in Europe. However, EPOS-ERIC Thematic Core Services (TCS) have not yet considered the implementation and definition of specific data models and schemes for petrophysical and gravimetric data. On the other hand, and after several discussions during the pre-implementation phase, EPOS has finally agreed to adopt the more advanced and developed paleomagnetic data scheme by MagIC (Pueyo et al., 2017; Jarboe et al., 2020).

The paleomagnetic community has been pioneer in Earth Sciences to boost the development of databases since more than 30 years. The Global Paleomagnetic Database (GPMDB) comprises paleomagnetic directions and pole positions, and it was firstly compiled by Lock and McElhinny (1991) and maintained by crowdfunding by the scientific community (McElhinny y Smethurst, 2001; Pisarevsky, 2005) until the arrival of the Magnetics Information Consortium (MagIC) (Jarboe et al., 2012; Tauxe et al., 2016), a keystone in the Earth Reference Data and Model (<https://www.earthref.org/MagIC>). EarthRef is a NSF/US initiative focused on maintaining an open community digital data archive for rock and paleomagnetic data with portals that allow to access, archive, search, visualize, download, and combine versioned datasets. The MagIC/EPOS/GFZ-Data-Services interoperability is granted with metadata to TCS MSL via DataCite records preventing the fragmenting of the GPMDB (Jarboe et al., 2020), and with other platforms providing data at the very base (specimen) level (Koymans et al., 2020). The MAGIC database already includes more than 4000 contributions that comprise more than 175,000 paleomagnetic sites and more than 6 million measurements (data January 26<sup>th</sup> 2021). Apart from standard sample/site information (ID, location, petrologic chronologic, stratigraphic, etc.), all key data fields needed in a petrophysical database focused on gravimetric exploration are already defined in the MagIC data model (<https://www2.earthref.org/MagIC/data-models/3.0>); like density, magnetic susceptibility and NRM, although some specific data fields (density method, field method, sample type, etc.) should be reviewed and implemented.



---

The GeoERA project (<https://geoera.eu/>) aims, among other goals, at building interoperable and transnational data and information services within the European Geological Data Infrastructure (EGDI) platform. EGDI was implemented in a first version in 2016 by the EuroGeoSurveys Spatial Information Expert Group (<https://www.europe-geology.eu>) and it has considerably grown during the GeoERA project life (2018-2021). Its main objective is to set up a common geoscience information platform capable of integrating and serve up-to-date data as well as interpretations and models from different and distributed sources.

In this frame, the 3DGeoEu project (WP6) has proposed a complete petrophysical data model focused on the exploration based on potential field geophysics (gravimetrics and magnetics). This data model starts from previous and independent European Geological Surveys experiences and other previous international initiatives (e.g. Enkin, 2018; Bär et al., 2020) but is has been significantly enriched and improved by a fruitful feed-back process among the project partners following ICON (Integrated, Coordinated, Open, and Networked) principles and pursuing for data repositories under FAIR (findability, accessibility, interoperability, and reusability) principles as well.



**Petrophysical data schema (focused on potential field geophysics; gravimetric and magnetic)**

**Basic site information**

Data fields	Description	Data format	Example
1 <b>Site name</b>	Original site name in the publication/report	Alphanumeric	NAT1
2 <b>Latitude</b>	Latitude coordinates (centesimal)	Numeric	42,717061
3 <b>Longitud</b>	Longitud coordinates (centesimal)	Numeric	-0,529597196
4 <b>Geographic description</b>	Closer localities, villages, etc..	Alphanumeric	Gabardito hiking trail (Canfranc, Huesca)
5 <b>Sample type</b>	hand-block/paleomagnetism	Alphanumeric	Paleomagnetic standard specimens
6 <b>Positioning accuracy</b>	Estimate of the accuracy; e.g. GPS model	Alphanumeric	Garming Oregon GPS (+/- 3-5m)
7 <b>Project</b>	Title of the project in which the data were acquired	Alphanumeric	Consistent 3D restoration in complex structures by using structural and paleomagnetic 3D references
8 <b>Project acronym</b>	Acronym of the project	Alphanumeric	Pmag3Drest
9 <b>Funding agency</b>	Funding agency	Alphanumeric	Spanish National Science Plan (CGL2009-14214-BTE)
10 <b>Ownership</b>	to whom the data belongs	Alphanumeric	University of Zaragoza
11 <b>Accessibility</b>	FAIR/embargo/restricted, etc..	Alphanumeric	FAIR
12 <b>Repository</b>	URL address of the data repository	Alphanumeric	<a href="https://info.igme.es/SIGEOF/">https://info.igme.es/SIGEOF/</a>
13 <b>Author/s</b>	(not necessarily the fist author)	Alphanumeric	Oliva-Urcia, B. and Pueyo, E.L.
14 <b>Reference's doi</b>	doi number of the reference	Alphanumeric	10.1016/j.jsrg.2008.11.002
15 <b>Reference</b>	Full reference (APA format)	Alphanumeric	Oliva-Urcia, B., Larrasoña, J. C., Pueyo, E. L., Gil, A., Mata, P., Parés, J. M., Schleicher, A. M. & Pueyo, O. (2009). Disentangling magnetic subfabrics and their link to deformation processes in cleaved sedimentary rocks from the Internal Sierras (west central Pyrenees, Spain). <i>Journal of Structural Geology</i> , 31(2), 163-176.
16 <b>Publication year</b>	Year of publication of the paper/report	Numeric	2009
17 <b>Stratigraphic age</b>	Following the International Stratigraphic Chart (IUGS)	Alphanumeric	Maestrician
18 <b>Numerical age</b>	Following Gradstein et al. (2012) or updated version (in Ma)	Numeric	70.5
19 <b>Numerical error</b>	If known; otherwise add +/- X Ma (X=half of the stage duration)	Numeric	5
20 <b>Stratigraphic formation</b>	Local formation (sedimentary rocks)	Alphanumeric	Marbore calcarenite Fm.
21 <b>Lithology</b>	Lithologies controlled vocabulary	Alphanumeric	Calcarenite
22 <b>Bedding</b>	Strike & dip (DD) following the RHR (even for overturned beds)	Alphanumeric	075,20 S
23 <b>Structural unit</b>	Description of the structural/geologic units	Alphanumeric	Internal Sierras (Southern Pyrenees)

**Density data**

Data fields	Description	Data format	Example
24 <b>Estimation method</b>	Method for estimating the volumen; Archimedes (w. or w/o paraffin), Geometric, etc..	Alphanumeric	Geometric estimate
25 <b>Laboratory</b>	Where the measurements were taken	Alphanumeric	Petrophysics Univ. Zaragoza
26 <b>Instrument</b>	If needed, specify the instrument	Alphanumeric	-
27 <b>Density units</b>	SI vs cgs	Alphanumeric	cgs
28 <b>N<sub>ρ</sub></b>	Number of density measurements in this site	Numeric	42
29 <b>min<sub>ρ</sub></b>	minimum density data in the site	Numeric	2.416
30 <b>Max<sub>ρ</sub></b>	Maximum density data in the site	Numeric	2.78
31 <b>Mean<sub>ρ</sub></b>	Mean density of the site	Numeric	2.659
32 <b>Median<sub>ρ</sub></b>	Median density of the site	Numeric	2.691
33 <b>RMS<sub>ρ</sub></b>	RMS of density in the site	Numeric	2.66
34 <b>Stdev<sub>ρ</sub></b>	Standard deviation of the density in the site	Numeric	0.099
35 <b>Variance<sub>ρ</sub></b>	Variance of the density in the site	Numeric	0.01
36 <b>Std Error<sub>ρ</sub></b>	Standard Error of the density in the site	Numeric	0.015
37 <b>Skewn<sub>ρ</sub></b>	Skewness index of the density in the site	Numeric	-1.081
38 <b>Kurtos<sub>ρ</sub></b>	Kurtosis index of the density in the site	Numeric	0.082
39 <b>Density raw data</b>	listing of data separated by ";"	Numeric	2.730; 2.590; 2.523; 2.682; 2.747; 2.489; 2.493; 2.745; 2.673; 2.707; 2.451; 2.718; 2.669; 2.716; 2.740; 2.741; 2.754; 2.655; 2.632; 2.759; 2.701; 2.506; 2.709; 2.420; 2.676; 2.665; 2.625; 2.570; 2.653; 2.737; 2.736; 2.581; 2.710; 2.748; 2.616; 2.416; 2.780; 2.720; 2.672; 2.751; 2.717; 2.735



**Susceptibility data-1** *maybe there are field and laboratory measurements. In that case use "-2" for the second set of measurements*

Data fields	Description	Data format	Example
40 <b>Estimation method</b>	Field or laboratory	Alphanumeric	Laboratory
41 <b>Laboratory</b>	Where the measurements were taken	Alphanumeric	Pastel group (Univ. Michigan at Ann Arbor)
42 <b>Instrument</b>	If needed, specify the instrument; KLY3, SM20	Alphanumeric	KLY2 (Geophysika Brno-AGICO)
43 <b>Susceptibility units</b>	SI vs cgs	Alphanumeric	10-6 S.I.
44 <b>N<sub>K</sub></b>	Number of magnetic susceptibility measurements in this site	Numeric	40
45 <b>min<sub>K</sub></b>	minimum magnetic susceptibility data in the site	Numeric	153.1
46 <b>Max<sub>K</sub></b>	Maximum magnetic susceptibility data in the site	Numeric	298.505
47 <b>Mean<sub>K</sub></b>	Mean magnetic susceptibility of the site	Numeric	210.538
48 <b>Median<sub>K</sub></b>	Median magnetic susceptibility of the site	Numeric	183.3
49 <b>RMS<sub>D</sub></b>	RMS of magnetic susceptibility in the site	Numeric	216.671
50 <b>Stdev<sub>K</sub></b>	Standard deviation of the magnetic susceptibility in the site	Numeric	51.839
51 <b>Variance<sub>K</sub></b>	Variance of the magnetic susceptibility in the site	Numeric	2687
52 <b>Std Error<sub>K</sub></b>	Standard Error of the magnetic susceptibility in the site	Numeric	8.196
53 <b>Skewn<sub>K</sub></b>	Skewness index of the magnetic susceptibility in the site	Numeric	0.876
54 <b>Kurtos<sub>K</sub></b>	Kurtosis index of the magnetic susceptibility in the site	Numeric	-0.93
55 <b>Density raw data</b>	listing of magnetic susceptibility data separated by ";"	Numeric	178.5; 169.1; 169.8; 181.5; 181.8; 153.1; 167.1; 181.3; 179.5; 183.1; 166.2; 178.6; 181.3; 184.4; 186.7; 183.5; 183.5; 177.1; 178.2; 179.8; 175.5; 170.1; 175.2; 154.6; 182.9; 180.4; 174.4; 188.4; 204.1; 178.1; 192; 159.6; 182; 185.3; 193.4; 189.9; 189.7; 198.9; 192.6; 197.7

**Natural Remanent Magnetization (NRM) data**

Data fields	Description	Data format	Example
56 <b>Laboratory</b>	Where the measurements were taken	Alphanumeric	Pastel group (Univ. Michigan at Ann Arbor)
57 <b>Instrument</b>	If needed, specify the instrument; e.g. 3G (model 755)	Alphanumeric	2G (model 755-1.65)
56 <b>NRM units</b>	SI vs cgs	Alphanumeric	10-6 A/m
57 <b>N<sub>NRM</sub></b>	Number of NRM measurements in this site	Numeric	12
56 <b>min<sub>NRM</sub></b>	minimum NRM data in the site	Numeric	175.2
57 <b>Max<sub>NRM</sub></b>	Maximum NRM data in the site	Numeric	198.9
56 <b>Mean<sub>NRM</sub></b>	Mean NRM of the site	Numeric	184.283
57 <b>Median<sub>NRM</sub></b>	Median NRM of the site	Numeric	183.2
56 <b>RMS<sub>NRM</sub></b>	RMS of NRM in the site	Numeric	184.385
57 <b>Stdev<sub>NRM</sub></b>	Standard deviation of the NRM in the site	Numeric	6.39
56 <b>Variance<sub>NRM</sub></b>	Variance of the NRM in the site	Numeric	40.836
57 <b>Std Error<sub>NRM</sub></b>	Standard Error of the NRM in the site	Numeric	1.845
56 <b>Skewn<sub>NRM</sub></b>	Skewness index of the NRM in the site	Numeric	0.928
57 <b>Kurtos<sub>NRM</sub></b>	Kurtosis index of the NRM in the site	Numeric	0.454
56 <b>NRM raw data</b>	listing of NRM data separated by ";"	Numeric	333.4; 498.3; 347.1; 387.5; 498.8; 474.1; 444.2; 649.8; 415.8; 948.5; 539.9; 859.6

Table 2.3.8. Petrophysical data model proposed in this project. Red fields are strongly required.



### 2.3.6 Uncertainty sources and challenges in petrophysical data

Petrophysical data related to gravity and magnetic interpretation (in particular rock density, magnetic susceptibility and remanence), as one of the three keystones for the 3D modeling based on potential-field geophysical data, is a significant source of uncertainty due to the large natural variability of these properties in rock volumes (Henkel, 1994; Enkin et al., 2020; among many others). In gravimetric modeling (from regional studies to micro-scales) petrophysical uncertainty is commonly obviated in many workflows. In fact, sometimes the raw data are poorly described or taken from the literature. However, the petrophysical information must be considered as primary and key data in 2D and 3D potential field modelling. Numerous samples for characterizing the natural density variability of the target formations have to be acquired directly from outcrops (and then processed in the laboratory), or harvested from databases (rock samples or well logging; e.g. Enkin, 2018). The final goal is to build robust histograms (i. e., characterizing the probability density function) for every modelled volume to constraint the mean density and its variability (both at surface and at depth), in order to be able to estimate a much more realistic uncertainty.

Uncertainty analysis on density (and other petrophysical variables) from borehole logging data has been performed by the oil industry (Pasternack , 2009; Poete, 2012; Moore et al., 2011; Reichel et al., 2012); instrumental (measurements and calibration) and processing (correction and conversion processes) sources of error have been identified. Error propagation has been also studied (Pasternack , 2009; Pakyuz-Charrier et al., 2018) . However, much work is pending in relation to the estimation of accurate uncertainties derived from the natural variability, among other factors (Adams, 2005; Gaillot et al., 2019). Using outcrop samples, uncertainty related to the estimation method (usually Archimedes principle) is often small. Natural variability at outcrop and formation scales is very seldom determined, although both density and magnetic susceptibility and magnetic remanence very frequently vary. In fact, magnetic properties  $k$  and NRM may range 1-2 orders of magnitude in a given outcrop. Uncertainty can be estimated using statistical parameters characterizing the probability distribution of the samples for each lithology (v.g. minimum and maximum values, mean, median, mode, RMS, standard deviation, variance, standard error, Skewness, Kurtosis, etc.).

All in all, and to the best of our knowledge, the uncertainty related to the natural variability of petrophysical data (rock density, magnetic susceptibility and remanence) assigned to rock volumes



---

and its impact in modeling of potential fields data have been very scarcely evaluated. During the past few years some researchers (Sun and Li, 2015 and 2017; Giraud et al., 2017 and 2019) have partially tackled this problem and have proposed joint inversion workflows of petrophysical data together with gravimetric and geologic ones. More has to be done concerning the quantification of the uncertainty derived from the petrophysical data. In our opinion, only the statistically robust characterization of the rock density of a target formation at surface (and at different depths if possible) is the only way to estimate the real impact of its natural variability on the derived uncertainty in the final 3D models.





## 3. Interpretation and modelling of gravity data

### 3.1 Gravity anomaly maps and enhancement techniques

#### 3.1.1 Introduction

Gravity is a potential field. As it is well known, the potential at a given point is defined as the work we need to move the unit mass (or charge) from an infinite distance to that point through the so called “ambient field”. Being a potential field, gravity obeys Laplace’s equation, which states that the sum of second derivatives (i. e. the rate of change of the gradient field in the three orthogonal spatial directions) is zero. In a normal Cartesian coordinate system with horizontal axes  $x$ ,  $y$  and a vertical axis  $z$ , the Laplace’s equation takes the form:

$$\frac{\partial^2 A}{\partial x^2} + \frac{\partial^2 A}{\partial y^2} + \frac{\partial^2 A}{\partial z^2} = 0$$

here  $A$  is the gravity field and is a function of  $(x, y, z)$ .

The solution of this partial differential equation is easily performed by separation of variables

$$A_k(x, z) = (a \cos kx + b \sin kx) c^{kz}$$

where  $a$  and  $b$  are constants, the positive variable  $k$  is the spatial frequency or wavenumber,  $A_k$  is the amplitude of the gravity field corresponding to the  $k$  wavenumber and  $z$  is the level of observation. This equation shows that we can represent the gravity field in terms of sine and cosine waves whose amplitudes are controlled exponentially by the level of observation.

This is a periodical function and therefore can be expressed as the sum of Fourier harmonics of a fundamental wavelength. By decomposing the signal into its discrete components, it is possible to filter the signal by removing some of the harmonics in the Fourier domain and reconstruct back the signal into the space domain thus obtaining a filtered version of the original anomaly. A common drawback is that the harmonic content is not as periodic and discrete as required. In gravity surveys, for example, the gravity acceleration between stations is usually not periodic.. Besides, if distinct multiples of a fundamental frequency or wave number constitute the harmonics of a function, the wavelength spectrum is made up by a number of distinct values.. Nonetheless, a significant number of functions used in geophysics are best characterized by a continuous spectrum of wavelengths. To tackle this sort of problem, the spatial changes of gravity are represented by a Fourier integral. Instead of a discrete set, the Fourier integral is made up by a continuous set of frequencies or wave numbers and used to represent non-periodic functions. All in all, by using complex numbers, gravity anomalies can be enhanced by Fourier transforms both in two and three dimensions (Lowrie, 2007).



In general terms, a filter is a x-y, spatial function. If the gravity data representing function  $\Delta g(x, y)$  is multiplied by the filter function (convolution), result is a new function that corresponds to the filtered gravity data. Filtering spatial domain data can be time consuming in terms of computation. *The two-dimensional Fourier transform of a gravity map usually speeds up the process to filter the gravity anomalies.* An alternative and faster solution is to filter the Fourier transforms of the gravity and then apply and inverse Fourier transport of the result to recover the spatial domain data.

As we have seen in section, 2.1.4.3 the Bouguer anomaly represents the difference between the observed and the theoretical gravity and it is mainly caused by the mass distribution in the Earth's crust in relation to the isostatic balance conditioned by regional changes in elevation (Hinze, 2012). The Bouguer gravity anomaly reflects the density distribution of the Earth's interior and from its interpretation, it is possible to build up crustal and lithospheric models (at any given scale) that provides information of the geological structures (geometry and density variations).

Analysis Techniques	Concept	Reference	Comments	Structures enhanced						
				Regional anomalies	Local anomalies	Anomaly at depth	Shallow sources	Fault & contacts location	Fault & contacts at depth	
1 Regional anomaly	RegA	Averaged of Bouguer values over a circle of a given radius	Griffin, 1949	Equivalent to the second vertical derivative (Roi, 1958)	X					
2 Regional anomaly	RegA	filtering with filters of different cutoff wavelengths	Zurflueh, 1967		X					
3		Analyzed the shape of power spectra	Spector&Grant, 1970	Low&high-frequency breaks used to band-pass or matched filters.						
4 Residual anomaly	ResA	ResA = BouguerA - (RegA)	Nettleton, 1954	Enhancement of local anomalies		X		X		
5 Upward & Downward continuation	UpC & DoC	Attenuation or emphasizing of shorter wavelength anomalies using Fourier transform techniques	Kellogg, 1953; Dean, 1958 and many others	Enhancement of regional (UpC) or local (DoC) anomalies	X (UpC)	X (DoC)	X (UpC)	X (DoC)		
6 First and second derivatives		Derivatives of the Bouguer surface	???	Enhance short-wavelength anomalies from shallow sources		X		X	X	
7 Horizontal first derivative	HFD	Square root of the sum of squares of the x- and y-derivatives	Cordell, 1979	Map near-vertical boundaries; faults plutonic contacts, etc...	X	X	X		X	X
8 Vertical first derivative	VFD		???			X	X		X	
9 Tilt angle	TA	Ratio of the first vertical derivative to the horizontal one	Miller & Singh, 1994	Enhances subtle and prominent features evenly; edges not biased toward the largest gradient	X	X		X	X	
10 Goussev filter	GF	Scalar difference between the total gradient and the horizontal gradient	Goussev et al., 2003	Used to highlight faults					X	X
11 Euler deconvolution	ED	Estimates the depth of causative sources. Based on the 3 derivatives (x,y,z) plus, the so called structural index (SI)	Keating, 1998	Define the lateral location and depth of isolated faults and other contacts		X	X		X	X
12 multiple-source Werner deconvolution	MSWD		Hansen & Simmonds (1993)							
13 Continuous and discrete wavelet transforms	CWT & DWT		Chapin, 1997; Marlet et al., 2001	Location & boundaries of causative bodies by tracking the extrema of wavelet transforms		X		X		
14 Terracing	Ter	Iterative filtering that gradually increases the slopes of anomalies until vertical while simultaneously flattens the field between gradient	Cordell & McCafferty, 1989	The color scheme (terraces) reflects relative density contrasts						
15										
16										
17										

Table 3.1.1 – Summary of the enhancement methods described in this section (synthesized from Blakely, 1996; Nabighian et al., 2005; Lowrie, 2007; Jacobi and Smilde, 2009; Hinze et al., 2012).



The Bouguer anomaly can be regarded as the contribution of the gravimetric response of deep (long wavelength) and shallow (short wavelength) sources associated to deep-seated and shallow mass heterogeneities respectively. If the target are the upper crustal bodies, separating out both components into regional and residual anomalies helps to focus the interpretation. Prior to modelling (forward or inversion), several enhancement methods can be carried out to highlight different patterns and wavelength components of the Bouguer and/or the residual anomalies and to improve our understanding of the nature of the causative sources.

There is a plethora of mathematical filters depending upon the goals of the survey (shallow, deep, faults, contacts, etc.) (Table 3.1.1). Basically these techniques are used to separate out the signal from the noise. Signal and noise have to be defined based on the objectives we want to achieve on the study area. More enhancement techniques and additional details can be found in classic manuals and review papers (e.g. Blakely, 1996; Nabighian et al., 2005; Jacobi and Smilde, 2009; Hinze et al., 2012).

In this section we review some of them frequently used in some European Geological Surveys. For example, at IGME we mainly use horizontal and vertical derivatives to highlight contacts and faults that might be covered by sediments and Euler deconvolution to estimate the depth of the anomalous bodies. We also use upward continuation, filtering and polynomial fitting as some of the methods to obtain the regional Bouguer anomaly. Some examples study from the South Central Pyrenees and the Ebro Foreland Basin help illustrating their application.

### ***3.1.2 Bouguer, regional and residual anomalies ( $\approx$ 2.1.4.3)***

Once the Bouguer anomaly for each gravity station has been calculated, several interpolation methods are used to obtain a grid to elaborate the Bouguer anomaly contour map. The more recommended ones being the minimum curvature (Briggs, 1974), gradient enhance minimum curvature (O'Connell et al., 2005) or kriging (Hansen, 1993). If the geological target is located at shallower levels, its signal may be superposed on the regional gravity field associated to a larger and deeper heterogeneity. In this situation, it is needed to isolate the gravity signal related to these shallow bodies, procedure known as regional-residual separation. This is a critical step on gravity data interpretation. The main objective is to isolate the short wavelength anomalies (Residual anomaly) from the long wavelength anomaly (Regional anomaly) by removing the latter from the Bouguer anomaly. A broad range of methods can be applied to separate the regional and residual gravity signal, either by using a simple graphical approach based on profile data and, eventually, gridded data or by means of mathematical methods. Some of the mathematical methods used to calculate the regional field are the second vertical derivative (Henderson and Zietz, 1949 and Roy, 1985 after Griffin, 1949), the least-squares fit (Agocs, 1951), gravity modelling (Hammer, 1963), 2D linear-wavelength filtering with filters of different cutoff wavelengths (Zurflueh, 1967; Agarwal and Kanasewich, 1971), spectral analysis (Spector and Grant, 1970; Guspini and Introcaso, 2000) or others (Syberg, 1972; Pawlowski and Hansen, 1990).



Despite the regional-residual separation is a historical problem, there is not yet a single right answer and the applied method should be based on, or at least check against if possible, the geological knowledge of the target area and surroundings (Nabighian et al., 2005). Sometimes it is recommendable to extend your regional gravity farther out of the studied area to have a broader overview of the long wavelength signal and prevent edge effects. Estimation of regional gravity anomaly maps from satellite data (like GOCE) may be also a choice (Eicker et al., 2014; Bouman et al., 2015).

At IGME the more common method used for the regional-residual separation is the polynomial fitting (see Beltrao et al., 1991 and references therein) although we have also used filtering, upward continuation and isostatic calculation. Once the regional field has been extracted from the Bouguer anomaly (Figure 2.1.20), the remaining Residual anomaly (Figure 2.1.21) may appear as an untrendy contour map where anomalies stand out over a “flat” background. But, this is not always the rule since in some situation “regional” but shallow-seated density trends may appear. In any case, the Residual anomaly reflects the signal of the geological bodies located relatively close to the surface having different densities, shape, lateral extent and emplacement depth (Hamdi-Nasr et al., 2010).

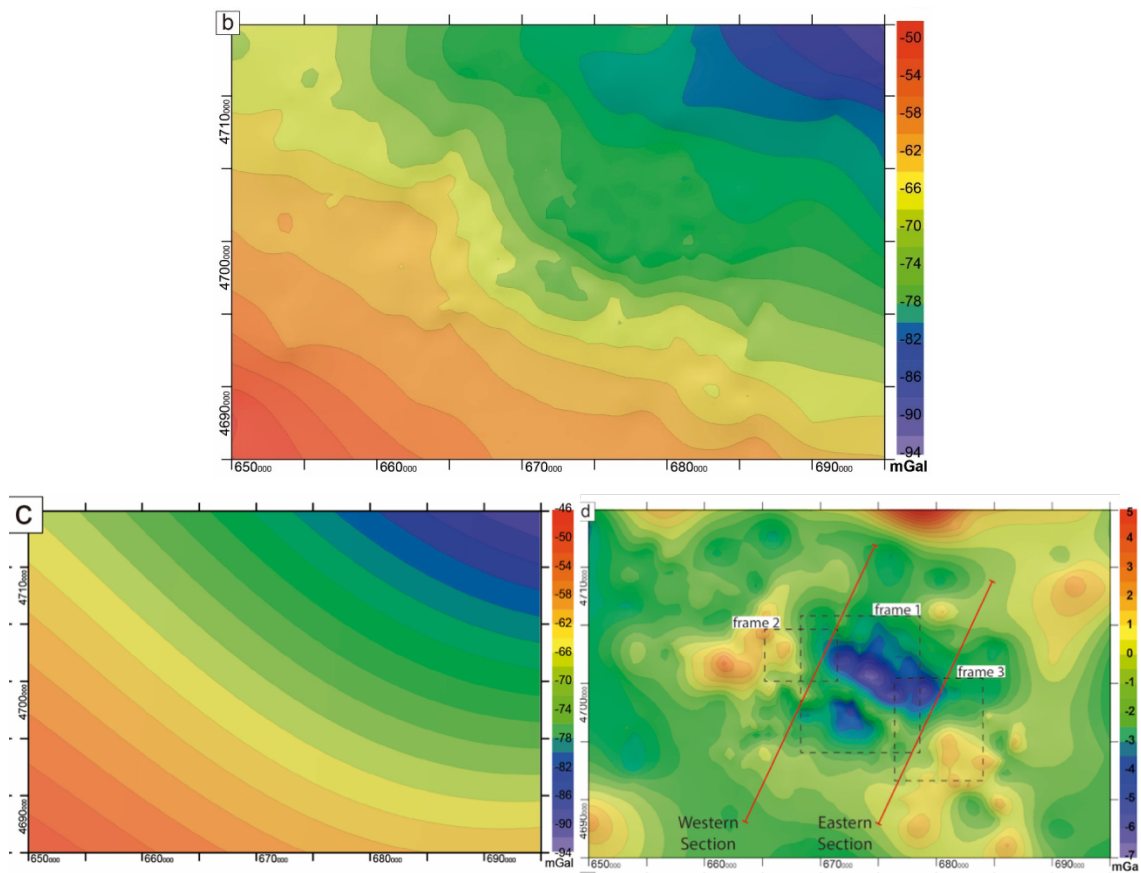


Figure 3.1.1. Top; Bouguer anomaly map from the Western External Sierras (Southern Pyrenees). Bottom; Regional and residual anomaly maps from the same region (Pueyo et al., 2021).



### 3.1.3 Filtering

As we have seen in the introduction, filtering is versatile way to enhance gravity anomalies. We can choose the characteristics of the filter we apply in the Fourier domain to eliminate specific wavelengths. For instance, a low-pass filter will cut out all the wavelengths shorter than a selected one and will let pass the longer wavelengths. Therefore, some Bouguer anomalies that can be considered spurious are removed with a suitable low-pass filter, leaving a filtered map, which is smoother than the original. Alternatively, the filter in the Fourier domain can be designed to eliminate wavelengths longer than a selected one and allow passing shorter wavelengths. The application of such a high-pass filter highlights the short-wavelength components (high wave number) of the gravity map.

Commonly, wavelength filtering is a method to enhance particular anomalies. They can be used to eliminate short wavelength, shallow-sourced gravity anomalies by using a low-pass filter or, conversely isolated them by removing the regional background by performing a high-pass filtering (Blakely 1996, Lowrie, 2007, Kim et al., 2020, Aydın & İşseven, 2021 and references therein)

### 3.1.4 Upward and downward continuation

The intensity and amplitude of an anomaly is a function of the distance of the mass that originates it from the observation plane. The potential field can be determined over an arbitrary surface if it is known over another surface below or above it (Peters, 1949). It is intuitively understood that if gravity can be measured or calculated at a height  $h$  meters above the surface, the Bouguer plane obtained will be more devoid of residual anomalies the higher  $h$  is. Contrary to measures or reductions by calculation to  $-h$  levels, anomalies of more superficial causes will be accentuated (Blakely, 1996).

Upward continuation can be used for obtaining of regional effects. Downward continuation, at least in gravimetry, has little physical significance, since it would require removing the effect of masses above the  $-h$  plane; In any case, the analytical calculations to obtain it are established from the mesh anomaly values, by systems analogous to those of derivation.

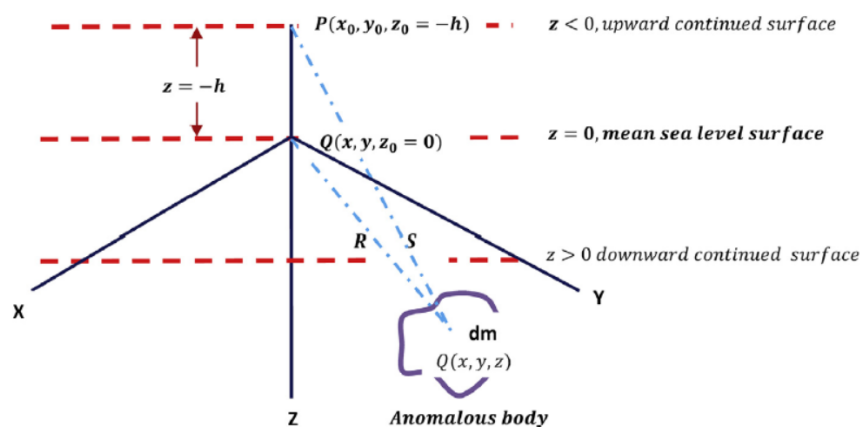


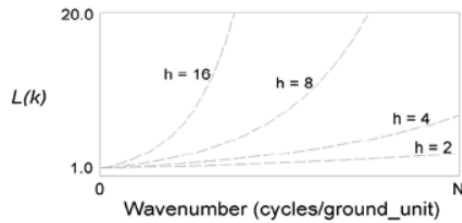
Figure 3.1.2. Representation of upward continuation technique in Cartesian coordinate system (taken from Kebede et al. 2020)



Kebede et al (2020) present an equation that can be used to developing an upward continuation filter, based in the gravitational attraction of an anomalous source body  $dm$  at a height,  $h$ , above mean sea level surface (see figure 3.12):

$$\Delta g_p = \frac{Gdm}{S^2} \frac{z+h}{S} = Gdm \frac{z+h}{S^3} = Gdm \frac{z+h}{[(x-x_0)^2 + (y-y_0)^2 + (z+h)^2]^{3/2}}$$

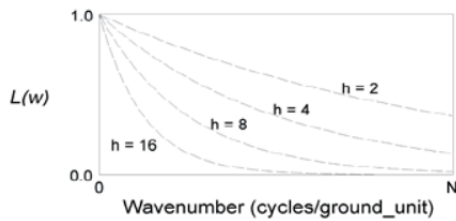
Oasis Montaj software, uses the next equations for doing the analytical continuation (upward and downward) (Geosoft, 2013)



$$L(\omega) = e^{h\omega}$$

**Parameter:**

$h$	Distance in ground_units, to continue down relative to the plane of observation.
-----	--



$$L(\omega) = e^{-h\omega}$$

**Parameter:**

$h$	Distance in ground_units, to continue up relative to the plane of observation.
-----	--

Figure 3.1.3. Graphical representation of upward (bottom) and downward continuation (top) (taken from How to guide applying filters with montaj Geophysics, Geosoft publication, 2013)

([http://updates.geosoft.com/downloads/files/how-to-guides/Applying\\_Filters\\_with\\_montaj\\_Geophysics.pdf](http://updates.geosoft.com/downloads/files/how-to-guides/Applying_Filters_with_montaj_Geophysics.pdf))



## 3.1.5 Derivatives of the gravity field

### 3.1.5.1 First derivatives; vertical, horizontal and tilt angle

The **first derivatives** of the gravity anomalies (horizontal, vertical and tilt angle filter of the Bouguer anomaly), also known as gradients, show the rate gravity is changing in any spatial direction and are very useful to resolve small variations in the gravity field that otherwise could go unnoticed. They depict lineaments, which can be correlated with geological structures like faults, thrusts and distinctive lateral lithological changes, and are especially useful in the absence of outcrops because they allow to correlate surficial structures with those that are total or partially buried and also reveal structures that do not crop out.

These derivatives act as a low frequency filter enhancing the short wavelength features (approximately less than 10 km following Blakely 1996) that allow identifying density contrasts mainly within the upper to mid crust levels since they filter the gravimetric response of the lower crust and the Moho topography (e. g. Readman et al., 1997). Once the horizontal (Cordell, 1979) and vertical (Evjen, 1936) derivatives are calculated, they can be represented in a map. We might choose the horizontal derivative in the X direction (i.e. W-E), in the Y direction (i.e. S-N), in any other particular direction we consider interesting and/or the complete horizontal derivative calculated as the root sum square of horizontal X first derivative and horizontal Y first derivative.

After identification of all possible lineaments in each map separately, we gather them to discuss its origin. Either they are related to outcropping geological features or to expressions of the subsurface geology. If the case is the latter, we try to establish a plausible hypothesis on the origin which will be later on proved or refuted during the modelling.

The **tilt angle filter or tilt derivative** is based on the ratio between the vertical derivative and the total horizontal derivative (e. g. Miller and Singh, 1994; Blakely, 1996), it can be used to define geological borders and mapping shallow subsurface structures avoiding the noise that tend to appear on the second vertical derivative or derivatives of higher order. It is also useful to highlight subtler gradient maxima in the gravity data because it acts as a “gain control”.

The derivatives can be calculated from a grid or from a profile. In the first case, the lineaments are depicted over the whole study area. In the second case, the lineaments can be directly associated with the features of a given geological cross section thus helping to improve the interpretation on the fly. All the mathematical formulation for the calculation of these derivatives can be found in classical books of potential fields (e.g. Blakely, 1996 or Hinze, 2012)

At IGME we mainly use the derivatives calculated from a grid and superimpose the results on the geological map to carry out a first interpretation prior the modelling. Our preferred software is Geosoft Oasis Montaj from Seequent. The derivatives along a profile can be imported in GM-SYS to support the interpretation and are very useful to reduce the uncertainties when other geological and geophysical information is scarce.



### 3.1.5.2 Second derivatives

The **second derivatives** measure the change of gradients in a given spatial direction and show the location of the maximum change of the corresponding gradient as well as the location of the inflexion points in the curvature of the function. Usually we calculate the second horizontal derivative that can help to distinguish geological features with similar horizontal gradient such as an intrusion or a basin (Figure 3.1.4 Kearey et al., 2002), estimate fault structures that are not clear from the first derivatives and enhance anomalies corresponding to shallow bodies.

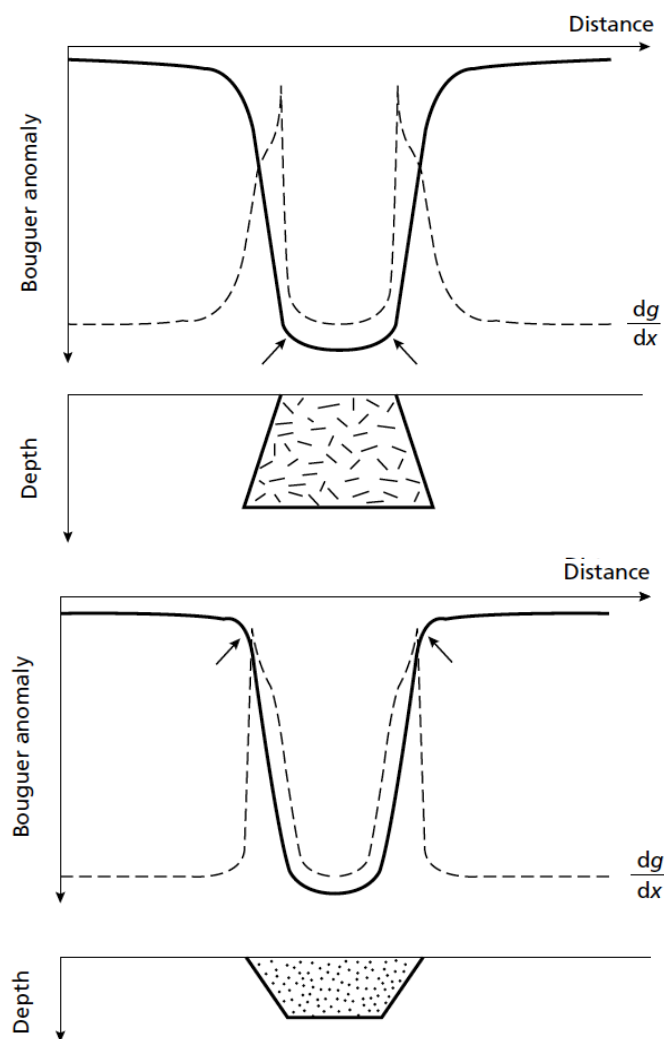


Figure 3.1.4. Bouguer anomaly profiles (black line) and their horizontal derivatives (dashed lines) of a granite body (left) and a sedimentary basin (right). Note how horizontal derivative values are at a maximum at the inflection point of the Bouguer anomaly profiles (taken from Kearey et al., 2002).

The second vertical derivative indicates how fast the vertical gradient is changing. It is less used than the second horizontal derivative because its interpretation is more complex.



### 3.1.6 Continuous and discrete wavelet transforms

A wavelet is a tiny oscillation in the shape of a wave that has an amplitude that starts at zero, then increases and decreases back to zero again. It can be used to harvest information from different kinds of data including many geophysical data as seismic or potential fields. The discrete wavelet transform is used mainly for signal codification and communication theory whereas continuous wavelet transform is commonly used in signal analysis.

In the last decades, the use of wavelet transform techniques has increased in the processing and interpretation of gravity data (Chapin, 1997) because they can be very helpful to obtain location-dependent spectral properties. The multi-scale analysis capabilities intrinsic of this technique makes it versatile.

The continuous wavelet transform (CWT) can be used for the regional-residual separation of the Bouguer anomaly (Fedi and Quarta, 1998; Xu et al., 2009), removing noise from the gravimetric signal (Lyrio et al., 2004), finding the boundaries of the anomalous bodies (Martelet et al., 2004), perform depth-base gravity data decomposition to evaluate the depth of causative sources (e. g. Handyarso and Kadir, 2017). The discrete wavelet (DWT) transform is mostly used for gravity inversion (e. g. Fedi et al., 2004).

At IGME we do not use the wavelet transforms because we calculate the regional-residual separation by means of the Zeng's method (Zeng et al., 2007), polynomial detrending, isostatic compensation or filtering; removing noise is carried out by filtering; the boundaries of anomalous bodies as well as identification of faults and other lineaments is performed using the first and second derivatives; depth of anomalous bodies is estimated using Euler solutions or Werner deconvolution and for gravity inversion we use the stochastic method implemented in GeoModeller.

### 3.1.7 Euler deconvolution

Euler Deconvolution is a method of grid analysis firstly developed by Thompson (1982) to make depth estimations from large amount of magnetic data. This technique serves at determine boundaries and estimate depths, used to recognize structures in the basement and to document depths of crystalline top basement beneath sedimentary cover. Nevertheless, this technique, based upon Euler's homogeneity relationship, is moreover applied to gravity method (Keating, 1998) and demonstrated on Bouguer anomaly, according to the equation developed by Thompson (1982).

$$(x - x_0) \frac{\partial T}{\partial x} + (y - y_0) \frac{\partial T}{\partial y} + (z - z_0) \frac{\partial T}{\partial z} = N(B - T)$$



Where  $T$  is the observed field,  $X_0$ ,  $Y_0$ ,  $Z_0$  are source anomaly locations,  $B$  is the base level of the observed field, and  $N$  is the degree of homogeneity and may be interpreted as a structural index (SI) which is a measure of the rate of change with distance of a field (Reid et al, 1990).

Choosing the right structural index (SI) is key to obtain the correct results. An index that is too low gives depths that are too shallow and a too high index gives too deep solutions (Reid et al, 1990). Generally speaking, the structural index is 0 for contacts, 1 for dike, 2 for vertical pipe and 3 for sphere if using magnetic data. But even if the index chosen is correct, it is demonstrated that depth estimates are more precise for high-index sources than for low (Reid et al, 1990). The real data always contain anomalies from different sources that can be depicted using different structural indices. So that, it is necessary to apply a range of indices and plot the results to decide which one better reflects the structure.

When we use gravimetric data we have to choose a lower index for each geological structure: 0 for dikes and contacts, 1 for vertical pipe and 2 for sphere. Both in magnetic and gravimetric data 0 index represents a physical limit, thus an index of 0.5 is often used to obtain reasonable results. Moreover, the anomalies arise from different sources and selecting a small window (spatial searching window for the data) will give lower sources while a larger window will depict broad and deeper sources. Once we choose the index we consider more appropriated according to the geological framework, different window sizes will arise deep sources and lower sources of anomalies. Therefore, to obtain reliable results we shall combine the right index and the right window. No matter the study we are dealing with, acceptable results are assumed when the solutions gather on trends that could be interpret as contacts, faults, dykes, intrusions etc. At this point is the expertise view the key to accept the solutions or try different ones.

Euler deconvolution is both useful to obtain depth estimation and boundary features with no initial geological prejudice. By varying the structural index and the searching window relatively good results are obtained which will help to investigate the subsurface geology.

### **3.1.8. Werner deconvolution**

The Werner deconvolution technique was developed by Werner (1953) aiming to improve the interpretation of the magnetic field. Hartman et al. (1971) computerized the interpretation and extended it to make the calculation valid for any magnetic inclination. Later on Ku and Sharp (1983) refined this method using Marquardt's least-squares method of inverse modelling to make the process automatic.

This technique is based on the use of the derivatives of the potential field and, as mentioned in the previous paragraph, is mainly used in the magnetic interpretation to estimate position,



depth, dip and magnetic susceptibility contrast along profiles. It is based on the assumption that the anomalies are originated by planar interfaces (like thin dikes or thin sheets) that have infinite strike and its depth extends perpendicularly to a profile. After the calculation, the results are analyzed to find and reject inconsistencies and spurious values. One of the most common applications is the calculation of the depth to basement (e. g. Stagg et al., 1989; Srivastava, 2004; Hassan et al., 2015)

Kilty (1983) generalized the Werner deconvolution method to be also applied to gravity data along profiles. Tsokas and Hansen (1997) developed a multi-source Werner deconvolution method applied to gravity data to study the variations of the crustal thickness in Greece along selected profiles; this method was later applied by Khair and Tsokas (1999) to investigate the crustal structure of the Levantine (Western Mediterranean). Other authors have been applying the Werner deconvolution in its investigations (e. g. Gimenez et al., 2009; Tassis et al., 2015) but its application using gravity data is not frequent. One of the advantages of the method is that provides a reasonable good estimation of the depth of the gravity anomalies' sources but only along profiles.

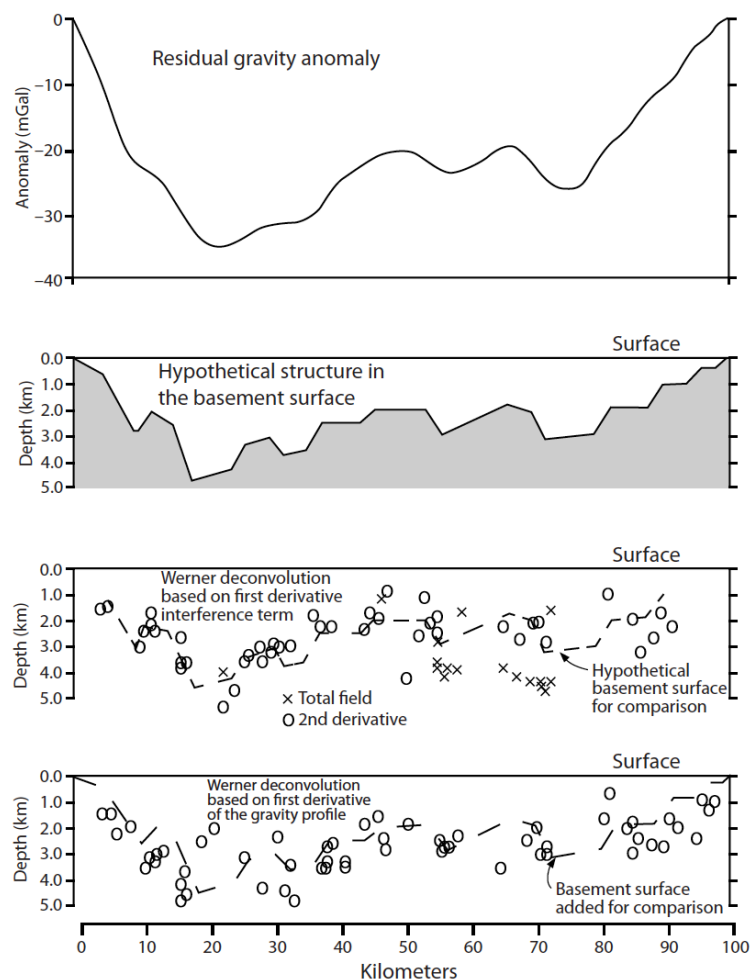


Figure 3.1.5. Classic example by Kilty (1983) illustrating the pioneer application of the Werner's deconvolution to gravity data (modified by Hinze et al., 2012, figure 7.10). The gravity effect of an hypothetical structure in the basement (vertical scale x4). Significant scatter precludes estimating an accurate depth of the basement but its maximum depth may be assessed since the deepest estimates fall near the basement surface.



### **3.1.9. Some case studies**

As long as an enough density contrast exists, the gravity method gathers a vast range of applicable scenarios. In a large scale, this method targets the shape of the Earth and isostasy observation and regional and global tectonics such as the structure and thickness of the crust or mantle anomalies, or studies of flexure and subsidence on continental margins (*e.g.*, Watts and Fairhead, 1999). In a smaller scale, gravity method is applied in the reconstruction of the structure, depth and density variation (i.e. lithology variations) of sedimentary basins and their inverted equivalents. A classical scenario where this approach is used is salt or igneous provinces, which are characterized by the presence of evaporites and igneous bodies; a more than suitable situation justified by the density contrast between these bodies and the host rocks. Even in a much smaller scale, (micro)gravimetry tackles engineering/construction site investigations, urban planning, cavity detection and glaciology.

As many other indirect techniques to study the Earth interior, gravity method developed hand in hand with exploration purposes such as fossil fuels (oil, gas and coal) or geothermal findings, energy and gas storages, the exploration of bulk mineral deposits (ore bodies, gravel, etc.) or the characterization of underground aquifers.



### 3.1.9.1. Detection of underground cavities in karstic areas in the Ebro basin.

Northeast of the Iberian Peninsula, the Ebro basin is limited by the Pyrenean (north), Iberian (south) and Catalan-Coastal (east) ranges. During the Pyrenean orogeny, it was the southern foreland basin of the Pyrenean range. In the Late Eocene, it was disconnected from the ocean and sedimentary system switched to continental with alluvial fans, shallow evaporitic and carbonate lacustrine systems, from the edges to the center of the basin. Later, the opening of the lacustrine system to the Mediterranean Sea (between 12,5 and 8,5 million years ago, Pérez-Rivarés et al. 2019; García-Castellanos et al. 2003) led to erosion of the terrigenous, calcareous and evaporitic (mainly gypsum and halite) rocks of the basin from the Late Miocene to the present. Quaternary deposits, fluvial terraces and mantled pediments, deposited over the eroded rocks in the Central Ebro Basin near Saragossa city.

Karst processes related to the dissolution of evaporites is a serious hazard in this area, resulting in property damages and potential cause of personal injuries. Depending on whether quaternary deposits are cohesive or non-cohesive, the sinking of evaporites-related sinkholes can be progressive or sudden (collapse) (Soriano and Simón 1995 and 2002; Soriano et al., 2019 and references therein). Preceding the collapse, an underground cavity exists. It is usually undetectable from surficial features since they are covered by nearly horizontal quaternary terrace deposits or already filled up by debris (natural and human-based). In this setting, microgravity prospecting together with other geophysics techniques (Mochales et al., 2007 and 2008) were used to characterize the geometry of underground cavities. The gravity measurements were taken with a Burris Gravity meter (ZLS corp.), with a precision of [c]0,001 mGal. The Z value (topographic elevation) of the station was constrained by a laser level with a precision greater than 1 mm (LEICA Sprinter). The measurement campaign was designed as a set of transects passing in and out the cavity (Figure 3.1.6). No topographic correction was applied due to the flat relief of the area and the Bouguer reduction density used was  $1,8 \text{ g/cm}^3$ . The transects crossing through the cavities display a well-defined gravity low: [c]-0,08 mGal. Out of the influence of the cavity, gravity values present a constant background with an oscillation of [c]0,02 mGal. Density measurements and gravity forward modelling allowed to characterize the infill of the studied karstic cavity.

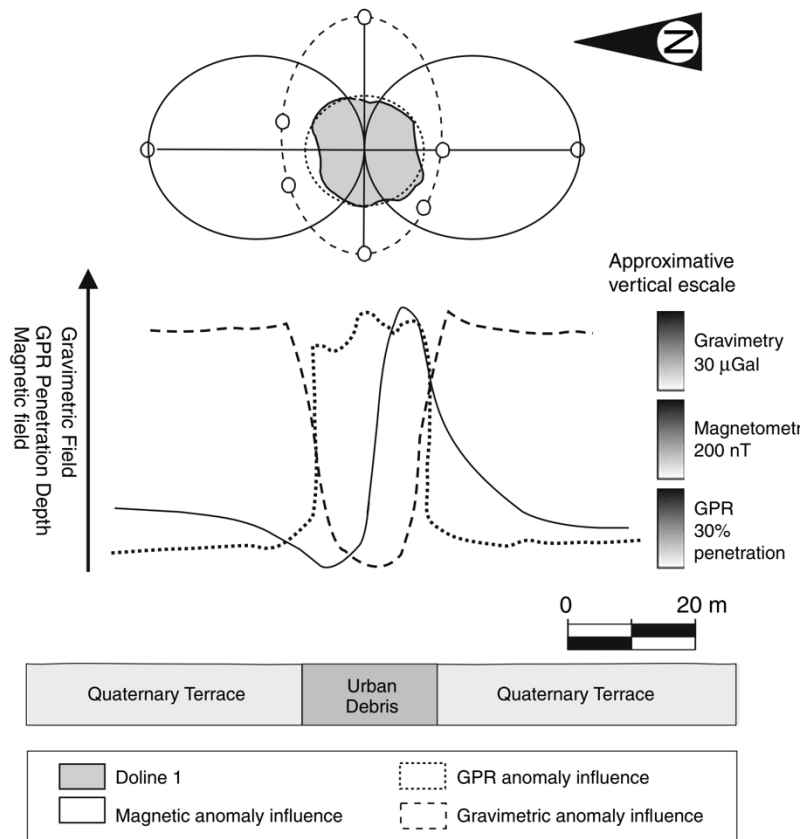


Figure 3.1.6. The gravity method is used, together other geophysical methods, to detect and characterize underground cavities (taken from Mochales et al., 2008).

### 3.1.9.2 Characterizing salt detachment distribution: Application of the gravity method in the South Central Pyrenees and Ebro foreland basin

The following case study is focused on the South Central Pyrenees. This mountain range arose from Late Cretaceous to Miocene because of the collision between the Iberian and Eurasian plates. South of the Axial Zone, the basement-related backbone of the chain, the South Pyrenean Zone is a fold-and-thrust belt commonly detached on Triassic salt units, the regional detachment of the Pyrenees. To the south, the Pyrenean units thrust over the Ebro foreland basin. The Ebro foreland basin registered the latest stages of deformation of the Pyrenean orogeny (Oligocene).



In the South Central Pyrenees, a prominent thrust salient stands out. It is constituted by a set of thrust sheets including, from north to south, the Cotiella-Boixols (Late Cretaceous), Peña Montañesa-Montsec thrust sheet (Paleocene-late Ypresian) and Gavarnie-Sierras (Lutetian-Oligocene) thrust sheets. This latter constitutes the southernmost and youngest structural unit. The Gavarnie-Sierras thrust sheet groups the following structural units: Sierras Marginales unit, Sierras Exteriores unit, its northeastern continuation, the Sobrarbe fold system and the transition area between them named as the Sierras Transition Zone. They detached along the Middle-Upper Triassic evaporites, that effectively uncoupled basement deformation resulting on a southward widening of the chain. Southward translation and internal deformation of this thrust sheet is mainly accounted by a diachronous succession of basement thrusts, named as the Gavarnie (from Early Lutetian), Bielsa and Guarga (from Late-Eocene) thrust sheets (Martínez-Peña and Casas, 2003; Casas y Pardo, 2004; Labaume et al., 2016; Muñoz, 2019).

The Gavarnie-Sierras thrust sheet consists of a southwards-thinning Santonian to Lutetian sequence that unconformably overlies remnants of Jurassic and the Middle-Upper Triassic evaporites and mudstones. Structurally, this domain is characterized by frequent, from restricted to few kms-wide outcrops of Middle-Upper Triassic evaporites and mudstones and embedded dolomites and dolerites which defines a diapiric province. To the south of the salient, several few kms-scale thrusts registered out-of-sequence thrusting and reactivations as recorded in alluvial Oligocene deposits. And, to the east of the salient, multiple, constantly spaced, N-S trending folds underwent vertical axis rotation during Eocene-Oligocene times (Pueyo et al., 2002; Mochales et al., 2012, 2016; Muñoz et al., 2013; Rodríguez-Pintó et al., 2016). Right in front of the southern limit of the Gavarnie-Sierras thrust sheet, the Barbastro anticline, a WNW-ESE, 90-km long, represents the deformation of the Ebro foreland basin as the southernmost deformation of the Pyrenean orogeny in this area. It is a continuous but geometrically variable along strike structure cored by Eocene evaporites and mudstones belonging to the Barbastro Fm. Our principal targets were to characterize the distribution of i) the Triassic detachment evaporites and mudstones along the Gavarnie-Sierras thrust sheet and ii) the Eocene evaporites along the Ebro basin (Santolaria et al., 2020) (Fig. 3.1.7A).



Density contrasts between the Eocene and Triassic evaporitic units ( $2,25 \text{ g/cm}^3$ ) and sedimentary rocks (*e.g.* Oligocene formations,  $2,40 \text{ g/cm}^3$ ; Cretaceous limestones,  $2,67 \text{ g/cm}^3$ ) or basement ( $2,75 \text{ g/cm}^3$ ) makes the gravimetric method suitable to characterize in 3D the spatial distribution (horizontal and vertical) of the evaporites in the southernmost Central Pyrenees and its foreland.

### Gravity survey and gravity anomalies

A total of 7376 gravity stations were used to obtain the Bouguer anomaly (Fig. 3.1.7B): 5469 stations from IGME and SITOPO databases (Ayala, 2013 and Ayala et al., 2016), 903 stations from Santolaria et al., (2016) and 1004 new stations (Santolaria et al., 2020). The gravity survey was focused on providing a homogeneous distribution of the stations to have a coverage of [ca] 1 station/ $\text{km}^2$ . New field measurements were made using Scintrex CG-5 and Burris gravimeters with a nominal resolution of 1microGal. Elevation and spatial coordinates were measured with differential GPS with a nominal precision of less than 0,05 m in X and Y and less than 0,1 m in Z. This precision gives a gravity uncertainty related to elevation below 0,03 mGal.

The new stations were linked to the International Gravimetric Network IGSN71 and the data was processed using the GRS80 formulation with a reduction density of  $2,67 \text{ g/cm}^3$  (Hinze, 2003). The topographic correction was applied to obtain the complete Bouguer anomaly. Once processed, the three sets of Bouguer anomaly databases were joined to obtain a continuous Bouguer anomaly map. Up to 6 anchor points between different surveys were taken to ensure a proper and robust link between datasets.

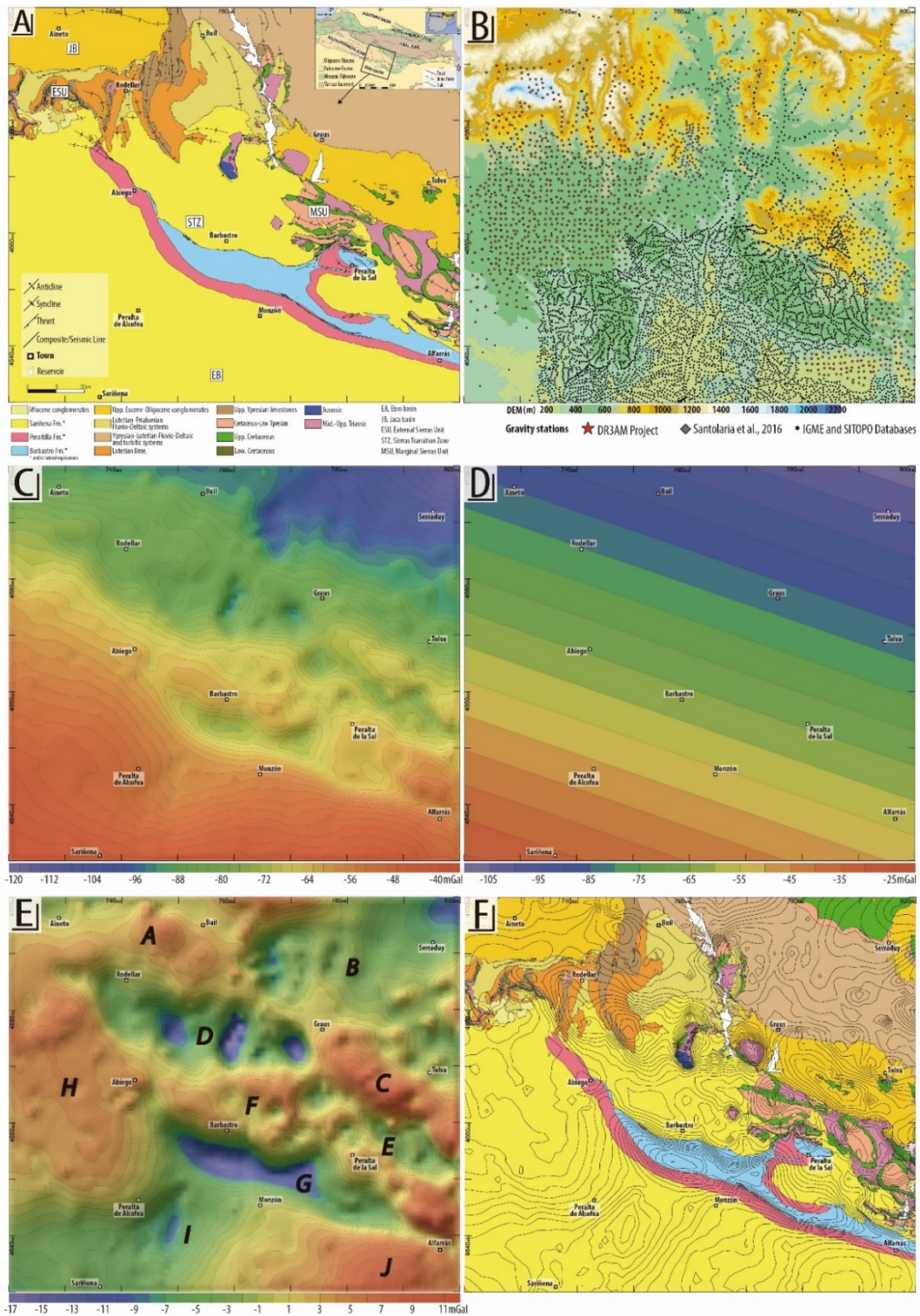


Figure 3.1.7. Application of the gravity method in the South Central Pyrenees and Ebro foreland basin. A) Geological map of the area where Triassic salts and mudstones and Upper Eocene-Oligocene evaporites are mapped in light purple and blue, respectively. B) Gravity station coverage by survey. C, D and E) Bouguer, regional and residual gravity anomaly contour maps. F) Residual anomaly contours are displayed together with the geological map to make easy the comparison and the gravity anomaly-lithology correlation.



The Bouguer anomaly map shows a long wavelength gradient that decreases from NW to SE ranging from -160 to 10 mGal (Fig. 3.1.7C). Superimposed to this gradient, there are relative maxima and minima of medium to short wavelength that are associated to density variations mainly related to Triassic salt accumulations within Pyrenean thrust sheets and Eocene evaporites in the Barbastro anticline (See Santolaria et al., 2016, 2020 for further details). In order to model these variations, a residual gravity anomaly (Fig. 3.1.7E) has been obtained by subtracting from the Bouguer anomaly a regional field (a degree 1 polynomial) (Fig. 3.1.7D) that reflects the contribution of the structures in the mid-lower crust and upper mantle. To perform the regional-residual separation, we tested several mathematical filters: polynomial kriging of the Bouguer anomaly values (Fig. 3.1.7D) and upward continuation of the Bouguer anomaly grid (Fig. 3.1.8). To illustrate the upward continuation processing, we display shallow upward continuation maps (1 km and 5 km, Fig. 2.1.25, A and B) where short-wavelength anomalies are still observed. Higher upward continuations eliminate these remaining short-wavelength anomalies (20 km, Fig. 3.1.8C) until the contours fit to a first order polynomial regional field like that found by polynomial kriging (50 km, Fig. 3.1.7D). The convergence of both methods highlights the suitability of the kriging approach that is done by defect at IGME.

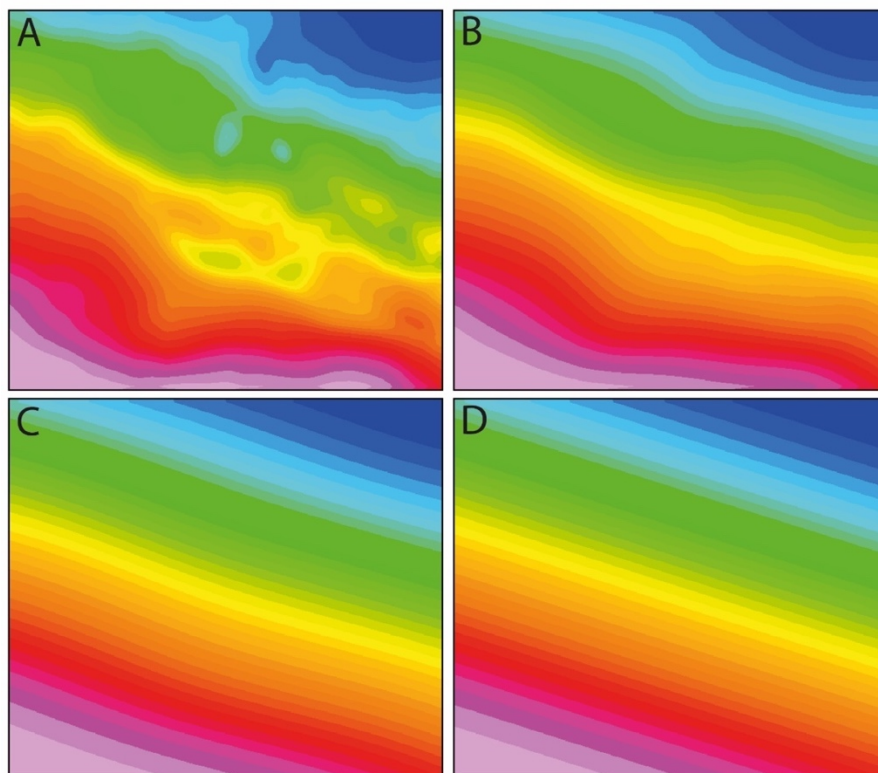


Figure 3.1.8. Upward continued Bouguer anomaly contour maps. Upward continuation heights are 1 km (A), 5 km (B), 20 km (C), 50 km (D).



The residual anomaly map (ranging -17 to 12 mGal, Fig. 3.1.7E) shows short to medium wavelength (5-15 km) highs and lows. Regarding the Sierras Marginales, the outstanding feature is the presence of several, evenly spaced, rounded to elongated gravity lows (-17 to -9 mGal). They correlate with the occurrence of Triassic evaporites and mudstones in outcropping diapirs or in the core of N-S trending anticlines (Figs. 3.1.7E and F). To the south east, several gravity lows (-6 to -3 mGal) also corresponds to outcrops of Triassic evaporites. The most prominent anomaly in the Ebro basin is a 30 km-long, WNW-ESE trending gravity low (-17 mGal) that correlates with the evaporitic core of the Barbastro anticline. This gravity low grades abruptly into a gravity high to the north but gradually disappears to the WNW and the ESE. To the south, it links to a NNW-SSE trending, 17 km wide gravity low bounded by two positive plateaus.

Broadly, gravity lows qualitatively correlate with evaporitic accumulations. But, to shed some light on the actual distribution of evaporites in depth, what it is the connection between anomalies or what is underneath sedimentary covered areas a more quantitative view is needed. This dense gravity station grid resulted in well-defined gravity anomaly maps. A proper starting point to use a quantitative approach: gravity forward and inverse modelling.

Prior to modelling, we also apply several mathematical filters that may help us to enhance the gravity signal, shed some light on the structural architecture at depth or guide us about the distribution of the sources of anomalies. All in all, this data processing and enhancement procedures could eventually assist during the subsequence modelling. The South Central Pyrenees and Ebro foreland basin residual gravity anomaly stands as an adequate scenario to test these methods and to illustrate their potential: i) variable structural trends from E-W to N-S, ii) shallow and deep-rooted gravity anomalies related to Triassic and Eocene evaporites and iii) abrupt (vertical faults) to gentle (facies changes) density boundaries.

North-South-trending salt accumulations are well depicted by the horizontal X axis derivative (Fig. 3.1.9A). They are displayed by low-high values pairs centered in salt body axes. Cropping out salt bodies pairs involved higher contrast than salt cored detachment anticline pairs. Conversely, thanks to the horizontal Y axis derivative (Fig. 3.1.9B), the Barbastro anticline axis



(N120E) it is shown by the limit between high (north) to low (south) values. To the West, this contrasting pair grades into a noisy area because the Barbastro anticline terminates and/or changes its trend to a more northern strike. Finally, the Z axis derivative highlights the salt outcropping and buried salt accumulation which are displayed in soft to dark blue (Fig. 3.1.9C).

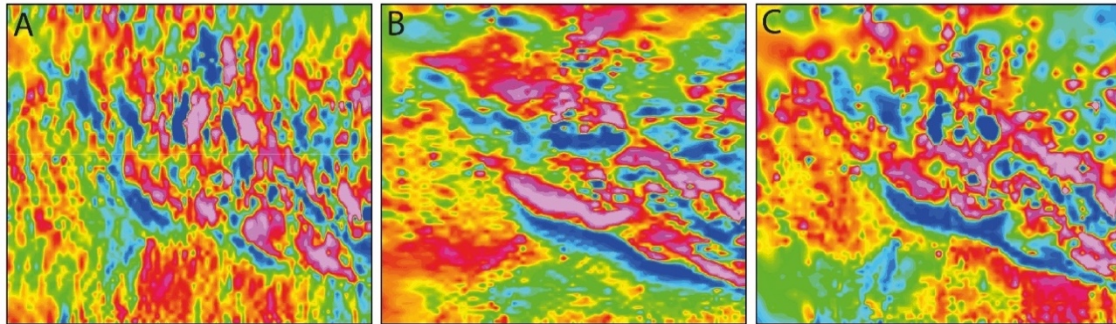


Figure 3.1.9. Horizontal X axis (A), Y axis (B) and Z axis (C) residual anomaly first derivative contour maps.

Procedures involving the aforementioned derivatives include the Tilt angle method and the Total Horizontal Gradient (Fig. 3.1.10). In both cases, the resulting contour map helps us to corroborate the usefulness of these enhancement methods to delineate salt body limits. For example, the signal of outcropping Triassic and Eocene salt bodies is enhanced by the Tilt angle method (Fig. 3.1.10A) while these bodies are bounded by net pink bands in the Total Horizontal Gradient contour map (Fig. 3.1.10B). One remarkable observation derived from all these enhancement methods is the evidence of Triassic salt bodies at the cores of almost all single thrust imbricates in the External Sierras thrust front (Balzes, Nasarre, Guara thrust sheets).

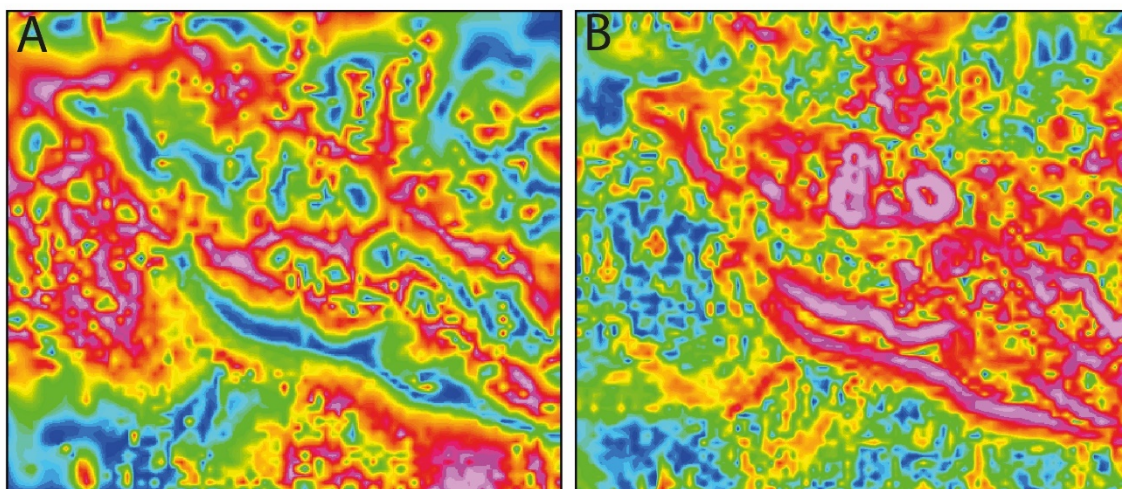


Figure 3.1.10. Tilt angle method (A) and Total Horizontal Gradient (B) applied to the South Central Pyrenees and Ebro foreland basin residual gravity anomaly.



As previously described for the first derivatives, the trend of structures is critical regarding the response to the second derivatives. In our case, second horizontal derivatives stand as a strong filter that only images the most prominent salt bodies: the North-South trending Triassic salt bodies in the center (Fig. 3.1.11A) and the Barbastro anticline core (Fig. 3.1.11B). Both structures are also recognized in the Z axis second derivatives (Fig. 3.1.11C).

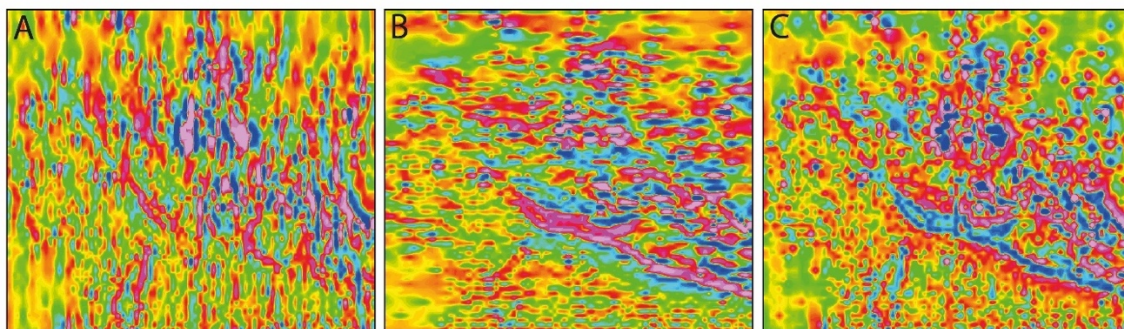


Figure 3.1.11. Horizontal X axis (A), Y axis (B) and Z axis (C) residual anomaly second derivative contour maps.

Finally, we apply Euler deconvolution to the gravity data to estimate depth of the sources as a straightforward method. We use Structural Index 1 and 2. Both indexes feature the Barbastro anticline due to the remarkable density contrast, but while index 1 provides shallower and more assembled solutions, index 2 gives deeper (around 1000 m deeper) and more scattered ones. To check the reliability of those data the next step should be 2D and 3D modelling that will help to unravel the morphology of the bodies related to the anomalies.

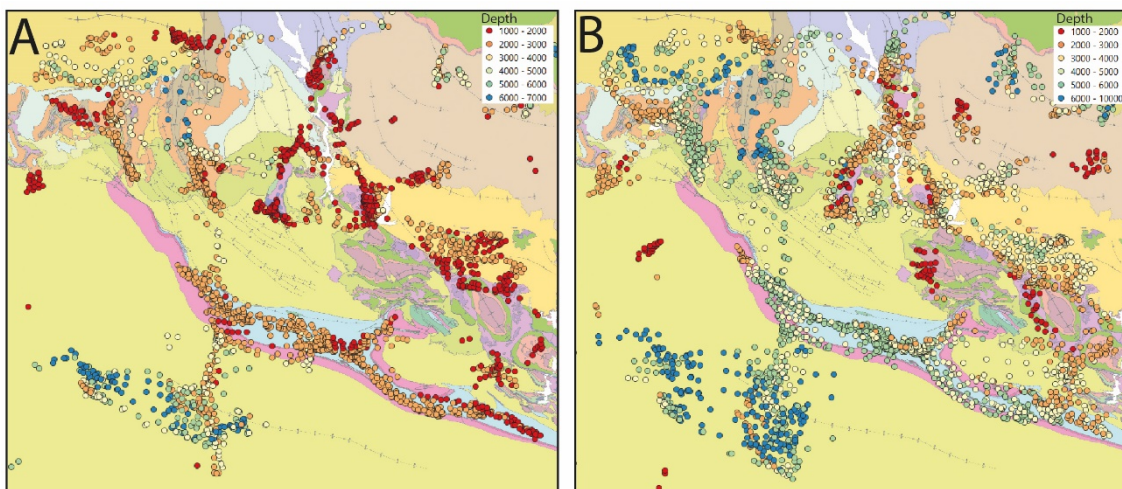


Figure 3.1.12. Geological map of South Central Pyrenees. On top Euler solutions points using structural indexes of 1 (A) and 2 (B).



### 3.1.9. Assessing structural style lateral variations: the Santo Domingo anticline

In the southwestern Pyrenees, the External Sierras represent the southernmost and frontal thrust sheet of the chain. Thrust sheet emplacement dates from Middle Eocene to Early Miocene as recorded in synorogenic sediments (Puigdefàbregas, 1975; Hogan and Burbank, 1996; Millán et al., 2000; Arenas et al., 2001; Oliva-Urcia et al., 2016 and 2019). The Santo Domingo anticline is the most prominent structural feature of the westernmost corner of the External Sierras. It is a 20 km long, WNW-ESE trending isoclinal anticline detached along the Middle and Upper Triassic evaporites (Nichols, 1984, 1987; Turner, 1988; Millán, 1996) (Fig. 3.1.13a). This structure was active from Late Oligocene to Early Miocene (Puigdefàbregas, 1975; Millán et al., 1995; Arenas et al., 2001). On the surface, it is characterized by nearly vertical to overturned vertical limbs. At depth, and due to the absence of seismic exploration, it has been interpreted as a large-scale detachment conical flexural fold (Millán et al., 1995) or as a cylindrical fold related to an underneath thrust ramp (Nichols, 1987; Teixell and García-Sansegundo, 1995; Teixell, 1996). These interpretations have direct implication on the amount and geometry of the Triassic rocks at depth (Fig. 3.1.13b): the detachment fold model involves a larger and symmetric salt core while the ramp anticline solution entails less salt and asymmetrically distributed.

As mentioned in the previous section, the density contrast between Triassic evaporites ( $2,28 \text{ gr/cm}^3$ ) and other sedimentary rocks in the External Sierras (*e.g.* Cretaceous or Eocene limestones,  $2,67 \text{ gr/cm}^3$ ) made gravimetry a suitable approach to distinct between these structural solutions (Calvín et al., 2017). Firstly, we designed the gravity station grid as series of longitudinal profiles and transversal sections (Calvín et al., 2017) that were lately densified (Pueyo et al., 2021). A total of 446 gravity stations, covering more than  $1000 \text{ km}^2$ , were considered (Fig. 3.1.14A).

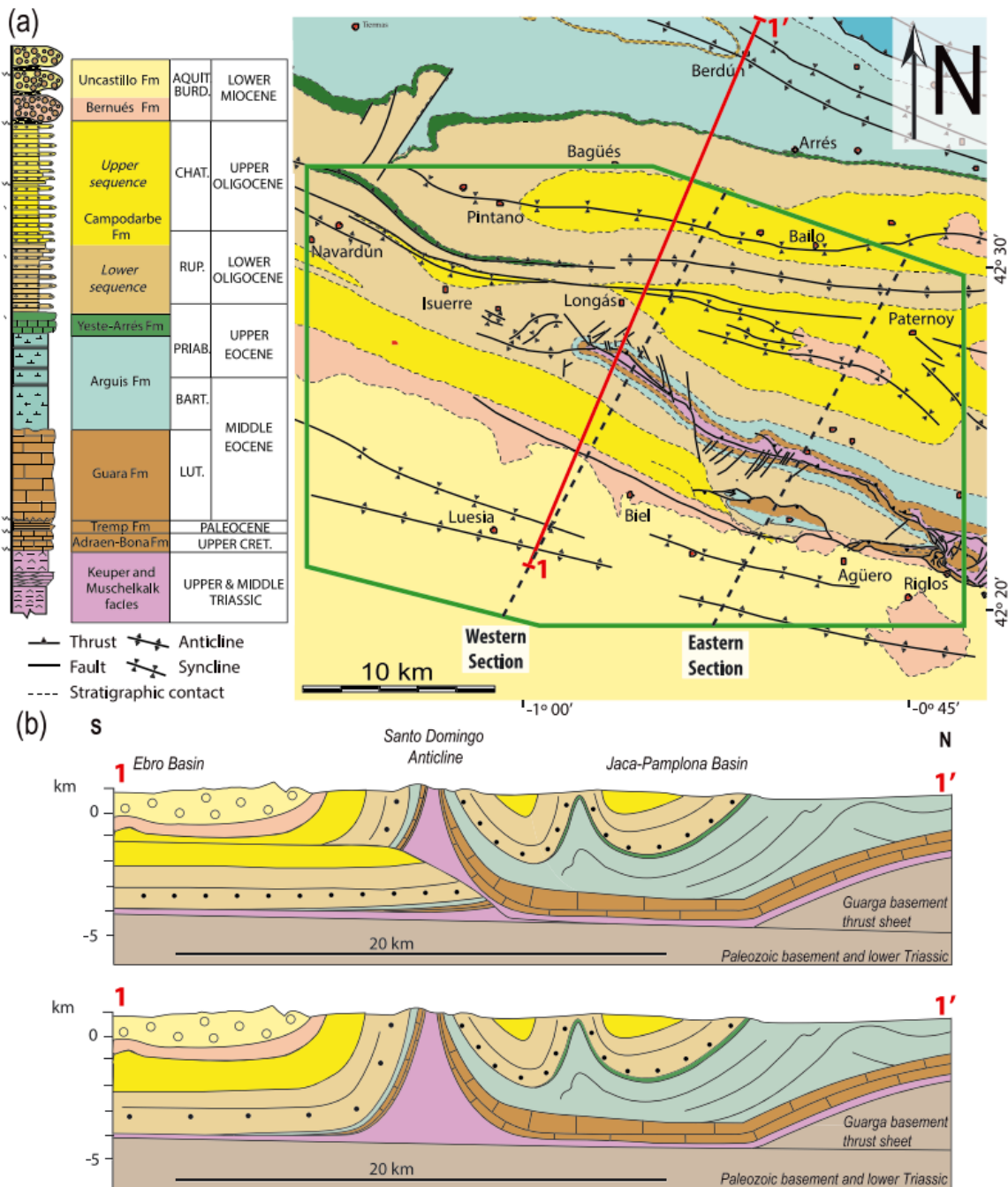


Figure 3.1.13. a) Geological map of the Santo Domingo anticline and surroundings. b) Two end-member solutions for the deep structure of the anticline: the ramp anticline (RA, top) and the detachment fold (DF, bottom) models. Taken from Calvin et al., 2017.



Differential GPS was used to establish the spatial location and elevation of new gravity stations; some of them periodically repeated during the campaigns to assure the internal consistency. As in Calvín et al. (2017), relative measurement were referred to the Spanish net for absolute gravity (REGA, Vaquero and Sainz-Maza, 2011) through the absolute gravity base located at the University of Zaragoza ( $g = 9.802241 \text{ m/s}^2$ ; E 674983, N 4612328, alt. 225 m, ETRS89-30 T zone). To ensure a reliable data merging previous and new gravity surveys, gravimeters used in both surveys (Scintrex, Lacoste&Romberg and Burris) were inter-calibrated and specific gravity stations revisited paying special attention in the GPS positioning and altitude estimation. The standard Geodetic Reference System (GRS80; Moritz, 1980) was used to calculate the Bouguer anomaly (Fig. 2.1.31 B) after applying the free-air correction (Hinze et al., 2005), the Bouguer correction (density reduction  $2,56 \text{ g/cm}^3$ ; see Calvín et al., 2017) and the terrain correction: near terrain correction was obtained in situ and medium to far terrain corrections were calculated from available DEMs (100 x 100m and 500 x 500m sampling grid respectively) using the Hammer Chart (Hammer, 1939) up to 167 km.

The Bouguer anomaly map (Fig. 3.1.14B). displays a SSW-NNW decreasing trend that was fitted to a third order polynomial surface (Fig. 3.1.14B C). After removing this regional signal from the Bouguer anomaly we obtained the residual anomaly map (Fig. 3.1.14B D). At the center of the area, a prominent symmetric gravity low (-5mGal) is separated by a relative gravity high. The boundary between gravity minimums trends N130E and correlates with the axis of the Santo Domingo anticline. To the NNW, it grades into a gravity high corresponding to the western termination of the anticline and likely the pinch-out of the salt detachment. To the east, a gravity high stands out over the surrounding background values (0 to -1,5 mGal).

The nature of the gravity anomalies in the area suggests along strike changes in the deep structure of the Santo Domingo anticline. Our results help to locate the transition from the occurrence of a footwall ramp in the east (Millán et al., 1995) to the periclinal termination of the Sierras Exteriores (Nichols, 1987).

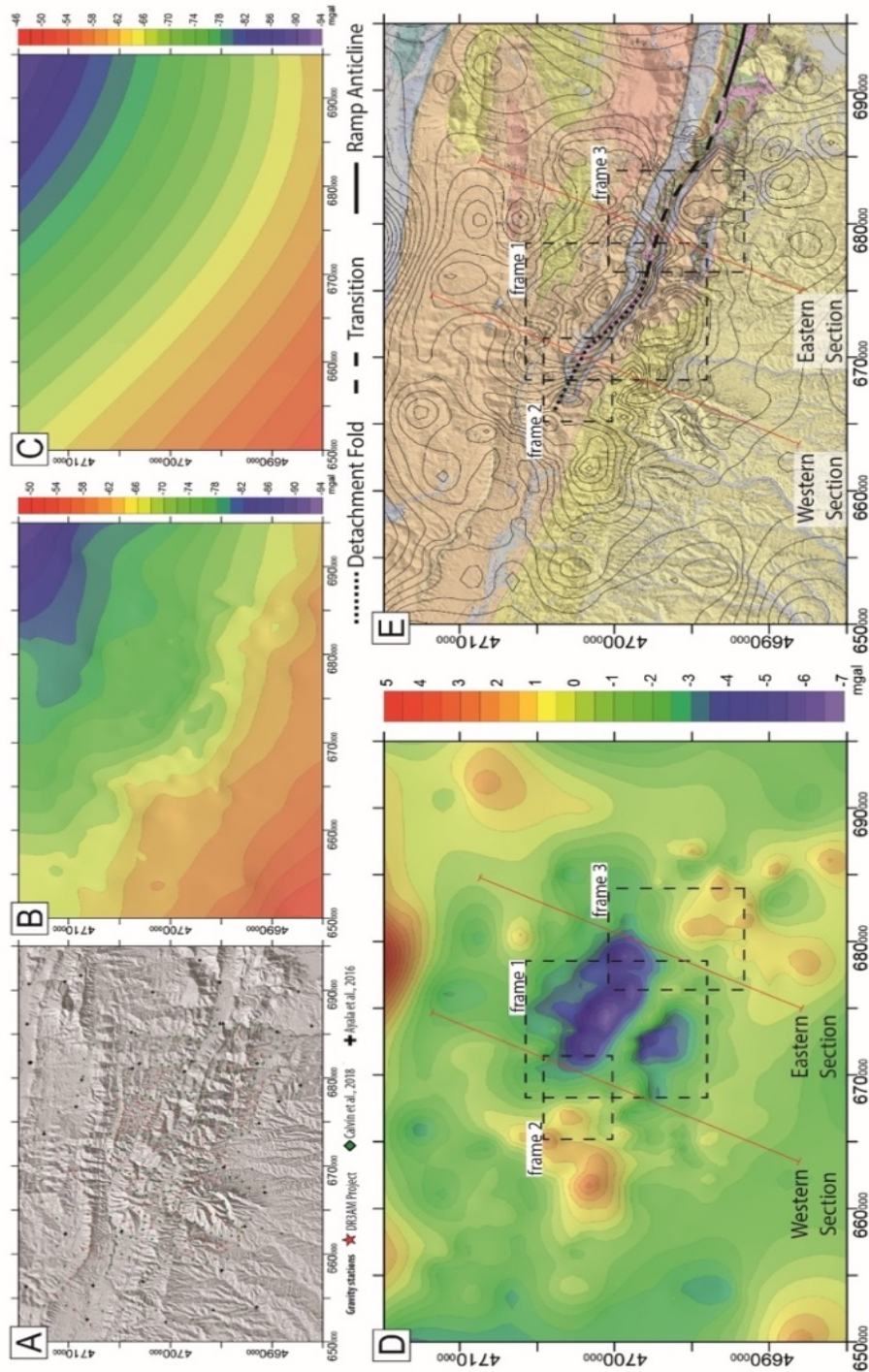


Figure 3.1.14. Application of the gravity method in the Santo Domingo anticline. A) Digital elevation model and gravity stations by survey. B, C and D) Bouguer, regional and residual gravity anomaly contour maps. E) Residual anomaly contours are displayed together with the geological map to make easy the gravity anomaly-geology correlation.



#### 3.1.9.4 Fault identification in the North German Basin by means of gravity interpretation

This study focusses on new evidence to the geological setting at the southern margin of the North German Basin (Fig. 3.1.15b). Prior to this study, two 3D geological models were separately developed for the cross-border region of the federal states of Saxony-Anhalt and Brandenburg (Malz et al., 2020; Schilling et al., 2018), which cover main parts of the study area. Both models base on depth maps of seismic reflection profiles and borehole data and cover the sediment column from the surface down to the Permian Zechstein layer. However, the models constraining data in the cross-border region are sparse and of low resolution (vintage seismic data), trend and shape of geological structures are poorly known and the 3D models are misaligned at the border by up to 500 m. Therefore, this study aims on harmonizing these two models in the scope of an integrated 3D geological and geophysical modelling. Main goal of the subsequent gravity interpretation is to obtain new information on the fault system, main geological structures and gravity anomaly sources in the cross-border region. Subsequently, this information will be accounted for in the gravity modelling process.

The gravity data were acquired in the course of five terrestrial gravity campaigns between the years 1934 and 1969 (Fig. 3.1.16a). Average spacing of the 5464 gravity readings is about 680 m (1.5 gravity stations per square kilometre). Originally, the gravity data were processed by different formulas and techniques and the surveys were tied to different gravimetric nets. For preparation of a new consistent gravity database, we reprocessed the data and applied a common datum by following the approach of Skiba (2011), as used for the preparation of the official Bouguer anomaly map of Germany (Skiba & Gabriel, 2010). In this approach, the gravity data are tied to the International Gravity Standardization Network 1971 (IGSN71) and the height are converted to the German First Order Levelling Network 1985 (DHHN85). The calculation of the complete Bouguer anomaly map (Fig. 3.1.16b) comprised a latitude correction, free-air correction, atmospheric correction, spherical Bouguer plate correction and topographic correction. The incorporated reduction density of  $1.85 \text{ g/cm}^3$  is based on 10 formation density logs in boreholes with Cenozoic cover and lignite.

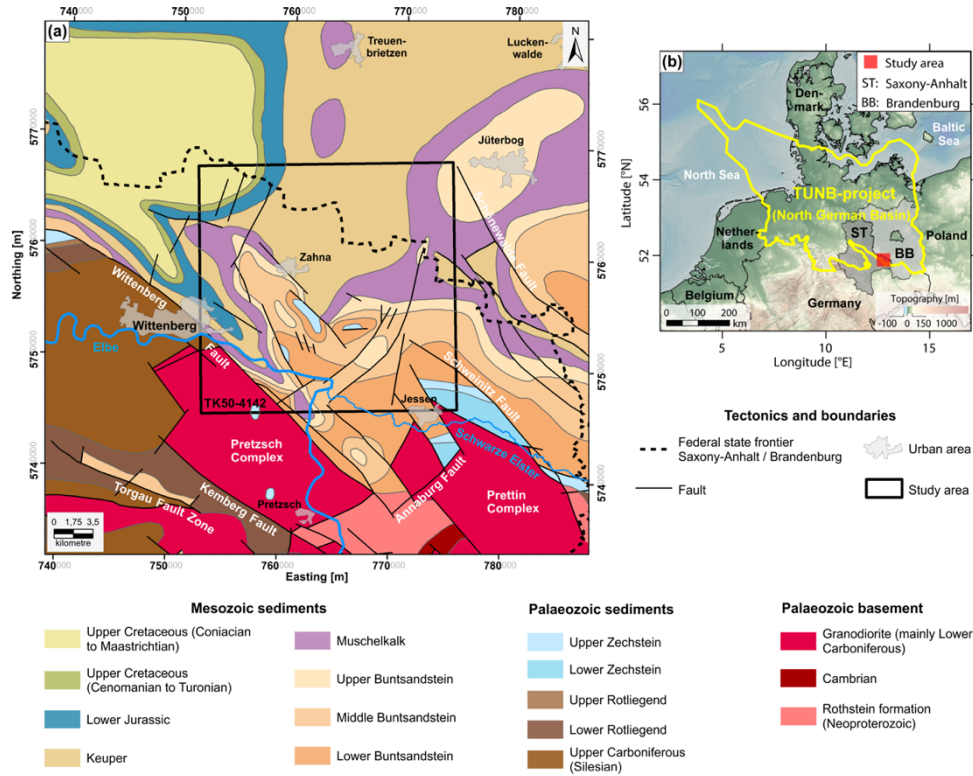


Figure 3.1.15. a) Geological setting of the study area (without Cenozoic cover). Structural information based on Martiklos et al. (2001). b) Overview map showing the study area's location at the southern margin of the North German Basin (modified from Mueller et al., 2021).

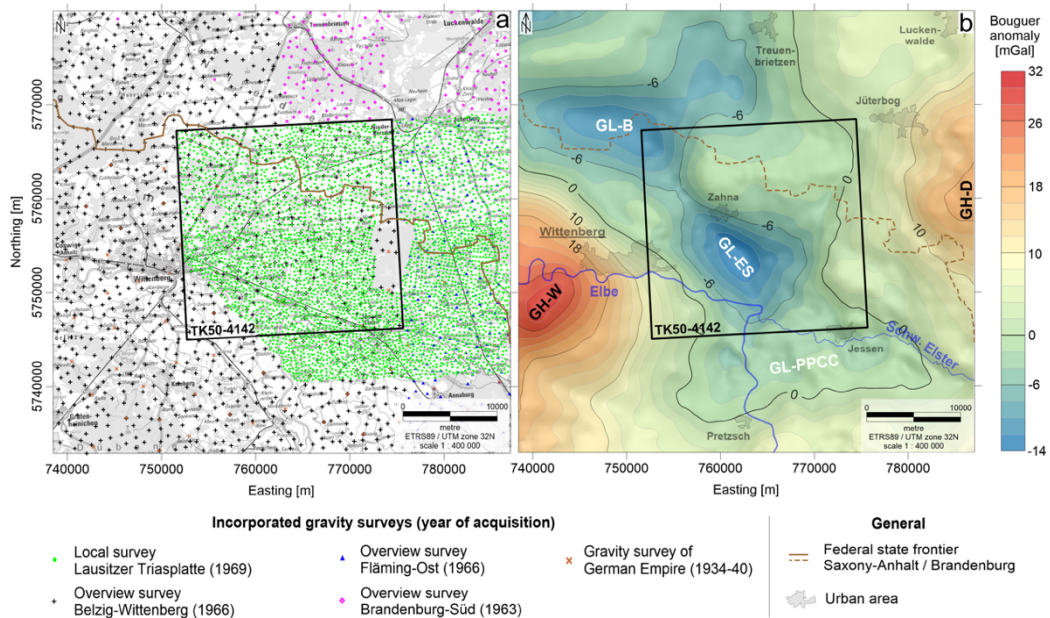


Figure 3.1.16. a) Available gravity stations in the study area at the southern margin of the North German Basin. The data were acquired in the 1960's to the 1990's and is colored by different surveys. b) New compiled complete Bouguer anomaly map of the study area. The gravity data is tied to the IGSN71 and was reduced with a density of  $1.85 \text{ g/cm}^3$  (based on lignite in Cenozoic cover). Abbreviations: GH-D: Gravity High of Dahme, GH-W: Gravity High of Wittenberg, GL-B: Gravity Low of Belzig, GL-ES: Gravity Low of Elster-Schweinitz, GL-PPCC: Gravity Low of Pretzsch-Prettin Crystalline Complex (Mueller et al., 2021).



The Bouguer anomaly of the study area is characterized by two main gravity lows, which are surrounded by prominent gravity highs. To obtain a first impression on the location of the gravity anomalies, we separated the Bouguer anomaly into regional and local component by wavelength filtering (Fig. 3.1.17). In the basin, short wavelength anomalies of the local field partly coincide with anti- and syncline structures. Long wavelength anomalies might either originate from deep-seated sources in the basement or shallow wide structures (e.g. small-scale sub-basins). Therefore, the horizontal gradient is calculated to highlight the position of density contrasts in the subsurface (Fig. 3.1.18). Some of the lineations coincide well with fault indications from vintage seismic data (red lines), which encouraged us to continue the fault indications throughout the entire cross-border area. The highest horizontal gradients are observed along the Wittenberg Fault and the Schweinitz Fault, which is in agreement with the largest fault displacements. To gain first rough insights into the depth extent and dip of the faults, the Bouguer anomaly map was bandpass filtered according to wavelengths caused by an isolated fault at different depths. Subsequently, the horizontal gradient was calculated for each of the wavelength filtered maps and plotted at the respective depth level. Preservation of a HDR maximum through several grids can be interpreted in terms of a fault's depth extent. However, the problem of non-uniqueness remains and requires careful interpretation.

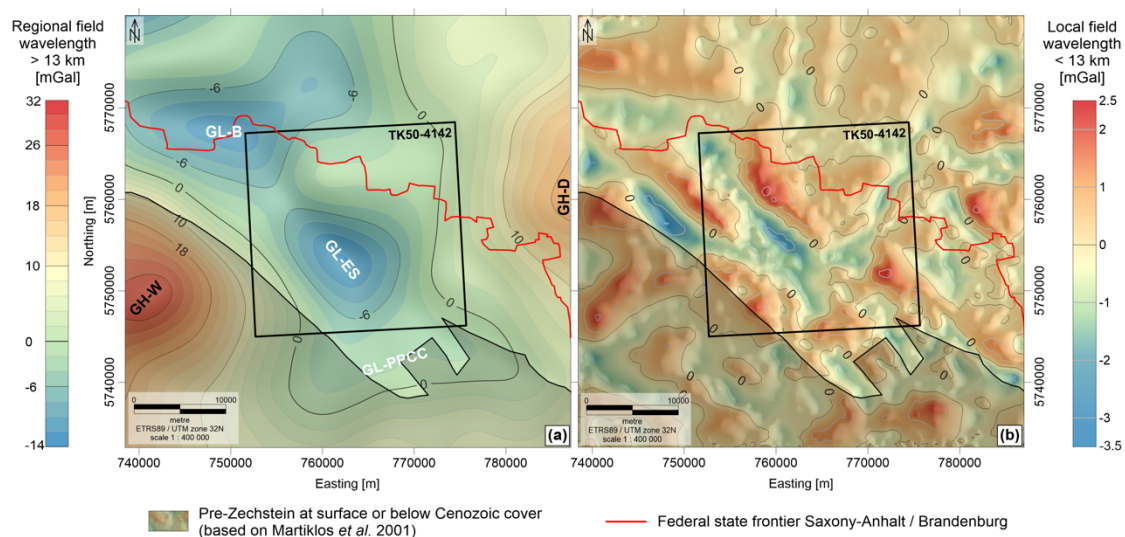


Figure 3.1.17. Gravity anomaly field separated into a) local and b) regional component by wavelength filtering of the complete Bouguer anomaly field (Mueller et al., 2021).

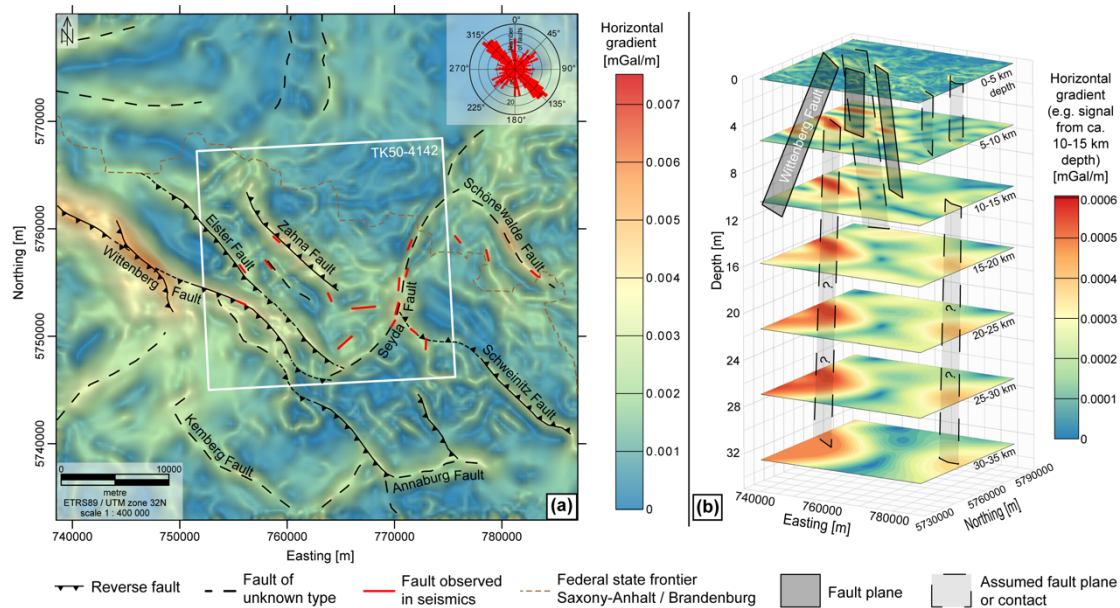


Figure 3.1.18. a) Horizontal gravity gradient with interpreted major faults. Their positions coincide with fault interpretations from seismic data (red lines) and allow a tracing away from the seismic profiles. The rose diagram in the upper right corner shows the main strike direction of all interpreted faults in the study area. b) Horizontal gradient maps of bandpass filtered Bouguer anomaly, which allow a first rough tracing of main faults with depth (Mueller et al., 2021).

Additionally, the vertical gravity gradient was calculated, as its characterized by narrow anomaly shapes and emphasizes shallow sources (Fig. 3.1.19a). In contrast, the tilt angle responds equally well to shallow and deeper sources and highlights sources of different depth level. For emphasizing the edges of these anomalies, the real part of the hyperbolic tangent function of the tilt angle is calculated (Fig. 3.1.19c).

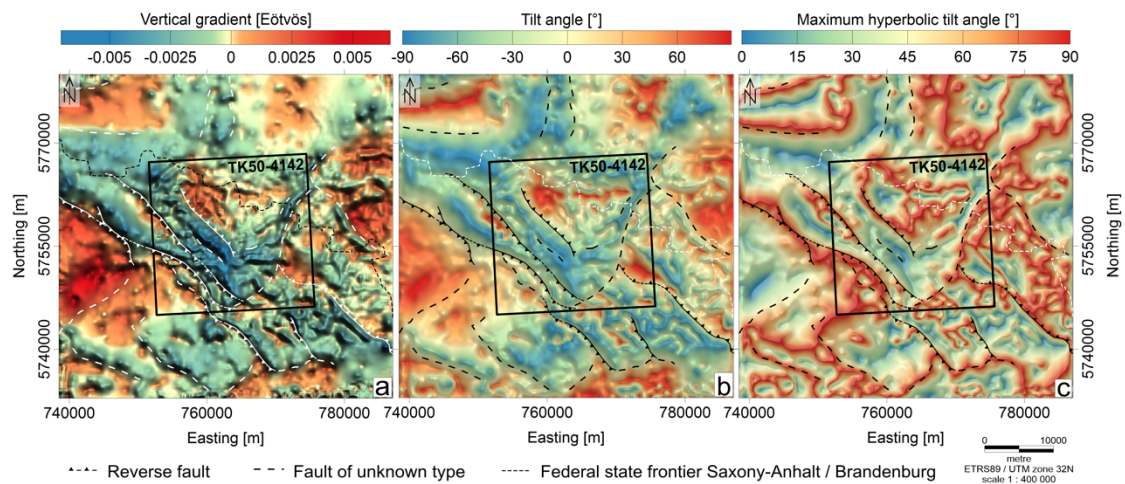


Figure 3.1.19. a) Vertical gravity gradient, b) tilt angle and c) maximum hyperbolic tilt angle for highlighting location, maxima and outline of main anomaly sources (Mueller et al., 2021).



So far, this investigation of the gravity gradients and their combination, did mostly provide information on the location of faults and main anomaly sources in the cross-border region as well as only rough information on the depth extent and dip. Therefore, we applied an Euler deconvolution (depth-to-source technique). According to our experience 3D Euler deconvolution for gravity data is most advantageous being applied to smaller regions to identify anomaly sources in the upper 5 km. For larger areas and depths the solutions hardly cluster or mostly in swirls. For larger study areas and deep sources, we obtained better results by 2D Euler deconvolution. Figure 3.1.20 shows the results of such an application for a structural index (SI) of 1. Here, the results are compared to fault indications in seismic reflection data. The Euler depth solutions cluster at most some to most of the seismic faults and show as well a different depth range. However, of course the Euler depth solutions are of lower resolution, leading to a partly ambiguous interpretation of the fault's dip. Application of the 2D Euler deconvolution to several profiles allow the subsequent spatial tracing of fault indications throughout the entire study area. All indications from gravity interpretation will be subsequently incorporated into the setup of a starting model and accounted for during the modelling process.

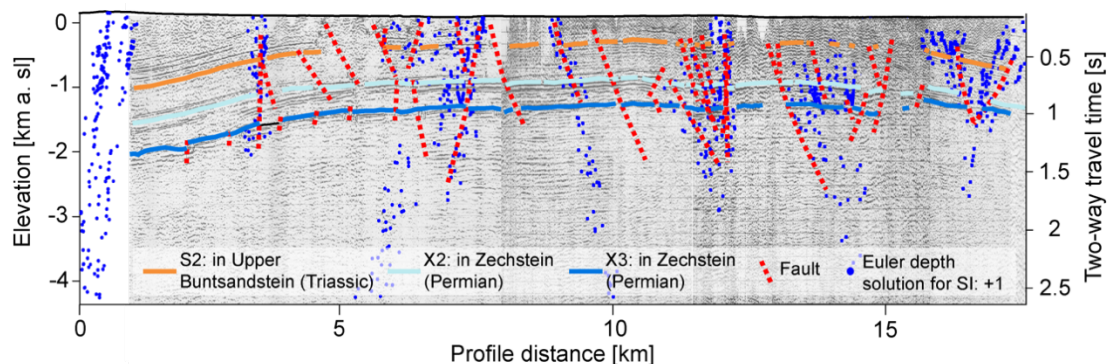


Figure 3.1.20. Comparison between fault interpretations based on seismic reflection data and depth solutions of a 2D Euler deconvolution. Noticeable is a good agreement between fault indications of both geophysical methods. However, Euler depth solutions (1) do not cluster along all faults, (2) are of lower resolution and (3) interpretation of the fault's trend and depth extent is partly ambiguous.



## 3.2. 2D & 3D Gravity modelling

### 3.2.1. Introduction

The objective of the gravimetric method is determining the density distribution of the subsurface rocks by analyzing the disturbances that geological bodies and structures cause in the Earth's gravitational field measured on the surface. This determination is achieved by gravity modelling, that focus on the understanding of the subsurface geometry and structure of the geological bodies. As we have seen in previous sections, the gravity data can be obtained either from public databases or by carrying out a gravimetric survey. In the first case, the gravimetric data will usually be available as free air or Bouguer anomalies. In the second case, the data is processed to obtain these anomalies. The objective of the gravity data processing on land is to obtain a complete Bouguer anomaly data (complete means that the topographic correction has been applied) and it contains information of the geological structures up to the lithosphere-asthenosphere boundary (section 2.1). When the target is at the upper crustal levels, we also need to remove the large regional gravimetric effects caused by the density variations in the lower crust and the mantle (see previous section 3.1.2 Bouguer, Regional and Residual anomalies) additionally, several filters can be also applied to enhance geological attributes before the modelling (section 3.1).

Geological modeling consists of the construction and visualization of a specific geological structure in order to determine its extension and internal structure as well as to characterize the geometry and physical properties of the different lithostratigraphic units. A geological model must be consistent with the entire set of available geophysical, geological and petrophysical data that, in turn, provide constraints for the geological and structural interpretation of the study area thus reducing the uncertainties.

Keeping in mind the main objective (imaging the subsurface geometry and its density distribution), the level of detail of the resulting model will depend on the spatial distribution of the measured data, the scale of the study area and of the petrophysical, geological and geophysical information available to be used as a priori information to limit the number of equivalent solutions inherent to the gravimetric modelling (and any geophysical method). It is important to note that level of detail is not to be confused with uncertainty: Detail means the dimensionality of the structures that can be resolved (in general of the scale from m to km) whereas uncertainty is a parameter, associated with the result of a measurement, that characterizes the dispersion of the values that could reasonably be attributed to the measured (<https://physics.nist.gov/cuu/Uncertainty/glossary.html>).

The modelling can be performed in 2D, in the so-called 2.5D and/or in 3D. We can also build 4D models provide we can know the evolution of the gravimetric field through time, for instance monitoring gas storages (Furre et al., 2017), geothermal reservoirs (Hinderer et al., 2015; Portier et al., 2018), volcanoes (Greco et al., 2012; Mouyen et al., 2016) etc. A 2D model is build up along a cross section perpendicular to the strike of the structures (whenever possible) assuming that the structures extend to the infinite either side of the cross section. In a 2.5D model it is possible to add a lateral limit in the third dimension to some of the structures thus



giving a more realistic model but still along a cross section. A 3D model offers a three-dimensional image of the variation of the petrophysical properties and geometries of the different subsurface geological bodies.

### 3.2.2. Gravity modelling techniques

Gravity investigates the subsurface geology taking into account the variations taking place in the gravitational field due to differences in the rocks density. In the modelling process, we build up a geological model and calculate its gravimetric response. The model is then modified in a feedback process between geology and gravity trying to obtain the best correlation between the observed and calculated anomalies with a model that is consistent with the geological data.

As any geophysical method, gravity modeling gives “non-unique” solutions and consequently the obtained model of the proposed structure is one of the possible solutions that honor all the available data. In this sense, starting with an initial geological model (usually balanced cross sections), gravity modeling helps to constrain the geometry and densities of the geological bodies at depth and is especially useful when limited or scarce seismic data are available or the seismic data lacks resolution. The number of possible solutions is further constrained when combining gravity with other geophysical data (e.g. magnetic), drillholes when available and petrophysical data.

Two techniques are used in geophysical modelling in general and in potential fields in particular: Forward modelling and inversion. When calculating forward modelling or inversion we have to be aware of the limitations that arise from the point gravity data we use. Usually the input data comes from a grid obtained interpolating between point data that usually has an uneven distribution. Therefore, we have to choose carefully the grid spacing in order create a grid that represents the observed gravity data without distortions. Although the grid is displayed as nice and colorful maps we have to keep in mind the original spatial distribution of the data. In general terms, the geological features we will be able to interpret will have a minimum extension of two times the grid spacing.

#### 3.2.2.1 Forward modelling

Conceptually, forward modelling basically consists of calculating the geophysical response of the model (gravimetric, magnetic, seismic, etc.), comparing it with the observations and varying the geometry and/or the physical properties manually or semi-automatically until the difference between observed and calculated anomalies are minimal. It is a trial and error process. The value of the “minimal differences” depends on different factors like the total amplitude of the observed anomaly, the resolution of the observed data, etc.

Forward modeling was firstly used in the interpretation of gravimetric and magnetic anomalies. It initially started estimating the gravimetric response in 2D caused by simple geometries, like polygons, as derived from the Green’s (1828) functions and identities (Nettleton, 1942; Talwani et al., 1959). Then, it followed the so-called 2.5D modelling (Rasmussen and Pedersen, 1960) which was based on the assumption of a finite length extension in the third dimension, that perpendicular to the modelled section. At the same time, the modelling of gravimetric



anomalies caused by 3D bodies (Talwani and Ewing (1960) was also initiated (see more details in Nabigian et al., 2005). The continuous improvement of computer performance during the 80's and onwards became in the launching of some pioneer software programs; Hypermag (Saltus and Blakely, 1983, 1993) or Gravmag (Pedley, 1991). For a more extended discussion on forward modelling the reader is referred to Blakely et al., (1995), Nabigian et al., (2005) Hirt, C., (2016) and references therein. Our workflow, strongly based on balanced and restored cross-sections, is aligned with the more recent concept of structural geophysics by Jessell et al., (1993) and Jessell (2001), where geological and geophysical information can be reconciled together according to a consistent geometric and kinematic model that explains the structural history of a region and its final gravimetric response.

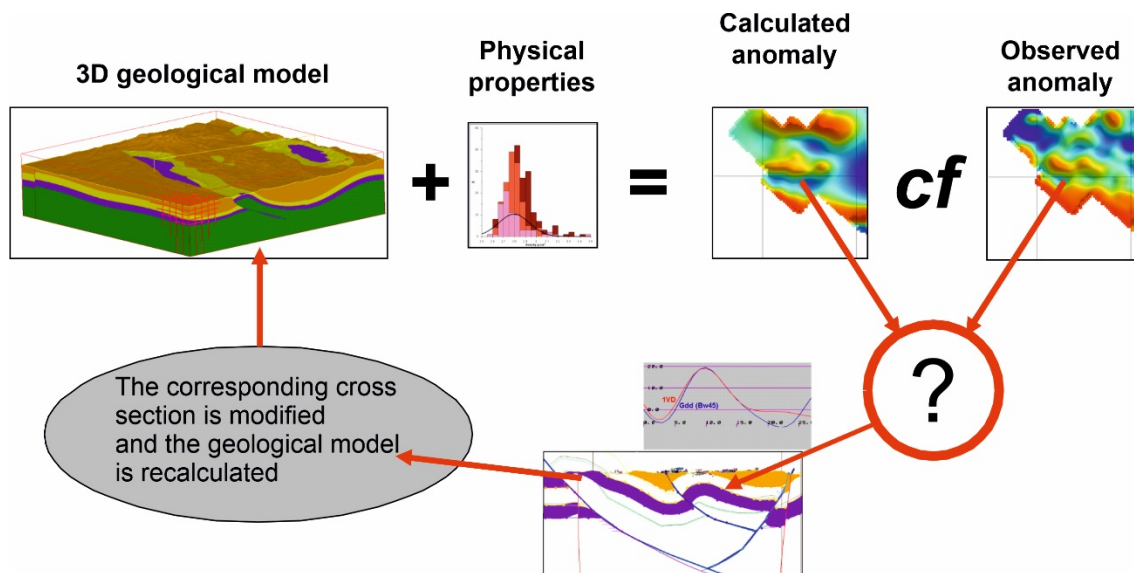


Figure 3.2.1 – Forward modelling workflow: We assign physical properties to the geological model and calculate its geophysical response. We compare the calculated and observed anomalies. If the difference is significant, we modify the model and recalculate. The process goes on until the observed and calculated anomalies are similar enough. This workflow can also be applied for 2D and 2.5D models. Figure modified from the GeoModeller manual.

### 3.2.2.2 Inversion

As we have seen in the forward modelling, the law of universal gravitation allows computing the expected gravity data from a given model (e.g. a 2D section with a given distribution of bodies of known densities) and then, comparing its goodness with the observations. Even if we can perfectly fit the data (the difference between observations and estimates is null), we find again the non-uniqueness problem “a given anomaly and a given density contrast may yield a wide range of possible interpretations” (Skeels, 1947). On contrary, the inverse problem (also called direct method; Blakely, 2005) applied to gravimetric data aims reconstructing a model of the subsurface from a set of gravity measurements (Tarantola & Valette, 1982; Snieder & Trampert, 1999; Oldenburg & Li, 2005; Sjöberg & Bagherbandi, 2017). In gravity modelling of the subsurface, and letting apart the inherent uncertainty of the data (and the processing behind), several physical laws (gravitation, mechanics, etc.) and geometrical rules (governing the stratigraphic and deformed bodies) are involved and the inverse problem is not straightforward. Therefore, some assumptions have to be taken because a precise and unique



formulation showing the way the data have to be transformed to replicate the model does not exist. The formulation overview is described in length by Blakely (2005), reference publications on inversion of geophysical data and a historical synopsis on inversion of gravimetric data can be found in Portniaguine & Zhdanov (1999) and Treitel & Lines (2001) Nabighian et al. 2005).

In a practical sense, the inverse modelling of gravimetric data consists of allowing the selected software (there are several available solutions) to automatically modify the model (geometry and/or physical properties) to minimize the difference between observed and calculated anomalies. We can let the calculation run free but there is the risk that the results might not have any geological meaning. Alternatively, we can introduce several constraints (well logs, interpreted seismic profiles, surface geology, etc. see following sections) to guide the software on how geometry or petrophysical properties can be modified. By doing so, the resulting parameter minimized observed versus calculated misfits while being consistent with the geological and geophysical observations.

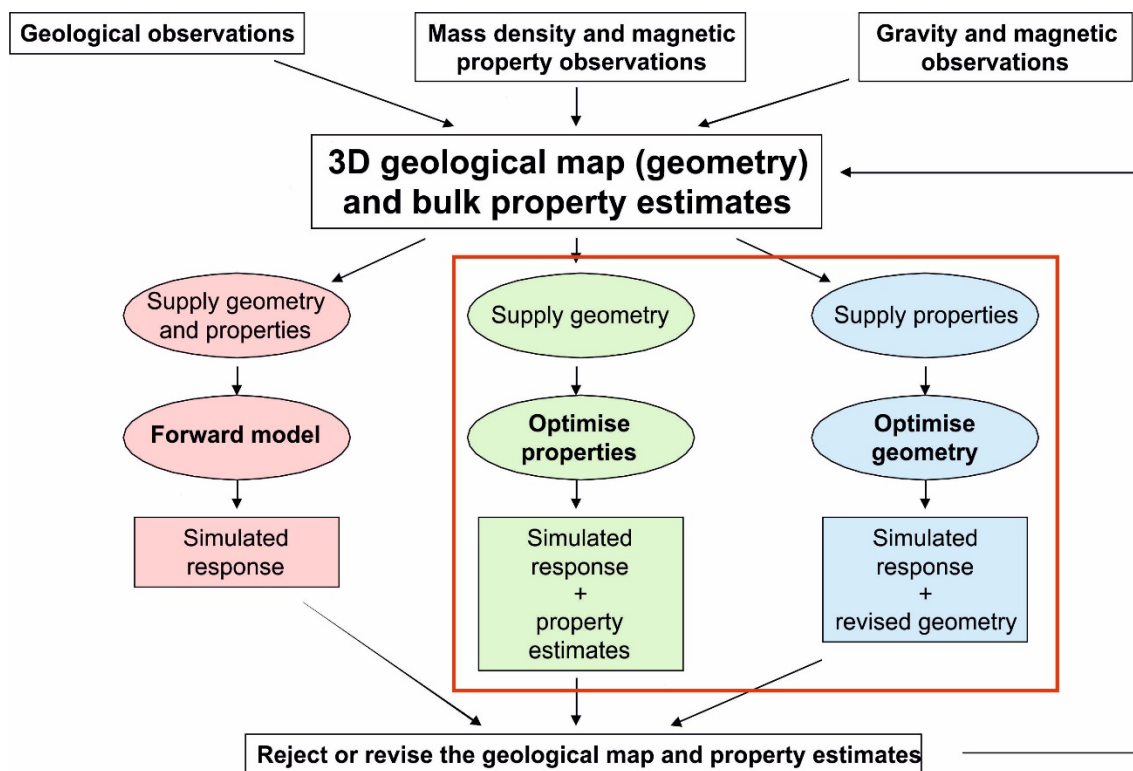


Figure 3.2.2 – Inversion workflow. Modified from GeoModeller manual.



### 3.2.3 Some current 2D & 3D Modelling software

Beyond the processing solutions for gravimetric (and magnetic) data (see table 2.1.7), software packages to model potential fields have been developed from the last 90 + years in research centers either public (universities, geological surveys, public research institutions, etc.) or private (Table 3.2.1). Some of the software developed in public research centers was “in house”, free for other academic users (e.g. Bott, 1960; Zeyen and Pous, 1993) other software evolved from “in house” to commercial and then was discontinued (e.g. Gravmag from BGS, Pedley et al., 1993) or evolved from “in house” to commercial and developed further expanding its capabilities (e.g. GeoModeller from BRGM, now available to purchase from Intrepid Geophysics; Lajaunie et al. 1997, Bosch et al., 2001, etc.).

Oasis Montaj GM-SYS & GMSYS 3D from Seequent (former Geosoft) and GeoModeller from Intrepid Geophysics are very complete, versatile and used software for 2D, 2.5D and 3D gravity and magnetic modelling. These software packages have a very thorough help system and a lot of information can be found on the Web pages so here we will only give a general outlook of the software main functions. Although the cost of the license acquisition and maintenance are expensive, academic agreements are often provided for public research and academic institutions. During the past few years, other computer programs for 3D modeling and inversion of potential field data have shown up; 3GRAINS (Snope & Casten, 2006), IGMAS+ (Schmidt et al., 2010), GinGER (Altwegg et al. (2015), GCH\_gravinv (Pham et al., 2018), DenInv3D (Tian et al., 2018), IGUG (Vatankhah et al., 2019).

At IGME for potential field processing and modelling we use Oasis Montaj (specifically the modules GM-SYS and GMSYS3D for 2D, 2.5D and 3D modelling) and 3D GeoModeller (only 3D modelling). We are familiar with Gravmag as well but we hardly ever use it because the complexity associated to build the initial model. See next section.

#### 3.2.3.1 Gravmag (BGS)

Gravmag started as an “in house” 2D – 2.5 D gravity and magnetic modelling package at BGS and then evolved up to a point where it was given to Ark Geophysics for commercial purposes. In 2005 this company was acquired by ARKeX and that company was bankrupt in 2015 thus making Gravmag almost disappear. Nonetheless, until Rob Pedley (one of the co-authors) retirement a while ago, BGS had held a Gravmag licensing system on demand for free to academic institutions. In any case Gravmag software is(was) much more affordable if compared to other computer packages produced by private companies as GM-SYS (Oasis Montaj; Gemperle et al., 1991; Whitehead et al., 2008) or 3DGeomodeller (Intrepid Geophysicis, 2006; Calcagno et al., 2008; Guillen et al., 2008) (Table 3.2.1).



	Gravmag (BGS)	GM-SYS Oasis Montaj	3D Geo modeller	IGMAS+	GinGER	GCH_gravinv	DenInv3D	IGUG	FatGrav	ZOND-GM2D&3D
<b>References</b>	Pedley et al., 1993	Gemperle et al. (1991) Whitehead & Musselman (2008)	Intrepid Geophysics (2006)	Götze & Lahmeyer (1988), Schmidt et al. (2020)	Altwegg et al (2015)	Pham et al. (2018)	Tian et al (2018)	Vatankhah et al (2019)	Price, Aaron	Kaminsky, A. E. Zond-programs for Geophysics
<b>used in...</b>	IGME/UZ	IGME	IGME	LAGB, GFZ, University of Kiel, Statoil						
<b>url</b>	????	<a href="https://www.geosoft.com/products/gm-sys">https://www.geosoft.com/products/gm-sys</a>	<a href="https://www.intrepid-geophysics.com/product/geomodeller/">https://www.intrepid-geophysics.com/product/geomodeller/</a>	<a href="http://www.gfz-potsdam.de/igmas">www.gfz-potsdam.de/igmas</a>		<a href="https://github.com/eroksum/gch-gravinv">https://github.com/eroksum/gch-gravinv</a>		<a href="http://fastgrav.com/download/">http://fastgrav.com/download/</a>	<a href="http://zond-geo.com/english/zond-software/gravity-magnetic-self-">http://zond-geo.com/english/zond-software/gravity-magnetic-self-</a>	
<b>Private/academic/governmentl</b>	Gov	Priv	Priv	Acad	Acad	Acad	Acad	Acad	Private	Private
<b>Affiliation</b>	BGS	Geosoft/Montaj	Intrepid Geophysics	GFZ	University Neuchâtel & RBR Geophysics	VNU University of Science/Süleyman Demirel University				
<b>License cost</b>	non-expensive/Free under academic agreement	Expensive	Expensive	Free under academic agreement	?	Free			Free (optional donation)	2.090 €
<b>Variables considered</b>	Grav/Mag, Petrophys, Geometry, Faults	Grav/Mag, Petrophys, Geometry, Faults, Stratigraphic thickness, Bedding data	Grav/Mag, Petrophys, Geometry, Faults, Stratigraphic thickness, Bedding data	Grav/Mag (incl. gradients and invariants), Geometry, Faults						
<b>Import formats</b>		Numerous	Numerous	Numerous						
<b>Export formats</b>		Numerous	Numerous	Numerous						
<b>Forward modelling</b>	Yes	Yes	Yes	Yes						
<b>Inversion</b>	No	Yes	Yes	Yes						
<b>...</b>										

Table 3.2.1. Overview of software packages and programs used by different geological surveys and institutions for different processes involved in gravimetric surveying.

Gravmag has been quite popular during the past three decades and enables all basic functionalities and tools for the forward modelling in 2,5D, that is the 2D (cross section) modelling with some assumptions in the third dimension. The first step was to import the gravity and/or magnetic anomalies together with topography and then build up the cross section either by hand or using a utility based on Cygwin that allowed digitizing a geological cross section and then importing it in Gravmag. As the input geological bodies were stored in an ASCII file, you also could modify them by changing the location of the corners within the file. Or you could digitize the polygons in with an external program and then change the format into a Gravmag readable one. Once the cross section in place and the physical properties (density and



magnetization, induced or remanent) assigned, the observed anomalies were fit by forward modelling, i.e. trial and error.

As other 2.5D approaches, the 2D geometries are characterized by a finite and variable length in the third dimension (perpendicular to the cross-sections). Therefore, lateral terminations of structures (i.e. changes across the modelling plane) should be avoided. Being a forward modelling software, the result depends on the feedback process; changing geometries and petrophysical data will lead to the fitting of the observed and estimated signals (Pedley et al., 1993).

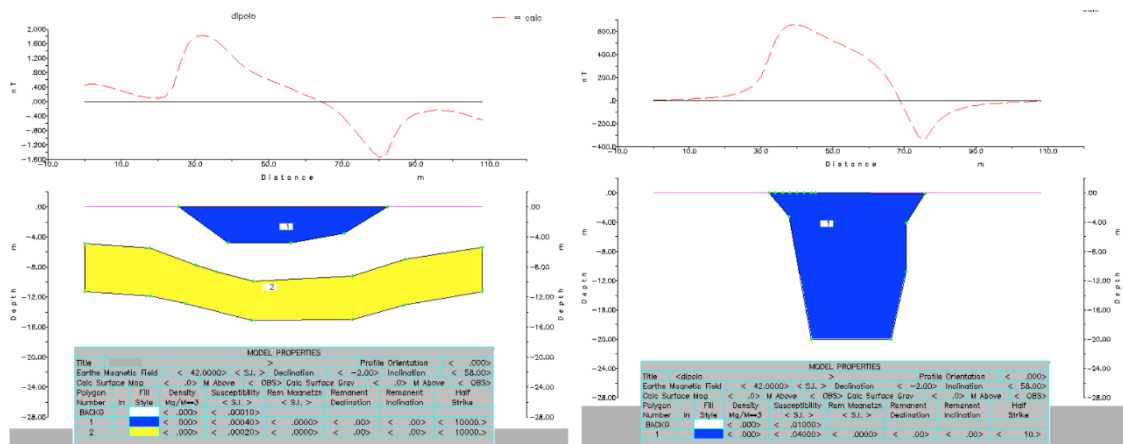


Figure 3.2.3. Simple sketches of sinkholes effects in the magnetic signal. Main menu of Gravmag (Mochales, 2006; Mochales et al., 2008).

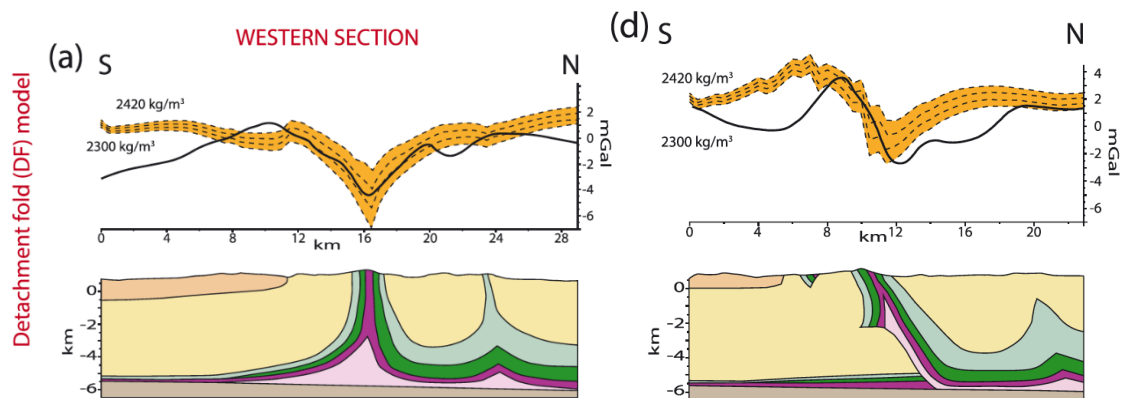


Figure 3.2.4. Salt tectonics modelling of gravimetric signal under Gravmag. An actual example from the Pyrenees; detachment fold versus ramp anticline geometries (Calvin et al., 2018)

### 3.2.3.2 2D, 2.5D & 3D Modelling with Oasis Montaj

Oasis Montaj can be used to process potential field data, create databases, grids and maps, to carry out semi quantitative interpretations (Euler solutions, derivatives, etc.) and 2D, 2.5D and 3D forward modelling and inversion. In order to do so, it includes two modelling modules: GM-SYS and GMSYS 3D (there is a more powerful module for 3D potential field modelling called VOXI but for models of more than 50 x 50 x 50 cells it have to be purchased separately).



Regarding data formats, Oasis provides seamless access to both original spatial data and processed information (grids, images and vector plots). The following list includes the supported data formats for the full version of Geosoft:

*Spatial data import formats include:* AMIRA format files; ASCII data files, CSV; ASEG GDF files; Blocked binary data files; Database table files (single or all tables); Excel Spreadsheets (a note of caution: Excel use ; as separator whereas Oasis use , as separator; not all Excel files can be imported in Oasis Montaj); Flat archive data files; Geosoft binary data files; Geosoft XYZ data files; ODBC data files; Picodas PDAS data files; RMS data files; USGS data files;

*Processed data import formats include:* ArcView shape files (SHP); AutoCAD DXF (DXF) (a note of caution: a DXF file can only be imported if it has a header); DATAMINE (DM); Geosoft plot (PLT); Geosoft map files (MAP); Grid and image formats; MapInfo TAB files; Maxwell Plate files; Microstation DGN files; Surpac (STR, DTM); GoCad (VO); UBC (MOD, MSH, DEN, SUS); LAS files (LAS);

*Common Grid Formats (GRD) including:* DEM formats (GLOBE, ETOPO5, USGS); EOSAT Fast Format; ER Mapper grid (ERS); ESRI Binary Raster (FLT); Landmark ZMAP (DAT); Geopack (GRD); Geosoft grid files (GRD); Geosoft Hypergrid (HGD); Grid eXchange Format (GXF); Surfer grid file (GRD); Texaco Startrax (GRD); USGS (DDF, DEM); World Geoscience (H);

*Common image formats (IMG) including:* EOSAT MSS (Old 4 Band BIL); ER Mapper algorithm (ALG); ER Mapper compressed (ECW); GeoTIFF Image (TIF); GIF (GIF); IMG Image (IMG); JPEG 2000 (J2K and JP2); JPEG File Interchange Format (JPG); Landsat MSS (4 band BSQ) and Landsat TM; PCIDSK Format (GIX); Portable Network Graphics Format (PNG); Tagged Image File Format (TIFF); Targa Image (TGA); Uncompressed PC Paintbrush (PCX); Windows Bitmap (BMP).

In the proposed workflow, GM-SYS is the keystone for modelling in 2D and 2.5D using as input the geological (balanced) cross sections and assigning to each lithology the available petrophysical information either from laboratory measurements, from well logs or from the literature. The integrated fitting of the potential field signal (gravimetric and/or magnetic) together with plausible geological images of the subsurface (balanced cross section) represents a combined adjustment of physical and geometrical properties together and a more robust final reconstruction of the subsurface.

## 2D and 2.5D Modelling GM-SYS

In 2D all the geological structures are considered infinite in the direction perpendicular to the strike. In 2.5D, we can choose some of the structures to be finite assigning a length perpendicular to the strike. We can choose different length in the two perpendicular directions counting from the modelled section. The advantage of 2.5 D modeling with respect to 2D is that some bodies in the direction perpendicular to the profile can be considered finite, which gives more realism to the modeling, for example: intrusive rocks whose dimensions are similar in the horizontal directions of the space.



Ideally, the initial model is a geometrically balanced geological cross section based on the available geological and, when available, geophysical information (seismic sections, boreholes, etc.). We start by creating the model and adding the topography and the observed anomalies (gravity and or magnetic) and then we can build up the model itself (geological cross section) either importing horizons (from an ASCII file or a grid file) or importing a georeferenced image (backdrop) and then digitizing it to create the initial model. We can also use gradients (gravimetric or magnetic) as observables. The image has to be georeferenced in Oasis Montaj prior importing in GM-SYS because GM-SYS cannot import shapefiles or other ArcGis, AutoCAD, GoCad or Move georeferenced formats.

Once the cross section is digitized in GM-SYS and the petrophysical properties are assigned (see section 2.3), we proceed to improve the model through a feedback process between geologists and geophysicists until we obtain a model that has geological meaning, has to be geometrically balanced again (if needed) and the calculated anomaly fits the observed anomaly.

The model has to be extended far enough at both ends of the profile in order to avoid edge effects. How much we have to extend the model depends on the dimensions of the model itself. For an upper crustal model, two or three times its length will be enough. For a lithospheric model, at least one order of magnitude of its total length. Sometimes it is a matter of trial and error until you find the desired distance. Calculations of the gravimetric response of the model are based on the methods of Talwani et al. (1959), Talwani and Heirtzler (1964) and the algorithms described in Won and Bevis (1987).

GM-SYS also allows calculating an inversion either of the physical properties or the geometry (in the x direction, in the z direction or the xz direction). We find it useful to get a feeling for the density variations within the model. The inversion of the geometry too often gives bizarre results, so we hardly ever use it. The GM-SYS Profile inversion routine utilizes a Marquardt inversion algorithm (Marquardt, 1963) to linearize and invert the calculations. GM-SYS Profile uses an implementation of that algorithm for gravity and magnetics developed by the USGS and used in their computer program, SAKI (Webring, 1985).

We evaluate the uncertainties of the final model manually, with sensitivity tests: How much we can vary the horizons or the densities and still keep the calculated anomaly adjusted. After achieving a reasonable fitting between the observation and the estimates (using robust petrophysical data), the main advantage of these 2D (or 2.5D) sections is they are, in fact, doubly balanced; for the geometry and for the gravimetric signal and therefore, they represent a very solid solution of the subsurface, and keystones in further modelling steps.

We can export each of the modelled horizons as ASCII files. In this case we can choose between using relative coordinates (distance from the origin of the profile, x and z), or real world coordinates (x, y and z). This second choice helps to export the section to be imported in 3D reconstruction standard programs (Petrel, Move, gOcad, etc.). In order to facilitate the exchange of information, GM-SYS has included a file conversion program called CVTGMS (Figure 3.2.5) that can handle different formats to make easy the export and import of the model.



**CVTGMS** is a file conversion program that is included in every GM-SYS configuration. CVTGMS can perform file conversion on the following geologic model files:

- DIG format - Generic 2-D ASCII digitized file,
- XYZ format - Generic 3-D ASCII digitized file,
- DXF format - AutoCAD® DXF format,
- IHF format -Paradigm Geophysical, Ltd., GeoSec® **Import** Horizon Format
- MMD format -Geophysical Micro Computer Applications, Ltd.,
- 2-Mod® format - Fugro-LCT, Inc. ,
- GAMMA format - Chevron-Texaco, and
- SAKI format - USGS.

Figure 3.2.5 – File conversion system for GM-SYS (screenshot taken from Oasis Montaj)

### 3D Modelling GM-SYS 3D

At IGME, we use GM-SYS 3D module (by Oasis Montaj) occasionally, when the geological structures to be modelled can be described using grids without too much complexity (like faults or thrusts). With this software, we build layered 3D models that accurately depict the variation in the geometry of the subsurface structures and calculate the models' gravity and magnetic responses. After building the model, we assign the petrophysical properties to each layer that can be constant, varying laterally, varying with depth or voxel distributed (we can have the physical properties discretized in a voxel). Please note that once you have established the limits of the 3D model in GM-SYS 3D these limits cannot be changed so it is important to think carefully about the adequate dimensions of the study area you want to investigate.

We construct the model by importing the layers as grids or importing a voxel that we can create in Oasis Montaj or import from other software (like gOcad). We can choose modelling at the topographic level or at zero level, and we can use as gravity observations either free air or Bouguer gravity anomaly (alternatively, we can use Bouguer onshore and free air offshore). Unfortunately, GM-SYS 3D disallow using gradients as observables.

The program extends the model automatically to avoid edge effects, we only have to indicate the percentage we want the model to be extended or leave the value given by default. We can calculate forward modelling or inversion using the inversion tools provided. We can invert the geometry of a layer (one layer at a time) or the physical properties (one layer at a time as well); we can invert the density of a given layer to find the best constant density to assign to that layer and we can use the isostatic gravity inversion.

The isostatic gravity inversion simultaneously fits the measured gravity anomaly and isostatically balances the crust. In this case the program modifies a given layer (the basement for instance) and at the same time the Moho layer in order to maintain the isostatic balance.

The forward calculations used in GMSYS-3D are based on the frequency-domain techniques published by Parker (1972) and Blakely (1995). The gravity structural and lateral density inversion schemes are based on unpublished algorithms developed by Bill Pearson. The



magnetic structural and the lateral susceptibility inversion schemes are based on the papers by Parker and Huestis (1974) and Oldenburg (1974). Blakely (1995) advanced these techniques and provided code examples for some of the key elements. The “1-step” magnetic susceptibility inversion scheme utilizes repeated applications of the Geosoft “Apparent Susceptibility” filter. The GM-SYS 3D Full-Tensor Gradient (FTG) Joint Inversion is based on the methods of Jorgensen and Kisabeth (2000), licensed from ConocoPhillips (Chavarria et al., 2006). The inversion utilizes a Monte-Carlo simulation and combined space-domain and FFT methods.

With this software, the sensitivity test to assess the uncertainty of the final model is carried out by changing the depth of each layer and/or the density (one parameter at a time) and calculating the gravimetric response to see how much we can vary depth or densities without varying much the calculated anomalies.

The different layers of the model as well as the calculated anomalies and misfits are Oasis Montaj grids that can be exported in a number of formats, in particular ASCII files.

A GM-SYS 3D quick tour: [https://www.youtube.com/watch?v=WjArLY9\\_5JI](https://www.youtube.com/watch?v=WjArLY9_5JI)

### 3.2.3.3 3D Modelling with 3DGeoModeller

This is a versatile software we use for 3D potential field modelling where we can build a complex geological model and improve it by performing forward & inverse geophysical modelling (e.g. Lajaunie et al., 1997; Bosch et al, 2001, McInerney et al., 2005). In the GeoModeller software, the calculations of the inversion are based on the Monte Carlo Markov Chain method (Tarantola, 2004), a well-known and widely used mathematical method in geophysical inversion (e.g. Keilis-Borok & Yanovskaya, 1967; Press, 1968, 1970; Anderssen & Seneta, 1971; Anderssen et al., 1972).

The program uses an implicit 3D geological modelling interpolator, which uses real field structural data (bedding, contacts), stratigraphic rules (e.g. thickness conservation) and borehole data to build the models. Although It allows users to model forward and inverse grav/mag/em signatures in the same application, here we only focus on gravity (or magnetic) modelling.

We start by setting up a project where we define its dimensions (x, y and z) at the beginning, large enough to avoid undesirable borders effects. Then we import the DTM that will be the top of our model (we also can have a flat top at a given elevation). Supported DTM file format comprises: ERMMapper and INTREPID grid datasets; Geosoft grids; GeoTIFF; Simple ASCII grid format (.semi); BRGM grid format; ASCII Arc grid format. Please note that once you have established the limits of the 3D model GeoModeller, these limits cannot be changed so it is important to think carefully about the adequate dimensions of the study area you want to investigate.

Once we have the project created, the first step is to build up the stratigraphic pile that defines the sequential order of geology formations or events. This “order of events” makes possible to manage the relationships of the different formations so the software can build up the geological 3D model. We can define the relationships of the formations as “onlap” (the formation on top



is younger than the formation below) or “erode” (one formation crosscut the one above). Since a stratigraphic surface may belong to two consecutive stratigraphic formations, for the calculations of the geological model, we also have to choose the top or the bottoms of these formations as reference at the beginning.

On the surface topography created together with the project, we can import the surface geological data as image (to digitize the formations we want to model) or as shape files containing the horizons and dips and we may add as many cross sections as we need to constraint the model.

GeoModeller uses cross sections to define the geological structures. We first create the cross section from a trace we draw on the surface topography section and then we can import an image and digitize the geology of the cross section or import the geological data as 2D GIS or binary data in a number of formats (Figure 3.2.6). When available, we may import the cross sections we have modelled in Oasis GM-SYS as main constraints of the model since these sections have been already geometrically balanced. One important difference between the modelled cross sections in GM-SYS and the 3D model in GeoModeller is that in GM-SYS densities are constants for each lithological body whereas in GeoModeller we can lateral and/or depth density variations. Each section must contain all the geological features: Contacts, faults and dips. In addition to the GIS Data, we can import other formats in our cross sections or the surface topography section (Figure 3.2.7). For instance, we can incorporate borehole data to add constraints to the geological model (see Figure 3.2.7 for the indications of the format).

### Importing GIS and other binary located data

Parent topic: [Points List](#)

You can import binary located data into the **Points List** and create sets of data points in your project. 3D GeoModeller supports at least the following **formats**. Contact our support service for information about other **formats**:

- Arc Shape
- MapInfo TAB
- MapInfo MIF/MID
- ASCII CSV
- INTREPID ..DIR databases
- Geosoft GDB databases

3D GeoModeller can only load one segment from the file at a time into the **Points List**.

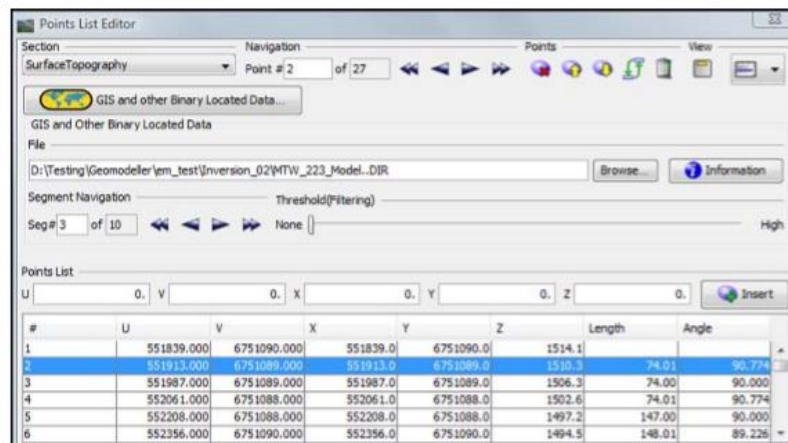


Figure 3.2.6 – 2D GIS data Formats that can be imported in a section.

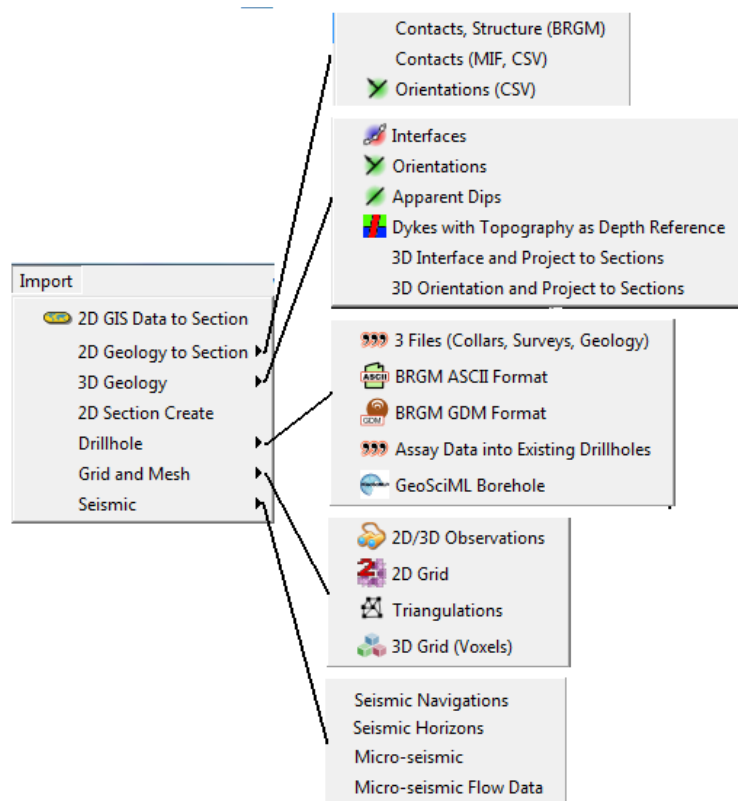


Figure 3.2.7 – Import formats other than the 2D GIS data. 2D/3D observations are CSV files that are imported using a Wizard. Triangulations can be 2D or 3D and the supported formats are GOCAD Tsurf, DXF or Vulcan wireframe. 3D Grid (Voxels) are GOCAD Voxet files. Seismic data are CSV files that are imported using the corresponding CSV data import wizard. For more detailed info about formats the reader is referred to the GeoModeller manual.

The sections can be saved as images in png, gif and eps (Encapsulated Postscript format) and can also be exported as ESRI shape, MIF, MID, ASCII BRGM format or CSV (Figure 3.2.8) allowing importing to a variety of 3D reconstruction software (GOCAD, Petrel, Move, etc.) or design programs (Adobe Illustrator, Canvas, etc.).

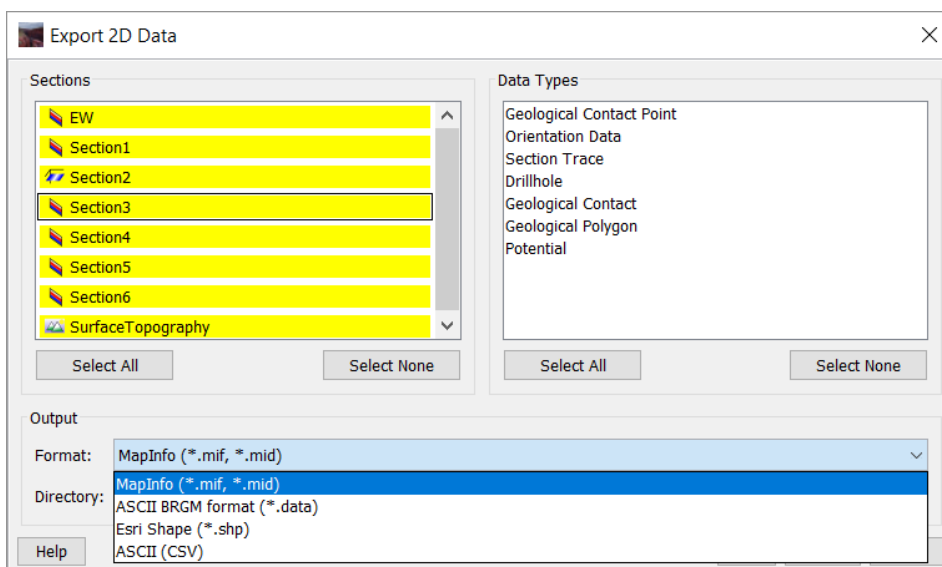


Figure 3.2.8 – Formats to export 2D data.

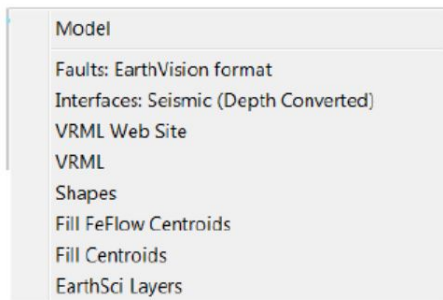


Once the 3D model is built, can be visualized in a 3D viewer. The model can be improved through potential field forward calculation and stochastic inversion. The inversion consists of minimizing the gravimetric misfits by changing either the density, the lithological boundaries or both. The changes are constrained to follow input probability distribution functions (PDF's) that reflect known uncertainties in the rock properties or the geometry of the geological units (Nawaz Sharif and Nazrul Islam, 1980).

In order to constraint the inversion, we set a percentage ratio to control the range of variations of the densities and the lithological boundaries. This percentage ratio at each iteration favors one change or the other. For instance, setting the percentage to 50/50 means that in each iteration two possible changes can occur: either the density for a randomly selected voxel away from the lithological boundary will be modified or, alternatively, the type of lithology of a voxel located near a given interface will be modified and a new density will be assigned accordingly.

In general terms, if the change in density of lithology reduces the misfit, the change is accepted. If not, it is rejected. As the number of iterations increase, the standard deviation of the inversion's misfits follows a decreasing trend. When the trend reaches and asymptotic value, it means that the inversion has converged. The calculations end after the number of iterations we establish at the beginning of the inversion, if the asymptotic value has not been reached, that means the inversion has not converged and more iterations are needed. For a detailed description of the inversion workflow, the reader is referred to the work of Guillen et al. (2008), Calcagno et al. (2008) and Gibson et al., (2013).

The result of the inversion is a set of models with a probability associated to each lithology and we can choose the model we think is most appropriated or simply choose the last model the program has calculated also with its associated probabilities. The model can be exported in different formats like a voxel (a format compatible with GOCAD or Oasis Montaj), as a tsurf (GOCAD surfaces) or grids in ASCII (Figure 3.2.9). An overview of GeoModeller can be found in: <https://www.youtube.com/watch?v=3TLcsi8cj8A>



You can export the 3D model as:

Item	Description
Model	Various computed surfaces and ascii voxets; See <a href="#">Model</a> below for details
Faults: Earth Vision format	Earth Vision faults
Interfaces: Seismic Depth Converted	Seismic depth converted interfaces
VRML Web Site	VRML Web site (requires Blaxun VRML plugin)
VRML	Standard VRML V2
Shapes	3D GeoModeller 3D shapes to most common 3D mesh formats. See <a href="#">Shapes</a> below for details
Fill <i>FEFLOW</i> Centroids	Fill a <i>FEFLOW</i> mesh with geological indices and also the computed formation gradients; requires a starting <i>FEFLOW</i> mesh. See <a href="#">PDF3D</a>
Fill Centroids	Fill ASCII mesh centroids
EarthSci Layers	Export geological surfaces as EarthSci Layers

### Model

Selecting Model in the 3D Model export menu opens the following interface:

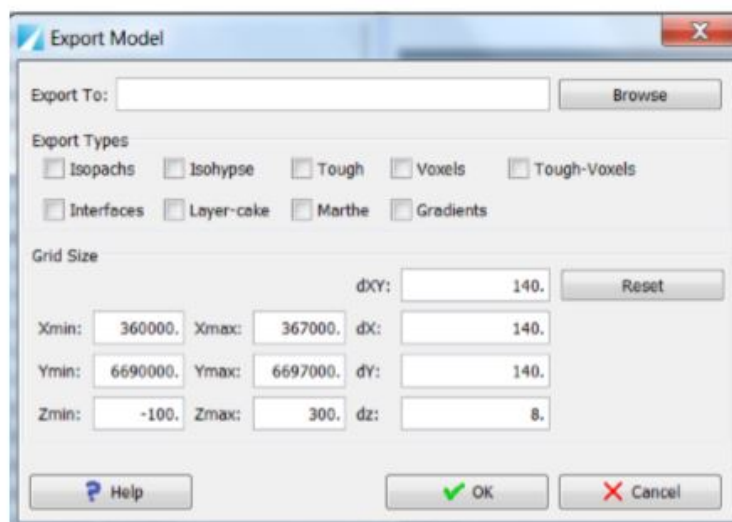


Figure 3.2.9 – Export formats for 3D models (see GeoModeller’s manual for more info)



### 3.2.4 Uncertainty in 2D, 2.5D and 3D modelling with Oasis Montaj and 3D GeoModeller

Direct uncertainty sources at the data acquisition level are derived from the three main types of information in the workflow; gravimetry, petrophysics and cross section balancing. We have already tackled part of them in section 2 and comprise, for example, **gravimetric** measurement (raw data), the assumption of linear drift (gravimeter), the near topographic correction (human bias), the density reduction (although homogeneous for the study case), the height estimation (quality of the GNSS network and instruments used in the field), etc. Those related to the balanced **cross section** construction; the bedding data (quality), dip domain (robustness), horizontality assumption (not always honored), definition of geological contacts, control of stratigraphic thickness, eroded cutoffs, conceptual sources, or those coming from the **density** determination (sample size, laboratory procedure), evolution of density at depth, density variability. In this subsection we evaluate additional sources of uncertainty occurring at the modeling level. Following the work of Mann (1973), Bárdossy and Fodor (2001), the main types of uncertainty in geology that can be extended also to geophysics and state that traditional methods of uncertainty analysis can be divided in two, deterministic and probabilistic.

With GM-SYS and GMSYS 3D we follow a deterministic approach namely sensitivity tests where we estimate the uncertainty of the geometry and density for each of the model bodies or layers by calculating how much we can vary each parameter and still have a good adjust between observed and calculated anomalies (e.g. Ayala et al., 2003).

The probabilistic approach is built in 3D GeoModeller where the result of the inversion is a set of different models that honor the input data from which we can choose the one that better fits the geological context and a final model where the boundaries of each lithology and their densities are provided with a probability (e.g. Guillen et al., 2008).

The propagation of errors from lower levels (raw data or earlier stages of processing) is being tackled within the Loop project (<https://loop3d.org/index.php>) but not implemented in any of the software used at IGME. We estimate these errors with the repetitions of gravity and GPS measurements of the gravity stations and with the statistics from the petrophysical measurements of the samples (we try to acquire at least 10 samples for each lithology so the statistics are meaningful).



	Source	Brief explanation (more details in text) ***	Raw data	Type	code *5	level*4	Impact*	tackled ? Y/N	Reference(s) **	Comments
2D/	1 <i>Geological data (geometry, dips, contacts, faults, etc.)</i>	Included in the geological cross-sections, propagated into the 3D model	2D/3D mod	Instrumental, conceptual and human	1,7	Data interpretation	Variable	Yes	See cross-section part of the table;	Have to be estimated for each model. Depends on its size, the scale of the work, the amount and quality of the geological data.
3D	2 <i>Size and dimensions of the target geological bodies</i>	Simplification of the geology to create a manageable model	2D/3D mod	Software, conceptual and human	2	Data interpretation	Variable	Yes	Pakyuz et al., 2018	Have to be estimated for each model. Depends on the level of simplification
M	3 <i>Initial geological model</i>	Simplification of the geology to create a manageable model; comes from the model construction	2D/3D mod	Instrumental, conceptual and human	3	Data interpretation	Variable	Yes	Pakyuz et al., 2018	Have to be estimated for each model. Depends on the level of simplification
O	4 <i>Observed gravity data (free air, Bouguer, residual, gradients, etc.)</i>	The uncertainty propagates into the calculated gravity data	2D/3D mod	Software and human	2, 3, 7	Data processing	Variable	Yes	See gravity section of the table	Depends on the objectives of the study
D	5 <i>Algorithms of calculation (forward modelling or inversion)</i>	Each software uses different algorithms for the calculations (Parker, Tarantola, etc.)	2D/3D mod	Software, conceptual and human	5, 6	Data interpretation	Variable	Yes	Sensitivity tests e.g., Ayala et al. 2003 Probabilistic e.g., McInerney et al., 2005	Depends on the uncertainty calculation method. Two main methods of estimate uncertainty: Sensitivity tests and probabilistic; have to be estimated for each model.
E										
L										

Table 3.2.2. Uncertainties associated to the modelling.



### 3.2.5 Case studies

In this section we illustrate the 2D/2.5D and 3D modelling steps of the workflow by showing examples from the Linking Zone (Iberian ranges) and the Barbastro anticline (Southern Pyrenees). In the Linking Zone, the inversion was focused in improving the geometry of the different lithologies, the basement in particular. In Barbastro anticline, the inversion was focused in obtain the density distribution within Barbastro Fm. and its lateral equivalents.

#### 3.2.5.1. Linking Zone (Iberian Range, Spain)

In this case study, the main goal was the characterization of a potential CO<sub>2</sub> storage site in a structure called The Linking zone. This site was earlier identified in a previous project of selection and characterization of favorable areas and structures for CO<sub>2</sub> geological storage. Therefore, we carried out a geological and geophysical integrated study aiming to build up a 3D model of the study area and to characterize the geometry and physical properties of the subsurface in order to help in the decision making process of additional investments.

The basement-cover boundary has a high density contrast, which makes the gravimetric method very effective to characterize this geometry, where the target formation is located.

Our work consisted of:

1) Building eight new radial balanced cross sections of the Linking Zone structure of about 70 km in length. The cross sections are roughly perpendicular to the strike of the structures. With these cross sections, we seek to characterize the geometry of the top of the basement and of the Buntsandstein facies (target formation).

2) Carrying out gravimetric and magnetic surveys. We acquired more than 1,200 new data points of potential fields on the ground, from which 938 were gravity stations. Potential field data was measured in the same direction of the geological cross-sections, perpendicularly to the strike. Some gravity stations were also measured longitudinally to link the different cross sections along strike. To complete the coverage of the study area, 1953 stations from the SITOP database (Ayala et al., 2016) were added (all the stations of the database that were within the study area).

Due to the size of the study area (11,325 km<sup>2</sup>) and the limitations of the budget, the number of data points and its spatial distribution was determined to ensure the completion of the milestones but was not possible to acquire enough new stations to have a homogeneous distribution of gravity stations (i.e. even surficial coverage).

3) Carrying out petrophysical surveys to acquire rock samples and measure their density and magnetic susceptibility. We obtained more than 800 control points in the outcropping rocks in the studied area. Additionally, we recovered more than 600 additional petrophysical data of the surrounding regions (Iberian Range and Ebro Basin) from published papers, academic works and borehole logs (Pueyo et al., 2016). This vast set of data allows reducing the uncertainty related to petrophysical properties in the 3D modeling.

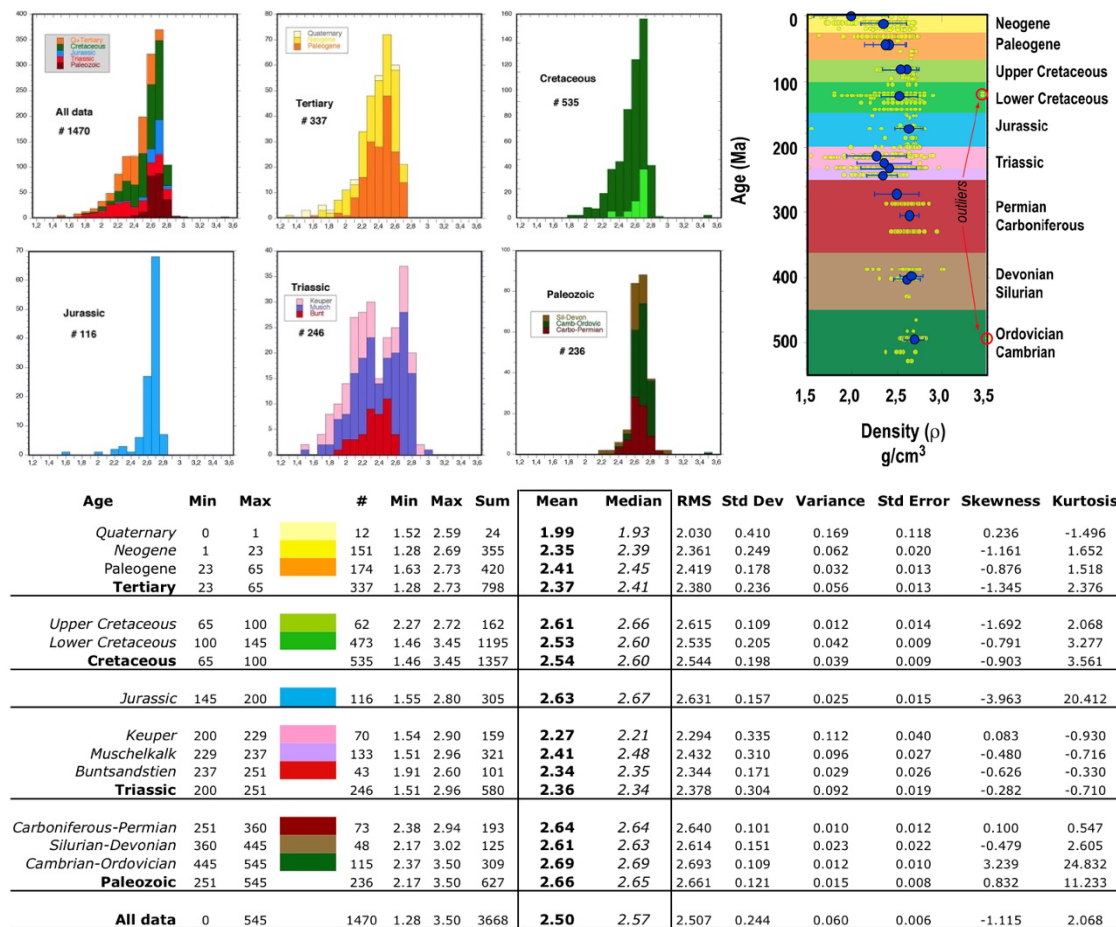


Figure 3.2.10 - Density histograms corresponding to the geological age of the studied rocks. Pseudo-log and statistical parameters used in the modelling of the Linking Zone (Pueyo et al., 2016)

4) Building up a 3D geological model and then refining the geometric interpretation of the subsurface through stochastic inversion. This model is based on the balanced cross-sections that also fit the gravity anomalies (feedback between geology and 2.5D gravity modeling with GM-SYS). Additionally, we also used the Move software (formerly Midland Valley Ltd, now Petex Ltd.) tools to parallel construct a 3D model just based on geometrical features. Further details can be found in Izquierdo-Llavall et al. (2019).

All the available geological and geophysical information is shown in Figure 3.2.11.

### Bouguer and residual Bouguer anomaly

The gravity observations were reduced to obtain first the Bouguer anomaly data with a reduction density of 2.67 g/cm<sup>3</sup> and then a grid for the Bouguer anomaly map (Figure 3.2.12). The grid has 2000m spacing and was constructed using minimum curvature algorithm.

Bouguer anomaly map reflects the overlap of anomalies produced by very different sources at different depths. To interpret the gravimetric geological structures in the upper crust, we have to remove the contribution of deeper sources, therefore, we subtracted from the Bouguer



anomaly a regional field, a 3<sup>rd</sup> degree polynomial in this case, to obtain the residual Bouguer anomaly (Figure 3.2.12).

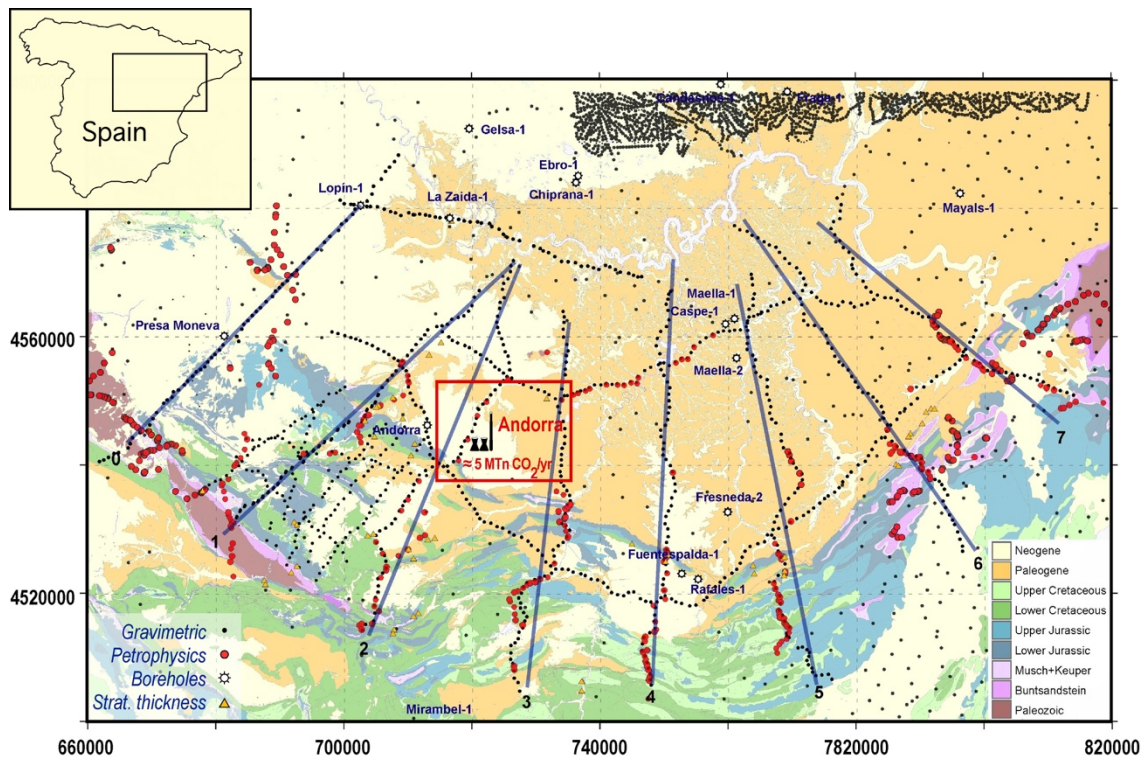


Figure 3.2.11 - Location on the geological map of the gravimetric stations used for the calculation of the Bouguer anomaly. The blue ones belong to the Obón-Oliete survey, the blacks to the Link Zone survey, while the red ones are the points available in the IGME database. Additionally, the petrophysical samples acquired and studied in this project are shown in red. The location of exploration boreholes and the position of the power energy "Andorra" are also displayed. Coordinates are UTM30N, ETRS89 in m.

### 3.5.1.2 2.5 D modelling with GM-SYS. Feedback geology-geophysics.

The modelling is performed through the following steps:

- 1- We projected the gravimetric (Figure 3.2.12), magnetic (Figure 3.2.13) and topographic data along the profile to be modeled and imported into GM-SYS. It should be remembered that gravimetric modeling is done at the topographic level. When using airborne data, the flight height must be entered.
- 2- We compile the available geological and geophysical information from public data repositories (e.g. [www.igme.es](http://www.igme.es)) in order to construct the initial geological cross-section. We also added geological information from field surveys specifically carried within the project. The cross sections were balanced throughout the modelling process. When well logs information is available, it can be also imported in GM-SYS to constrain the geometry in depth at their locations.
- 3- The geological cross sections are imported to GM-SYS as images and then digitized. After digitization, we assign the physical properties (density and magnetic susceptibility) thus



obtaining the initial model. Petrophysical values are derived from the mean and the mode of the histograms (for every modelled lithology) and we used the standard deviation as the error bar.

It is also possible to import a seismic profile with depth. In this case, once the geological bodies have been digitized, they are assigned a seismic velocity and the program converts the depth model into times at depth in units of length. The model must be extended sufficiently at the ends of the cross sections to avoid edge effects. By default, GM-SYS allows you extending the model up to  $10^6$  km but when modelling the upper crust, 5 times the length of the profile is usually enough.

4- Once the cross section has been digitized and the physical properties defined, the geometry of the different geological bodies is modified (and the density, if necessary, within the range of uncertainty allowed by petrophysics) until the calculated anomaly adjusts the observed anomaly, the final model makes geological sense and is compatible with all observables.

For the modelling of the cross sections in the Link Zone, only few wells are available, and the only one crosscutting a profile is that of Lopín. The wells are shown in Figure 3.2.11. In this area, no seismic data is available (there are only very shallow reflection profiles carried out for oil interest but we did not had access to them) and therefore, for the 2.5D modeling we have reduced the uncertainties in different ways: Constraining the physical properties using petrophysical data with a representative number of samples for each lithology, join forward modelling of gravity and magnetic data and make sure that at the end we had balanced cross sections that fit the observables. We assess uncertainty by making sensitivity tests: Maintaining the density, how much we can change each horizon and still fit the observed gravity. The results indicate that uncertainty is of the order of tens of meters.

The profile length ranges from 48.5 km (cross-section 7) to 66 km (cross-section 4); depth of the profiles is 10 km BSL and the total amplitude of the anomalies along the profiles are 10 mGal and 20 nT, approximately. The workflow followed in the 2.5D modelling process prior the 3D modelling is shown in Figure 3.2.14

The workflow includes a feedback process that can have any number of iterations until the calculated anomalies fit the observables. That depend on the knowledge of the structures (balanced cross sections) and their physical properties. A scheme of this process is shown on Figure 3.2.15.

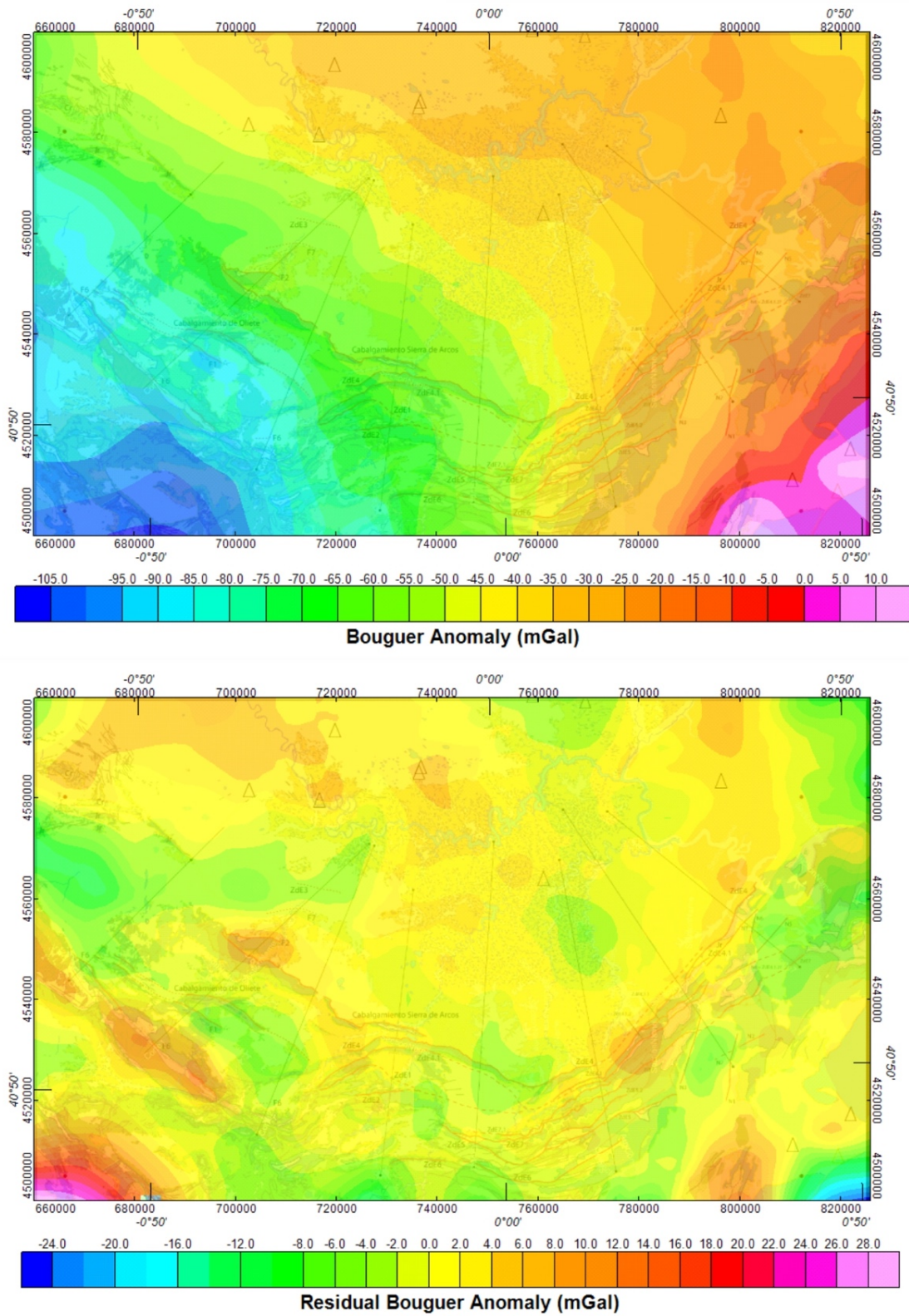


Figure 3.2.12 - Bouguer and residual Bouguer anomaly with the geological structures as a background. Coordinates are UTM30N, ETRS89 in m.

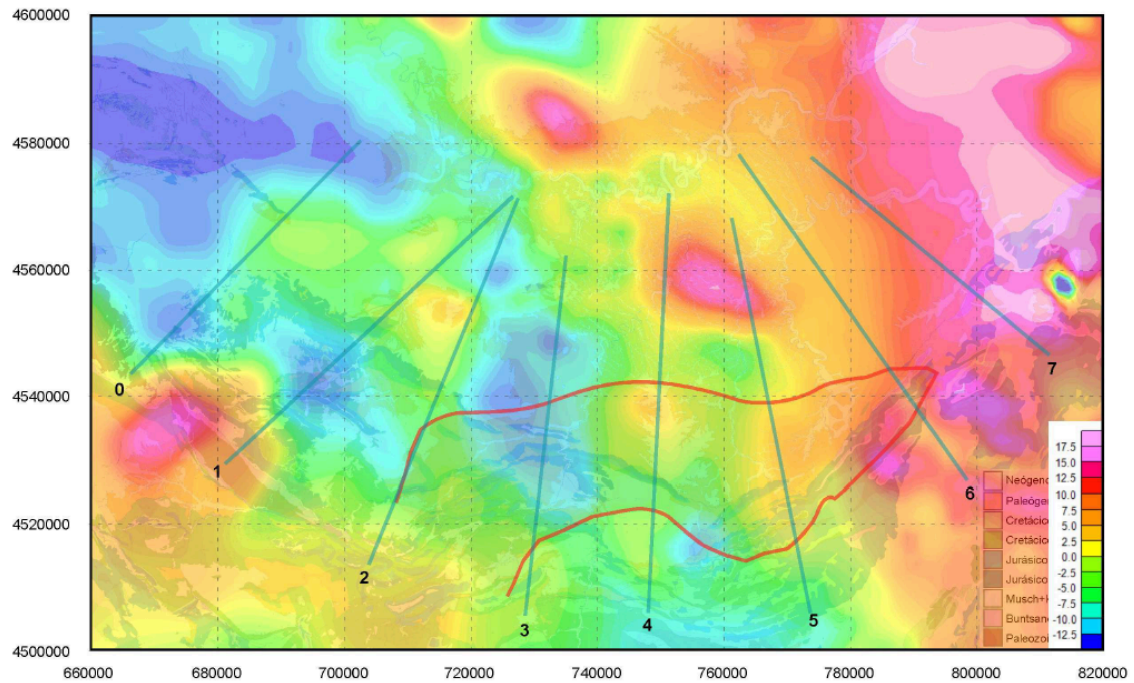


Figure 3.2.13. Total magnetic field in nT with the geological structures as a background. Coordinates are UTM30N, ETRS89 in m. The target study area is outlined by the red line.

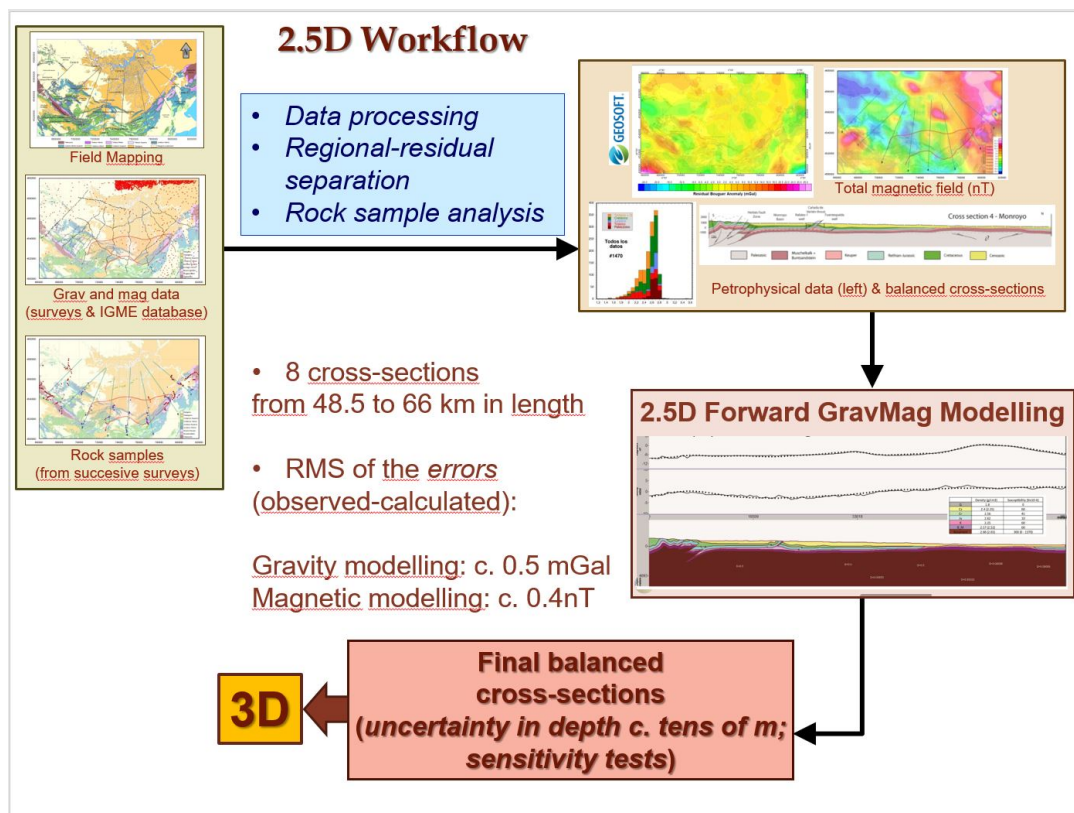


Figure 3.2.14 – Workflow followed in the 2.5 modelling process.

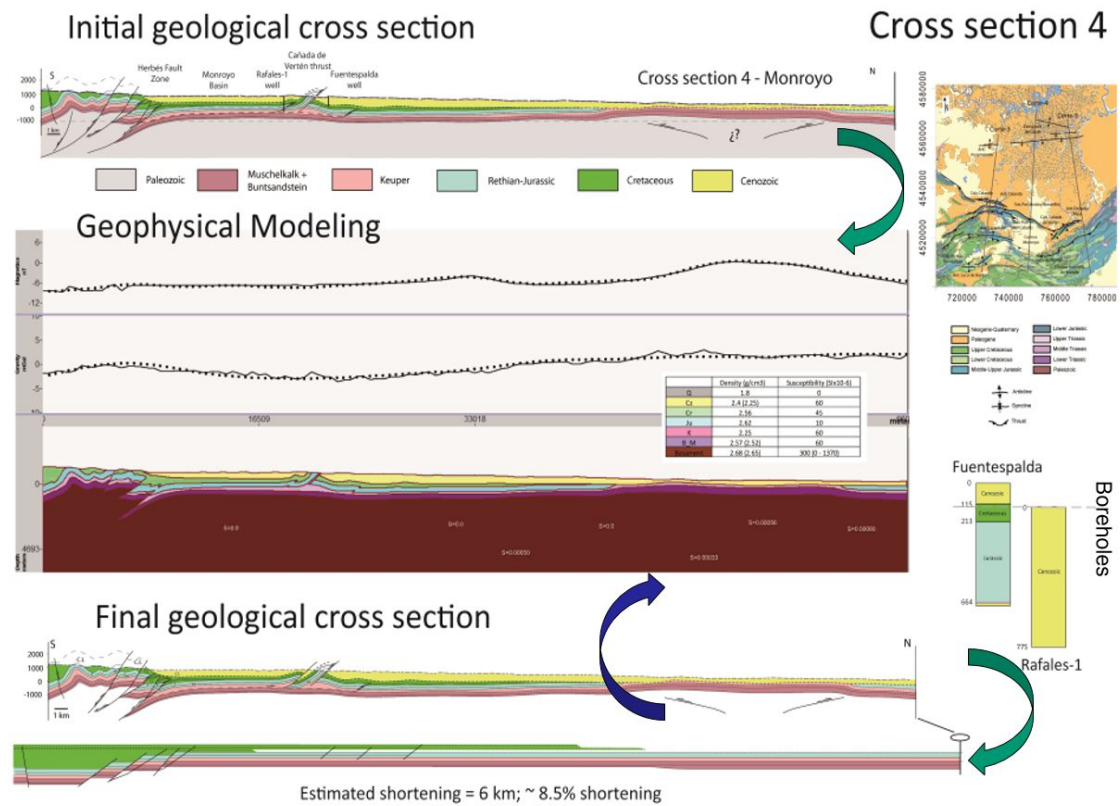


Figure 3.2.15 - An example of the feedback process from the initial balanced geological cross-section to the final balanced geological cross-section that fits the observables. The final cross section has also been restored to the undeformed stage (to check its validity).

As an example, we describe the feedback for section 4. In the example shown we start from an initial balanced geological cross section (Figure 3.2.16 A). Once the digitization is finished and the densities implemented, we observe that there is a significant mismatch between the observed and calculated anomalies (Figure 3.2.16 B). Initially, densities are considered well known because they come from the analysis and compilation of more than 1,400 petrophysical samples (Pueyo et al., 2016), thus, we consider them fixed or with very little variation (i.e. standard deviation). Therefore, the parameter that is free to change in order to adjust the anomalies is the geometry of the different horizons.

The anomalies are adjusted simply by modifying the geometries of the horizons of the digitized model, leaving the densities of each lithology constant. When only by modifying the horizons, we cannot obtain a model that adjusts the anomalies and that makes geological sense, the density of some of the geological bodies can also be modified, always within the range of densities provided by sampling (usually plus/minus the standard deviation).

Some modifications were made for the model to be consistent with the data from Lopín well, located at the northern end of the profile: Thickening of the Tertiary to the South, was not compatible with the geological observations therefore some other modifications regarding changes in thickness of the Jurassic, Cretaceous and B\_M layers were made. After these modifications (Figure 3.2.16 C) there was still a mismatch between observed and calculated anomaly that required adding a body between K and B\_M with a density close to B\_M, as shown in Figure 3.2.16 D, which is compatible with the lithological data from the Lopín well.

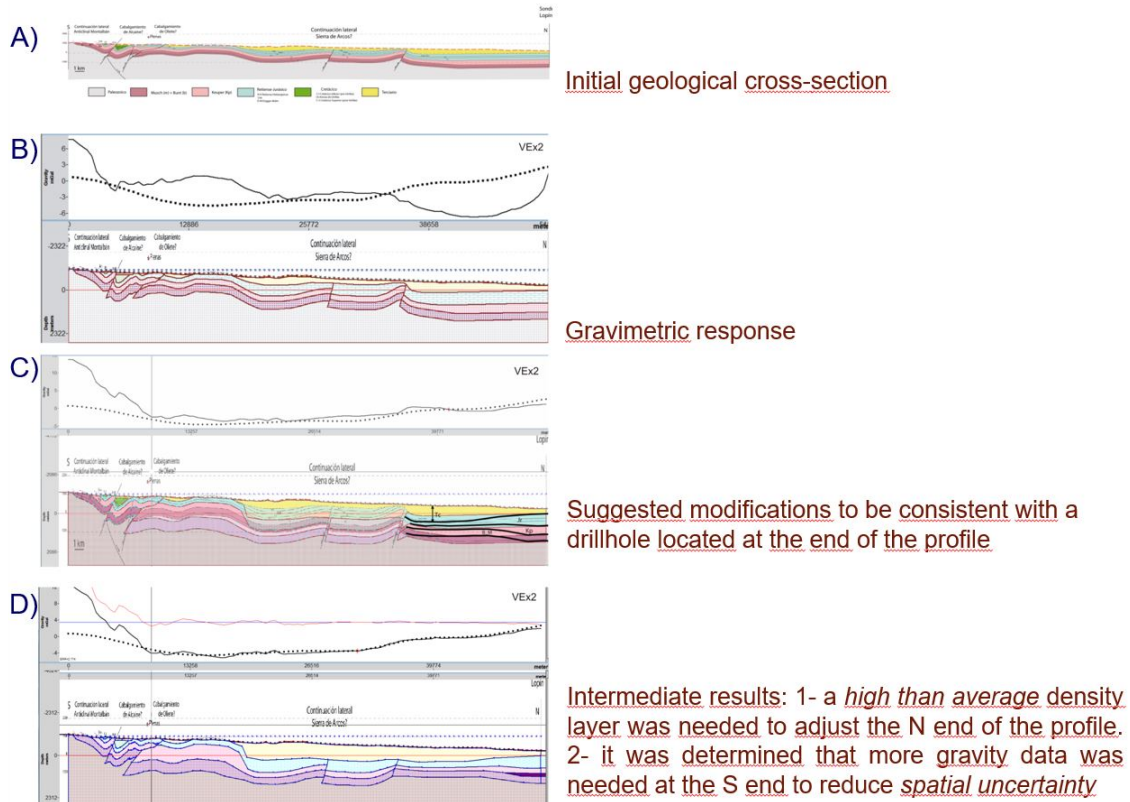


Figure 3.2.16 - A) Initial cross-section; B) gravimetric response of the cross-section; C) and D) successive modifications to adjust the model. Please note that the mismatch of the southern part of the model has not been resolved yet.

What remains is to resolve the mismatch of the southern part of the profile where part of the basement crops out. However, not even making the basement finite laterally taking into account that 3 km towards the E and 400 m towards the S the basement is beneath the B\_M and extending the model southwards according to the surface geology, can be adjusted. Looking at the distribution of the stations, we saw that there were not enough measured stations to have good control on the amplitude of the gridded residual anomaly. In this case, the conclusion is that more measures are required to resolve this part of the profile.

The solution was to acquire additional gravity data (Figure 3.2.17 A show the gravity stations after acquiring this new gravity data) and with few small changes we were able to adjust the observed gravity data. The final model is also consistent with the rest of geological and geophysical data (Figure 3.2.17 B).

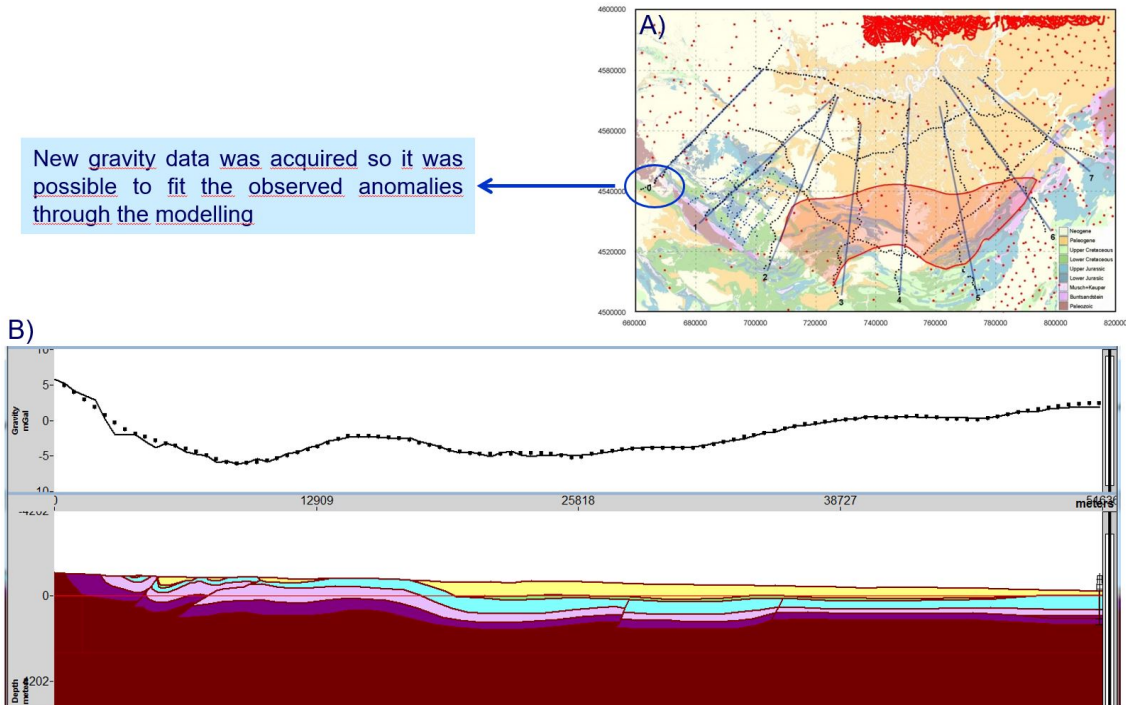


Figure 3.2.17 – A) Location of the new gravity data acquired to improve the resolution of the observed gravity anomalies and final modelled section. B) Final modelled cross-section.

### 3D gravity modelling (forward modelling and stochastic inversion)

The objective of the potential fields modelling in 3D is to obtain an image of the geometry and spatial distribution of densities and magnetic susceptibilities at the subsurface whose gravimetric and magnetic response fits the observed anomalies and the final structure is consistent with the available geological and geophysical data. The level of detail of the model obtained will depend on the spatial distribution of the measured data; of the scale of the work we carry out; and of the petrophysical, geological and geophysical information available as a priori information (constraint) and thus limit the number of equivalent solutions.

The advantage of 3D modeling versus to 2D or 2.5 D is that the first one offers a three-dimensional image of the variation of the petrophysical properties and geometries of the different geological bodies in the subsurface while in 2D only the image is taken along a profile, considering the bodies as infinites in the direction perpendicular to the strike. Workflow to build up the geological model is depicted in Figure 3.2.18.

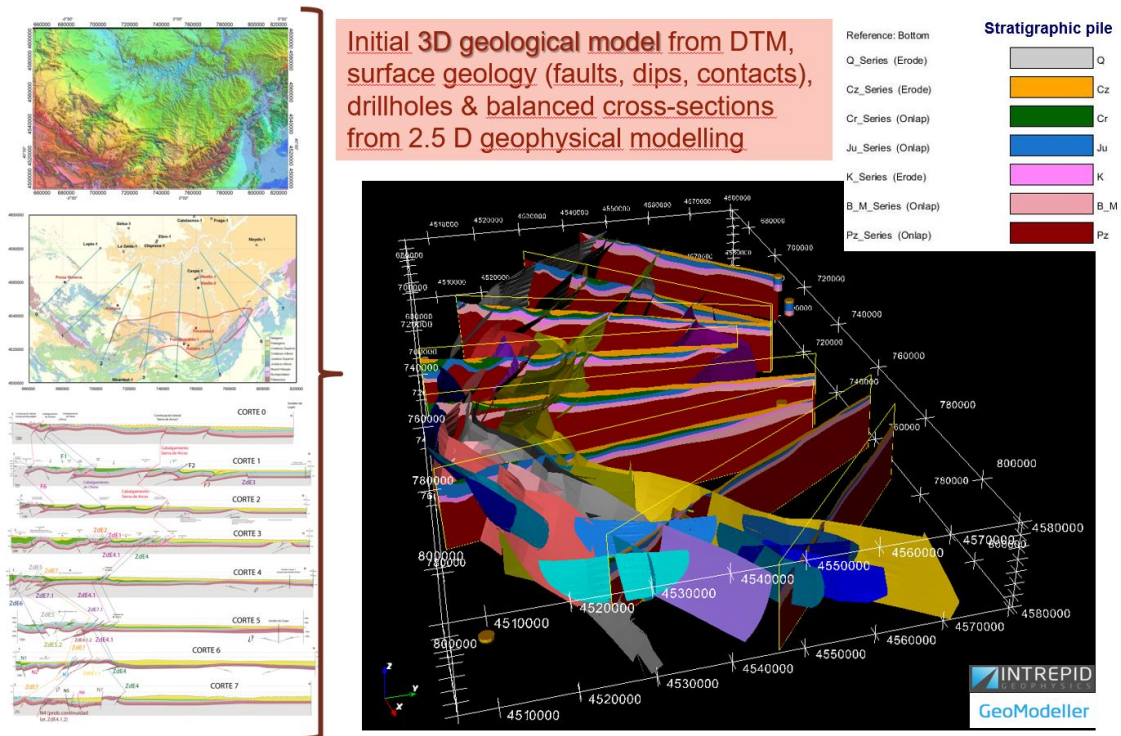


Figure 3.2.18 – Input data to build up the initial geological 3D model. Note that the 2D sections have been already balanced for their gravimetric signal and therefore, represent very robust data.

The construction of the geological model begins with the definition of the volume within which we are going to build up the model, which has a defined surface as a top above the topography and as a bottom the maximum depth at which data are available or it is considered that an acceptable extrapolation can be performed. It works in rectangular coordinates in meters or kilometers. It is important to bear in mind that once the study volume is defined, this cannot be changed.

The area chosen to build the 3D model also covers closer areas (Caspé and Obón) where additional surveys were carried out to explore their potentiality as gas storages. Merging all together will help unifying the results of the geological modeling in all three. Their boundaries are delineated by the following coordinates (in meters, UTM 30N, ETRS89): 659000/825000/4499000/4600000

#### Input data (Figure Workflow3D)

**Digital terrain model** - The DTM is imported as regular grid, with a suitable grid spacing that will depend on the resolution of the model. The format can be ERMapper or a Geosoft grid. The DTM becomes part of a reference surface that, by default, it is called “Surface Topography”, and constitutes the top of the geology. In this work, and due to the large size of the study area (13,500 km<sup>2</sup>), we have used a 100 m DTM from the IGME databases.

\* *Surface geology: contacts and faults with its direction, dips, etc.* (the faults and contact information must be accompanied by orientation and dips' data) that will be modelled:



- The surface geology is digitized on the Surface Topography, since the program considers the influence of topographic relief on the geological configuration.
- If the geological map is an image, we import the image and manually georeferenced it within the program. Then we digitize contacts, faults and dips of the structures that we want to model.
- If the geological map is digital it can be imported in several ways (shapes for instance). Depending on the number of points, it might have to be simplified. The import includes contacts, faults and dips of the structures we want to model.
- Faults can be defined as finite faults (that is, with a limited extension) or infinite (that extend throughout the entire area to be modeled or until ending up in another fault).

In this work, we used the geology of the SIGECO database from IGME in image format, on which the contacts and faults relevant for modeling were digitized.

\* *Wells*, which help refining the starting model. GeoModeller uses the wells directly as data to calculate the model. The wells are imported and can be projected in the different sections. Once projected, the geological horizons can be modified, if necessary, to fit the horizons of the wells. The information from the wells available in the area, 12 in total with depths reaching between 300 and 2300 m, was incorporated in the model (Table 3.2.3).

\* *Geological cross-sections* - First we create a vertical section within the program and then we import the image of the geological cross-section, georeferenced it and digitize contacts, faults and dips. It is also possible to create a horizontal cross-section at a given depth and digitizing the geology from an imported image. Or we can project our current geology downwards. The objective is to have a better understanding of the model. The vertical cross-sections come from the 2D / 2.5D gravimetric model and are already balanced from a geometrical point of view. In this sense, represent a robust data in the model.

HoleID	East	North	CollarRL	EOH_Deptl
CASPE	760892	4562827	200	1810
LOPIN	702534	4580441	223.8	1652
MAYALS	796101	4582334	356	1401
CHIPRANA	736130	4584020	315	1845
EBRO	736499	4585069	327	1969
FRAGA	769124	4598164	296	2143
CANDASNOS	758724	4599315	278	1550
AMPOSTA	819189	4507573	0	1646
DELTADELEBR	821744	4515913	1	604
GELSA	719478	4592395	245	2388
LAZAIDA	716454	4578474	162	1698
SANCARLOS	810227	4509757	2	306

Table 3.2.3. Location of the wells are taken into account in the models (East and North are UTM30, ETRS89 coordinates in m; CollarRL is the orthometric height in m; EOH\_Depth is depth in m)

Regarding the faults and thrusts, we started digitizing only 7 (Figure 3.2.19) but a measure we advanced in the construction of the model, we added more faults and thrust as we needed them to build up a consistent geological model. We ended up with a total of 22 thrusts and 7 normal faults taking special care of linking faults with faults and faults with formations to obtain a meaningful model. Figure 3.2.20 A and B show the relationship between faults and formations.

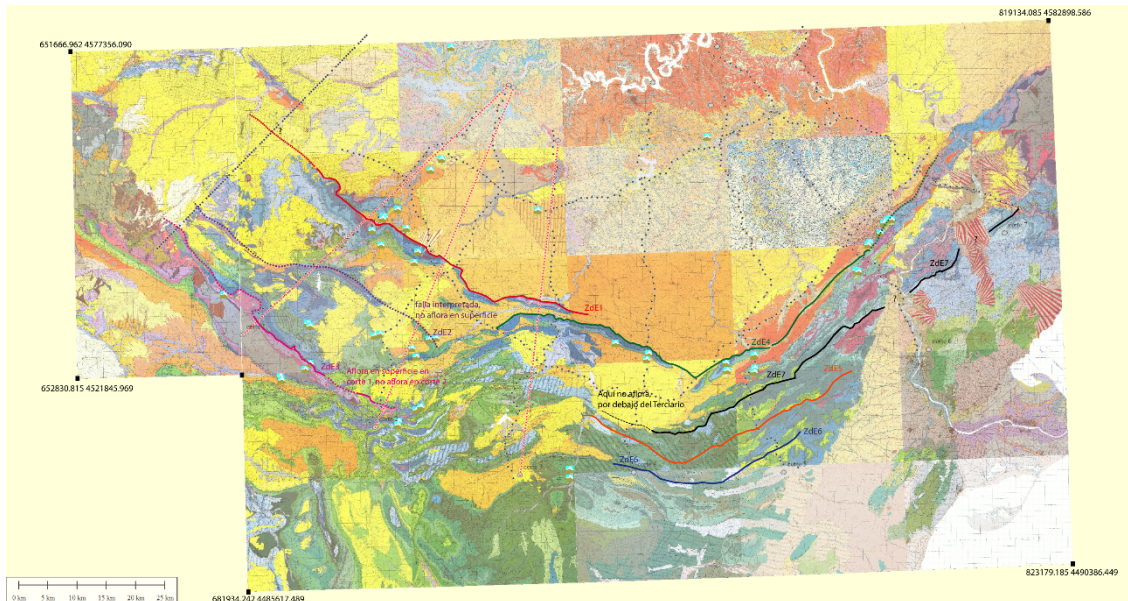


Figure 3.2.19 – Initial (main) faults and thrusts included in the model.

Similarly, selected digital dips acquired in the field or from digital databases were imported or digitized on the geological map in order to have enough information for the modelling and not too much information that sometimes is redundant and make the modelling uselessly complicated. Ideally, robust dip domains (in the sense of Suppe, 1985; Groshong, 2006; Carrera et al., 2009 and references therein), that is areas of constant dip, should be used.

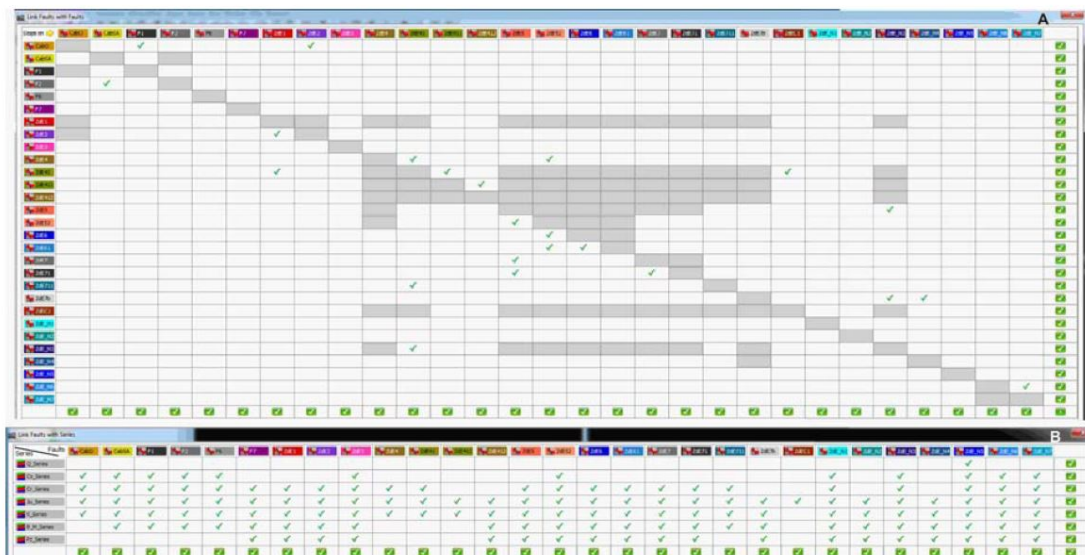


Figure 3.2.20. A) Relationship between faults. B) Relationship between faults and the stratigraphic series of the model.

\* *Stratigraphic pile*, formed by the lithological units, establish the temporal sequence of geological events with their corresponding relationship that can be "onlap" (layers are concordant) or "erode" (discordant layers). The stratigraphic pile has a fundamental influence on the correct construction of the geological model, since if stratigraphic relationships are not



correct, the resulting model will not make geological sense. The stratigraphic pile can be modified throughout the modeling process. Inside the stratigraphic pile, the lithological units can be grouped into series. Each series will be modelled using a different interpolator. In this model, the stratigraphic pile (Figure 3.2.21) is made of seven lithologies. The digitized contacts are the base of the corresponding formations.

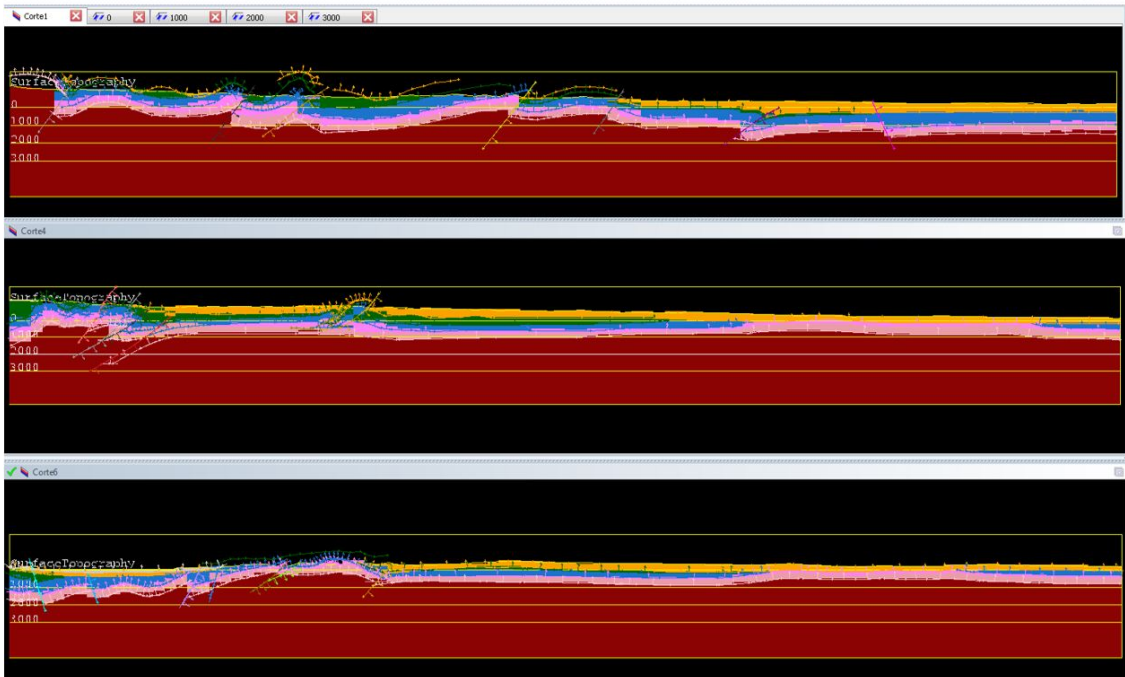


Figure 3.2.21 – Stratigraphic pile with the relationships between formations in brackets. Q – Quaternary, Cz – Cainozoic, Cr – Cretaceous, Ju – Jurassic, K – Keuper, B\_M – Buntsandstein-Muschelkalk, Pz – Paleozoic (the basement of the model).

Some notes of caution:

- When digitizing the dips in the cross-sections you have to be careful with the direction of digitization, since the dips can be normal or overturned.
- In some cases, once you have the initial model, it may be convenient to create additional sections to refine the model in a given area or to include new data (another geological cross-section, more surveys if available, etc.).
- Sections do not have to be straight, they can also have an irregular path. To prevent smoothing in areas where the section that is being digitized makes an angle, we must duplicate the point that constitutes the vertex of the angle (the GeoModeller tends to smooth the lines so that aZ-shaped trace would draw in the form of S).
- Prior to the calculation of the geological model, it is important to check the consistency of all the input data, that is, between the sections both vertical and horizontal and with the stratigraphic pile. This is done by projecting the data in the different sections (option “Project data onto sections”). If the data projected do not match the digitized section on which they have been projected said data, the errors must be corrected.

Figure 3.2.22 show the initial model through three selected cross-sections and in 3D view of the cross-sections, faults and the basement represented as a surface.



A)

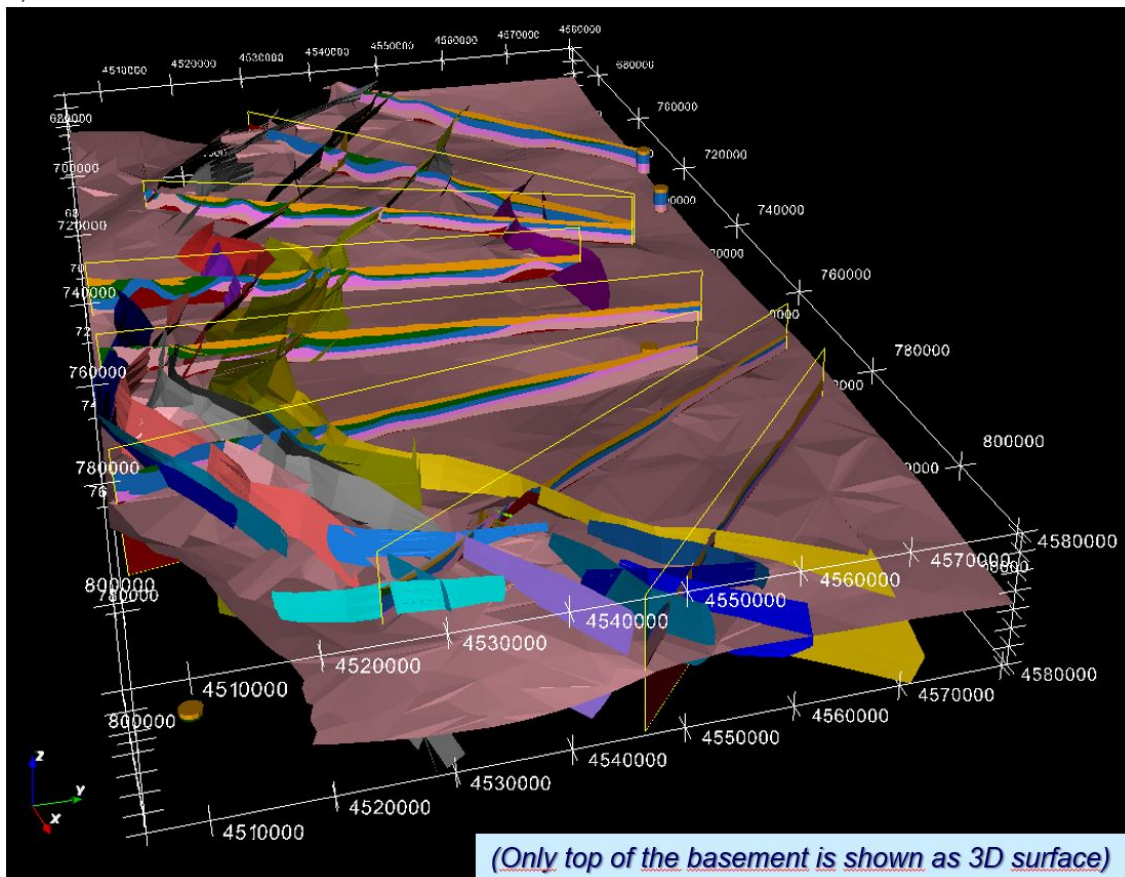


Figure 3.2.22 – Upper image: 2D view of three selected cross-sections. Lower image: 3D view of the model showing the cross sections, the faults and the basement as 3D surface.



Once we have integrated all geological data and we have built a consistent 3D model, we begin the **geophysical modelling** that starts with forward modelling to achieve a model whose gravimetric response is close to the observations and ends with the stochastic inversion process based on the Monte Carlo method that results in a range of models with its corresponding probability from where we choose the geological model most consistent with the observations and the geological and geophysical data available.

The first step prior to inversion is to discretize the geological model by transforming it into a voxel and assign to each voxel its physical properties (density, magnetic susceptibility and remanence if known) according to the lithology at which the voxel belongs. The program calculates density contrasts with respect to a reference density that is defined at the beginning of the inversion, which is the reduction density of the Bouguer anomaly ( $2.67 \text{ g/cm}^3$  in this case; Hinze, 2003). Bear in mind that you have to reach a compromise between the size of each of the voxels that make up the voxel, the required resolution and the calculation time.

We enter the gravimetric and magnetic data as a regular grid in Geosoft grd format or ERMappers format with the appropriate grid spacing. Depending on the objective of the work, Bouguer anomaly can be calculated at the topographic level or carry out an analytical extension upwards to place the observations above the higher topographic elevation or filter the high frequency anomalies in order to eliminate short wavelengths of the gravimetric anomalies that can be considered as noise in our calculations. In this work, which was focus on the basement/cover relationships, we entered directly our residual Bouguer anomaly.

Physical properties are assigned using a distribution function that can be exponential, normal or lognormal and that allows to define, in addition, if a property has a monomodal, bimodal or trimodal distribution. The densities used in the 3D model are the same as those of the 2D models and are shown in table 3.2.4. The first number is the density, in  $\text{g/cm}^3$ ; the second number is the associated standard deviation, which has been chosen based on the variation of the range of densities used in 2D modeling; the third number (100 in all cases) indicates that 100% of the lithology has the indicated density. Taking into account the results of the 2D modeling, we have not considered bimodality for any of the formations.

Formation	Density ( $\text{g/cm}^3$ )
 Q	Normal(1.8,0.05,100)
 Cz	Normal(2.4,0.025,100)
 Cr	Normal(2.56,0.025,100)
 Ju	Normal(2.62,0.025,100)
 K	Normal(2.25,0.025,100)
 B_M	Normal(2.57,0.025,100)
 Pz	Normal(2.68,0.025,100)

Table 3.2.4. Densities used in the model. See text for more info.



The program extends the model far enough to avoid edge effects.

The workflow for the stochastic inversion is shown in Figure 3.2.23 where the input data is the geological model, the residual Bouguer anomaly and the densities assigned for each lithology and the output gives the inverted 3D model and the misfits, that gives you an idea of where the model needs to be improved when new data becomes available.

The figure with the model shows only the basement in 3D because this was one of the main target structures of the modelling.

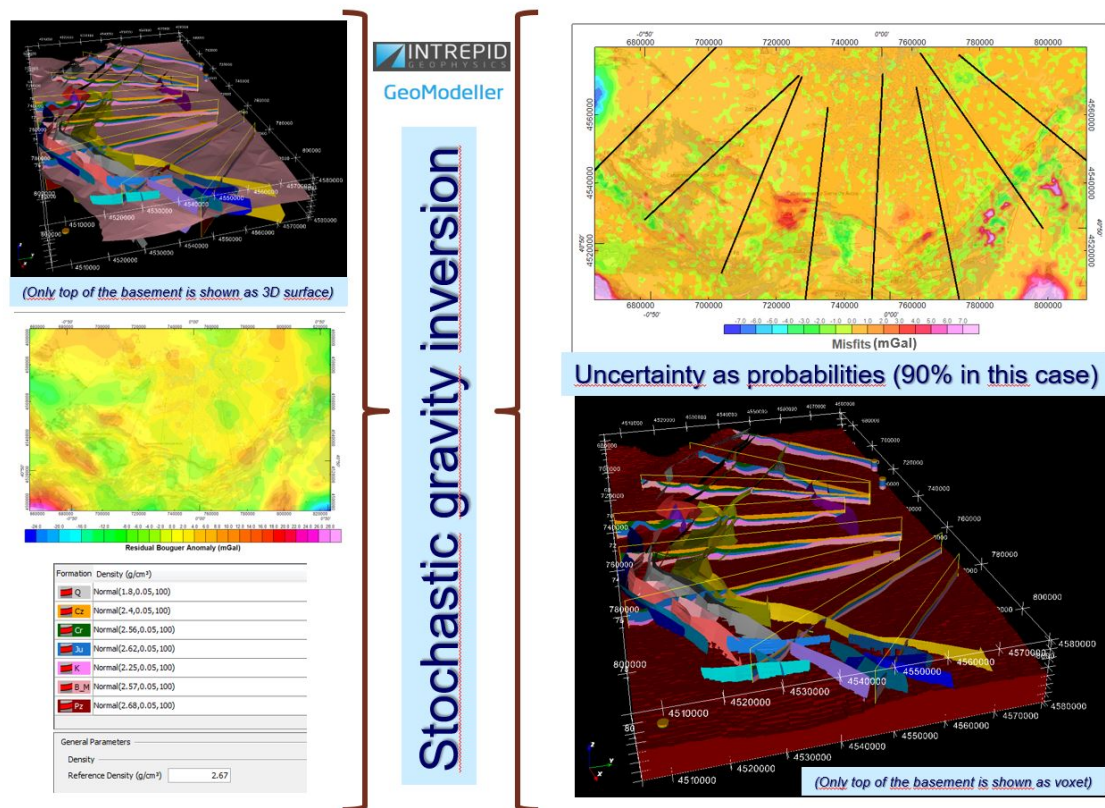
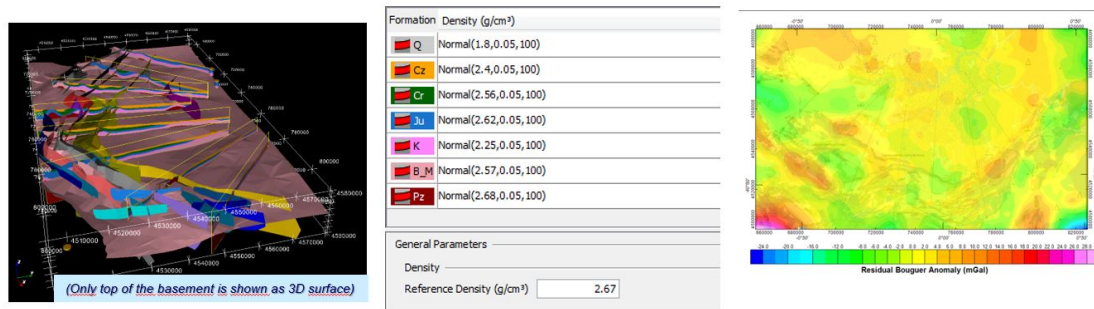


Figure 3.2.23 – Stochastic inversion workflow. See explanation on the text.

Figure 3.2.24 is a summary of the inversion process, showing the input model, physical properties, observed residual Bouguer anomaly, the discretization of the voxel and the graph with the RMS versus iterations. We set the inversion in  $5 \times 10^6$  iterations because for this calculation, an RMS below 1.5 mGal was considered good enough and that is the reason the RMS graph does not end in a completely flat curve.

For this inversion, given the size of the working area, the spacing between the cross sections and the estimated resolution of the geological model we decided to build up a voxel with 1000 m x 1000 m x 50 m voxels which gives a total of 1533000 voxels (146 x 75 x 140 voxels). We also choose the threshold probability of 90% because we considered the model to be good enough for that threshold.



**Voxel:**

- 1000m x 1000 m x 50m
- 146 x 75 x 140 (1533000 voxels)

Threshold probability: 90%

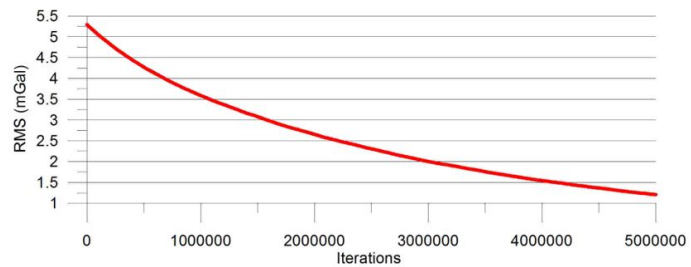


Figure 3.2.24 – Summary of the inversion process. See explanation on the text.

Figure 3.2.25 show the comparison between observed and calculated anomalies (upper map) and the misfits (difference between observed and calculated anomalies, lower map). There is a good fitting between observed and calculated gravity anomalies with most of the differences between -1 and 1 mGal. The biggest misfits are located on the edges of the model and in places where the geological structures are not well constrained so there are doubts regarding its geometry, like in the central part of the Sierra de Arcos thrust (SW).

The geological results from the inversion projected along selected 2D cross sections and in 3D view projected along the cross sections for a better visualization of the results are displayed in Figure 3.2.26. The figure also shows the final basement voxel, one of the target structures, together with the projected cross sections, 3D faults and drill holes.

We can conclude that the gravimetric inversion has allowed refining the initial geological model and better assesses the uncertainty of the structures in depth. From the 90% threshold we assume an uncertainty in depth for each lithology up to c. 150 m. For a more detailed explanation about the results and its geological significance see Izquierdo-Llavall et al. (2019).

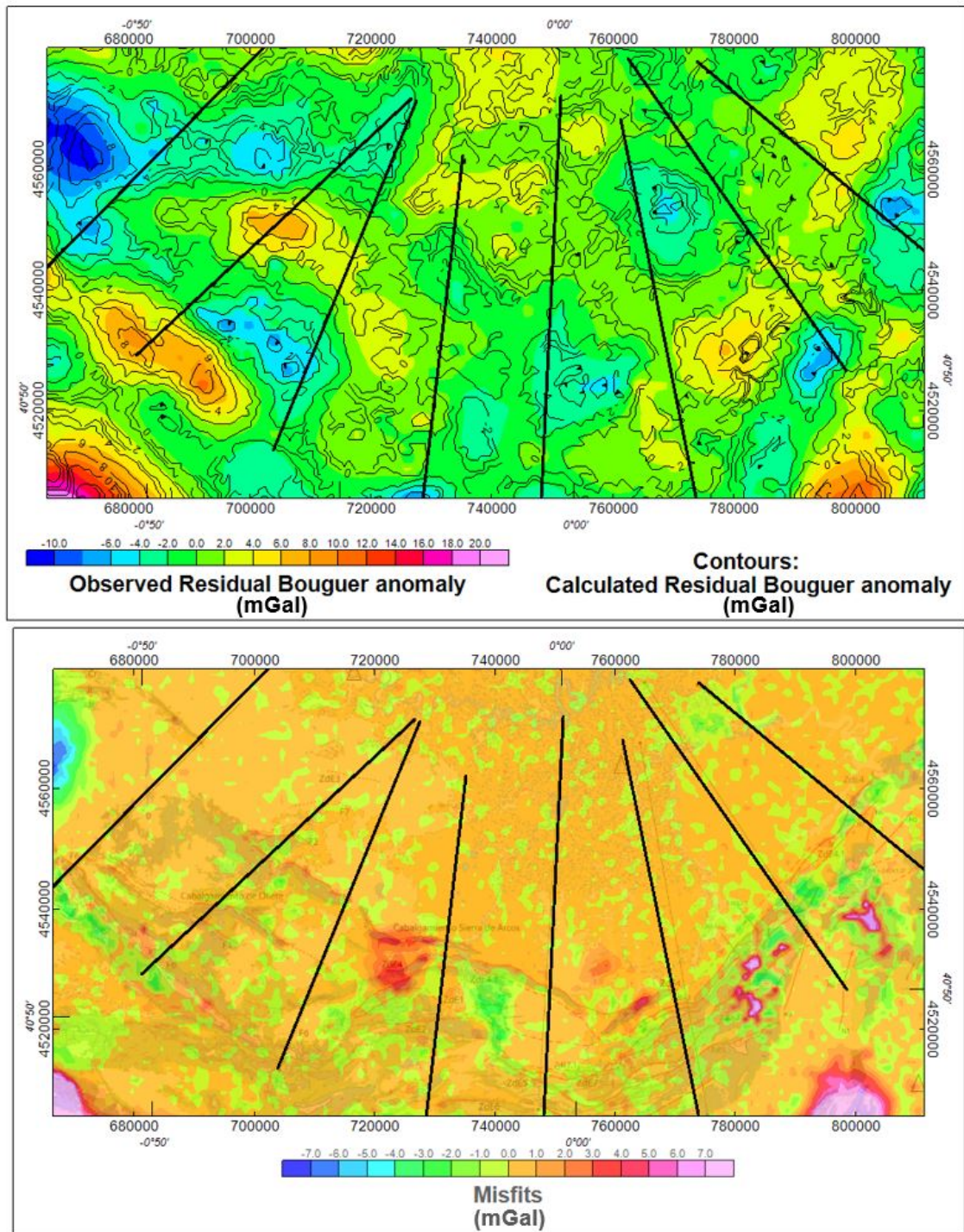


Figure 3.2.25 - Map at the top: Color figure corresponds to the observed residual Bouguer anomaly with the superimposed contours corresponding to the calculated residual Bouguer anomaly for comparison. Map at the bottom: Misfits (observed minus calculated anomaly).

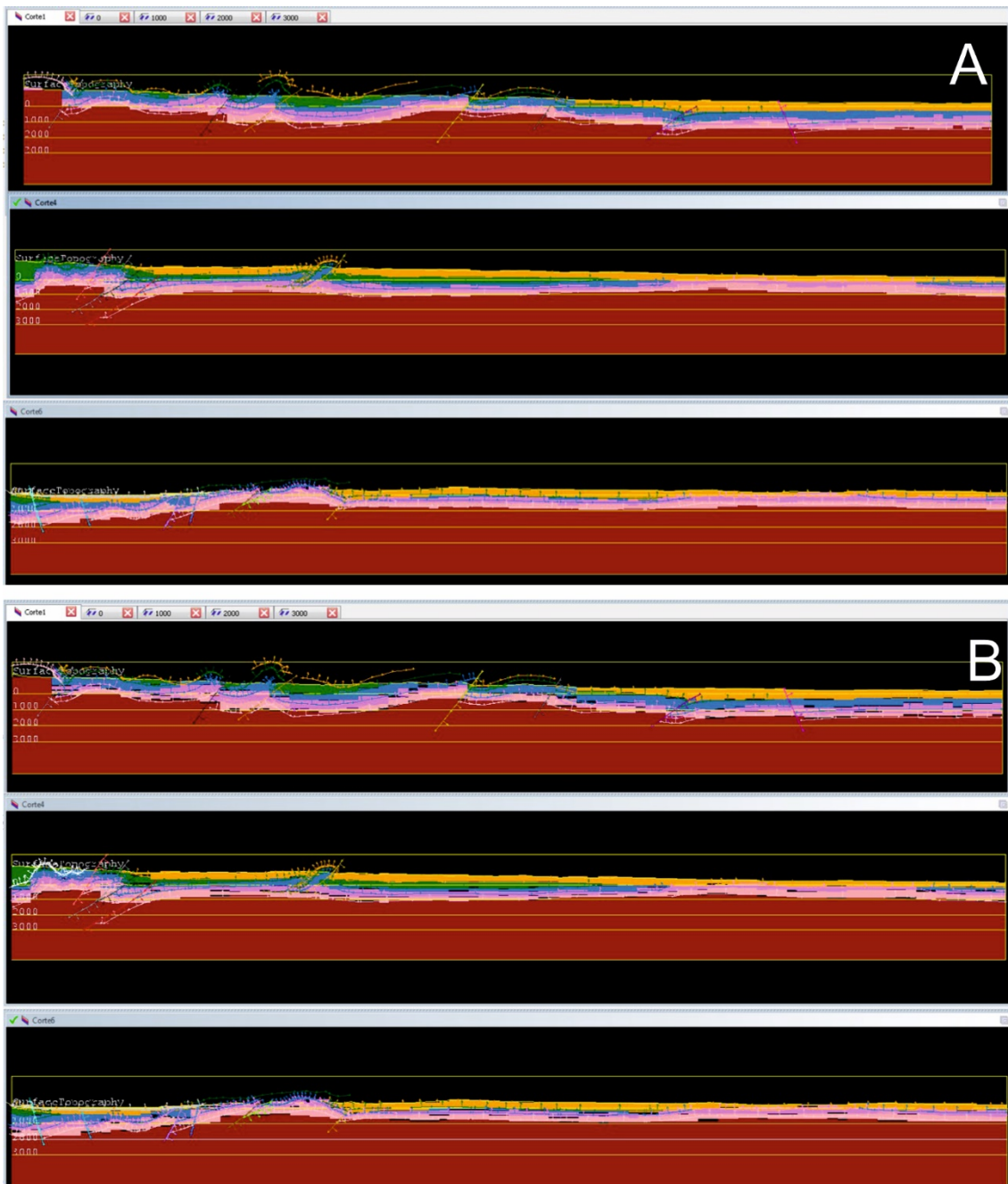


Figure 3.2.26 - Final model after the inversion. A) – Lithologies in three selected sections. B) Lithologies with a 90% probability along the same sections: Black cells indicate the uncertainty.

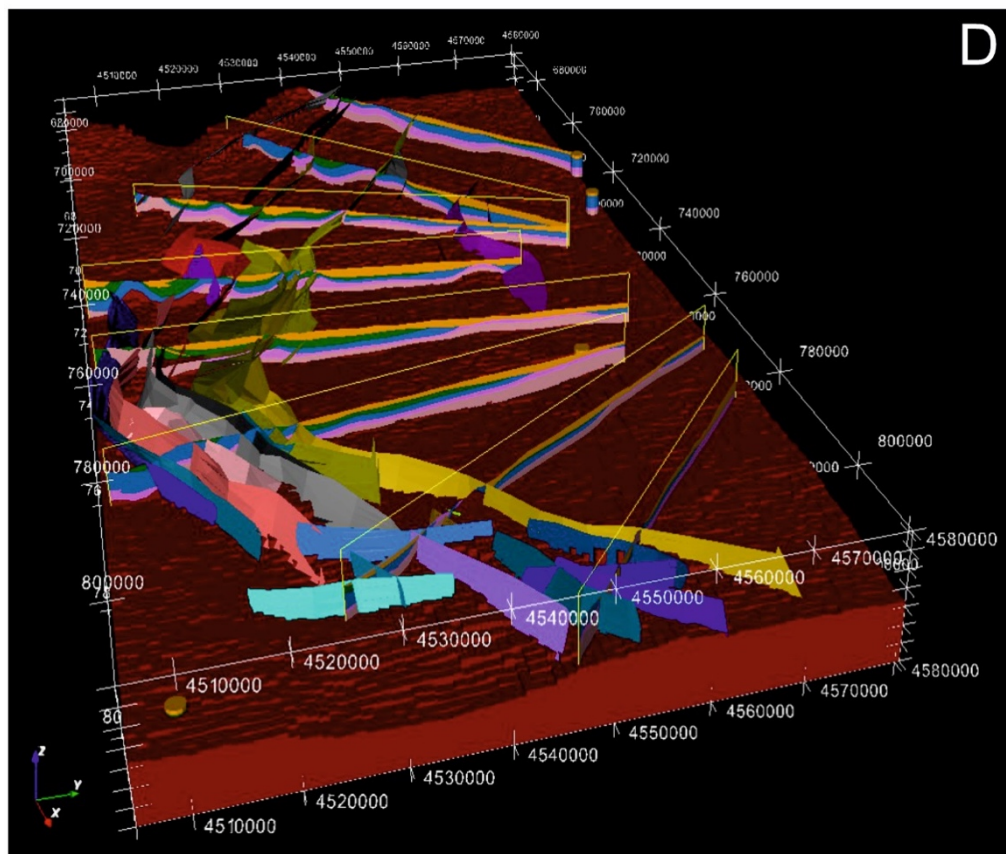
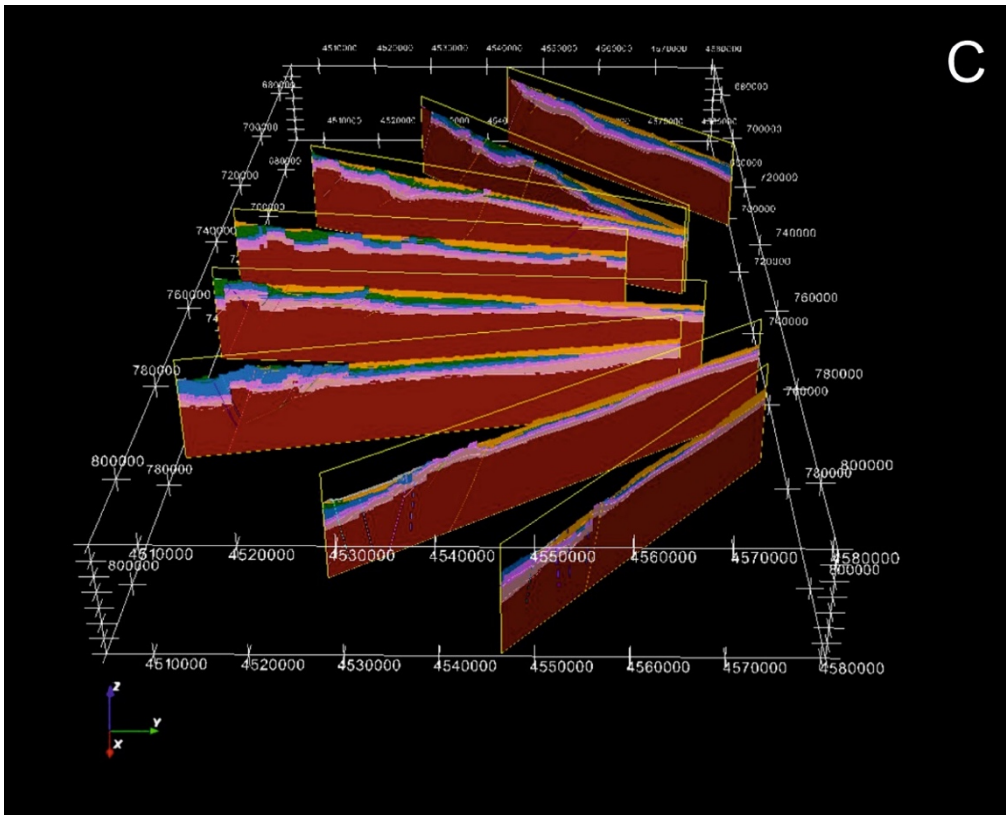


Figure 3.2.26 (Cont.) - C) View in 3D along the modelled cross-sections. D) View in 3D with the modelled faults and the voxel corresponding to the basement. See text for further explanation.



Finally, we have performed a comparison between the initial balanced sections (0) (just geometrically balanced), those corrected after the balancing of the gravimetric signal (A) (Oasis forward modelling feedback) and those extracted from the 3D model after the inversion (B) (Geomodeller). Figure 3.2.27 shows the comparison for cross-section 2.

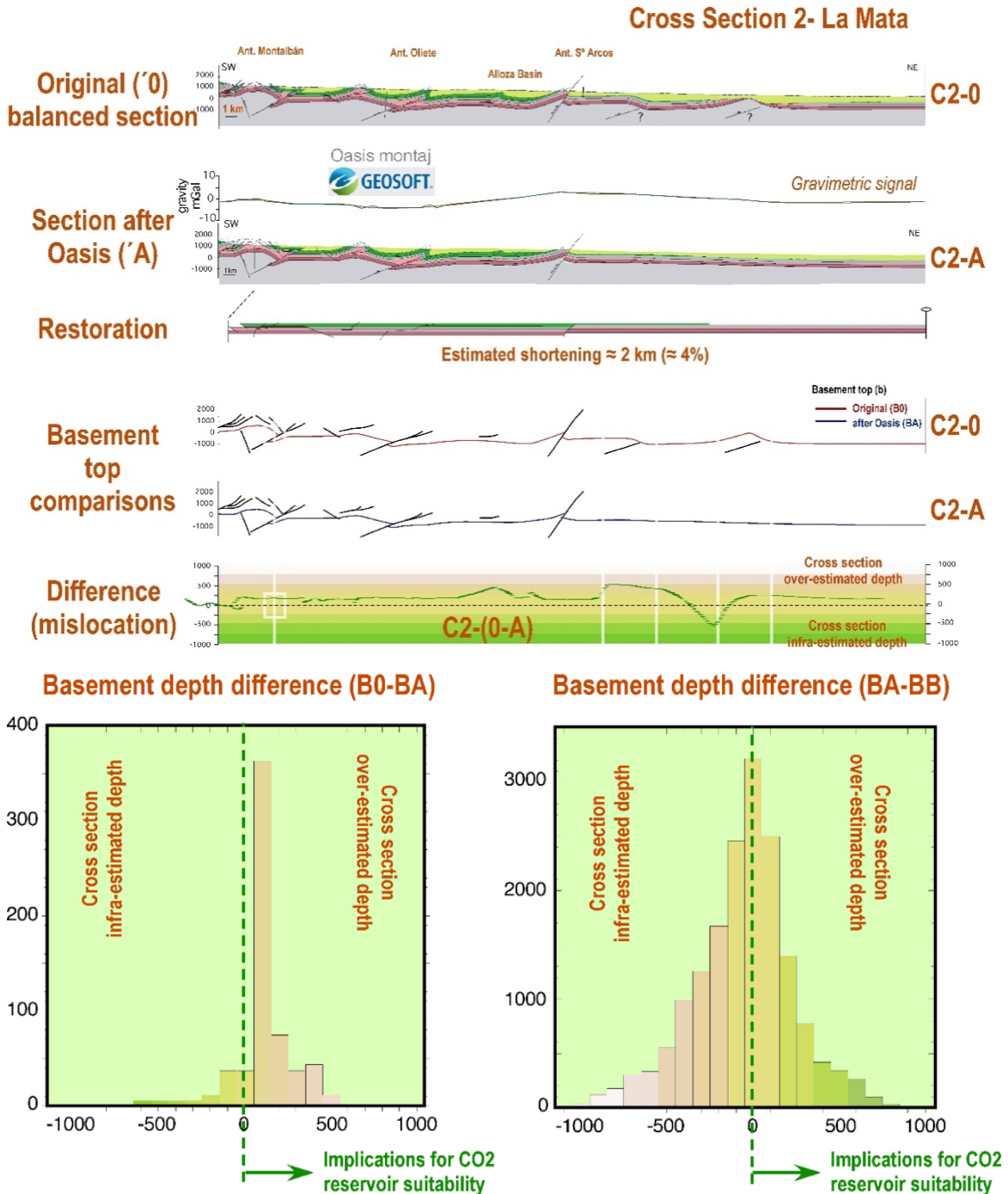


Figure 3.2.27- Comparison between initial balanced sections (0) (just geometry), the section corrected after the balancing of the gravimetric signal (A) (Oasis feedback) and the section extracted from the 3D model after the inversion (B) (Geomodeller) for section 2.



We have focused on the comparison in the location of certain horizons before and after that feedback (Bundsandstein top) due to its implications in the CO<sub>2</sub> storage potential. In some cases, mislocation of some horizons may reach up to 0.4 km, which represents up to 50% of the expected depth. After fitting the gravity data with balanced cross-sections we carried out a stochastic inversion that allowed reducing the uncertainty to a maximum of 0.15 km, i. e. c. 20%. Further error analysis may be focused on the double-checking with seismic section information from the industry, if and when available. The attached figure displays an example of one of the performed sections. There, extrapolation of subsurface structures under the Ebro foreland basin based on lateral information cannot be supported by the measured gravimetric signal. The mislocations of the basement top in A and B zones reach - 0.4 and + 0.8 km respectively, with critical implications for any potential CO<sub>2</sub> storage.

### 3.2.5.2. Barbastro anticline (South Pyrenean triangle zone, Spain)

Following the case study of the gravity prospecting in the South Central Pyrenees and the Ebro foreland basin presented in sections 2 and 3.1 (see there additional details and extended geological geophysical settings), we describe the quantitative approach: 3D gravity forward and inverse modelling.

We have used the same workflow as in the previous case study, the only difference being that the geometry of the cross sections imported in GeoModeller, to build up the 3D model, was constrained with a new interpretation of 42 seismic reflection profiles and five exploration wells (see Santolaria et al., 2020 for more details).

Therefore, a reasonably understanding of the geometry and structural architecture of the study area can be assumed as it is based on the surface geology, the interpretation of the available seismic reflection profiles and well data, and the 2.5D gravity modelling of selected cross sections. The final goal of the gravity stochastic inversion was to obtain the density distribution and 3D volume of the gypsiferous Barbastro Formation and lateral equivalents.

The 3D model is based on available surface geological data and 13 cross-sections from 3 different sources: i) four cross-sections from Santolaria et al. (2016) that were extended ~5 km to the S and slightly modified using 2.5D gravity forward modelling in order to better fit the new model boundary conditions and updated subsurface interpretation from seismic reflection profiles, ii) two new geological sections constrained by 2.5D gravity forward modelling, and iii) seven cross-sections build up from the interpreted reflection seismic data. 2.5D gravity forward modelling of cross-sections highlighted the necessity of considering significant density variation along the Late Eocene units (basically Barbastro Formation. and lateral equivalents) (Santolaria et al., 2016, 2020).

The 3D model has an extension of 80 x 70 km (5,600 km<sup>2</sup>), it is topped by a 100m-resolution DEM of the topography and the bottom is located at -6500 m, encompassing the upper part of the Palaeozoic basement. To carry out the calculations, each lithology



has been discretized in 500 x 500 x 200 m voxels. The total number of cells is 1,008,000 (160 x 140 x 45 cells) and in each cell the initial density value was assigned according to its lithology.

The geological model includes 290 representative bedding dips carefully selected in the surface geology to be consistent among them. Also includes contacts of the target units, and the main faults interpreted from surface geology and seismic profiles which are represented in the geological cross-sections.

Density data comes from a petrophysical data set (>3,000 density values): 1109 samples from Santolaria et al. (2016), 429 additional samples acquired during this study and also density data from the Iberian Range and the Ebro Basin (Pueyo et al., 2016). Unfortunately, formation density logs from oil well were not accessible this time (restricted information). The stratigraphic section has been divided into seven units. For the initial models, a density value with its standard deviation (SD) was assigned to each unit: (1) Basement,  $2.68 \pm 0.01 \text{ g/cm}^3$ ; (2) Triassic-Jurassic rocks of the Ebro Basin,  $2.5 \pm 0.08 \text{ g/cm}^3$ ; (3) autochthonous Cretaceous to Eocene,  $2.67 \pm 0.01 \text{ g/cm}^3$  and  $2.62 \pm 0.01 \text{ g/cm}^3$  (Eocene Marls); (4) Barbastro Fm. and lateral equivalents,  $2.35 \pm 0.15 \text{ g/cm}^3$ ; (5) Oligocene-Miocene terrigenous units (Peraltila Fm.,  $2.45 \pm 0.03 \text{ g/cm}^3$ ; and Sariñena Fm.,  $2.42 \pm 0.05 \text{ g/cm}^3$ ), (6) Middle-Upper Triassic evaporates,  $2.27 \pm 0.05 \text{ g/cm}^3$ ; and (7) non-evaporitic rocks involved in the Gavarnie-Sierras thrust sheets,  $2.67 \pm 0.05 \text{ g/cm}^3$ .

The inversion runs for  $25 \times 10^6$  iterations, all the lithological boundaries were fixed and we allowed 100% property change in each unit. The change was allowed within the SD associated to each density. The most significant density changes occur within the Barbastro Formation and lateral equivalents. This unit has a SD one order of magnitude higher than the rest of units and therefore more prone to change its density through the inversion process. Barbastro Formation low, medium and high density facies (Fig. 3.2.28) are correlated with evaporitic facies, evaporitic and marly-sandy facies, and marly-sandy to conglomeratic facies respectively.

The results of the inversion allowed mapping the transition between low to high density rocks within the Barbastro Formation and lateral equivalents. Along the eastern part, this transition shows a N090E to N110E trend which coincides with the facies transition described to the north of the Azanuy syncline (Senz and Zamorano, 1992) which help validating our inversion method. This approach demonstrates that gravity is a powerful tool to characterize evaporitic units and also highlights the importance of controlling the 3D variability and distribution of evaporitic detachments in salt and thrust tectonics. An extended discussion on the results of the inversion can be found in Santolaria et al. 2020.

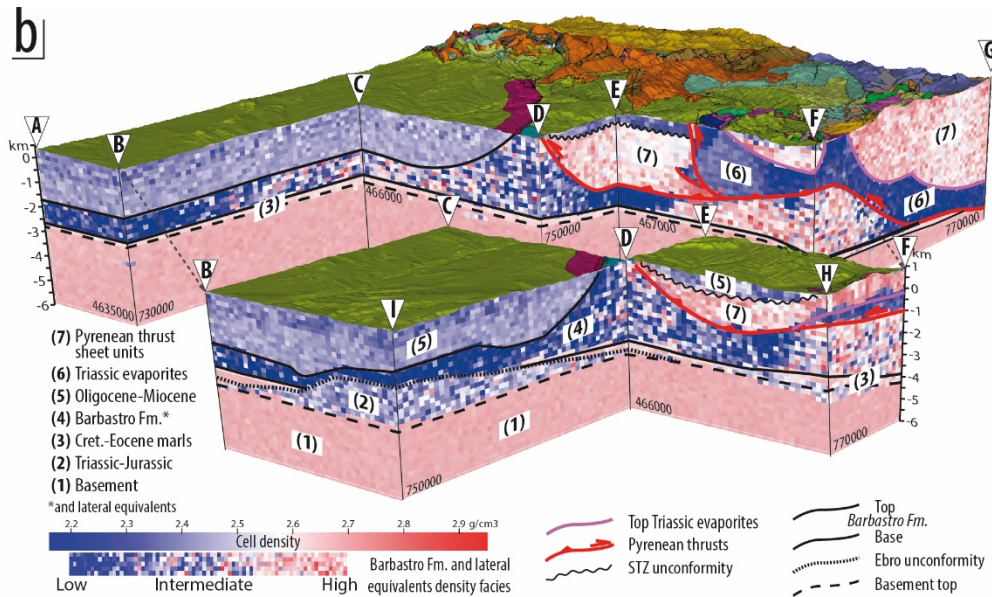


Figure 3.2.28. 3D view of the density voxel resulting from the gravity inversion in the Barbaastro anticline case study (modified from Santolaria et al., 2020).

### 3.2.5.3. Gravity modelling in the North German Basin with software IGMAS+

3D gravity modelling was performed at the southern margin of the North German Basin. Main goal was to achieve additional information on the structural setting in the cross-border area between the two federal states of Saxony-Anhalt and Brandenburg to harmonize the existing but misaligned 3D geological models in this area (Malz et al, 2020; Schilling et al, 2018). These models base on depth maps of interpreted interfaces from seismic reflection data and borehole data. However, data coverage in the cross-border region is sparse and of lower quality.

Prior modelling, terrestrial gravity data of five surveys were compiled to a consistent dataset (Fig. 3.2.29a). The resulting complete Bouguer anomaly map was utilized for gravity interpretation to obtain new information on the fault system and main gravity anomalies in the cross-border region. The main steps of gravity data processing and interpretation are described in chapter 3.1.9.4.

Density data for the sediment layers base on hand on a compilation of density values from the eastern part of the North German Basin of Köhler & Eichner (1973), which compiled laboratory measurements on rock samples from boreholes and correlation values derived from seismic velocities. Additionally, we added newly digitized density values from rock samples of other boreholes to this compilation. All values are saturation densities, representing densities as to be expected at in-situ conditions. We used a 2-stage petrophysical model for regression of the density-depth-relation. A



constant density or linear increase of density with depth was mostly not suitable to fit the density measurements. Densities of the basement rocks base on one hand on laboratory measurements on rock samples from the field. Combined with information on the rock composition from thin slices, zones of different densities were initially identified and later confirmed and refined during gravity modelling. No density information were available for the Early Palaeozoic and Proterozoic crust. Therefore, we converted seismic P-wave velocities from seismic refraction data by the approach of Christensen & Mooney (1995). Additional constraints for the sediment und crustal setting base on seismic reflection and refraction data.

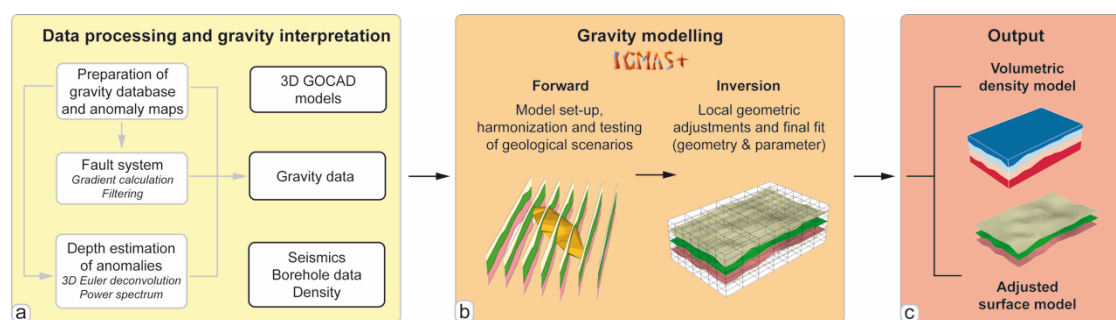
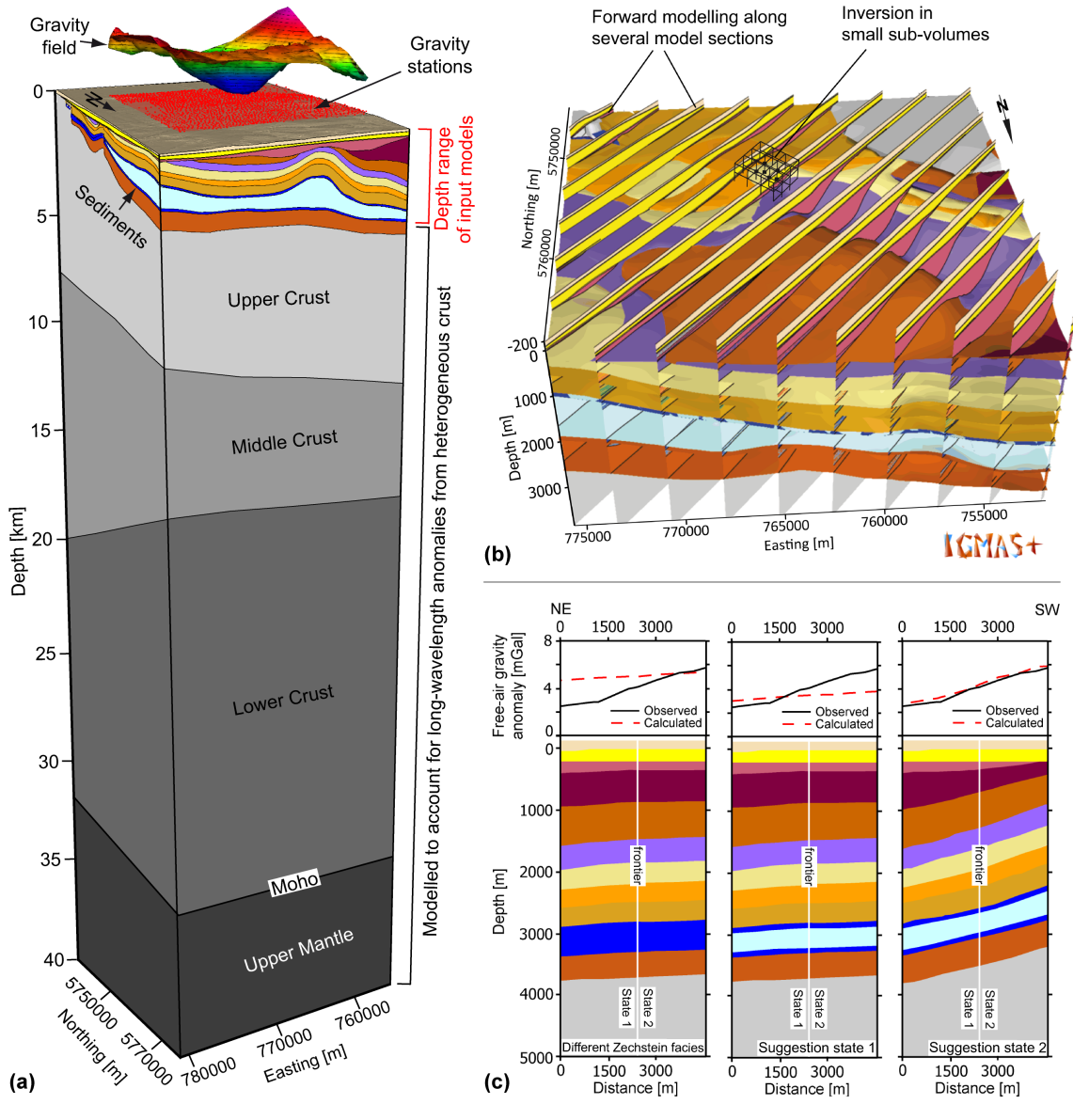


Figure 3.2.29. Flow chart of the modelling workflow: a) preparation of input data (gravity data, seismic profiles, borehole logs, petrophysical data) and gravity interpretation for model-wide fault detection. b) 3D gravity modelling with software IGMAS+. Working steps included at first forward modelling for testing geological scenarios and model harmonization. Afterwards gravity inversion for local adjustments. c) interpretation and utilization of output models (Mueller et al., 2021).

For setup of the starting model we transferred at first the sediment surfaces from the two 3D geological models (Malz et al, 2020; Schilling et al, 2018) to 26 2D model section in IGMAS+ (Götze & Lahmeyer, 1988; Schmidt et al., 2020). These sections are separated by 2 km in the main study area and 4 km in the extended study area (Fig. 3.2.29b). All model sections are extended by 250 km to avoid edge effects during gravity calculation. The top of the model (top Quaternary) is based on a digital elevation model with 5 m resolution. The reference density of the models' surrounding space was set to the standard density value of 2.67 g/cm<sup>3</sup>. To account for density inhomogeneities from the deeper surface and for adequate modelling of long wavelength anomalies, we introduced additional layer for the Permo-Carboniferous sediments and the for basement (upper, middle, lower crust and upper mantle). These new surfaces base on drilling results and seismic refraction profiles. Subsequently, the model was triangulated in between the model sections. In total, the model consists of 17 layers and extends from the surface down to 40 km depth (Fig. 3.2.30a). Afterwards, all seismic profiles and borehole data, as well as the new indications on the fault system and depth information from the Euler deconvolution are imported to IGMAS+. For parametrization, the model was gridded by 125 m in horizontal direction and 25 m in vertical direction. Subsequently, the respective densities and density gradients were assigned to the voxels (Fig. 3.2.31). As the gradients are assigned individually to each layer, they can change at layer interfaces and at faults. In a last step, the free-air gravity anomaly and horizontal



gradient of the measured gravity data are imported and the gravity signal of the starting model is calculated.



Quaternary	Keuper	Lower Buntsandstein	Upper Crust
Neogene & Oligocene	Muschelkalk	Mostly anhydrite and dolomite (Zechstein)	Middle Crust
Eo- & Palaeocene	Upper Buntsandstein	Staßfurt salt (Zechstein z2NA)	Lower Crust
Jurassic	Middle Buntsandstein	Permo-Carboniferous	Upper Mantle

Figure 3.2.30. a) General view of the 3D model in IGMAS+ with all modelled layers from the surface down to 40 km depth. b) Illustration of the applied gravity modelling techniques, comprising at first forward modelling along several 2D model sections and subsequent triangulation in-between the sections. Afterwards parameter inversion is used for density adjustment and geometric inversion in-between the model sections. c) Example for the harmonization process across the states' frontier. Therefore, several different scenarios are tested (Mueller et al., 2021).

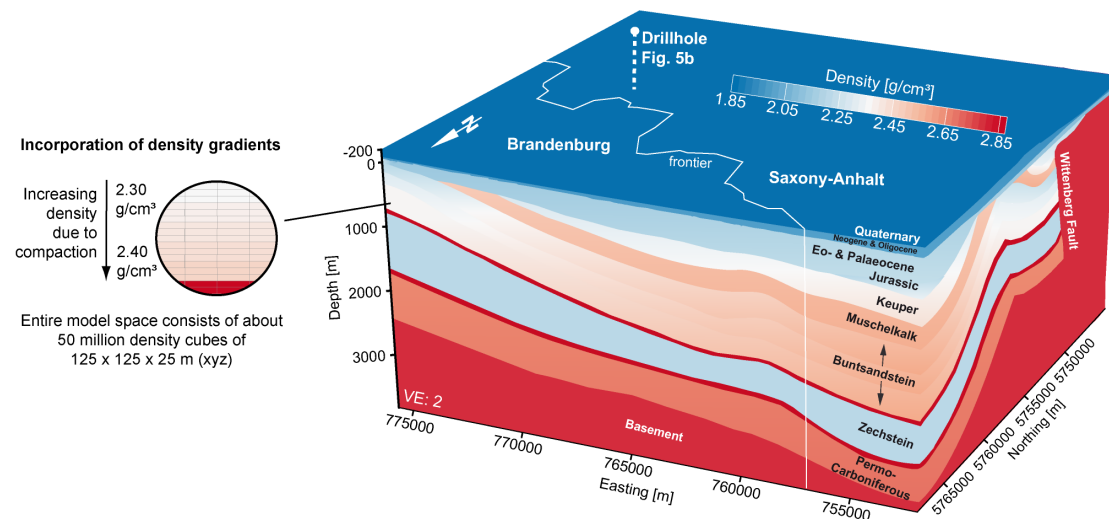


Figure 3.2.31. a) Density cube of the 3D model (upper 4 km). Model area was divided into about 50 million voxels (small inset) for parametrization to allow the layer-wise incorporation of density gradients (Mueller et al., 2021).

We began with a forward modelling approach, to keep the full control on the models' consistency to the regional geological setting. The modelling process followed a bottom-to-top approach, wherein at first the long wavelength anomalies are modelled. As already known from the compilation of the density dataset, the upper crust is characterized by zones of different densities, whose adequate modelling required a division of the upper crust into separate bodies. After fitting the long wavelength anomalies, we tested several geological scenarios. On one hand, this comprised different geological settings along the cross-border region to harmonize the two 3D geological input models. On the other hand, we tested several scenarios in areas with sparse or ambiguous information or even no constraints (e.g. different tested scenarios for the setting of an anticline structure). Selection of the most suitable scenario is based on the misfit to the measured data as well as its geological plausibility. Usually at first it was tried to obtain an adequate fit by changing the densities within their deviation. If this did not produce an acceptable fit, then the layer's geometry was iteratively changed. Gravity gradient modelling (horizontal gradient) was especially incorporated for modelling of the geometry and trend of faults. In a second step we applied parameter inversion to the layer's densities to further improve the fit of small-scale anomalies to the measured gravity data. Required uncertainties of the measured and processed gravity data are in the range of 0.05 g/cm<sup>3</sup>. The standard error of regression of the density-depth-relations of the sediment layers ranges between 0.02 – 0.1 g/cm<sup>3</sup> and 0.03 g/cm<sup>3</sup> for the basement densities measured at rock samples. Standard deviation for densities converted from velocities of seismic refraction studies are about 0.1 g/cm<sup>3</sup>.



Finally, an automatic geometric inversion was applied to small sub-volumes in between the model sections to further increase the fit to the measured gravity data.

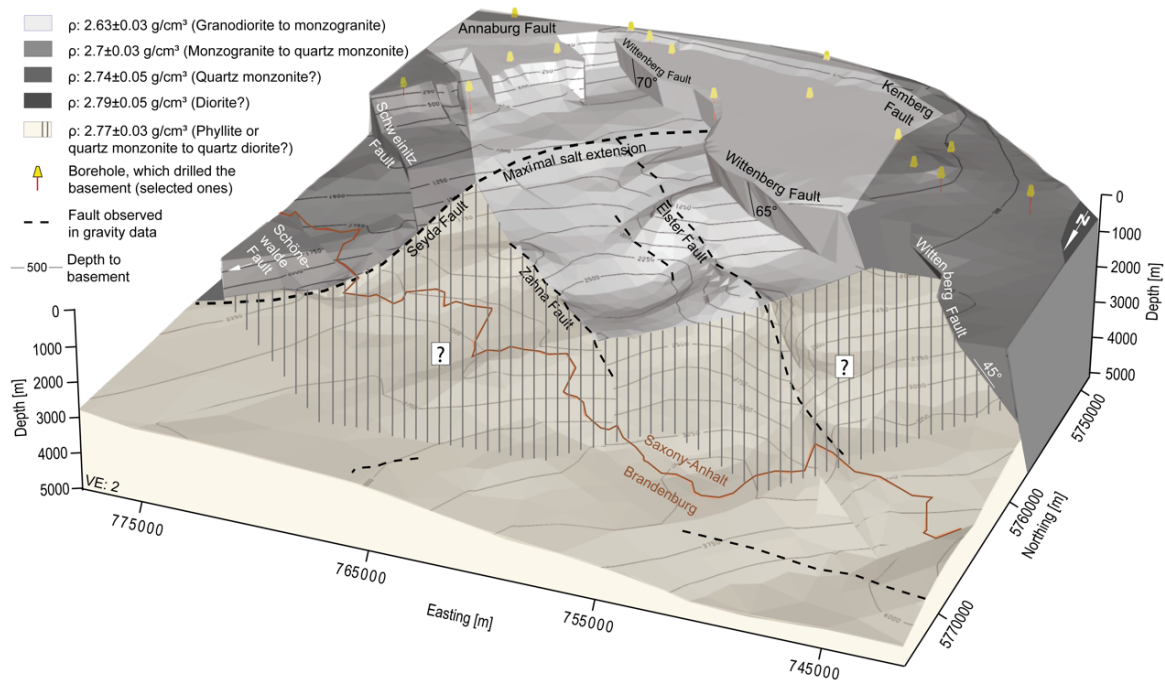


Figure 3.2.32. 3D perspective view of the basement topography. Zones of different density are marked in different colours (Mueller et al., 2021).

Estimation of the model's uncertainty is hard to assume, as gravity modelling is always affected by the non-uniqueness problem and several subjective decisions are made during the modelling process. IGMAS+ does not offer the possibility for incorporating uncertainty grids or the calculation of the model's entropy. However, to access the significance of the depth information and shape of the modelled layers, we tested the gravity anomaly's sensitivity to geometrical changes of individual layers. The test showed the greatest sensitivity to changes in density or geometry for the near-surface layers of the Cenozoic and the interfaces of the Muschelkalk and the Zechstein. These layers are characterized by prominent density contrasts to the adjacent layers. As a consequence, geometrical changes at the interfaces of the Jurassic and inner boundaries of the Buntsandstein do not affect the calculated gravity signal. Therefore, these layers are only modelled to follow the trend of the adjacent layers and their depth information are of lower precision.

Main results of the gravity modelling are on the hand the set-up of a harmonized 3D geological model, which is aligned in the cross-border region and is consistent to the measured gravity signal. Furthermore, we obtain new geophysical evidence on the geological setting. We interpret a low-density zone within the basement of the North German Basin as the northward extension of the Pretzsch-Prettin Crystalline Complex (Fig. 3.2.32). This is surrounded by dense granodiorites and diorites with a larger portion of mafic minerals. Additionally, we observe two types of anticlines within in the North





#### 4. Conclusions and lessons to be learnt.

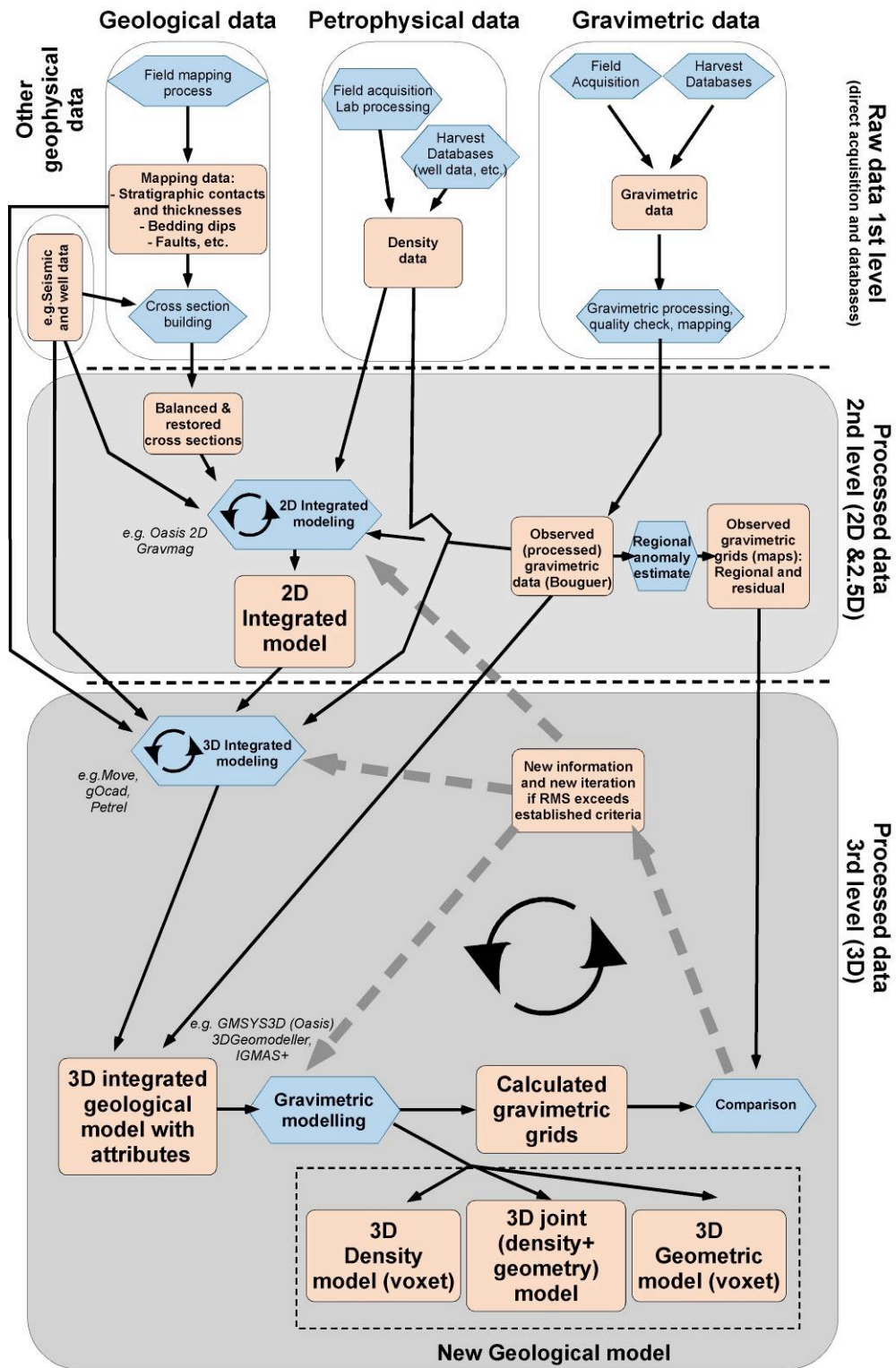
Providing an enough density contrast exists among the subsurface rocks, the gravity method is a well-founded, quick, cost-effective and efficient technique for subsurface exploration and thus, an excellent technique for harmonizing 3D models, in particular when scarce and heterogeneous subsurface information is only available or for harmonizing cross-border regions. Similarly happens for the magnetic susceptibility and remanence contrast and the magnetic method.

In this report, we propose a workflow of 3D modelling of gravimetric signals emphasizing the need of two key elements; the use of structural techniques (in particular balanced and restored cross sections) and the attaining of robust petrophysical data for the modeling. The report does not pretend to be a reference book, but a practical manual based on common procedures used by some EGS members (and academic institutions). The workflow we propose is organized in three levels.

The first one refers to the three main data types needed for the modelling; gravimetric, structural and the petrophysical data. We have focused on these three main pillar by doing a practical review, likely incomplete, of methods, instrumentation and software, etc. that are later on illustrated with examples from previous works (as in the other levels).

The second level deals with 2D joint modelling of the three variables together, both in map-view (gravity maps) and in 2D cross-sections. Standard processing techniques are required to obtain the Bouguer, regional and residual maps, as well as many possible enhancement methods (derivatives, upward continuation, etc.). Ideally, these maps should be interpreted (squeezed) together with geological knowledge to get insights on the origin of the anomalies. The 2D (2.5D) step is a feedback process (forward modelling) where geometry, gravity and petrophysics are all balanced together until the calculated gravity anomaly consistently matches the observations (2D integrated model). Ideally, a set of serial geometrically balanced cross sections should be initially designed and built. After the forward modelling, these serial sections (with all properties balanced) are an excellent approach of the 3D model of the target area.

In the third level, an integrated 3D structural model is build merging all data together – petrophysical, geological and gravimetric - to obtain a 3D geological model with attributes (and associated uncertainties). In regions without seismic coverage, the implementation of the aforementioned serial cross sections (2D integrated models) is critical to derived further reliable results. This 3D model can be subjected to geophysical inversion in several software platforms during a feedback process that will last until a reasonable solution is achieved (calculated gravity signal reasonably matches the observed one). The derived results are new density grids and new topography information for the modelled volumes/horizons and represent a more accurate reconstruction of the subsurface that will aid in further decision-making processes.





## Lessons to be learnt

- The gravimetric method is a well-founded and established technique for subsurface exploration since decades. Besides, it is quick, cost-effective and efficient and can be essential for harmonization of 3D models in cross-border regions or areas of scarce subsurface data. However, the final resolution of the method depends on a number of factors, among them, the petrophysical contrast is a key one. Density contrast, together with the desired resolution, will condition the gravimetric measuring grid density. This means that the **harmonization process based on gravimetric acquisition may take time**, especially if the target area includes rough terrains (1/3 efficiency). Harmonization is very sensitive (even hampered) by data sharing regulations in case of cross-border projects. Unfortunately, many existent databases are not ruled by FAIR principles.
- An initial petrophysical characterization (from previous data) is, therefore, a relevant factor to estimate the possible final resolution of the method (or even its suitability). Besides, a **robust characterization of petrophysical** data of target formations (both at surface and at depth) must be attained during the project development (new data, databases, wells, etc.). Currently, there exist several data models, data schemes and databases for petrophysical data (those needed for gravimetric/magnetic modeling), but their interoperability is limited, since part of them are not governed by FAIR access principles. Establishing a standard petrophysical data model is needed.
- In areas of poor or absent seismic coverage, the correct design of a **set of serial balanced cross sections** is a key factor for the joint workflow with gravimetric and petrophysical data. Besides, the spacing among them must be enough to guarantee the 3D characterization of the subsurface, especially in areas of superposed deformation. **Outcropping conditions** are important to ensure the construction of reliable subsurface images, their lack can compromise the suitability of the workflow. Seismic and well data (if exist) are keystones in cross section building. Unfortunately, access to this information is very often not governed by FAIR access policies.
- Therefore, current **European data infrastructure platforms (EGDI, EPOS)** should tackle the lack of FAIR principles affecting many of the required data for subsurface harmonization (gravimetric, petrophysical, seismic, wells, etc.).
- **Estimation of uncertainty** in the workflow using structural, geophysical and petrophysical data is controlled to a certain extent, but its **propagation during the modeling** levels is very little known. Future efforts should be done to evaluate the final uncertainty in the subsurface reconstruction.



## 5 References

- Adams, S. J. (2005, January). Quantifying petrophysical uncertainties. In *SPE Asia Pacific Oil and Gas Conference and Exhibition*. Society of Petroleum Engineers.
- Agarwal, R. G., and Kanasewich, E. R. (1971). Automatic trend analysis and interpretation of potential field data. *Geophysics*, 36, 339–348.
- Agocs, W. B. (1951). Least-squares residual anomaly determination. *Geophysics*, 16, 686–696.
- Aldana, M., Costanzo-Alvarez, V., & Díaz, M. (2003). Magnetic and mineralogical studies to characterize oil reservoirs in Venezuela. *The Leading Edge*, 22(6), 526-529.
- Allerton, S. (1998). Geometry and kinematics of vertical-axis rotations in fold and thrust belts. *Tectonophysics*, 299(1-3), 15-30.
- Allmendinger, R.W. (1998). Inverse and forward numerical modelling of trishear fault-propagation folds. *Tectonics*, 17, 640-656.
- Allmendinger, R.W. (2015). *Modern Structural Geology. A structural geology laboratory manual for the 21st century*. <http://www.geo.cornell.edu/geology/faculty/RWA/structure-lab-manual/>
- Alonso, F. (1975). Presentación de la primera edición de los Mapas Gravimétricos de la Península Ibérica. F. Alonso IGC. XVI Asamblea General de la IUGG en Grenoble.
- Altwegg, P., Renard, P., Schill, E., & Radogna, P. V. (2015). GInGER (Gravimetry for Geothermal Exploration): a new tool for geothermal exploration using gravity and 3D modelling software. In *Proc. World Geothermal Congress* (p. 7).
- Améglío, L., Vignerresse, J. L., & Bouchez, J. L. (1997). Granite pluton geometry and emplacement mode inferred from combined fabric and gravity data. In *Granite: From segregation of melt to emplacement fabrics* (pp. 199-214). Springer
- Andersen, M. A., Duncan, B., & McLin, R. (2013). Core truth in formation evaluation. *Oilfield Review*, 25(2), 16-25.
- Antolín-Tomás, B., Román-Berdiel, T., Casas-Sainz, A., Gil-Peña, I., Oliva, B., & Soto, R. (2009). Structural and magnetic fabric study of the Marimanha granite (Axial Zone of the Pyrenees). *International Journal of Earth Sciences*, 98(2), 427-441.
- Arenas, C.; Millán, H.; Pardo, G.; Pocoví, A., 2001 Ebro Basin continental sedimentation associated with late compressional pyrenean tectonics (NE Iberia): controls on margin fans and alluvial systems. *Basin Research*, 13; 65-89.
- Arriagada, C., Roperch, P., Mpodozis, C., & Cobbold, P. R. (2008). Paleogene building of the Bolivian Orocline: Tectonic restoration of the central Andes in 2-D map view. *Tectonics*, 27(6).
- Asfahani, J., & Tlas, M. (2008). An automatic method of direct interpretation of residual gravity anomaly profiles due to spheres and cylinders. *Pure and Applied Geophysics*, 165(5), 981-994.
- Asquith, G. B., Krygowski, D., & Gibson, C. R. (2004). *Basic well log analysis* (Vol. 16). Tulsa: American Association of Petroleum Geologists.
- Asquith, G., & Gibson, C. (1982). *Basic Well-log Analysis for Geologist: AAPG, Tulsa Oklahoma. Series, 3*, 41-100.
- Athy, L. F. (1930). Density, porosity, and compaction of sedimentary rocks. *Aapg Bulletin*, 14(1), 1-24.
- Aubourg, C., Pozzi, J. P., & Kars, M. (2012). Burial, claystones remagnetization and some consequences for magnetostratigraphy. *Geological Society, London, Special Publications*, 371(1), 181-188.
- Ayala, C. (2013). A new compilation of gravity data over the Iberian Peninsula and surrounding areas. *Internal Report Topolberia project (Consolider-Ingenio)*. IGME, 20 pp., 3 figures.
- Ayala, C., Bohoyo, F., Maestro, A., Reguera, M. I., Torne, M., Rubio, F., ... & García-Lobón, J. L. (2016). Updated Bouguer anomalies of the Iberian Peninsula: a new perspective to interpret the regional geology. *Journal of Maps*, 12(5), 1089-1092.
- Ayala, C., Torné, M. and Pous, J., The lithosphere-asthenosphere boundary in the western Mediterranean from 3D joint gravity and geoid modelling: tectonic implications. (2003). *Earth and Planetary Science Letters*, 209, 3-4, pp 275-290
- Aydın, N. G., & İşseven, T. (2021). GravPack: a MATLAB-based gravity data processing package. *Arabian Journal of Geosciences*, 14(4), 1-8.



- Badgley, P.C. (1959). *Structural methods for the exploration geologist*. Harper & Brothers Publishers, New York, 34-67.
- Bailo, D., Jeffery, K. G., Spinuso, A., & Fiameni, G. (2015). Interoperability oriented architecture: The approach of EPOS for solid earth e-infrastructures. In 2015 IEEE 11th International Conference on e-Science (pp. 529–534). IEEE.
- Baldwin, B., Butler, C.O. (1985). *Compaction Curves*. AAPG Bulletin 69, 622–626.
- Bally, A.W., Gordy, P.L., & Stewart, G.A. (1966). Structure, seismic data and orogenic evolution of the Southern Canadian Rocky Mountains. *Bull. Can. Pet. Geol.* 14, 337-381.
- Bär, K., Reinsch, T., & Bott, J. (2020). The PetroPhysical Property Database (P<sup>3</sup>)—a global compilation of lab-measured rock properties. *Earth System Science Data*, 12(4), 2485-2515.
- Bär, K.; Reinsch, T.; Bott, J. (2019): P<sup>3</sup> - PetroPhysical Property Database. V. 1.0. GFZ Data Services. <https://doi.org/10.5880/GFZ.4.8.2019.P3>
- Bárdossy, G., & Fodor, J. (2001). Traditional and new ways to handle uncertainty in geology. *Natural Resources Research*, 10(3), 179-187.
- Barlow, M. (2019). *Geoscience Australia: News. Preview*, 2019(203), 21-24
- Bell, R. E., Jackson, C. A.-L., Elliott, G. M., Gawthorpe, R. L., Sharp, I. R., & Michelsen, L. (2014). Insights into the development of major rift-related unconformities from geologically constrained subsidence modelling: Halten Terrace, offshore mid Norway. *Basin Research*, 26(1), 203–224. <https://doi.org/10.1111/bre.12049>
- Beltrao, J. F., Silva, J. B. C., & Costa, J. C. (1991). Robust polynomial fitting method for regional gravity estimation. *Geophysics*, 56(1), 80-89.
- Berné Valero, J.L., Anquela, A.B. and Garrido N. (2014). *GNSS. GPS: fundamentos y aplicaciones en Geomática*. Valencia: Universitat Politècnica de València.
- Beutner, E. C., & Charles, E. G. (1985). Large volume loss during cleavage formation, Hamburg sequence, Pennsylvania. *Geology*, 13(11), 803-805.
- Bishop, D & Buchanan, P.G. (1995). Development of structurally inverted basins: a case study from the West Coast, South Island, New Zealand. In: Buchanan, J.G., Buchanan, P.G. (Eds.), *Basin Inversion*. *Geol. Soc. London Spec. Publ.* 88, 549-586.
- Blakely, R.J., 1995 (2005), *Potential Theory in Gravity & Magnetic Applications: Cambridge University Press*, pp.441. doi:10.1017/CBO9780511549816
- Bleakly, D. C., Van Alstine, D. R., & Packer, D. R. (1985). Controlling errors minimizes risk and cost in core orientation. *Oil and Gas Journal*, 83, 48..
- Boedecker, G. (2002). World gravity standards-present status and future challenges. *Metrologia*, 39(5), 429.-
- Bond, C. E. (2015). Uncertainty in structural interpretation: Lessons to be learnt. *Journal of Structural Geology*, 74, 185-200.
- Bond, C. E., Gibbs, A. D., Shipton, Z. K., & Jones, S. (2007). What do you think this is? "Conceptual uncertainty" in geoscience interpretation. *GSA today*, 17(11), 4.
- Bonté, D., Van Wees, J. D., & Verweij, J. M. (2012). Subsurface temperature of the onshore Netherlands: new temperature dataset and modelling. *Netherlands Journal of Geosciences*, 91(4), 491-515.
- Bott, M.P.H., 1960. The use of rapid digital computing methods for direct gravity interpretation of sedimentary basins. *Geophys. J. Roy. Astr. Soc.* 3, 63-67.
- Bouchez, J. L. (1997). Granite is never isotropic: an introduction to AMS studies of granitic rocks. In *Granite: from segregation of melt to emplacement fabrics* (pp. 95-112). Springer, Dordrecht.
- Bouman, J., Ebbing, J., Meeke, S., Fattah, R. A., Fuchs, M., Gradmann, S., ... & Bosch, W. (2015). GOCE gravity gradient data for lithospheric modeling. *International Journal of Applied Earth Observation and Geoinformation*, 35, 16-30.
- Bourne, J. H. (1993). Use of magnetic susceptibility, density, and modal mineral data as a guide to the composition of granitic plutons. *Mathematical geology*, 25(3), 357-375.
- Boyer, S. E., & Mitra, G. (1988). Relations between deformation of crystalline basement and sedimentary cover at the basement/cover transition zone of the Appalachian Blue Ridge Province. *Geol. Soc. Am. Spec. Paper*, 222, 119-136.



- Boyko, T., Scholger, R., Stanjek, H., & MAGPROX Team. (2004). Topsoil magnetic susceptibility mapping as a tool for pollution monitoring: repeatability of in situ measurements. *Journal of Applied Geophysics*, 55(3-4), 249-259.
- Breili, K., & Pettersen, B. R. (2009). Effects of surface snow cover on gravimetric observations. *Journal of Geodynamics*, 48(1), 16-22.
- Briggs, I.C. (1974). Machine contouring using minimum curvature. *Geophysics*, 39, 39-48.
- Bulnes, M. & McClay, K.R. (1999). Benefits and limitations of different 2D algorithms used in cross-section restoration of inverted extensional faults: application to physical experiments. *Tectonophysics*, 312, 175-189.
- Bulnes, M. & Poblet, J. (1999). Estimating the detachment depth in cross sections involving detachment folds. *Geol. Mag.*, 136 (4), 395-412.
- Burberry, C. M. (2015). Spatial and temporal variation in penetrative strain during compression: Insights from analog models. *Lithosphere*, 7(6), 611-624.
- Burov, E.B., Diament, M. (1995). The effective elastic thickness ( $T_e$ ) of continental lithosphere: What does it really mean? *Journal of Geophysical Research: Solid Earth* 100, 3905–3927. <https://doi.org/10.1029/94JB02770>
- Busk, H. G. (1929). *Earth flexures*. Cambridge University Press, London, 186 pp.
- Butler, R. F. (1992). *Paleomagnetism, Magnetic domains to geologic terranes*. Blackwell. 238 pp
- Butler, R.W.H. (1989). The influence of pre-existing basin structure on thrust system evolution in the Western Alps. In: Cooper, M.A., Williams, G.D. (Eds.), *Inversion Tectonics*. *Geol. Soc. London Spec. Publ.* 44, 105-122.
- Buxtorf, A. (1916). *Prognosen und Befunde beim Hauensteinbasis und Grenchenbergtunnel und die Bedeutung der letzteren für die Geologie des Jura-Gebirges*. *Verh Naturforsch Ges Basel*, 27, 185-254.
- Calcagno, P., Chilès, J. P., Courrioux, G., & Guillen, A. (2008). Geological modelling from field data and geological knowledge: Part I. Modelling method coupling 3D potential-field interpolation and geological rules. *Physics of the Earth and Planetary Interiors*, 171(1-4), 147-157.
- Calcagno, P., Courrioux, G., Guillen, A., Fitzgerald, D., & McInerney, P. (2006). How 3D implicit geometric modelling helps to understand geology: The 3D-geomodeller methodology. In *XIth International Congress, Society for Mathematical Geology* (p. 27).
- Calvín, P., Santolaria, P., Casas, A. M., & Pueyo, E. L. (2017). Detachment fold vs. ramp anticline: a gravity survey in the southern Pyrenean front (External Sierras). *Geological Journal*, 53(1), 178-190.
- Cannon, S. (2015). *Petrophysics: a practical guide*. John Wiley & Sons.
- Carbone et al., 2020 (EGU2020-16329, <https://doi.org/10.5194/egusphere-egu2020-16329>, EGU General Assembly 2020)
- Cardozo, N., & Oakley, D. (2019). Inverse modeling for possible rather than unique solutions. *Journal of Structural Geology*, 125, 285-295. Non cited in the text
- Carmichael, R. S. (2017). *Practical Handbook of Physical Properties of Rocks and Minerals* (1982). CRC press.
- Carrera, N., Muñoz, J. A., & Roca, E. (2009). 3D reconstruction of geological surfaces by the equivalent dip-domain method: An example from field data of the Cerro Bayo Anticline (Cordillera Oriental, NW Argentine Andes). *Journal of Structural Geology*, 31(12), 1573-1585.
- Casas, A. M.; Pardo, G., 2004. Estructura pirenaica y evolución de las cuencas sedimentarias en la transversal Huesca-Oloron. In: *Itinerarios geológicos por Aragón* (Edited by Colombo, F.; Liesa, C. L.; Meléndez, G.; Pocij, A.; Sancho, C.; Soria A. R. ), *Geo Guías* (Sociedad Geológica de España), 1, 63-96 (ISBN: 84-930160-2-0).
- Casas-Sainz, A.M., (1992). El frente Norte de las Sierras de Cameros: Estructuras cabalgantes y campos de esfuerzos. *Zubia, Monográfico 4*, Instituto de Estudios Riojanos, Logroño, 219 p
- Cattin, R., Mazzotti, S., & Baratin, L. M. (2015). GravProcess: An easy-to-use MATLAB software to process campaign gravity data and evaluate the associated uncertainties. *Computers & geosciences*, 81, 20-27.
- CG5 Autograv (2012). *Operation manual*. Scintrex limited. Document part N° 867700. Revision 8. (<http://www.scintrexltd.com>)



- Chai, Y., & Hinze, W. J. (1988). Gravity inversion of an interface above which the density contrast varies exponentially with depth. *Geophysics*, 53(6), 837-845.
- Chamberlin, R.T. (1910). The Appalachian folds of central Pennsylvania. *Journal of Geology*, 18, 228-251.
- Chandler, V.W.; Lively, R.S. (2015). 2011 Rock Properties Database: Density, Magnetic Susceptibility, and Natural Remanent Magnetization of Rocks in Minnesota. Retrieved from the Data Repository for the University of Minnesota, <http://dx.doi.org/10.13020/D63S3D>.
- Chapin, D.A. (1996). The theory of the Bouguer gravity anomaly: A tutorial. *The Leading Edge*, 15, 361-363.
- Chapin, D. A. (1997). Wavelet transforms: A new paradigm for interpreting gravity and magnetics data?. In *SEG Technical Program Expanded Abstracts 1997* (pp. 486-489). Society of Exploration Geophysicists.
- Chapin, D. (1998). Gravity instruments: Past, present, future. *The leading edge*, 17(1), 100-100.
- Chapin, D. A., & Ander, M. E. (1999). Borehole gravity: New life for borehole gravity. *AAPG Explorer*, 20, 24-29.
- Chapin, D. A., & Mann, E. H. (1999). The bold new world of borehole gravimetry. In *SEG Technical Program Expanded Abstracts 1999* (pp. 393-396). Society of Exploration Geophysicists.
- Chapman, T.J. (1989). The Permian to Cretaceous structural evolution of the Western Approaches Basin (Melville sub-basin), UK. In: Cooper, M.A. Williams, G.D. (Eds.), *Inversion Tectonics*. *Geol. Soc. London Spec. Publ.* 44, 177-200.
- Chavarría et al., 2006, Modeling gravity and tensor gravity data using Poisson's Equation for airborne, surface and borehole applications: US Patent No. 6,993,433 B2, ConocoPhillips Company.
- Christensen, N.I. & Mooney, W.D. (1995). Seismic velocity structure and composition of the continental crust: A global view. *J. Geophys. Res.*, 100, 9761-9788, <http://dx.doi.org/10.1029/95JB00259>.
- Clark, D. A. (1983). Comments on magnetic petrophysics. *Exploration Geophysics*, 14(2), 49-62.
- Clark, D. A. (1997). Magnetic petrophysics and magnetic petrology: aids to geological interpretation of magnetic surveys. *AGSO Journal of Australian Geology and Geophysics*, 17, 83-104.
- Clark, D. A. (1999). Magnetic petrology of igneous intrusions: implications for exploration and magnetic interpretation. *Exploration Geophysics*, 30(2), 5-26.
- Clark, D. A., & Emerson, D. W. (1991). Notes on rock magnetization characteristics in applied geophysical studies. *Exploration Geophysics*, 22(3), 547-555.
- Coates, J. (1945). The construction of geological cross sections. *Quat. Jour. Geol. Min. Met. Soc. India*, 17.
- Compton, A. H. (1923). A quantum theory of the scattering of X-rays by light elements. *Physical review*, 21(5), 483.
- Cooper, G. R. J. (2006). Interpreting potential field data using continuous wavelet transforms of their horizontal derivatives. *Computers & Geosciences*, 32(7), 984-992.
- Cooper, M. A. (1983). The calculation of bulk strain in oblique and inclined balanced sections. *Journal of Structural Geology*, 5(2), 161-165.
- Cordell, L. (1973). Gravity analysis using an exponential density-depth function; San Jacinto Graben, California. *Geophysics*, 38(4), 684-690.
- Cordell, L. (1979). Gravimetric expression of graben faulting in Santa Fe Country and the Espanola Basin. In *New Mexico Geological Society Guidebook, 30<sup>th</sup> Field Conference*, New Mexico, 1979 (pp. 59-64).
- Cordell, L., & McCafferty, A. E. (1989). A terracing operator for physical property mapping with potential field data. *Geophysics*, 54(5), 621-634.
- Costanzo-Álvarez, V., Aldana, M., Bayona, G., López-Rodríguez, D., & Blanco, J. M. (2012). Rock magnetic characterization of early and late diagenesis in a stratigraphic well from the Llanos foreland basin (Eastern Colombia). *Geological Society, London, Special Publications*, 371(1), 199-216.
- Criss, R. E., & Champion, D. E. (1984). Magnetic properties of granitic rocks from the southern half of the Idaho batholith: Influences of hydrothermal alteration and implications for aeromagnetic interpretation. *Journal of Geophysical Research: Solid Earth*, 89(B8), 7061-7076.
- Dahlstrom, C. D. A. (1969). Balanced cross sections. *Canadian Journal of Earth Sciences*, 6(4), 743-757.



- Davis, G.H., George, H., Reynolds, S.J., & Kluth, C. (2012). *Structural Geology of Rocks and Regions*, third ed. John Wiley and Sons, New York, 839 p.
- Davis, J. L., Prescott, W. H., Svarc, J. L., & Wendt, K. J. (1989). Assessment of Global Positioning System measurements for studies of crustal deformation. *Journal of Geophysical Research: Solid Earth*, 94(B10), 13635-13650.
- Davison, I. (1986). Listric normal fault profiles: calculation using bed-length balance and fault displacement. *Jour. Struct. Geol.*, 8 (2), 209-210.
- De Vicente, G., Vegas, R., Muñoz-Martín, A., Van Wees, J. D., Casas-Sáinz, A., Sopeña, A., Sánchez-Moya, Y., Arche, A., López-Gómez, J., Olaiz, A., & Fernández-Lozano, J. (2009). Oblique strain partitioning and transpression on an inverted rift: The Castilian Branch of the Iberian Chain. *Tectonophysics*, 470(3-4), 224-242
- Dean, W.C. 1958. Frequency analysis for gravity and magnetic interpretation. *Geophysics*, 23, 97-127
- Dentith, M., Enkin, R. J., Morris, W., Adams, C., & Bourne, B. (2020). Petrophysics and mineral exploration: a workflow for data analysis and a new interpretation framework. *Geophysical Prospecting*, 68(1-Cost-Effective and Innovative Mineral Exploration Solutions), 178-199.
- Dering, G. M., Micklethwaite, S., Thiele, S. T., Vollgger, S. A., & Cruden, A. R. (2019). Review of drones, photogrammetry and emerging sensor technology for the study of dykes: Best practises and future potential. *Journal of Volcanology and Geothermal Research*.
- Díaz-Molina, M., Arribas, J., Gómez, J.J., & Tortosa, A. (1995). Geological modelling of a reservoir analogue: Cenozoic meander belts, Loranca Basin, Spain. *Petroleum Geoscience* 1, 43-48.
- Dickinson, G. (1953). Geological Aspects of Abnormal Reservoir Pressures in Gulf Coast Louisiana. *AAPG Bulletin* 37, 410-432. <https://doi.org/10.1306/5CEADC6B-16BB-11D7-8645000102C1865D>
- Dilalos, S., Alexopoulos, J. D., & Tsatsaris, A. (2018). Calculation of Building Correction for urban gravity surveys. A case study of Athens metropolis (Greece). *Journal of applied geophysics*, 159, 540-552.
- Dixon, J. S. (1982). Regional structural synthesis, Wyoming salient of western overthrust belt. *AAPG Bulletin*, 66(10), 1560-1580.
- Doornenbal, H., & Stevenson, A. (2010). *Petroleum geological atlas of the Southern Permian Basin area*. EAGE.
- Doré, A. G., Lundin, E. R., Fichler, C., & Olesen, O. (1997). Patterns of basement structure and reactivation along the NE Atlantic margin. *Journal of the Geological Society*, 154(1), 85-92. <https://doi.org/10.1144/gsjgs.154.1.0085>
- Dufréchoy, G., Tiberi, C., Martin, R., Bonvalot, S., Chevrot, S. and Seoane, L. (2018). Deep structure of Pyrenees range (SW Europe) imaged by joint inversion of gravity and teleseismic delay time. *Geophysical Journal International*, 214 (1), 282-301.
- Dula, W.F. (1991). Geometric models of listric normal faults and rollover folds. *A.A.P.G. Bull.*, 75 (10), 1609-1625.
- Eaton, B. A. (1969). Fracture gradient prediction and its application in oilfield operations. *Journal of petroleum technology*, 21(10), 1-353.
- Egan, S. S., Buddin, T. S., Kane, S. J., & Williams, G. D. (1997). Three-dimensional modelling and visualisation in structural geology: new techniques for the restoration and balancing of volumes. In *Proceedings of the 1996 Geoscience Information Group Conference on Geological Visualisation. Electronic Geology Special Volume (Vol. 1, pp. 67-82)*.
- Eichelberger, N. W., Hughes, A. N., & Nunns, A. G. (2015). Combining multiple quantitative structural analysis techniques to create robust structural interpretations. *Interpretation*, 3(4), SAA89-SAA104.
- Eicker, A., Schall, J., & Kusche, J. (2014). Regional gravity modelling from spaceborne data: case studies with GOCE. *Geophysical Journal International*, 196(3), 1431-1440.
- Elliott, D. (1983). The construction of balanced cross-sections. *Journal of Structural Geology* 5 (2), Pag. 101.
- Elliott, G. M., Wilson, P., Jackson, C. A.-L., Gawthorpe, R. L., Michelsen, L., & Sharp, I. R. (2012). The linkage between fault throw and footwall scarp erosion patterns: An example from the Bremstein Fault Complex, offshore Mid-Norway. *Basin Research*, 24(2), 180-197. <https://doi.org/10.1111/j.1365-2117.2011.00524.x>



- Ellwood, B. B. & Wenner, D. B. (1981) - Correlation of magnetic susceptibility with 180/160 data in late orogenic granites of the southern Appalachian Piedmont. *Earth Planet. Sci. Letters*, 54: 200-202.
- Elmore, R. D., Kelley, J., Evans, M., & Lewchuk, M. T. (2001). Remagnetization and orogenic fluids: testing the hypothesis in the central Appalachians. *Geophysical Journal International*, 144(3), 568-576.
- Endignoux, L., & Mugnier, J. L. (1990). The use of a forward kinematic model in the construction of balanced cross sections. *Tectonics* 9(5), 1249-1262.
- Enkin, R. J. (2014). The rock physical property database of British Columbia, and the distinct petrophysical signature of the Chilcotin basalts. *Canadian Journal of Earth Sciences*, 51(4), 327-338.
- Enkin, R. J. (2018). The Canadian Rock Physical Property Database: First public release. Geological Survey of Canada, Open File 8460, 68p. <https://doi.org/10.4095/313389>
- Enkin, R. J., Cowan, D., Tigner, J., Severide, A., Gilmour, D., Tkachyk, A., ... & Baker, J. (2012). Physical property measurements at the GSC Paleomagnetism and Petrophysics Laboratory, including electric impedance spectrum methodology and analysis. Geological Survey of Canada, Open File, 7227, 42.
- Enkin, R. J., Vidal, B. S., Baker, J., & Struyk, N. M. (2007). Physical properties and paleomagnetic database for south-central British Columbia. *Geological Fieldwork*, 2008-1.
- Enkin, R. J., Hamilton, T. S., & Morris, W. A. (2020). The Henkel Petrophysical Plot: Mineralogy and Lithology from Physical Properties. *Geochemistry, Geophysics, Geosystems*.
- Epard, J.L., & Groshong, R.H.Jr. (1993). Excess area and depth to detachment. *A.A.P.G. Bull.*, 77 (8), 1291-1302.
- EuroGeoSurveys (2021). Strategic Research & Innovation Agenda 2021-2027. *The Geological Surveys of Europe*.
- Evjen, H. M. (1936). The place of the vertical gradient in gravitational interpretations. *Geophysics*, 1(1), 127-136.
- Fail, R.T. (1973). Kink band folding, valley and Ridge Province, Central Pennsylvania. *Geol. Soc. Am. Bull.* 84, 1289-1314.
- Fairhead, J. D., Green, C. M., & Blitzkow, D. (2003). The use of GPS in gravity surveys. *The Leading Edge*, 22(10), 954-959.
- Faure, J.L. & Chermette, J.C. (1989). Deformation of tilted blocks, consequences on block geometry and extension measurements. *Bull. Soc. Géol. France*, 8 (3), 461-476.
- Fedi, M. & Quarta, T., Wavelet Analysis for the Regional-Residual and Local Separation of the Potential Field Anomalies, *Geophys Prospect*, 46(5), pp. 507-525, 1998.
- Fedi, M., Primiceri, R., Quarta, T., & Villani, A. V. (2004). Joint application of continuous and discrete wavelet transform on gravity data to identify shallow and deep sources. *Geophysical Journal International*, 156(1), 7-21.
- Fernández, O., Muñoz, J. A., & Arbués, P. (2003). Quantifying and correcting errors derived from apparent dip in the construction of dip-domain cross-sections. *Journal of Structural Geology*, 25(1), 35-42.
- Fomel, S., & Landa, E. (2014). Structural uncertainty of time-migrated seismic images. *Journal of Applied Geophysics*, 101, 27-30.
- Fong Chao, B., Hwang, C. and Hsieh W. C. (2016). Gravity monitoring of Tatun Volcanic Group activities and inference for underground fluid circulations, *J. Volcanol. Geotherm. Res.*, <http://dx.doi.org/10.1016/j.jvolgeores.2016.1>
- Fossen, H., & Hesthammer, J. (1998). Structural geology of the Gullfaks field, northern North Sea. Geological Society, London, *Special Publications*, 127(1), 231-261.
- Fossen, H., & Tikoff, B. (1997). Forward modeling of non-steady-state deformations and the 'minimum strain path'. *Journal of Structural Geology*, 19(7), 987-996.
- Fukao, Y., Yamamoto, A. and Nozaki, K. (1981). A method of density determination for gravity correction. *J. Phys. Earth*, 29, 163-166.
- Furre, A. K., Eiken, O., Alnes, H., Vevatne, J. N., & Kiær, A. F. (2017). 20 Years of Monitoring CO<sub>2</sub>-injection at Sleipner. *Energy procedia*, 114, 3916-3926.



- Gabalda, G., Bonvalot, S., & Hipkin, R. (2003). CG3TOOL: an interactive computer program to process Scintrex CG-3/3M gravity data for high-resolution applications. *Computers & Geosciences*, 29(2), 155-171.
- Gaillot, P., Lewandowski, J., & Nursaidova, R. (2019). *Uncertainty Analysis in Formation Evaluation: Rationale, Methods and Examples*. In SPWLA 60th Annual Logging Symposium. Society of Petrophysicists and Well-Log Analysts.-
- García-Castellanos D, Vergés J, Gaspar-Escribano J, Cloetingh S (2003) Interplay between tectonics, climate, and fluvial transport during the Cenozoic evolution of the Ebro Basin (NE Iberia). *J Geophys Res* 108:2347–2364.
- García-Lobón, J. L., Rey-Moral, C., & Ayala, C. (2006). Comprehensive petrophysics of rocks from the Monesterio antiformal (Ossa Morena Zone, SW SPAIN). *Journal of applied geophysics*, 59(3), 190-204.
- García-Lobón, J. L., Rey-Moral, C., Ayala, C., Martín-Parra, L. M., Matas, J., & Reguera, M. I. (2014). Regional structure of the southern segment of Central Iberian Zone (Spanish Variscan Belt) interpreted from potential field images and 2.5 D modelling of Alcudia gravity transect. *Tectonophysics*, 614, 185-202.
- Gardner, G. H. F., Gardner, L. W., & Gregory, A. R. (1974). Formation velocity and density—The diagnostic basics for stratigraphic traps. *Geophysics*, 39(6), 770-780.
- Gasparikova, E., & Hoversten, G. M. (2008). Gravity monitoring of CO<sub>2</sub> movement during sequestration: Model studies. *Geophysics*, 73(6), WA105-WA112.
- Gassmann, F. (1951). Über die elastizität poröser medien *Vierteljahresschr. d J. Naturforsch. Ges. Zürich*, 96(1), 1-22.
- Geiser, J., Geiser, P.A., Kligfield, R. Ratcliff, R., & Rowan, M. (1988). New applications of computer-based section construction: strain analysis, local balancing and subsurface fault projection. *The Mountain Geologist*, 25, 47-59.
- Gemperle, M., Conrad, G., Sargen, M. Y., & Starr, S. (1991). *Geosoft GM-SYS, Version 1.8*. Northwest Geophysical Associates Inc., New York.
- GeoModeller manual online: [https://docs.intrepid-geophysics.com/geomodeller/topics/3D\\_GeoModeller\\_Reference.html#3D\\_GeoModeller](https://docs.intrepid-geophysics.com/geomodeller/topics/3D_GeoModeller_Reference.html#3D_GeoModeller)
- Geosoft (2013). *How-To guide applying filters with montaj Geophysics*, [http://updates.geosoft.com/downloads/files/how-to-guides/Applying\\_Filters\\_with\\_montaj\\_Geophysics.pdf](http://updates.geosoft.com/downloads/files/how-to-guides/Applying_Filters_with_montaj_Geophysics.pdf)
- Gibbs, A.D., (1983). Balanced cross-sections from seismic sections in areas of extensional tectonics. *Jour. Struct. Geol.* 5, 153-160
- Gibbs, A.D. (1985). Discussion on the structural evolution of extensional basin margins. *Jour. Geol. Soc. London*, 142, 939-942.
- Gibson, H., Sumpton, J., Fitzgerald, D., Seikel, R., 2013. *3D Modelling of Geology and Gravity Data: Summary Workflows for Minerals Exploration*. East Asia: Geology, Exploration Technologies and Mines - Bali, 24- 26.
- Gill, W.D. (1953). Construction of geological sections of folds with steep limb attenuation. *A.A.P.G. Bull.*, 37, 2389-2406.
- Giménez, M.E., Martínez, M.P., Jordan, T., Ruíz, F. and Klinger, F.L. (2009) Gravity characterization of the La Rioja Valley Basin, Argentina. *Geophysics*, Volume 74, Issue 3, mei-2009, Pages B83-B94
- Giraud, J., Pakyuz-Charrier, E., Jessell, M., Lindsay, M., Martin, R., & Ogarko, V. (2017). Uncertainty reduction through geologically conditioned petrophysical constraints in joint inversion. *Geophysics*, 82(6), ID19-ID34.-
- Giraud, J., Ogarko, V., Lindsay, M., Pakyuz-Charrier, E., Jessell, M., & Martin, R. (2019). Sensitivity of constrained joint inversions to geological and petrophysical input data uncertainties with posterior geological analysis. *Geophysical Journal International*, 218(1), 666-688.
- Gleizes, G., Nédélec, A., Bouchez, J. L., Autran, A., & Rochette, P. (1993). Magnetic susceptibility of the Mont-Louis andorra ilmenite-type granite (Pyrenees): A new tool for the petrographic characterization and regional mapping of zoned granite plutons. *Journal of Geophysical Research: Solid Earth*, 98(B3), 4317-4331.
- Glover, P. W. (2000). *Petrophysics*. University of Aberdeen, UK.



- GMSYS old manual (still useful): [http://pages.geo.wvu.edu/~wilson/gmsys\\_49.pdf](http://pages.geo.wvu.edu/~wilson/gmsys_49.pdf)
- Godson, R. H., and Plouff, D. (1988). BOUGUER Version 1.0. A microcomputer gravity-terrain-correction program: U.S. Geological Survey Open-File Report 88-644.
- Götze, H. -J. & Lahmeyer, B. (1988). Application of three-dimensional interactive modeling in gravity and magnetics. *Geophysics*, 53(8), 1096-1108.
- Goetze, H. J., & Pail, R. (2018). Insights from recent gravity satellite missions in the density structure of continental margins—With focus on the passive margins of the South Atlantic. *Gondwana Research*, 53, 285-308.
- Goguel, J., 1952. *Traité de tectonique*. Comptes Rendus Critiques. Paris, Masson, in-8°, 383 p. (translated in 1962 as *Tectonics* [San Francisco, Freeman, 384p]. by H.E. Thalman).
- Goldstein, B., G. Hiriart, R. Bertani, C. Bromley, L. Gutiérrez-Negrín, E. Huenges, H. Muraoka, A. Ragnarsson, J. Tester, V. Zui, 2011: *Geothermal Energy*. In te [O. Edenhofer, R. Pichs-Madruga, Y. Sokona, K. Seyboth, P. Matschoss, S. Kadner, T. Zwickel, P. Eickemeier, G. Hansen, S. Schlömer, C. von Stechow (eds)], Cambridge University Press, Cambridge, United Kingdom and New York, NY, USA.
- Gómez, J.J., Díaz Molina, M., & Lendínez, A. (1996). Tectonosedimentary analysis of the Loranca Basin (Upper Oligocene-Miocene, central Spain): a "non sequenced" foreland basin. *Tertiary basins of Spain*. Cambridge University Press, 285-294.
- Goodell, R. R., & Fay, C. H. (1964). Borehole gravity meter and its application. *Geophysics*, 29(5), 774-782
- Goussev, S. A., Charters, R. A., Peirce, J. W., & Glenn, W. E. (2003). Jackpine Creek magnetic anomaly Identification of a buried meteorite impact structure. *The Leading Edge*, 22(8), 740-741.
- Granser, H. (1987). Three-dimensional interpretation of gravity data from sedimentary basins using an exponential density-depth function. *Geophysical Prospecting*, 35(9), 1030-1041.
- Grant, F. S., and Elsharty, A.F. (1962). Bouguer gravity corrections using a variable density. *Geophysics*, 27, 616-626.
- Grant, F.S. and West, G.F. (1965). *Interpretation theory in applied geophysics*. McGraw-Hill, 583 pp.
- Gratier, J. P., & Guillier, B. (1993). Compatibility constraints on folded and faulted strata and calculation of total displacement using computational restoration (UNFOLD program). *Journal of structural geology*, 15(3-5), 391-402.
- Gratier, J. P., Guillier, B., Delorme, A., & Odonne, F. (1991). Restoration and balance of a folded and faulted surface by best-fitting of finite elements: principle and applications. *Journal of structural Geology*, 13(1), 111-115.
- Groshong, R.H. (1989). Half-graben structures: balanced models of extensional fault-bend folds. *GSA Bull.*, 101, 96-105.
- Greco, F., Currenti, G., D'Agostino, G., Germak, A., Napoli, R., Pistorio, A., & Del Negro, C. (2012). Combining relative and absolute gravity measurements to enhance volcano monitoring. *Bulletin of volcanology*, 74(7), 1745-1756.
- Green, G. (1828, March). *An Essay on the Application of Mathematical Analysis to the Theories of Electricity and Magnetism*. Sneinton near Nottingham.
- Griffin, W. R. (1949). Residual gravity in theory and practice. *Geophysics*, 14, 39-56.
- Groshong, R.H. (1990). Unique determination of normal fault shape from hanging-wall bed geometry in detached half grabens. *Eclogae Geologicae Helveticae*, 83, 455-471
- Groshong, R.H.Jr. (1994). Area balance, depth to detachment and strain in extension. *Tectonics*, 13, 1488-1497.
- Groshong, R.H.Jr. (1996). Construction and validation of extensional cross sections using lost area and strain, with application to the Rhine Graben, In: Buchanan, P.G. & Nieuwland, D.A. (eds.): *Modern developments in structural interpretation, validation and modelling*. Spec. Publ. Geol. Soc. London, 99, 79-87.
- Groshong, R.H.Jr. (2019). Area-constant strain and dilation in sandbox models: Insights from whole-model area balance. *Journal of Structural Geology*, 118, 279-283.
- Groshong, R.H. (2006). *3-D Structural Geology a Practical Guide to Quantitative Surface and Subsurface Map Interpretation*, second ed. Springer-Verlag, Berlin, Heidelberg/New York. 400 pp.
- Groshong Jr, R., Bond, C., Gibbs, A., Ratcliff, R., & Wiltschko, D. (2012). Preface: Structural balancing at the start of the 21st century: 100 years since Chamberlin. *Journal of Structural Geology*, 41, 1-5.



- Groshong Jr, R. H., Withjack, M. O., Schlische, R. W., & Hidayah, T. N. (2012). *Bed length does not remain constant during deformation: Recognition and why it matters*. *Journal of Structural Geology* 41, 86-97.
- Guillen, A., Calcagno, Ph., Courrioux, A., Joly, A., Pedru, P., 2008. *Geological modelling from field data and geological knowledge: Part II. Modelling validation using gravity and magnetic data inversion*. *Physics of the Earth and Planetary Interiors*, 171, 1-4, 158-169.
- Guimerà, J. (1988). *Estudi estructural de l'enllaç entre la Serralada Ibèrica i la Serralada Costanera Catalana*. Universitat de Barcelona.
- Guspi, F., and Introcaso, B. (2000). *A sparse spectrum technique for gridding and separating potential field anomalies*. *Geophysics*, 65, 1154–1161.
- Hackney, R.I. and Featherstone, W.E. (2003). *Geodetic versus geophysical perspectives of the “gravity anomaly”*. *Geophysical Journal International*, 154, 35–43.
- Hamdi-Nasr, I., Amiri, A., Hédi-Inoubli, M., Ben-Salem, A., Chaqui, A. and Tlig, S. (2010). *Structural setting of northern Tunisia insights from gravity data analysis Jendouba case study*. *Pure Appl. Geophys.*, 168 (10), 1835-1849.
- Hammer, S. (1939). *Terrain corrections for gravimeter stations*. *Geophysics*, 4, 184–194.
- Hammer, S. (1950). *Density determinations by underground gravity measurements*. *Geophysics*, 15(4), 637-652.
- Hammer, S. (1963). *Deep gravity interpretation by stripping*. *Geophysics*, 28, 369-378.
- Hammer, S. (1965). *Density determinations by underground gravity measurements—Sequel*. *Geophysics*, 30(6), 1133-1134.
- Handyarso, A., & Kadir, W. G. A. (2017). *Gravity Data Decomposition Based on Spectral Analysis and Halo Wavelet Transform, Case Study at Bird's Head Peninsula, West Papua*. *Journal of Engineering & Technological Sciences*, 49(4).
- Hansen, R.O. (1993). *Interpretative gridding by anisotropic kriging*. *Geophysics*, 58, 1491-1497.
- Hansen, R. O., & Simmonds, M. (1993). *Multiple-source Werner deconvolution*. *Geophysics*, 58(12), 1792-1800.
- Hartman, R. R., Teskey, D. J., & Friedberg, J. L. (1971). *A system for rapid digital aeromagnetic interpretation*. *Geophysics*, 36(5), 891-918.
- Hassan, H, H., Charters, R. A. and Peirce, J. W. (2015) *Mapping Depth to Basement Using 2D Werner Inversion of High-Resolution AeroMagnetic (HRAM) Data*. Search and Discovery Article #41595, Adapted from extended abstract prepared for presentation at CSPG CSEG GeoConvention 2007, Calgary, Alberta, Canada, May 14-17, 2007, Datapages/CSPG © 2015
- Hector, B., & Hinderer, J. (2016). *pyGrav, a Python-based program for handling and processing relative gravity data*. *Computers & geosciences*, 91, 90-97.
- Hedberg, H. D. (1936). *Gravitational compaction of clays and shales*. *American Journal of Science*, (184), 241-287.
- Heintz, K. O., & Alexander, M. (1979). *Sulfur exploration with core hole and surface gravity*. In *Geophysics Vol. 44, No. 3*, pp. 370-370
- Heiskanen, W.A. and Moritz, H. (1969). *Physical geodesy*. W. H. Freeman Co.
- Henderson, R.G., and Zietz, I. (1949). *The computation of second vertical derivatives of geomagnetic fields*. *Geophysics*, 14, 508–516.
- Henkel, H. (1976). *Studies of density and magnetic properties of rocks from northern Sweden*. *Pure and applied geophysics*, 114(2), 235-249.
- Henkel, H. (1991). *Petrophysical properties (density and magnetization) of rocks from the northern part of the Baltic Shield*. *Tectonophysics*, 192, 1–19.
- Henkel, H. (1994). *Standard diagrams of magnetic properties and density—A tool for understanding magnetic petrology*. *Journal of Applied Geophysics*, 32(1), 43–53.
- Hernaiz, P., Cabra, P., Solé, J., Portero, J., & Del Olmo, P. (1998). *Mapa Geológico de España, Hoja 537 (Auión)*. Memoria + Mapa 1:50000. Instituto Geológico y Minero de España, Madrid.
- Hill, K.C. & Cooper, G.T. (1996). *A strategy for palinspastic restoration of inverted basins: thermochronology and structural analyses in SE Australia*. In: Buchanan, P.G. & Nieuwland, D.A. (Eds.), *Modern Developments in Structural Interpretation, Validation and Modelling*. *Geol. Soc. London Spec. Publ.*, 99, 99-115.



- Hinderer J, Calvo M, Abdelfettah Y, Hector B, Riccardi U, Ferhat G, Bernard J-D. Monitoring of a geothermal reservoir by hybrid gravimetry; feasibility study applied to the Soultz-sous-Forêts and Rittershofen sites in the Rhine graben. *Geothermal Energy*. 2015.
- Hinze, W.J. (2003). Bouguer reduction density — Why 2.67?. *Geophysics*, 68, 1559–1560.
- Hinze, W.J., Aiken, C., Brozena, J., Coakley, B., Dater, D., Flanagan, G., Forsberg, R., Hildenbrand, T., Randy-Keller, G., Kellogg, J., Kucks, R., Li, X., Mainville, A., Morin, R., Pilkington, M., Plouff, D., Ravat, D., Roman, D., Urrutia-Fucugauchi, J., Véronneau, M., Webring, M. and Winester, D. (2005). New standards for reducing gravity data: The North American gravity database. *Geophysics*, 70, 125-132.
- Hinze, W. J., Von Frese, R. R., & Saad, A. H. (2013). *Gravity and magnetic exploration: Principles, practices, and applications*. Cambridge University Press.
- Hirt, C. (2016). Gravity forward modelling. In: *Encyclopaedia of Geodesy* (Ed. E. Grafarend), doi:
- Hofmann-Wellenhof, B., Lichtenegger, H., and Wasle, E. (2007). *GNSS-global navigation satellite systems: GPS, GLONASS, Galileo, and more*. Editorial Springer Science & Business Media, Wien New York. ISBN 978-3-211-73017-1
- Hogan, P. J., & Burbank, D. W. (1996). Evolution of the Jaca piggyback basin and emergence of the External Sierra, southern Pyrenees. In: *Tertiary Basins of Spain: the Stratigraphic Record of Crustal Kinematics*. Cambridge Univ. Press. 6, 153-160.
- Holl, J. E., & Anastasio, D. J. (1995). Cleavage development within a foreland fold and thrust belt, southern Pyrenees, Spain. *Journal of Structural Geology*, 17(3), 357-369.
- Homza, T.X. & Wallace, W.K. (1995). Geometric and kinematic models for detachment folds with fixed and variable detachment depths. *Jour. Struct. Geol.*, 17 (4), 575-588.
- Hooke, R. (1678). *De Potentia Restitutiva*, London.
- Hossack, J. R. (1979). The use of balanced cross-sections in the calculation of orogenic contraction: A review. *Journal of the Geological Society*, 136(6), 705-711.
- Hossack, J.R. (1994). Geometric rules of section balancing of salt structures in the Gulf of Mexico. *Abstr. Vol. Modern Development in Structural Interpretation, Validation and Modelling*. London, UK.
- Hossack, J.R. (1995). Geometric rules of section balancing for salt tectonics. In Jackson, M.P.A., Roberts, D.G., Snelson, S. (Eds.), *Salt Tectonics. A Global Perspective*. A.A.P.G. Mem. 65, 29-40.
- Howell, L. G., Heintz, K. O., & Barry, A. (1966). The development and use of a high-precision downhole gravity meter. *Geophysics*, 31(4), 764-772.
- Hrouda, F., Chlupacova, M., & Chadima, M. (2009). *The use of magnetic susceptibility of rocks in geological exploration*. Terraplus, Brno, 2016.
- Hugill, A. (1990). Scintrex CG-3 automated gravity meter: Description and field results. In *SEG Technical Program Expanded Abstracts 1990* (pp. 601-604). Society of Exploration Geophysicists.
- Hurtado-Cardador M., Urrutia-Fucugauchi J. 2006. Data reduction and tying in regional gravity surveys—results from a new gravity base station network and the Bouguer gravity anomaly map for northeastern Mexico, *Journal of Geophysics and Engineering*, Volume 3, Issue 4, Pages 329–337, <https://doi.org/10.1088/1742-2132/3/4/004>
- Huyghe, D., Mouthereau, F., Castellort, S., Filleaudeau, P. Y., & Emmanuel, L. (2009). Paleogene propagation of the southern Pyrenean thrust wedge revealed by finite strain analysis in frontal thrust sheets: Implications for mountain building. *Earth and Planetary Science Letters*, 288(3-4), 421-433.
- Iacopini D., & Butler R.W. (2011). Imaging deformation in submarine thrust belts using seismic attributes. *Earth and Planetary Science Letters* 302, 414-422.
- IGME, 1990. *Documentos sobre la Geología del Subsuelo de España*. Tomo III (Madrid-Depresión Intermedia).
- IGN (2019). *Teoría gravimétrica*. <https://www.ign.es/web/ign/portal/gmt-area-gravimetria>
- Imanishi, Y., Sato, T., Higashi, T., Sun, W., & Okubo, S. (2004). A network of superconducting gravimeters detects submicrogal coseismic gravity changes. *Science*, 306(5695), 476-478.
- Intrepid Geophysics (2006). *3D GeoModeller Reference Manual*. BRGM and Desmond Fitzgerald & Associates Pty. Ltd., 67p.
- IPCC, 2011 – Ottmar Edenhofer, Ramón Pichs-Madruga, Youba Sokona, Kristin Seyboth, Patrick Matschoss, Susanne Kadner, Timm Zwickel, Patrick Eickemeier, Gerrit Hansen, Steffen



- Schloemer, Christoph von Stechow (Eds.) Cambridge University Press, Cambridge, United Kingdom and New York, NY, USA, 1075 pp. Available from Cambridge University Press, The Edinburgh Building Shaftesbury Road, Cambridge CB2 2RU ENGLAND
- Ishihara, S. (1977). The magnetite-series and ilmenite-series granitic rocks. *Mining geology*, 27(145), 293-305.
- Izquierdo-Llavall, E., Sainz, A. C., Oliva-Urcia, B., Burmester, R., Pueyo, E. L., & Housen, B. (2015). Multi-episodic remagnetization related to deformation in the Pyrenean Internal Sierras. *Geophysical Journal International*, 201(2), 891-914.
- Izquierdo-Llavall, E., Ayala, C., Pueyo, E. L., Casas-Sainz, A. M., Oliva-Urcia, B., Rubio, F., ... & García-Crespo, J. (2019). Basement-Cover Relationships and Their Along-Strike Changes in the Linking Zone (Iberian Range, Spain): A Combined Structural and Gravimetric Study. *Tectonics*, 38(8), 2934-2960.
- Jacoby, W., & Smilde, P. L. (2009). *Gravity interpretation: fundamentals and application of gravity inversion and geological interpretation*. Springer Science & Business Media.
- Jamison, W. R. (1987). Geometric analysis of fold development in overthrust terranes. *Journal of Structural Geology*, 9(2), 207-219.
- Jarboe, N., Koppers, A., Tauxe, L., Minnett, R., & Constable, C. (2012). The online magic database: Data archiving, compilation, and visualization for the geomagnetic, paleomagnetic and rock magnetic communities. *AGU Fall Meeting Abstracts*.
- Jarboe, N., Minnett, R., Constable, C., Koppers, A., Tauxe, L., & Jonestrask, L. (2020, December). MagIC Updates: New Compact File Format Supports XPEEM, SQUID Microscopy, and FORC Contributions; Successful Interoperability with EPOS, GFZ Data Services; Continuing Collaboration with EarthCube's GeoCODES and ESIP's schema. org cluster. In *AGU Fall Meeting 2020*. AGU.
- Jessell, M. (2001). Three-dimensional geological modelling of potential-field data. *Computers & Geosciences*, 27(4), 455-465.
- Jessell, M. W., Valenta, R. K., Jung, G., Cull, J. P., & Geiro, A. (1993). Structural geophysics. *Exploration Geophysics*, 24(4), 599-602.
- Jones, O. T. (1944). The compaction of muddy sediments. *Quarterly Journal of the Geological Society*, 100(1-4), 137-160.
- Jones, R. R., McCaffrey, K. J., Wilson, R. W., & Holdsworth, R. E. (2004). Digital field data acquisition: towards increased quantification of uncertainty during geological mapping. *Geological Society, London, Special Publications*, 239(1), 43-56.
- Jorgensen, G. and Kisabeth, J., 2000, Joint 3-D inversion of gravity, magnetic and tensor gravity fields for imaging salt formations in the deepwater Gulf of Mexico: 70th Ann. Internat. Mtg.: SEG, pp. 424-426.
- Judge, P. A., & Allmendinger, R. W. (2011). Assessing uncertainties in balanced cross sections. *Journal of Structural Geology*, 33(4), 458-467.
- Jussiani, E. I., & Appoloni, C. R. (2015). Effective atomic number and density determination of rocks by X-ray microtomography. *Micron*, 70, 1-6.
- Kanaya, H., & Ishihara, S. (1973). Regional variation of magnetic susceptibility of the granitic rocks in Japan. *The Journal of the Japanese Association of Mineralogists, Petrologists and Economic Geologists*, 68(7), 211-224.
- Kaplan, E. D., & Hegarty, C. J. (2017). *Understanding GPS/GNSS: principles and applications*. In *GNSS technology and applications series*. Artech House Publisher.
- Katz, B., Elmore, R. D., Cogoini, M., & Ferry, S. (1998). Widespread chemical remagnetization: Orogenic fluids or burial diagenesis of clays?. *Geology*, 26(7), 603-606.
- Kaub, L., Seruge, C., Chopra, S.D., Glen, J.M., Teodorescu, M., 2018. Developing an autonomous unmanned aerial system to estimate field terrain corrections for gravity measurements. *Lead. Edge* 37 (8), 584–591.
- Kearey, P., Brooks, M. and Hill, I., (2002). *An introduction to geophysical exploration*. 3rd ed. ix + 262 pp. Oxford: Blackwell Science.
- Keating, P. B., 1998. Weighted Euler deconvolution of gravity data, *Geophysics*, 63, 1595–1603



- Kebede, H., Alemu, A., & Fisseha, S. (2020). Upward continuation and polynomial trend analysis as a gravity data decomposition, case study at Ziway-Shala basin, central Main Ethiopian rift. *Heliyon*, 6(1), e03292.
- Keefer, D. A. (2007). A framework and methods for characterizing uncertainty in geologic maps. Three dimensional geologic mapping for groundwater applications. Minnesota Geological Survey, Open File Report, 07-4.
- Keller, P. (1990). Geometric and kinematic model of bed length balanced graben structures. *Eclogae Geologicae Helvetiae*, 83, 473-493.
- Kellogg, O.D. 1953. *Foundations of Potential Theory (Vol 31)*. Dover Publications.
- Khair, K., & Tsokas, G. N. (1999). Nature of the Levantine (eastern Mediterranean) crust from multiple-source Werner deconvolution of Bouguer gravity anomalies. *Journal of Geophysical Research: Solid Earth*, 104(B11), 25469-25478.
- Khair, K., Tsokas, G. N., & Sawaf, T. (1997). Crustal structure of the northern Levant region: multiple source Werner deconvolution estimates for Bouguer gravity anomalies. *Geophysical Journal International*, 128(3), 605-616.
- Kilty, K. T. (1983). Werner deconvolution of profile potential field data. *Geophysics*, 48(2), 234-237.
- Kim, H.R., Choi, SY., Suh, M. et al. Moho modeling of the Yellow Sea (West Sea) from spectrally correlated free-air and terrain gravity data. *Geosci J* 24, 531–540 (2020). <https://doi.org/10.1007/s12303-019-0044-5>
- Kligfield, R., Geiser, P. & Geiser, J. (1986). Construction of geologic cross-sections using microcomputer systems. *Geobyte* 1, 60-66.
- Kobranova, V. N. (1990). *Petrophysics*. Edited by MIR, 375 pp.
- Köhler, R. & Eichner, M. (1973). *Regionaler Dichteanatz für den Nordteil der DDR*. VEB Geophysik, Leipzig.
- Koenigsberger, J. G. (1938). Natural residual magnetism of eruptive rocks. *Terrestrial magnetism and atmospheric electricity*, 43(3), 299-320.
- Koyi, H. (1995). Mode of internal deformation in sand wedges. *Journal of Structural Geology*, 17(2), 293-300.
- Koyi, H. A., Sans, M., Teixell, A., Cotton, J., & Zeyen, H. (2003). The significance of penetrative strain in the restoration of shortened layers—Insights from sand models and the Spanish Pyrenees. In: McClay, K.R. (Ed.), *Thrust tectonics and hydrocarbon systems*. AAPG Memoir 82, 207-222:
- Koymans, M. R., van Hinsbergen, D. J. J., Pastor-Galán, D., Vaes, B., & Langereis, C. G. (2020). Towards FAIR paleomagnetic data management through Paleomagnetism. org 2.0. *Geochemistry, Geophysics, Geosystems*, 21(2), e2019GC008838.
- Krahenbuhl, R. A., & Li, Y. (2012). Time-lapse gravity: A numerical demonstration using robust inversion and joint interpretation of 4D surface and borehole data. *Geophysics*, 77(2), G33-G43.
- Kryniski, J. (2012). Gravimetry for geodesy and geodynamics-brief historical review. *Reports on Geodesy*.
- Ku, C.C., and J.A. Sharp, 1983, Werner deconvolution for automated magnetic interpretation and its refinement using Marquardt inverse modeling: *Geophysics*, v. 48, p. 754-774.
- Labauve, P., Meresse, F., Jolivet, M., Teixell, A., & Lahfid, A. (2016). Tectonothermal history of an exhumed thrust-sheet-top basin: An example from the south Pyrenean thrust belt. *Tectonics*, 35(5), 1280-1313.
- LaCoste Jr, L. J. (1934). A new type long period vertical seismograph. *Physics*, 5(7), 178-180.
- LaCoste, L. (1959). Surface ship gravity measurements on the Texas A. and M. College ship, the "Hidalgo". *Geophysics*, 24(2), 309-322.
- LaCoste, L. J. (1967). Measurement of gravity at sea and in the air. *Reviews of geophysics*, 5(4), 477-526.
- LaCoste&Romberg, (2004) *Instruction manual model G & D gravity meters*. Copyright 2004 LaCoste&Romberg, 1102 Metric Blvd., Ste 100 Austin, Texas 78758 U.S.A.
- LaFehr, T. R. (1983). Rock density from borehole gravity surveys. *Geophysics*, 48(3), 341-356.
- LaFehr, T.R. (1991). Standardization in gravity reduction. *Geophysics*, 56, 1170–1178.
- Lathrop, B. A., & Burberry, C. M. (2017). Accommodation of penetrative strain during deformation above a ductile décollement. *Lithosphere*, 9(1), 46-57.
- Laubscher, H.P. (1961). Die Fernschubhypothese der Jurafaltung. *Eclogae Geologicae Helvetiae*, 54, 221-282.



- Leica Geosystems AG, 1999. "GPS Basics 1.0.0es". Manual con referencia interna de la casa Leica 713285-1.0.0es.
- Leick (2004). *GPS Satellite Surveying*. Editorial Wiley. New Jersey 840 pp. ISBN: 978-1-118-67557-1
- Lindsay, M. D., Aillères, L., Jessell, M. W., de Kemp, E. A., & Betts, P. G. (2012). Locating and quantifying geological uncertainty in three-dimensional models: Analysis of the Gippsland Basin, southeastern Australia. *Tectonophysics*, 546, 10-27.
- Lingrey, S., & Vidal-Royo, O. (2015). Evaluating the quality of bed length and area balance in 2D structural restorations. *Interpretation*, 3(4), SAA133-SAA160.
- Liu, H. (2017). *Principles and applications of well logging*. Springer Berlin Heidelberg.
- Lock, J., & McElhinny, M. W. (1991). The global paleomagnetic database: design, installation and use with ORACLE. *Surveys in Geophys.*, 12, 317-491.
- Loi, F.; Román-Berdiel, M.T.; Casas-Sainz, A.M.; Pueyo, E.L. *Correlación entre propiedades petrofísicas del granito de Marimanha (Pirineo Axial) (2019)*. In: MAGIBER XI- PALEOMAGNETISMO EN ESPANHA E PORTUGAL (Livro de Resumos)- Universidade de Coimbra. Edited by; Font, E.; Beamud, E.; Oliva-urcia, B.; Pueyo, E.L.; Lopez, F.C. ISBN 9789899891470. 87-90 pp
- Lopez-Mir, B. (2019). Cross-section construction and balancing: examples from the Spanish Pyrenees. In *Developments in Structural Geology and Tectonics (Vol. 5, pp. 3-23)*. Elsevier.
- Lowrie W., (2007). *Fundamentals of Geophysics*. Cambridge University Press. ISBN: 9780521675963. Pp 387
- Lyrio, J.C.S., Tenorio, L. & Li, Y., *Efficient Automatic Denoising of Gravity Gradiometry Data*, *Geophysics*, 69(3), pp. 772-782, 2004.
- MacQueen, J. D. (2007). High-resolution density from borehole gravity data. In *SEG Technical Program Expanded Abstracts 2007 (pp. 741-744)*. Society of Exploration Geophysicists.
- Maerten, L., & Maerten, F. (2006). Chronologic modeling of faulted and fractured reservoirs using geomechanically based restoration: Technique and industry applications. *AAPG bulletin* 90(8), 1201-1226.
- Maerten, F., & Maerten, L. (2015). On a method for reducing interpretation uncertainty of poorly imaged seismic horizons and faults using geomechanically based restoration technique. *Interpretation*, 3(4), SAA105-SAA116.
- Mallet, J. L. (1992). Discrete smooth interpolation in geometric modelling. *Computer-aided design*, 24(4), 178-191.
- Marret, R. & Benthm, P.A. (1997). Geometric analysis of hybrid fault-propagation/detachment folds. *Jour. Geol. Soc. London*, 136, 705-711
- Mallick K., Vasanthi A. and Sharma K.K. 2012., *Bouguer Gravity Regional and Residual Separation: Application to Geology and Environment*, DOI 10.1007/978-94-007-0406-0\_9, © Capital Publishing Company
- Malz, A., Nachtweide, C., Emmerlich, S. & Schimpf, L. (2020). Mesozoic intraplate deformation in the southern part of the Central European Basin - results from large-scale 3D modelling. *Tectonophysics*, 776, 228315.
- Mann, C. J. (1993). Uncertainty in geology. In *Computers in geology---25 years of progress (pp. 241-254)*.
- Marqardt, D.W., 1963, An algorithm for least-squares estimation of non-linear parameters: *J.SIAM*, v.11:431-441.
- Marshak, S., & Mitra, G. (1988). *Basic methods of structural geology*. Prentice Hall, Englewood Cliffs, 309-314, 320-324.
- Marshak, S., & Woodward, N. (1988). Introduction to cross-section balancing. *Basic methods of structural geology*, 303-332.
- Marson, I. (2012). A short walk along the gravimeters path. *International Journal of Geophysics*, 2012.
- Martelet, G., Sailhac, P., Moreau, F., & Diament, M. (2001). Characterization of geological boundaries using 1-D wavelet transform on gravity data: Theory and application to the Himalayas. *Geophysics*, 66(4), 1116-1129.
- Martiklos, G., Beutler, G., Ehling, B.-C., Spieß, H., Klowsky, C. & Rappsilber, I. (2001). *Geological Map of Saxony-Anhalt 1:400000 – Map without Cenozoic cover*. Geological Survey of Saxony-Anhalt, Halle (Saale).



- Martínez Peña, B. and Casas, A. M., 2003. Cretaceous-Tertiary tectonic inversion of the Cotiella Nappe (Southern Pyrenees, Spain). *Int J Earth Sci (Geol Rundsch)* 92:99–113.
- Maxant, J. (1980). Variation of density with rock type, depth, and formation in the Western Canada basin from density logs. *Geophysics*, 45(6), 1061-1076.
- McCaig, A. M., & McClelland, E. (1992). Palaeomagnetic techniques applied to thrust belts. In *Thrust tectonics* (pp. 209-216). Springer, Dordrecht.
- McCubbine, J., Tontini, F. C., Staggpoole, V., Smith, E., & O'Brien, G. (2018). Gsolve, a Python computer program with a graphical user interface to transform relative gravity survey measurements to absolute gravity values and gravity anomalies. *SoftwareX*, 7, 129-137
- McElhinny, M. W., & Smethurst, M. A. (2001). The global paleomagnetic database: current status. *Eos, Transactions American Geophysical Union*, 82(39), 434-434.
- McInerney, P., Guillen, A., Courrioux, G., Calcagno, P. and Lees, T. (2005). Building 3D Geological Models Directly from the Data ? A new approach applied to Broken Hill, Australia. [https://web.archive.org/web/20080718213311/http://www.geomodeller.com/ig/knowledgebase/special\\_topics/3DGM\\_BuildModelFromData.pdf](https://web.archive.org/web/20080718213311/http://www.geomodeller.com/ig/knowledgebase/special_topics/3DGM_BuildModelFromData.pdf)
- McKenzie, D. (1978). Some remarks on the development of sedimentary basins. *Earth and Planetary Science Letters*, 40(1), 25–32. [https://doi.org/10.1016/0012-821X\(78\)90071-7](https://doi.org/10.1016/0012-821X(78)90071-7)
- Ménoret, V., Vermeulen, P., Le Moigne, N., Bonvalot, S., Bouyer, P., Landragin, A., & Desruelle, B. (2018). Gravity measurements below 10– 9 g with a transportable absolute quantum gravimeter. *Scientific reports*, 8(1), 1-11.
- Mertie Jr, J.B. (1940). Stratigraphic measurements in parallel folds. *Bulletin of the Geological Society of America*, 51(8), 1107-1134.
- Miall, A. D. (2010). *The Geology of Stratigraphic Sequences*. Springer Berlin Heidelberg. <https://doi.org/10.1007/978-3-642-05027-5>
- Millán, H., 1996. Estructura y cinemática del frente de cabalgamiento surpirenaico en las Sierras Exteriores Aragonesas. Tesis Doctoral Universidad de Zaragoza. 330 pp.
- Millán Garrido, H., Pocoví Juan, A., & Casas Sainz, A. M. (1995). El frente cabalgamiento surpirenaico en el extremo occidental de las Sierras Exteriores. *Revista de la Sociedad Geológica de España*, 8(1-2), 73-90.
- Millán, H; Pueyo, E. L; Aurell , M.; Luzón, A.; Oliva-Urcia, B.; Martínez Peña, M. B. y Pocoví, A. (2000). Actividad tectónica registrada en los depósitos terciarios del frente meridional del Pirineo central. *Revista de la Sociedad Geológica de España*, 13(2) 117 – 138.
- Miller, H. G., & Singh, V. (1994). Potential field tilt—a new concept for location of potential field sources. *Journal of applied geophysics*, 32(2-3), 213-217.
- Minette, D. C., Hubner, B. G., Harris, M., & Fertl, W. H. (1988, January). Field observations and test pit measurements of the accuracy of the Z-Densilog gamma-gamma instrument. In *SPWLA 29th Annual Logging Symposium*. Society of Petrophysicists and Well-Log Analysts.
- Mitra, G. (1978). Ductile deformation zones and mylonites; the mechanical processes involved in the deformation of crystalline basement rocks. *American Journal of Science*, 278(8), 1057-1084.
- Mitra, G. (1994). Strain variation in thrust sheets across the Sevier fold-and-thrust belt (Idaho-Utah-Wyoming): Implications for section restoration and wedge taper evolution. *Journal of Structural Geology*, 16(4), 585-602.
- Mitra, S., & Namson, J. S. (1989). Equal-area balancing. *American Journal of Science*, 289(5), 563-599.
- Mochales, T. (2006). Prospección magnética aplicada a la detección y caracterización de dolinas en el entorno de Zaragoza. Unpublished MSc University of Zaragoza.
- Mochales, T; Pueyo, E. L.; Casas, A. M.; Soriano, A. (2007). Magnetic prospection as an efficient tool for doline detection. A case study in the central Ebro Basin (Northern Spain). In: *Natural and anthropogenic hazards in karst areas* (Edited by: Parise, M.; Klimchouk, A.; Gunn, J.). Geological Society of London Special Publication 279, 73-84
- Mochales, T.; Casas, A.M.; Pueyo, E.L.; Pueyo, O.; Román, M. T.; Pocoví, A.; Soriano, M.A.; Ansón, D. (2008) Detection of underground cavities by combining gravity, magnetometry and ground penetrating radar surveys. A case study from the Zaragoza area, NE Spain. *Environmental Geology*, 53 (5); 1067 – 1077



- Mochales, T., Casas, A. M., Pueyo, E. L., & Barnolas, A. (2012). Rotational velocity for oblique structures (Boltaña anticline, Southern Pyrenees). *Journal of Structural Geology*, 35, 2-16.
- Mochales, T.; Pueyo, E.L.; Casas, A.M.; Barnolas, A. (2016). Restoring paleomagnetic data in complex superposed folding settings: the Boltaña anticline (Southern Pyrenees). *Tectonophysics*, 671, 281–298. doi:10.1016/j.tecto.2016.01.008
- Moore, G. E. (1965). Cramming more components onto integrated circuits. *Electronics*, 38 (8), 6 pp,
- Moore, G. F., Saffer, D., Studer, M., & Pisani, P. C. (2011). Structural restoration of thrusts at the toe of the Nankai Trough accretionary prism off Shikoku Island, Japan: Implications for dewatering processes. *Geochemistry, Geophysics, Geosystems*, 12(5).
- Moore, William R., Y. Zee Ma, Jim Urdea, and Tom Bratton, (2011). Uncertainty analysis in well-log and petrophysical interpretations, in Y. Z. Ma and P. R. La Pointe, eds., *Uncertainty analysis and reservoir modeling: AAPG Memoir 96*, p. 17 – 28.
- Morelli, C., Gantar, C., Honkasalo, T., McConnell, R.K., Tanner, J.G., Szabo, B., Uotila, U. and Whalen, C.T. 1972. The international gravity standardization net 1971 (I.G.S.N. 71). *International Union of Geodesy and Geophysics*. 192 pp
- Moreno-Atanasio, R., Williams, R. A., & Jia, X. (2010). Combining X-ray microtomography with computer simulation for analysis of granular and porous materials. *Particuology*, 8(2), 81-99.
- Moret-Fernández, D., Latorre, B., Peña, C., González-Cebollada, C., & López, M. V. (2016). Applicability of the photogrammetry technique to determine the volume and the bulk density of small soil aggregates. *Soil Research*, 54(3), 354-359.
- Moretti, I. (2008). Working in complex areas: New restoration workflow based on quality control, 2D and 3D restorations. *Marine and Petroleum Geology* 25,205–218. doi:10.1016/j.marpetgeo.2007.07.001
- Moretti, I., & Larrère, M. (1989). LOCACE: computer-aided construction of balanced geological cross-sections. *Geobyte* 4, 16-24.
- Moretti, I., & Callot, J. P. (2012). Area, length and thickness conservation: Dogma or reality?. *Journal of Structural Geology*, 41, 64-75.
- Moretti, I., Colletta, B., & Vially, R. (1988). Theoretical model of block rotation along circular faults. *Tectonophysics*, 153, 313-320.
- Moretti, I., Lepage, F., & Guiton, M. (2006). KINE3D: a new 3D restoration method based on a mixed approach linking geometry and geomechanics. *Oil & Gas Science and Technology*, 61(2), 277-289.
- Moritz, H. (1980). Geodetic Reference System 1980. *Bulletin Géodésique*, 54, 395-405.
- Morris, A.P. & Ferrill, D.A. (1999). Constant-thickness deformation above curved normal faults. *Jour. Struct. Geol.*, 21, 67-83.
- Mueller, C.O., Wächter, J., Jahnke, C., Pueyo Morer, E.L., Riefstahl, F., & Malz, A. (2021). Integrated geological and gravity modelling to improve 3-D model harmonization – Methods and benefits for the Saxony-Anhalt/Brandenburg cross-border region (North German Basin). *Geophysical Journal International*, 227, 1295-1321, doi: 10.1093/gji/ggab256.
- Muñoz, J. A. (2019). Alpine Orogeny: Deformation and Structure in the Northern Iberian Margin (Pyrenees sl). In *The Geology of Iberia: A Geodynamic Approach* (pp. 433-451). Springer, Cham.
- Muñoz, J. A., Beamud, E., Fernández, O., Arbués, P., Dinarès-Turell, J., & Poblet, J. (2013). The Ainsa Fold and thrust oblique zone of the central Pyrenees: Kinematics of a curved contractional system from paleomagnetic and structural data. *Tectonics*, 32(5), 1142-1175.
- Muñoz-Martín, A., & De Vicente, G. (1998). Cuantificación del acortamiento alpino y estructura en profundidad del extremo sur-occidental de la Cordillera Ibérica (Sierras de Altomira y Bascunñana). *Rev. Soc. Geol. Esp.* 11 (3/4), 39–58.
- Murata, Y. (1990). Estimation of Bouguer reduction density Using ABIC minimization method. *Zisin (J. Seismol. Soc. Japan)*, 43, 327-339 (in Japanese with English abstract).
- Murata, Y. (1993). Estimation of optimum average surficial density from gravity data: An objective Bayesian approach. *J. Geophys. Res.*, 98, 12097-12109.
- Murray, A. S. and R. M. Tracey. 2001. Best practice in gravity surveying. *Technical Report of the Australian Geological Survey*, 43 pp.



- Nabighian, M.N., Ander, M.E., Grauch, V.J.S., Hansen, R.O., LaFehr, T.R., Li, Y., Pearson, W.C., Peirce, J.W., Phillips, J.D. and Ruder, M.E. (2005a). Historical development of the gravity method in exploration. *Geophysics*, 70, 63ND-89ND.
- Nabighian, M. N., Grauch, V. J. S., Hansen, R. O., LaFehr, T. R., Li, Y., Peirce, J. W., ... & Ruder, M. E. (2005b). The historical development of the magnetic method in exploration. *Geophysics*, 70(6), 33ND-61ND.
- Nawaz Sharif, M., Nazrul Islam, M., 1980. The Weibull distribution as a general model for forecasting technological change. *Technological Forecasting and Social Change* 18, 3, 247-256. doi:10.1016/0040-1625(80)90026-8
- Nettleton, L.L. (1939). Determination of density for reduction of gravimeter observations. *Geophysics*, 4, 176-183.
- Nettleton, L. L. (1942). Gravity and magnetic calculations. *Geophysics*, 7(3), 293-310.
- Nettleton, L. L. (1954). Regionals, residuals, and structures. *Geophysics*, 19(1), 1-22.
- Nettleton, L.L. (1976). *Gravity and magnetics in oil prospecting*. McGraw-Hill, New York, 464 pp.
- Neumann, R. (1963), Contribution au calcul simplifié des corrections de relief a grande distance en gravimetrie. *Geophysical prospecting*, volume 11, issue 4, 523-534. <https://doi.org/10.1111/j.1365-2478.1963.tb02050.x>
- Newton, I. (1726). *Philosophiae naturalis principia mathematica, Editio tertia aucta & emendata*. Londini: Apud Guil. & Joh. Innys, Regiæ Societatis typographos.
- Nichols, G. J., 1984. Thrust tectonics and alluvial sedimentation, Aragón, Spain. Unpublished Ph. D. Thesis, Univ. of Cambridge. 243pp.
- Nichols, G. J., 1987. The Structure and Stratigraphy of the Western External Sierras of the Pyrenees, Northern Spain. *Geological Journal*, 22: 245-259.
- Nowell, D. A. G. (1999). Gravity terrain corrections—an overview. *Journal of Applied Geophysics*, 42(2), 117-134.
- Nunns, A. G. (1991). Structural Restoration of Seismic and Geologic Sections in Extensional Regimes (1). *AAPG bulletin*, 75(2), 278-297.
- Nussbaum, C., Kloppenburg, A., Caër, T., & Bossart, P. (2018). Tectonic evolution around the Mont Terri rock laboratory, northwestern Swiss Jura: constraints from kinematic forward modelling. *Swiss J Geosci* 110, 39-66. DOI 10.1007/s00015-016-0248-x
- Nyquist, H. (1928). Certain topics in telegraph transmission theory. *Transactions of the American Institute of Electrical Engineers*, 47(2), 617-644.
- O'Brien, M. J., & Gray, S. H. (1996). Can we image beneath salt?. *The Leading Edge*, 15(1), 17-22.
- O'Connell, M.D., Smith, R.S. and Vallee, M.A. (2005). Gridding aeromagnetic data using longitudinal and transverse gradients with the minimum curvature operator. *The Leading Edge*, 24, 142-145.
- Oldenburg, D. W., 1974, The inversion and interpretation of gravity anomalies: *Geophysics*, v.39:526-536
- Oldenburg, D. W., & Li, Y. (2005). Inversion for applied geophysics: A tutorial. *Near-surface geophysics*, 89-150.
- Olesen, A. V. (2002). *Improved airborne scalar gravimetry for regional gravity field mapping and geoid determination*. Copenhagen: University of Copenhagen.
- Olhoeft, G.R., Johnson, G.R., 1989. Densities of rocks and minerals. In: Carmichael, R.S. (Ed.), *Practical Handbook of Physical Properties of Rocks and Minerals, Section II*. CRC Press, Boca Raton, FL.
- Oliva-Urcia, B., Pueyo, E. L., & Larrasoana, J. C. (2008). Magnetic reorientation induced by pressure solution: a potential mechanism for orogenic-scale remagnetizations. *Earth and Planetary Science Letters*, 265(3-4), 525-534.
- Oliva-Urcia, B., Larrasoana, J. C., Pueyo, E. L., Gil, A., Mata, P., Parés, J. M., ... & Pueyo, O. (2009). Disentangling magnetic subfabrics and their link to deformation processes in cleaved sedimentary rocks from the Internal Sierras (west central Pyrenees, Spain). *Journal of Structural Geology*, 31(2), 163-176.
- Oliva-Urcia, B., Casas, A. M., Ramón, M. J., Leiss, B., Mariani, E., & Román-Berdiel, T. (2012). On the reliability of AMS in ilmenite-type granites: an insight from the Marimanha pluton, Central Pyrenees. *Geophysical Journal International*, 189(1), 187-203.



- Oliva-Urcia, B., Beamud, E., Garcés, M., Arenas, C., Soto, R., Pueyo, E. L., & Pardo, G. (2016). New magnetostratigraphic dating of the Palaeogene syntectonic sediments of the west-central Pyrenees: tectonostratigraphic implications. *Geological Society, London, Special Publications*, 425, SP425-5.
- Oliva-Urcia, B., Beamud, E., Arenas, C., Pueyo, E. L., Garcés, M., Soto, R., ... & Pérez-Rivarés, F. J. (2019). Dating the northern deposits of the Ebro foreland basin; implications for the kinematics of the SW Pyrenean front. *Tectonophysics*, 765, 11-34.
- Olivier, P., de Saint Blanquat, M., Gleizes, G., & Leblanc, D. (1997). Homogeneity of granite fabrics at the metre and dekametre scales. In *Granite: from segregation of melt to emplacement fabrics* (pp. 113-127). Springer, Dordrecht.
- Paffenholz, J., McLain, B., Zaskie, J., & Keliher, P. J. (2002, January). Subsalt multiple attenuation and imaging: Observations from the Sigsbee2B synthetic dataset. In *2002 SEG Annual Meeting*. Society of Exploration Geophysicists.
- Pakyuz-Charrier, E., Giraud, J., Ogarko, V., Lindsay, M., & Jessell, M. (2018). Drillhole uncertainty propagation for three-dimensional geological modeling using Monte Carlo. *Tectonophysics*, 747, 16-39.-
- Parasnis, D.S. (1952). A study of rock density in the English Midlands. *Mon. Not. R. Astron. Soc. Geophys. Suppl.*, 6, 252-271.
- Parasnis, D.S. (1979). *Principles of applied geophysics*. Third edition, Chapman and Hall, London, 275 pp.
- Parés, J. M. (2015). Sixty years of anisotropy of magnetic susceptibility in deformed sedimentary rocks. *Frontiers in Earth Science*, 3, 4.
- Paris Agreement (2015). In *Report of the Conference of the Parties to the United Nations Framework Convention on Climate Change (21st Session, 2015: Paris)*. Retrived December (Vol. 4, p. 2017).
- Parker, R.L. and Huestis, S.P., 1974, *The Inversion of Magnetic Anomalies in the Presence of Topography: JGR*, v.79:1587-1593.
- Parker, R.L., 1972, *The rapid calculation of potential anomalies: Geophysical Journal of the Royal Astronomical Society*, v.42:315-334.
- Pascoe, R., Hooper, R., Storhaug, K., & Harper, H. (1999). Evolution of extensional styles at the southern termination of the Nordland Ridge, Mid-Norway: A response to variations in coupling above Triassic salt. *Geological Society, London, Petroleum Geology Conference Series*, 5(1), 83–90. <https://doi.org/10.1144/0050083>
- Pasternack, E. (2009). *Uncertainty in Petrophysical Evaluation*. Search and Discovery. Article, (120011).
- Pavlis, N. K., Holmes, S. A., Kenyon, S. C., & Factor, J. K. (2008). An earth gravitational model to degree 2160: EGM2008. *EGU general assembly*, 10, 13-18.
- Pavlis, N. K., S. A. Holmes, S. C. Kenyon, and J. K. Factor (2012). The development and evaluation of the Earth gravitational model 2008 (EGM2008). *Journal of Geophysical Research*, volme117, B04406, doi:10.1029/2011JB008916. 38 pp.
- Pawlowski, R. S., and Hansen, R. O. (1990). Gravity anomaly separation by Wiener filtering. *Geophysics*, 55, 539–548.
- Paziresh, M., Kingston, A. M., Latham, S. J., Fullagar, W. K., & Myers, G. M. (2016). Tomography of atomic number and density of materials using dual-energy imaging and the Alvarez and Macovski attenuation model. *Journal of Applied Physics*, 119(21), 214901.
- Pedley, R.C., 1991. GRAVMAG User Manual: Interactive 2.5D Gravity and Magnetic Modelling Program. British Geological Survey, Keyworth, Nottingham .
- Pedley, R. C., Busby, J. P., & Dabek, Z. K. (1993). GRAVMAG user manual-interactive 2.5 D gravity and magnetic modelling. British Geological Survey (p. 497). Technical Report WK/93/26/R.
- Pérez-Rivarés, F. J., Arenas, C., Pardo, G., & Garcés, M. (2018). Temporal aspects of genetic stratigraphic units in continental sedimentary basins: Examples from the Ebro basin, Spain. *Earth-Science Reviews*, 178, 136-153.
- Perroud, H., Chauvin, A., & Rebelle, M. (1995). Hydrocarbon seepage dating through chemical remagnetization. *Geological Society, London, Special Publications*, 98(1), 33-41.
- Peters, L. J. (1949). The direct approach to magnetic interpretation and its practical application. *Geophysics*, 14(3), 290-320.



- Petrovsky, E., & Ellwood, B. B. (1999). Magnetic monitoring of air-, land-and water pollution. *Quaternary climates, environments and magnetism*, 279-322.
- Pham, L. T., Oksum, E., & Do, T. D. (2018). GCH\_gravin: a MATLAB-based program for inverting gravity anomalies over sedimentary basins. *Computers & geosciences*, 120, 40-47.
- Phillips, W.E.A. & Byrne, J.G. (1969). The construction of sections in areas of highly deformed rocks. In: Kent P.E. Satterthwaite, G.E. & Spencer, A.M. (eds.): *Time and place in orogeny*. Geol. Soc. Spec. Publ., 3, 81-93.
- Pickell, J. J., & Heacock, J. G. (1960). Density logging. *Geophysics*, 25(4), 891-904.
- Pisarevsky, S. (2005). New edition of the global paleomagnetic database. *Eos, Transactions American Geophysical Union*, 86(17), 170-170.
- Plata, J.L. (1992). Manual program CCT BLOQUES. IGME, informe inédito Área Geofísica.
- Plata, J.L. (2009). Establecimiento de bases metodológicas para la obtención de Cartografía gravimétrica 1:50.000. Aplicación a la modelización 2D y 3D en varias zonas de la Península Ibérica. Capítulo 3: Informe de Petrofísica. IGME, área de Geofísica. 113 pp. [http://info.igme.es/SidPDF/151000/878/151878\\_0000001.pdf](http://info.igme.es/SidPDF/151000/878/151878_0000001.pdf)
- Plata, J.L. (2014). Manual program CCT BLOQUES. IGME, informe inédito Área Geofísica.
- Plata, J. L., Riveira, M., & Ibarra, P. (2008). Recovering Old Geophysical Documents for Deep Aquifer Research. In *Near Surface 2008-14th EAGE European Meeting of Environmental and Engineering Geophysics* (pp. cp-64). European Association of Geoscientists & Engineers.
- Poblet, J. (2006). Técnicas gráficas y numéricas de construcción de interpretaciones estructurales en 2D. Curso de formación del IGME, Madrid.-
- Poblet, J. & McClay, K. (1996). Geometry and kinematics of single-layer detachment folds. *Am. Assoc. Pet. Geol. Bull.*, 80, 1085-1109.
- Pocoví, A.; Ó. Pueyo Anchuela, E.L. Pueyo, A.M. Casas-Sainz, M.T. Román Berdiel, A. Gil Imaz, J. Ramajo Cordero, T. Mochales, C. García Lasanta, E. Izquierdo, J.M. Parés, E. Sánchez, R. Soto Marín, C. Oliván, A. Rodríguez Pintó, B. Oliva-Urcia, J.J. Villalaín (2014). Magnetic fabrics in the Central-Western Pyrenees: an overview. In: *ASM in deformed rocks a tribute to Graham J. Borradaile*. Edited by: Almqvist, B.; Henry, B.; Jackson, M.; Werner, T.; Lacroix, F. *Tectonophysics* 629, 303-318.
- Poete, N (2012). Quantitative petrophysical uncertainties modeling and its impact on reserves estimates. In *SPWLA 2011-12 Kuwait Annual Logging Symposium*. Society of Petrophysicists and Well-Log Analysts
- Porquet, M., Pueyo, E. L., Román-Berdiel, T., Olivier, P., Longares, L. A., Cuevas, J., ... & Auréjac, J. B. (2017). Anisotropy of magnetic susceptibility of the Pyrenean granites. *Journal of Maps*, 13(2), 438-448.
- Portier, N., Hinderer, J., Riccardi, U., Ferhat, G., Calvo, M., Abdelfettah, Y., & Bernard, J. D. (2018). New results on the gravity monitoring (2014–2017) of Soultz-sous-Forêts and Rittershoffen geothermal sites (France). *Geothermal Energy*, 6(1), 1-20.
- Portniaguine, O., & Zhdanov, M. S. (1999). Focusing geophysical inversion images. *Geophysics*, 64(3), 874-887.
- Porzucek, S., & Matwijn, W. (2017). Comparison of terrain correction in microgravimetry using airborne and terrestrial laser scanning data. *International Multidisciplinary Scientific GeoConference: SGEM: Surveying Geology & mining Ecology Management*, 17(1.4), 57-64.
- Pueyo, E.L.; Millán, H.; Pocoví, A. (2002). Rotation velocity of a thrust: a paleomagnetic study in the External Sierras (Southern Pyrenees) . *Sedimentary Geology*, 146, 191 – 208
- Pueyo, E. L., Pocoví, A., Millán, H., Sussman, A. J., & Weil, A. B. (2004a). Map-view models for correcting and calculating shortening estimates in rotated thrust fronts using paleomagnetic data. *Orogenic Curvature: Integrating Paleomagnetic and Structural Analyses*, 383, 55-71.
- Pueyo, E. L., Román-Berdiel, M. T., Bouchez, J. L., Casas, A. M., & Larrasoaña, J. C. (2004b). Statistical significance of magnetic fabric data in studies of paramagnetic granites. *Geological Society, London, Special Publications*, 238(1), 395-420.
- Pueyo, E. L., Izquierdo-Llavall, E., Ayala, C., Oliva-Urcia, B., Rubio, F. M., Rodríguez-Pintó, A., ... & García Crespo, J. (2015). Feedback of balanced cross sections and gravity modeling: numerical



- estimation of horizon mislocations. A case study from the Linking Zone (Northeastern, Spain). In *American Geophysical Union, Fall Meeting 2015*, abstract id. S21B-2683.
- Pueyo, E. L., Izquierdo-Llavall, E., Rodríguez-Pintó, A., Rey-Moral, C., Oliva-Urcia, B., Casas, A. M., ... & Rubio, F. M. (2016a). Petrophysical properties in the Iberian Range and surrounding areas (NE Spain): 1-density. *Journal of Maps*, 12(5), 836-844.
- Pueyo, E. L., Sussman, A. J., Oliva-Urcia, B., & Cifelli, F. (2016b). Palaeomagnetism in fold and thrust belts: use with caution. *Geological Society, London, Special Publications*, 425(1), 259-276.
- Pueyo, E.L.; García-Lasanta, C.; López, M.A.; Oliván, C. ; San Miguel, G. ; Gil-Garbi, H.; Oliva-Urcia, B.; Beamud, E.; Hernández, R.; Elger, K.; Ulbricht, D.; Lange, O. & GeoKin3DPyr group (2017). Metodología para el desarrollo de la BBDD paleomagnética de Iberia (EPOS-DDSS Iberian Paleomagnetism). *Proceedings de la Reunión de la Comisión de Paleomagnetismo de la SGE-MAGIBER-X (Valle del Grío) IUCA-Universidad de Zaragoza ISBN: 978-84-16723-40-9* pags, 94-99.
- Pueyo, E.L.; Román-Berdiel, M.T.; Ayala, C.; Loi, F; Soto, R.; Beamud, E.; Fernández, E.; Gimeno, A.; Galán, L.; Schamuells, S.; Bach-Oller, N.; Clariana, P.; Rubio, F.M.; Casas, A.M.; Oliva-Urcia, B.; García Lobón, J.L.; Rey Moral, C.; (2021). Density and magnetic susceptibility relationships in non-magnetic granites; a “wildcard” for modeling potential fields geophysical data. *EGU General Assembly (EGU2020-8736)*.
- Pueyo, E.L.; Santolaria, P.; Calvín, P.; Casas, A.M.; Sánchez, E.; Oliva-Urcia, B.; Silva-Casal, R.; Ayala, C.; Scholger, R; Rubio, F.; Rey-Moral., A.; Rodríguez-Pintó, A.; Pocoví, A. (2021 in review). Regional, local and apparent vertical-axis rotations, detachment folding and salt remobilization in the southwestern Pyrenean termination. *Journal of Structural Geology*
- Pueyo-Anchuela, Ó., Gil-Imaz, A. G., & Pocoví-Juan, A (2010). Significance of AMS in multilayer systems in fold-and-thrust belts. A case study from the Eocene turbidites in the southern Pyrenees (Spain). *Geological Journal*, 45(5-6), 544-561.
- Pueyo-Anchuela, Ó., Pocoví-Juan A., Gil-Imaz, A. & Casas-Sainz, A. M. (2013b). Factors influencing magnetic susceptibility in the southern Pyrenees. *Studia Geophysica et Geodaetica*, 57(4), 692-709.
- Pueyo-Anchuela, Ó., Casas-Sainz, A. M., Pueyo, E. L., Pocoví, A., & Gil-Imaz, A. (2013a). Analysis of the ferromagnetic contribution to the susceptibility by low field and high field methods in sedimentary rocks of the Southern Pyrenees and Northern Ebro foreland basin (Spain). *Terra Nova*, 25(4), 307-314.
- Puigdefábregas, C., 1975. La sedimentación molásica en la cuenca de Jaca. *Pirineos*, 104: 1-188.
- Querol, R. (1989). *Geología del subsuelo de la Cuenca del Tajo*. Escuela Técnica Superior de Ingenieros de Minas de Madrid, 48.
- Radogna, V., Olivier, R. and Logean, P. (2004). A subway project in Lausanne, Switzerland, as an urban microgravimetry test site: acquisition, correction of buildings influence and modeling. *Conference Proceedings, 17th EEGS Symposium on the Application of Geophysics to Engineering and Environmental Problems*.
- Ramón, M. J. (2013). Flexural unfolding of complex geometries in fold and thrust belts using paleomagnetic vectors. Unpublished PhD, University of Zaragoza, Spain, <http://zaguan.unizar.es/record/11750>
- Ramón, M. J., Pueyo, E. L., Briz, J. L., Pocoví, A., & Ciria, J. C. (2012). Flexural unfolding of horizons using paleomagnetic vectors. *Journal of Structural Geology*, 35, 28-39.
- Ramón, M. J., Pueyo, E. L., Caumon, G., & Briz, J. L. (2016a). Parametric unfolding of flexural folds using palaeomagnetic vectors. *Geological Society, London, Special Publications*, 425(1), 247-258.
- Ramón, M. J., Briz, J. L., Pueyo, E. L., & Fernández, O. (2016b). Horizon restoration by best fitting of finite elements and rotation constraints: sensitivity to the mesh geometry and pin-element location. *Mathematical Geosciences*, 48(4), 419-437.
- Ramsay, J.G. & Huber, M.I. (1987). *The techniques of modern structural geology*. Vol. 2: folds and fractures. Academic Press, London, 365-382.
- Randle, C. H., Bond, C. E., Lark, R. M., & Monaghan, A. A. (2018). Can uncertainty in geological cross-section interpretations be quantified and predicted?. *Geosphere*, 14(3), 1087-1100.



- Rao, D. B. (1986). Modelling of sedimentary basins from gravity anomalies with variable density contrast. *Geophysical Journal International*, 84(1), 207-212.
- Rasmussen, N. F., 1975, *The successful use of borehole gravity meter in northern Michigan: The Log Analyst*, September-October, p. 1-10
- Rasmussen, R., & Pedersen, L. B. (1979). End corrections in potential field modeling. *Geophysical prospecting*, 27(4), 749-760.
- Readman, P. W., O'Reilly, B. M., & Murphy, T. (1997). Gravity gradients and upper-crustal tectonic fabrics, Ireland. *Journal of the Geological Society*, 154(5), 817-828.
- Rebhan, H., Aguirre, M., & Johannessen, J. (2000). The gravity field and steady-state ocean circulation explorer mission-GOCE. *ESA Earth Observation Quarterly*, 66, 6-11.
- Reich, M., Mikolaj, M., Blume, T., & Güntner, A. (2019). Reducing gravity data for the influence of water storage variations beneath observatory buildings. *Geophysics*, 84(1), EN15-EN31.
- Reichel, N., Evans, M., Allioli, F., Mauborgne, M. L., Nicoletti, L., Haranger, F., ... & Rabrei, R. (2012). Neutron-Gamma Density (NGD): Principles, field test results and log quality control of a radioisotope-free bulk density measurement. In *SPWLA 53rd Annual Logging Symposium. Society of Petrophysicists and Well-Log Analysts*.
- Reid, A.B., J.M. Allsop, H. Granser, A.J. Millett, and I.W. Somerton, 1990). Magnetic interpretation in three dimensions using Euler deconvolution: *Geophysics*, 55, no. 1, 80–91, <http://dx.doi.org/10.1190/1.1442774>.
- Rikitake, T., Tajima, H., Izutuya, S., Hagiwara, Y., Kawada, K. and Sasai, Y. (1965). Gravimetric and geomagnetic studies of Onikobe area. *Bull. Earthq. Res. Inst., Univ. Tokyo*, 43, 241-267.
- Rim, H., & Li, Y. (2012). Single-hole imaging using borehole gravity gradiometry. *Geophysics*, 77(5), G67-G76.
- Rim, H., & Li, Y. (2015). Advantages of borehole vector gravity in density imaging. *Geophysics*, 80(1), G1-G13
- Robbins, S. L. (1989). Borehole gravimetry reviews. *U.S. Geological Survey Circular 890*, 65 pp
- Roberts, A. M., Kuszniir, N. J., Yielding, G., & Styles, P. (1998). 2D flexural backstripping of extensional basins; the need for a sideways glance. *Petroleum Geoscience*, 4(4), 327–338. <https://doi.org/10.1144/petgeo.4.4.327>
- Roberts, A. M., Corfield, R. I., Kuszniir, N. J., Matthews, S. J., Hansen, E.-K., & Hooper, R. J. (2009). Mapping palaeostructure and palaeobathymetry along the Norwegian Atlantic continental margin: Møre and Vøring basins. *Petroleum Geoscience*, 15(1), 27–43. <https://doi.org/10.1144/1354-079309-804>
- Rochette, P. (1987). Magnetic susceptibility of the rock matrix related to magnetic fabric studies. *Journal of Structural Geology*, 9(8), 1015-1020.
- Rodríguez-Pintó, A.; Pueyo, E. L.; Sánchez, E.; Calvin, P.; Ramajo, J.; Ramón, M.J.; Pocoví, A.; Barnolas, A.; Casas, A. M.; (2016). Rotational kinematics of a curved fold: a structural and paleomagnetic study in the Balzes anticline (Southern Pyrenees). *Tectonophysics*, 677–678, 171–189. [10.1016/j.tecto.2016.02.049](https://doi.org/10.1016/j.tecto.2016.02.049)
- Rodríguez-Pujol, E. R. (2005). Medidas gravimétricas en Madrid y en España. *Anuario Astronómico del Observatorio de Madrid*.
- Roeder, D., Gilbert, E. & Witherspoon, W. (1978). Evolution of macroscopic structure of Valley and Ridge thrust belt, Tennessee and Virginia. *Studies in Geology (Dept. of Geol. Sci., Univ. of Tennessee)*, 2, 1-25.
- Rogelj, J., Shindell, D., Jiang, K., Fifita, S., Forster, P., Ginzburg, V., ... & Waterfield, T. (2018). Mitigation pathways compatible with 1.5 C in the context of sustainable development. In *Global warming of 1.5° C (pp. 93-174)*. Intergovernmental Panel on Climate Change (IPCC)
- Román-Berdiel, T., Pueyo-Morer, E. L., & Casas-Sainz, A. M. (1995). Granite emplacement during contemporary shortening and normal faulting: structural and magnetic study of the Veiga Massif (NW Spain). *Journal of Structural Geology*, 17(12), 1689-1706.
- Rouby, D., Cobbold, P. R., Sztatmari, P., Demercian, S., Coelho, D., & Rici, J. A. (1993). Least-squares palinspastic restoration of regions of normal faulting—application to the Campos basin (Brazil). *Tectonophysics*, 221(3-4), 439-452.



- Rowan, M.G. (1993). A systematic technique for the sequential restoration of salt structures. *Tectonophysics*, 228, 331-348.
- Rowan, M.G. (1994). Structural styles and evolution of allochthonous salt, Central Louisiana Outer Shelf and Upper Slope. In Jackson, M.P.A., Roberts, D.G. Snelson, S. (Eds.), *Salt Tectonics. A Global Perspective*. A.A.P.G. Mem. 65, 199-228.
- Rowan, M.G. (1996). Benefits and limitations of section restoration in areas of extensional salt tectonics: an example from offshore Louisiana. In: Buchanan, P.G., Nieuwland, D.A. (Eds.), *Modern Developments in Structural Interpretation, Validation and Modelling*. Geol. Soc. London Spec. Publ. 99, 147-161.
- Rowan, M.G. & Kligfield, R. (1989). Cross-section restoration and balancing as aid to seismic interpretation in extensional terranes. *A.A.P.G. Bull.* 73. 955-966.
- Rowan, M. G., & Ratliff, R. A. (2012). Cross-section restoration of salt-related deformation: Best practices and potential pitfalls. *Journal of Structural Geology*, 41, 24-37.
- Rowland, S.M., Duebendorfer, E.M. & Schiefelbein, I.M. (2007). *Structural Analysis and Synthesis: A Laboratory Course in Structural Geology*, third. ed. Blackwell Publishing, Oxford. 300 pp.
- Roy, A. (1958). Letter on residual and second derivative of gravity and magnetic maps: *Geophysics*, 23, 860–861.
- Roy, A. (1962). Ambiguity in geophysical interpretation. *Geophysics*, 27(1), 90-99.
- Rybakov, M.; Goldshmidt, V.; Rotstein, Y.; Fleischer, L.; & Goldberg, I., 1999. Petrophysical constraints on gravity/magnetic interpretation in Israel. *Leading Edge*, vol. 18, no. 2, pp. 269– 272, 1999.
- Saltus, R. W., & Blakely, R. J. (1993). HYPERMAG; an interactive, 2-and 2 1/2-dimensional gravity and magnetic modeling program; version 3.5 (No. 93-287). *US Geological Survey*.
- Saltus, R. W., & Blakely, R. J. (2011). Unique geologic insights from “non-unique” gravity and magnetic interpretation. *GSA Today*, 21(12), 4-11.
- Sans, M., Vergés, J., Gomis, E., Parés, J. M., Schiattarella, M., Travé, A., Calvet, F., Santanach, P., Doulcet, A. (2003). Layer parallel shortening in salt-detached folds: constraint on cross-section restoration. *Tectonophysics*, 372(1-2), 85-104.
- Santolaria, 2015. *Salt and thrust tectonics in the South Central Pyrenees*. PhD Thesis. Universidad de Zaragoza.
- Santolaria, P., Casas-Sainz, A. M., Soto, R., & Casas, A. (2017). Gravity modelling to assess salt tectonics in the western end of the South Pyrenean Central Unit. *Journal of the Geological Society*, 174(2), 269-288.
- Santolaria, P., Ayala, C., Pueyo, E. L., Rubio, F. M., Soto, R., Calvín, P., ... & Casas-Sainz, A. M. (2020). Structural and geophysical characterization of the western termination of the South Pyrenean triangle zone. *Tectonics*, 39(8), e2019TC005891.
- Scheck-Wenderoth, M., Raum, T., Faleide, J. I., Mjelde, R., & Horsfield, B. (2007). The transition from the continent to the ocean: A deeper view on the Norwegian margin. *Journal of the Geological Society*, 164(4), 855–868. <https://doi.org/10.1144/0016-76492006-131>
- Schiavone, D., Capolongo, D., & Loddo, M. (2009). Near-station topographic masses correction for high-accuracy gravimetric prospecting. *Geophysical Prospecting*, 57(4), 739-752.
- Schilling, M., Simon, A., Jahnke, C. & Höding, T. (2018). Brandenburg 3D – Das geologische 3D Modell Brandenburgs im Internet veröffentlicht. *Brandenburgische Geowissenschaftliche Beiträge*, 25(1/2), 39–46.
- Schlische, R. W., Groshong Jr, R. H., Withjack, M. O., & Hidayah, T. N. (2014). Quantifying the geometry, displacements, and subresolution deformation in thrust-ramp anticlines with growth and erosion: From models to seismic-reflection profile. *Journal of Structural Geology*, 69, 304-319.
- Schmidt, S., Götze, H. J., Fichler, C., & Alvers, M. (2010). IGMAS+—a new 3D gravity, FTG and magnetic modeling software. *GEO-INFORMATIK Die Welt im Netz*, edited by: Zipf, A., Behncke, K., Hillen, F., and Scheffermeyer, J., Akademische Verlagsgesellschaft AKA GmbH, Heidelberg, Germany, 57-63.
- Schmidt, S. et al. (2020). IGMAS+—a tool for interdisciplinary 3D potential field modelling of complex geological structures. *EGU General Assembly*, EGU2020–8383.



- Schmoker, J. W. (1977). Borehole gravity survey to determine density variations in the Devonian shale sequence of Lincoln County, West Virginia (No. MERC/CR-77/7). Geological Survey, Denver, CO (USA).
- Schön, J. H. (2015). *Physical properties of rocks: Fundamentals and principles of petrophysics*. Elsevier.
- Schultz-Ela, D. D. (1992). Restoration of cross-sections to constrain deformation processes of extensional terranes. *Marine and Petroleum Geology*, 9(4), 372-388.
- Schulz, H. R. (2018). A new PC control software for ZLS-Burriss gravity meters. *Geodesy and Geodynamics*, 9(3), 210-219.
- Schumacher, D., 1996, Hydrocarbon-induced alteration of soils and sediments, in D. Schumacher and M. A. Abrams, eds., *Hydrocarbon migration and its near-surface expression: AAPG Memoir 66*, p. 71-89.
- Slater, J. G., & Christie, P. A. F. (1980). Continental stretching: An explanation of the Post-Mid-Cretaceous subsidence of the central North Sea Basin. *Journal of Geophysical Research: Solid Earth*, 85(B7), 3711–3739. <https://doi.org/10.1029/JB085iB07p03711>
- Seeber (2003). *Satellite Geodesy*. Editorial Walter de Gruyter. Berlín. New York. ISBN 3-11-017549-5
- Seigel, H.O., 1995. *A guide to high precision land gravimeter surveys*. Scintrex Limited, 122.
- Seoane, L., Bonvalot, S., Briais, A., Carassus, V., Gabalda, G., Reinquin, F., & Wziontek, H. (2018). International Gravimetric Bureau (BGI): database, services and products. In *EGU General Assembly Conference Abstracts* (p. 9485).
- Sibson R. (1977). Fault rocks and fault mechanisms. *Journal of the Geological Society* 133, 191-213.
- Siddiqui, S., & Khamees, A. A. (2004, January). Dual-energy CT-scanning applications in rock characterization. In *SPE annual technical conference and exhibition*. Society of Petroleum Engineers. SPE-90520-MS
- Silva, J. B., Costa, D. C., & Barbosa, V. C. (2006). Gravity inversion of basement relief and estimation of density contrast variation with depth. *Geophysics*, 71(5), J51-J58.
- Simón, J. L., & Liesa, C. L. (2011). Incremental slip history of a thrust: diverse transport directions and internal folding of the Utrillas thrust sheet (NE Iberian Chain, Spain). *Geological Society, London, Special Publications*, 349(1), 77-97.
- Sjöberg, L. E., & Bagherbandi, M. (2017). *Gravity inversion and integration*. Springer International Publishing AG.
- Skeels, D. C. (1947). Ambiguity in gravity interpretation. *Geophysics*, 12(1), 43-56.
- Skiba, P. (2011). *Homogene Schwerekarte der Bundesrepublik Deutschland (Bouguer-Anomalien)*. Leibniz Institute for Applied Geophysics.
- Skiba, P. & Gabriel, G. (2010). *Schwerekarte der Bundesrepublik Deutschland 1:1000000 - Bouguer-Anomalien*. Leibniz Institute for Applied Geophysics.
- Smith, N. J. (1950). The case for gravity data from boreholes. *Geophysics*, 15(4), 605-636.
- Snieder, R., & Trampert, J. (1999). Inverse problems in geophysics. In *Wavefield inversion* (pp. 119-190). Springer, Vienna.
- Snopek, K., & Casten, U. (2006). 3GRAINS: 3D Gravity Interpretation Software and its application to density modeling of the Hellenic subduction zone. *Computers & geosciences*, 32(5), 592-603.
- Somigliana, C., (1930). *Geofisica — Sul campo gravitazionale esterno del geoide ellissoidico*. *Atti della Accademia nazionale dei Lincei. Rendiconti. Classe di scienze fisiche, matematiche e naturali*, 6, 237– 243.
- Song, T. & Cawood, P.A. (2001). Effects of subsidiary faults on the geometric construction of listric normal faults systems. *A.A.P.G. Bull.*, 85, 221-232.
- Soriano, M. A., & Simón, J. (1995). Alluvial dolines in the central Ebro Basin, Spain: a spatial and developmental hazard analysis. *Geomorphology*, 11(4), 295-309.
- Soriano, M., & Simon, J. (2002). Subsidence rates and urban damages in alluvial dolines of the Central Ebro basin (NE Spain). *Environmental geology*, 42(5), 476-484.
- Soriano, M. A., Pocióv, A., Gil, H., Perez, A., Luzón, A., & Marazuela, M. Á. (2019). Some evolutionary patterns of palaeokarst developed in Pleistocene deposits (Ebro Basin, NE Spain): Improving geohazard awareness in present-day karst. *Geological Journal*, 54(1), 333-350.
- Spector, A., and Grant, F. S. (1970). Statistical models for interpreting aeromagnetic data. *Geophysics*, 35, 293–302 (discussion and reply — 36, 617 and 39, 112; errata — 36, 448 and 42, 1563).



- Srivastava, R. P. (2004). *Determination of Magnetic Basement using Werner Deconvolution*. 5th Conference & Exposition on Petroleum Geophysics, Hyderabad-2004, India PP 953-956
- Stagg H.M.J., J.B. Willcox & D.J.L. Needham (1989) *Werner deconvolution of magnetic data: Theoretical models and application to the Great Australian Bight*, *Australian Journal of Earth Sciences*, 36:1, 109-122, DOI: 10.1080/14400958908527954
- Stewart, R. D., Abou Najm, M. R., Rupp, D. E., & Selker, J. S. (2012). *An image-based method for determining bulk density and the soil shrinkage curve*. *Soil Science Society of America Journal*, 76(4), 1217-1221.
- Sun, J. & Li, Y. (2015). *Advancing the understanding of petrophysical data through joint clustering inversion: A sulfide deposit example from Bathurst Mining Camp*. In *SEG Technical Program Expanded Abstracts 2015* (pp. 2017-2021). Society of Exploration Geophysicists.
- Sun, J. and Li, Y. (2017). *Joint inversion of multiple geophysical and petrophysical data using generalized fuzzy clustering algorithms* *Geophysical Journal International*, Volume 208, Issue 2, February 2017, Pages 1201–1216,
- Suppe, J. (1983). *Geometry and kinematics of fault-bend folding*. *American Journal of science*, 283(7), 684-721.
- Suppe, J. (1985). *Principles of structural geology*. Prentice Hall, New Jersey, 537
- Suppe, J., & Medwedeff, D. A. (1990). *Geometry and kinematics of fault-propagation folding*. *Eclogae Geologicae Helveticae*, 83(3), 409-454.
- Suppe, J., Connors, C.D. & Zhang, Y. (2004). *Shear fault-bend folding*. In: McClay, K.R. (ed.): *Thrust tectonics and hydrocarbon systems*. A.A.P.G. Mem., 82, 303-323.
- Sussman, A. J., Pueyo, E. L., Chase, C. G., Mitra, G., & Weil, A. B. (2012). *The impact of vertical-axis rotations on shortening estimates*. *Lithosphere*, 4(5), 383-394.
- Suzuki, K., Takayama, T., & Fujii, T. (2015). *Density structure report from logging-while-drilling data and core data at the first offshore gas production test site on Daini-Atsumi Knoll around eastern Nankai Trough*. *Marine and Petroleum Geology*, 66, 388-395.
- Syberg, F. J. R. (1972). *A Fourier method for the regional residual problem of potential fields: Geophysical Prospecting*, 20, 47–75.
- Talwani, M., & Ewing, M. (1960). *Rapid computation of gravitational attraction of three-dimensional bodies of arbitrary shape*. *Geophysics*, 25(1), 203-225.
- Talwani, M., and Heirtzler, J. R., 1964, *Computation of magnetic anomalies caused by two-dimensional bodies of arbitrary shape*, in Parks, G. A., Ed., *Computers in the mineral industries, Part 1: Stanford Univ. Publ., Geological Sciences*, 9, 464-480.
- Talwani, M., Worzel, J. L., & Landisman, M. (1959). *Rapid gravity computations for two-dimensional bodies with application to the Mendocino submarine fracture zone*. *Journal of geophysical research*, 64(1), 49-59.
- Tang, S., Liu, H., Yan, S., Xu, X., Wu, W., Fan, J., ... & Tu, L. (2019). *A high-sensitivity MEMS gravimeter with a large dynamic range*. *Microsystems & nanoengineering*, 5(1), 1-11.
- Tarantola, A., & Valette, B. (1982). *Inverse problems= quest for information*. *Journal of geophysics*, 50(1), 159-170.
- Tarney, J. (1998). *Plate Tectonics: Geological Aspects – Extension & Sedimentary Basins, Lecture 4*, University of Leicester. Available at: [Http://www.le.ac.uk/geology/art/gl209/lecture4/lecture4.html](http://www.le.ac.uk/geology/art/gl209/lecture4/lecture4.html).
- Tassis G.A., C.B. Papazachos, G.N. Tsokas, I.N. Tziavos, I. Vasiljević and A. Stampolidis (2015). *Moho Depth Determination of the Adriatic Sea Region Using a New Bouguer Anomaly Database*. *Conference Proceedings, 8th Congress of the Balkan Geophysical Society, Oct 2015, Volume 2015, p.1 – 5*. DOI: <https://doi.org/10.3997/2214-4609.201414213>
- Tauxe, L., Shaar, R., Jonestrask, L., Swanson-Hysell, N. L., Minnett, R., Koppers, A. A. P., et al. (2016). *PmagPy: Software package for paleomagnetic data analysis and a bridge to the Magnetism Information Consortium (MagIC) database*. *Geochemistry, Geophysics, Geosystems*, 17, 2450–2463. <https://doi.org/10.1002/2016gc006307>
- Tearpock, D.J. & Bischke, R.E. (1991). *Applied subsurface geological mapping*. Prentice Hall, Englewood Cliffs (New Jersey), 648 p.



- Teixell, A. (1996). *The Ansó transect of the southern Pyrenees: basement and cover thrust geometries*. *Journal of the Geological Society*, 153(2), 301-310.
- Teixell, A., & García-Sansegundo, J. (1995). *Estructura del sector central de la Cuenca de Jaca (Pirineos meridionales)*. *Revista de la Sociedad Geológica de España*, 8(3), 215-228.
- Tenzer, R., & Gladkikh, V. (2014). *Assessment of density variations of marine sediments with ocean and sediment depths*. *The Scientific World Journal*, 2014
- Tenzer, R., Sirguey, P., Rattenbury, M., & Nicolson, J. (2011). *A digital rock density map of New Zealand*. *Computers & geosciences*, 37(8), 1181-1191.
- Terrinha, P., Pueyo, E. L., Aranguren, A., Kullberg, J. C., Kullberg, M. C., Casas-Sainz, A., & do Rosário Azevedo, M. (2018). *Gravimetric and magnetic fabric study of the Sintra Igneous complex: laccolith-plug emplacement in the Western Iberian passive margin*. *International Journal of Earth Sciences*, 107(5), 1807-1833.
- Terzaghi, R. A. D. (1940). *Compaction of lime mud as a cause of secondary structure*. *Journal of Sedimentary Research*, 10(2), 78-90.
- Teunissen, Peter J.G. and Montenbruck, Oliver. (2017). *Springer Handbook of Global Navigation Satellite Systems*. Editorial Springer Wien New York. ISBN 978-3-319-42928-1
- Thompson, D. T., 1982. *EULDPH: A new technique for making computer-assisted depth estimates from magnetic data*, *Geophysics*, 47, 31–37, <http://dx.doi.org/10.1190/1.1441278>.
- Tiab, D., & Donaldson, E. C. (2016). *Petrophysics: theory and practice of measuring reservoir rock and fluid transport properties*. Gulf professional publishing.
- Tian, Y., Ke, X., & Wang, Y. (2018). *DenInv3D: a geophysical software for three-dimensional density inversion of gravity field data*. *Journal of Geophysics and Engineering*, 15(2), 354-365.
- Tittman, J., & Wahl, J. S. (1965). *The physical foundations of formation density logging (gamma-gamma)*. *Geophysics*, 30(2), 284-294.
- Torge, W. (1989). *Gravimetry*. Editorial deGruyter. 482 pages. ISBN-10:3110107023; ISBN-13: 978-3110107029.
- Tracey, R., Bacchin, M., & Wynne, P. (2007). *AAGD07: A new absolute gravity datum for Australian gravity and new standards for the Australian National Gravity Database*. *ASEG Extended Abstracts*, 2007(1), 1-3.,
- Treitel, S., & Lines, L. (2001). *Past, present, and future of geophysical inversion—A new millennium analysis*. *Geophysics*, 66(1), 21-24.
- Tsokas, G. N., & Hansen, R. O. (1997). *Study of the crustal thickness and the subducting lithosphere in Greece from gravity data*. *Journal of Geophysical Research: Solid Earth*, 102(B9), 20585-20597.
- Turner, J. P. (1990). *Structural and stratigraphic evolution of the West Jaca thrust-top basin, Spanish Pyrenees*. *Journal of the Geological Society*, 147(1), 177-184.
- Tziavos, I.N., Vergos, G.S. and Grigoriadis, V.N. (2010). *Investigation of topographic reductions and aliasing effects on gravity and the geoid over Greece based on various digital terrain models*. *Surv. Geophys*, 31, 23-67.
- UNE 22-611-85. (1985). *Prospección geofísica terrestre. Método gravimétrico (Geophysics terrestrial prospecting. Gravimetric method)*.
- UNE-EN 1936 (2007). *Densidad y porosidad de una roca. Determinación de la densidad real y aparente y de la porosidad abierta y total*.
- Vajk, R. (1956). *Bouguer corrections with varying surface density*. *Geophysics*, 21, 1004–1020.
- Valcárcel Rodríguez, M.M. (2015). *Reconstrucción y restitución 3D del anticlinal de Puerta-Pareja y estudio de su evolución deformacional y cinemática en su contexto regional (cuenca de Loranca y Sierra de Altomira)*. PhD Thesis, 269 pp.
- Valcárcel, M., Soto, R., Beamud, E., Oliva-Urcia, B., Muñoz, J. A., & Biete, C. (2016). *Integration of palaeomagnetic data, basement-cover relationships and theoretical calculations to characterize the obliquity of the Altomira–Loranca structures (central Spain)*. *Geological Society, London, Special Publications*, 425(1), 169-188.
- van der Meijde, M., Pail, R., Bingham, R., & Floberghagen, R. (2015). *GOCE data, models, and applications: A review*. *International journal of applied earth observation and geoinformation*, 35, 4-15



- Vaquero, P.A., Sainz-Maza, S. 2011. *Reseña de Punto Destacado de Gravimetría Absoluta, Red Española de Gravimetría Absoluta*. IGN: Madrid; 2
- Vatankhah, S., Ardestani, V. E., Niri, S. S., Renaut, R. A., & Kabirzadeh, H. (2019). IGUG: A MATLAB package for 3D inversion of gravity data using graph theory. *Computers & geosciences*, 128, 19-29.
- Verrall, P. (1981). *Structural interpretation with application to North Sea problems*. Joint Association of Petroleum Exploration Courses (JAPEC) Course Notes, 3, UK.
- Vidal-Royo, O., Cardozo, N., Muñoz, J. A., Hardy, S., & Maerten, L. (2012). Multiple mechanisms driving detachment folding as deduced from 3D reconstruction and geomechanical restoration: The Pico del Aguila anticline (External Sierras, Southern Pyrenees). *Basin Research*, 24(3), 295-313.
- Visser, P. N. A. M. (1999). Gravity field determination with GOCE and GRACE. *Advances in Space Research*, 23(4), 771-776.
- Vitushkin, L. (2011). Measurement standards in gravimetry. *Gyroscopy and navigation*, 2(3), 184.
- Vrijlandt, M. A. W., Struijk, E. L. M., Brunner, L. G., Veldkamp, J. G., Witmans, N., Maljers, D., & van Wees, J. D. (2019, June). ThermoGIS update: a renewed view on geothermal potential in the Netherlands. In *Proceedings of the European Geothermal Congress, The Hague, The Netherlands* (pp. 11-14).
- Wahl, J. S., Tittman, J., & Johnstone, C. W. (1964). The dual spacing formation density log. *Journal of Petroleum Technology*, 16(12), 1-411.
- Waid, C. B. (2018) *High-resolution subsurface mapping of depositional cycles within the lower part of the Huron Member of the Ohio Shale: detailed snapshots of basin development in central and eastern Ohio*. Geological Note 13 State of Ohio Department of Natural Resources Division of Geological Survey 24pp
- Waltham, D. (1989). Finite difference modelling of hangingwall deformation, *Jour. Struct. Geol.*, 11 (4), 433-437.
- Waltham, D. (1990). Finite difference of sandbox analogues, compaction and detachment free deformation. *Jour. Struct. Geol.*, 12 (3), 375-381.
- Watkins, H., Bond, C. E., & Butler, R. W. (2014). Identifying multiple detachment horizons and an evolving thrust history through cross-section restoration and appraisal in the Moine Thrust Belt, NW Scotland. *Journal of Structural Geology*, 66, 1-10.
- Watts, A. B. (2001). *Isostasy and Flexure of the Lithosphere*. Cambridge University Press.
- Watts, A., and Fairhead, J. (1999). A process-oriented approach to modeling the gravity signature of continental margins. *The Leading Edge*, 18, 258-263
- Webring, M., 1985, SAKI: A Fortran program for generalized linear inversion of gravity and magnetic profiles: USGS Open File Report 85-122, 29p.
- Wehr, H., Chevrot, S., Courrioux, G., & Guillen, A. (2018). A three-dimensional model of the Pyrenees and their foreland basins from geological and gravimetric data. *Tectonophysics*, 734, 16-32.
- Wellington, S. L., & Vinegar, H. J. (1987). X-ray computerized tomography. *Journal of Petroleum Technology*, 39(08), 885-898.
- Wellmann, J. F., Thiele, S. T., Lindsay, M. D., & Jessell, M. W. (2016). pynoddy 1.0: an experimental platform for automated 3-D kinematic and potential field modelling. *Geoscientific Model Development*, 9(3), 1019. Non cited in the text
- Wenzel, H. (1985). *Hochauflösende Kugelfunktionsmodelle für des Gravitationspotential der Erde*. Wissenschaftliche arbeiten der Fachrichtung Vermessungswesen der Universität Hannover, 137pp.
- Werner, S., "Interpretation of magnetic anomalies at sheet-like bodies," *Sveriges Geologiska Undersök., Arsbok* 43, no. 6, series C, no. 508 (1953).
- White, N., Jackson, J.A. & McKenzie, D.P. (1986). The relationships between the geometry of normal faults and that of the sedimentary layers in their hanging walls. *Jour. Struct. Geol.*, 8, 897-909.
- White, N.J. (1987). Constraints on the measurement of extension in the brittle upper crust. *Norsk geol. Tidsskr.*, 67, 269-279.
- Whitehead, N., & Musselman, C. (2008). *Montaj Gravity/Magnetic Interpretation: Processing, Analysis and Visualization System for 3D Inversion of Potential Field Data for Oasis montaj v6*. 3, Geosoft Incorporated, 85 Richmond St. W., Toronto, Ontario, M5H 2C9, Canada.



- Whiting, M., Salley, S. W., James, D. K., Karl, J. W., & Brungard, C. W. (2020). Rapid bulk density measurement using mobile device photogrammetry. *Soil Science Society of America Journal*, 84(3), 811-817.
- Wilkerson, M. S., & Dicken, C. L. (2001). Quick-look techniques for evaluating two-dimensional cross sections in detached contractional settings. *AAPG bulletin*, 85(10), 1759-1770.
- Wilkinson, M. D., Dumontier, M., Aalbersberg, I. J., Appleton, G., Axton, M., Baak, A., ... & Mons, B. (2016). The FAIR Guiding Principles for scientific data management and stewardship. *Scientific data*, 3(1), 1-9.
- Williams, G. & Vann, I. (1987). The geometry of listric normal faults and deformation in their hanging walls. *Jour. Struct. Geol.*, 9, 789-795.
- Williams, G. D., Kane, S. J., Buddin, T. S., & Richards, A. J. (1997). Restoration and balance of complex folded and faulted rock volumes: flexural flattening, jigsaw fitting and decompaction in three dimensions. *Tectonophysics*, 273(3-4), 203-218.
- Won, I. J., and Bevis, M., 1987, Computing the gravitational and magnetic anomalies due to a polygon: Algorithms and Fortran subroutines: *Geophysics*, 52, 232-238.
- Woodward, N. B. (2012). Evaluation, analysis and prediction of geologic structures. *Journal of Structural Geology*, 41, 76-85.
- Woodward, N.B., Boyer, S.E., & Suppe, J. (1985). An outline of balanced cross-sections. *Studies in Geology* 11. Department of Geological Sciences, University of Tennessee, Knoxville, 170pp.
- Woodward, N.B., Boyer, S.E. & Suppe, J. (1989). *Balanced geological cross sections: An essential technique in geological research and exploration. Short Course in Geology*, 6, AGU, Washington, D.C., 132 p.
- Worral, D.M. & Snelson, S., (1989). Evolution of the northern Gulf of Mexico, with emphasis on Cenozoic growth faulting and the role of salt. In: Bally, A.W., Palmer, A.R. (Eds.), *The Geology of North America – An Overview*. *Geol. Soc. Am.*, 97-138.
- Wright, T. O., & Henderson, J. R. (1992). Volume loss during cleavage formation in the Meguma Group, Nova Scotia, Canada. *Journal of Structural Geology*, 14(3), 281-290.
- Wziontek, H., Wilmes, H., & Bonvalot, S. (2012). AGrav: An international database for absolute gravity measurements. In *Geodesy for Planet Earth* (pp. 1037-1042). Springer, Berlin, Heidelberg.
- Xiao, H. & Suppe, J. (1992). Origin of rollover. *A.A.P.G. Bull.* 76 (4), 509-529.
- Xu, Y., Hao, T., Li, Z., Duan, Q. & Zhang, L., *Regional Gravity Anomaly Separation Using Wavelet Transform and Spectrum Analysis*, *Journal of Geophysics and Engineering*, 6(3), 2009.
- Yamaha, Y. & McClay, K (2003). Application of geometric models to inverted listric fault systems in sandbox experiments. Paper 1: 2D hanging wall deformation and section restoration. *Jour. Struct. Geol.*, 25, 1551–1560.
- Yamamoto, A. (1999). Estimating the Optimum Reduction Density for Gravity Anomaly: A Theoretical Overview. *Journal of the Faculty of Science, Hokkaido University. Series 7, Geophysics*, 11(3), 577-599
- Yang, S., & Wei, J. (2017). *Fundamentals of petrophysics*. Springer Berlin Heidelberg.
- Yang, T.; Gao, J.; Gu, Z.; Dagva, B. & Tserenpil, B., 2013. Petrophysical properties (density and magnetization) of rocks from the Suhbaatar-Ulaanbaatar-Dalandzadgad geophysical profile in Mongolia and their implications. *The Scientific World Journal (Hindawi)*, vol. 2013, Article ID 791918, 12 pp.
- Yonkee, W. A. (1992). Basement-cover relations, Sevier orogenic belt, northern Utah. *Geological Society of America Bulletin*, 104(3), 280-302.
- Zeng, H., Xu, D., & Tan, H. (2007). A model study for estimating optimum upward-continuation height for gravity separation with application to a Bouguer gravity anomaly over a mineral deposit, Jilin province, northeast China. *Geophysics*, 72(4), 145-150.
- Zeyen, H. and Pous, J. 3-D Joint Inversion of Magnetic and Gravimetric Data with a priori Information, *Geophysical Journal International*, Volume 112, Issue 2, February 1993, Pages 244–256, <https://doi.org/10.1111/j.1365-246X.1993.tb01452.x>
- Zinszner, B., & Pellerin, F. M. (2007). *A geoscientist's guide to petrophysics*. Editions Technip
- Zurflueh, E. G. (1967). Applications of two-dimensional linear wavelength filtering. *Geophysics*, 32, 1015–1035.



## Web resources

<http://bgi.omp.obs-mip.fr/>

<http://cuarzo.igme.es/sitopo/>

<http://epncb.oma.be/>

<http://euref.eu/>

<http://igfs.topo.auth.gr/>

<http://info.igme.es/SIGEOF/>

<http://www.europe-geology.eu/> - EGD data repositories,

<http://www.newton-q.eu/> - EU project on MEMS

[http://zlscorp.com/?page\\_id=46](http://zlscorp.com/?page_id=46)

[https://en.wikipedia.org/wiki/Satellite\\_navigation#Global\\_navigation\\_satellite\\_systems](https://en.wikipedia.org/wiki/Satellite_navigation#Global_navigation_satellite_systems)

<https://getech.com/gravity-magnetic/>

<https://glossary.oilfield.slb.com/>

<https://gnss.araqon.es/>

<https://inspire.ec.europa.eu/>

<https://inspire.ec.europa.eu/id/document/tg/ge/>

<https://inspire.ec.europa.eu/id/document/tg/mr>

<https://petrowiki.spe.org/>

<https://scintrexltd.com/about/history/>

<https://www.bgs.ac.uk/products/geophysics/landGravity.html>

[https://www.brgm.eu/sites/default/files/plaquette\\_gravimetrie.pdf](https://www.brgm.eu/sites/default/files/plaquette_gravimetrie.pdf)

<https://www.epos-ip.org/>

<https://www.qo-fair.org/fair-principles/>

<https://www.icgc.cat/es/Administracion-y-empresa/Herramientas/Transforma-coordenadas-y-formatos/ETRS89/Aspectos-geodesicos-del-ETRS89>

<https://www.javad.com/jgnss/products/receivers/triumph-1.html>